University of New Mexico
UNM Digital Repository

Physics & Astronomy ETDs | Electronic Theses and Dissertations

Spring 5-11-2018

High-Throughput Automated Multi-Target Super-resolution Imaging

Farzin Farzam
University of New Mexico

Follow this and additional works at: https://digitalrepository.unm.edu/phyc_etds

 Part of the Astrophysics and Astronomy Commons, and the Physics Commons

Recommended Citation
Farzam, Farzin. "High-Throughput Automated Multi-Target Super-resolution Imaging." (2018). https://digitalrepository.unm.edu/phyc_etds/185

This Dissertation is brought to you for free and open access by the Electronic Theses and Dissertations at UNM Digital Repository. It has been accepted for inclusion in Physics & Astronomy ETDs by an authorized administrator of UNM Digital Repository. For more information, please contact disc@unm.edu.

Candidate

Department

This dissertation is approved, and it is acceptable in quality and form for publication:

Approved by the Dissertation Committee:

, Chairperson

High-Throughput Automated Multi-Target Super-resolution Imaging

by

Farzin Farzam

M.Sc., Optical Science and Engineering, University of New Mexico, 2017

DISSERTATION

Submitted in Partial Fulfillment of the
Requirements for the Degree of

Doctor of Philosophy
Optical Science and Engineering

The University of New Mexico

Albuquerque, New Mexico

July, 2018

©2018, Farzin Farzam

Dedication

To my wife, Aliyeh, for love, support, and countless sacrifices.

To my father's spirit, and to my mother, for all their love and encouragement.

Acknowledgments

I would like to thank my advisor, Dr. Keith A. Lidke for everything he taught me. I would like to thank Dr. Diane S. Lidke for her advice. I would like also to thank Dr. Kevin E. Cahill for his good spirits. I am thankful for Michael Wester's input on the dissertation and for all the discussions we had about life and literature. I am thankful also of my lab mates who made my life as a graduate student easier from time to time, and sometimes harder. I like to show gratitude toward my dissertation committee for their time and good advice which shed light on my scientific path . . .

High-Throughput Automated Multi-Target Super-resolution Imaging

by

Farzin Farzam

M.Sc., Optical Science and Engineering, University of New Mexico, 2017

Ph.D., Optical Science and Engineering, University of New Mexico, 2018

Abstract

Super-resolution microscopy techniques developed through the past few decades enable us to surpass the classical diffraction limit of light, and thus open new doors to investigate the formerly inaccessible world of nanometer-sized objects. Most importantly, by using super-resolution microscopy, one can visualize sub-cellular structures in the range of 10 to 200 nm. At this range, we can investigate exciting problems in biology and medicine by visualizing protein-protein interactions and spatiotemporal analysis of structures of interest on the surface or inside cells. These techniques (collectively known as nanoscopy) have a high impact on understanding and solving biological questions.

This dissertation starts with a brief and general description of current super-resolution techniques and then moves toward a multi-target super-resolution imaging strategy using sequential imaging that has benefits over conventional multi-color imaging methods.

Sequential microscopy takes advantage of the photo-physical properties of the most suitable dye for a particular technique to achieve the optimal and consistent resolution for each of multiple targets of imaging. For example, for dSTORM imaging, this is currently AlexaFluor647. Sequential dSTROM has an advantage for multi-target imaging due to having a single imaging channel which avoids dealing with differential aberration-problems between multiple emission paths unlike other multi-color imaging based methods. We show that sequential imaging method can be facilitated using automated imaging.

In this dissertation, a sequential microscope is designed, calibrated, and tested on multiple structures. We show that it can automatically re-find the position of each initially registered cell and can account for sample drift through an entire experiment. The microscope has been used in multiple collaborations with other groups to investigate biological problems of interest.

Two labeling strategies that facilitate sequential imaging are described. The first strategy is DNA-strand-displacement , which allows imaging of multiple structures in a controlled and time-efficient binding-unbinding scenario. The second strategy is imaging with the small, actin binding peptide Lifeact.

Finally, future directions and suggestions are made about how we can further improve the microscope. In the Appendix I provide a guide on how to use and troubleshoot the microscope, how to measure the efficiency of the microscope, as well as how to fix and label cells for optimal imaging and how to prepare various imaging buffers.

Contents

List of Figures

Chapter 1

A Brief Introduction to Super-resolution Microscopy

Microscopes make quantitative observations possible in life sciences. From the invention of the first microscope until present day, numerous groundbreaking discoveries have been made by using these instruments; among them are the discovery of blood cells, bacteria, and yeast, [14] to name a few. These discoveries and many more created new horizons in cell biology.

In life sciences, we prefer to investigate biological systems in their natural environment. However, in practice, there are issues to consider. Initially one needs to decide between looking at live cells in the body of the specimen (in-vivo) vs. looking at them live and on glass (in-vitro) vs. looking at them dead and on glass but with preserved structure. Since doing experiments in the body of a human or animal is challenging, a reasonable comprimise is to do in-vitro experiments, but there still are multiple limitations born by this choice. Two of the main experimental challenges in collecting live cell data are to have the least amount of photodamage while maintaining a high signal-to-noise ratio and to create a proper environment for cells to

replicate physiological cell dynamics [15, 16].

Finally, although fluorescence super-resolution techniques successfully break the diffraction limit, they are still inferior to electron microscopy techniques concerning resolution. Electron microscopes can achieve Angstrom resolution but at the same time bring multiple disadvantages when used for sub-cellular imaging; using an electron microscope, structures without contrast can not be distinguished from one another, electron microscopy techniques are not suitable for live imaging, and cryogenic temperatures for sample preparation is desirable.

1.1 The Diffraction Limit

A longstanding challenge, once commonly thought to be impossible, in microscopy was to find a way to surpass the diffraction limit. The diffraction limit is the fundamental limit of the resolution of an optical system. Each imaging system has a limiting aperture. The resolution of an optical system is proportional to the wavelength of the observed light source and has an inverse relationship with the aperture. If a circular aperture receives uniform illumination, the diffraction pattern will be an Airy disk, shown in Figure 1.1.

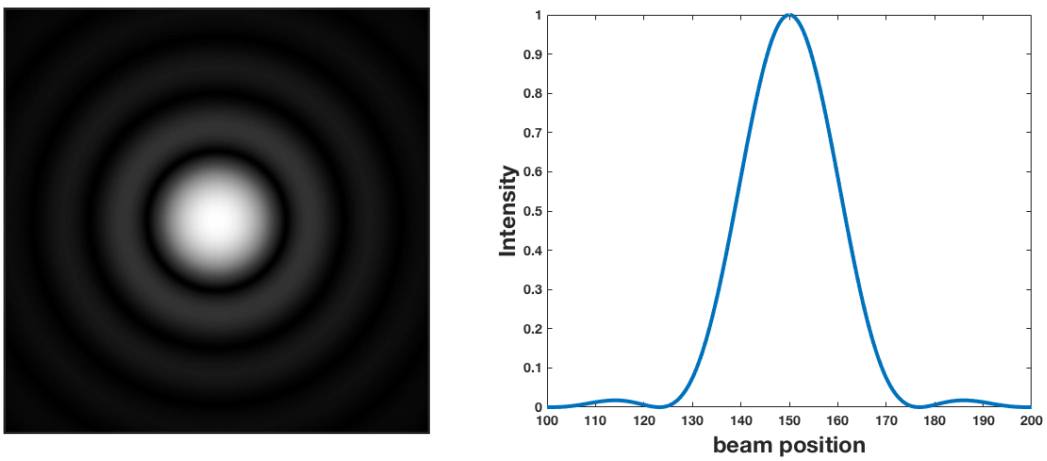

Figure 1.1: Airy pattern formed by diffraction of a uniform illumination from a circular aperture: on the left there is the diffraction pattern and on the right there is the intensity profile for a horizontal line bisecting the left image.

There are three common definitions for diffraction limit. The first two definitions (i.e., Rayleigh and Sparrow limits) are based on arbitrary choices while the third one (i.e., Abbe limit) is based on a spatial frequency cut off due to diffraction of light [17].

Lord Rayleigh defined a limit that is known as Rayleigh criterion for minimum resolvable detail. Mathematically, this criterion is written as $\sin(\theta) = 1.22\lambda/d$ for a circular aperture with radius d that gathers light from emitting point sources as shown in Figure 1.2. Here, λ is the wavelength of light and θ is the angle between two resolvable points. As an example, consider using a telescope with a mirror of the diameter of 1 m to look at two apparently adjacent stars with almost the same brightness at the wavelength of 500 nm, the stars will be resolvable only if they are farther than 6.1×10^{-7} rad, which means, If the stars are both 1 million light years away from earth, they need to be at least 0.61 light years apart from each other, for the telescope to be able to resolve them.

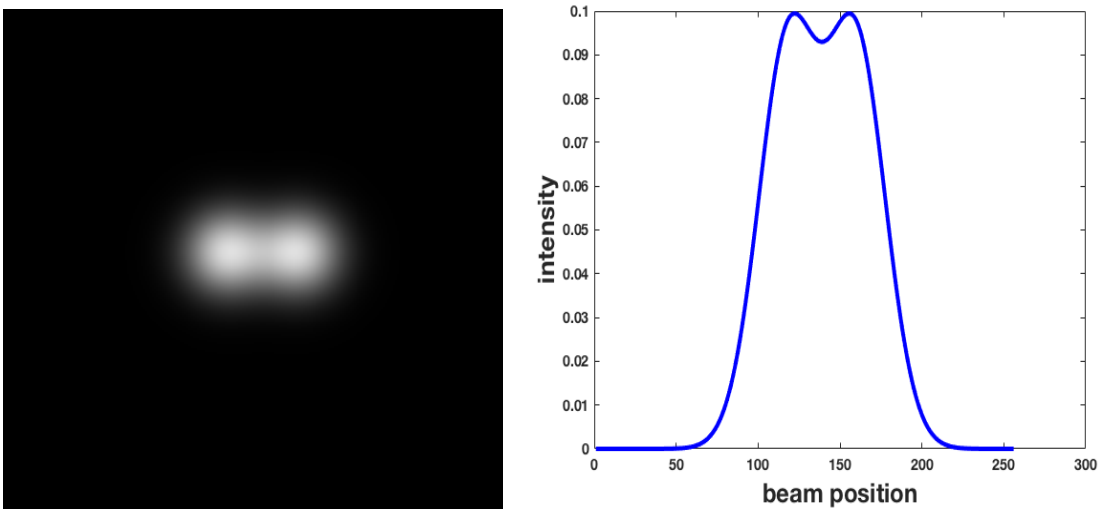

Figure 1.2: Rayleigh criterion for two emitters: on the left are two emitters separated by the Rayleigh distance and on the right is the intensity profile for the horizontal bisection of the left image.

The Rayleigh criterion gives a mathematical measure for separating two light sources, but when using an optical telescope, two stars at distances smaller than this criterion are still distinguishable. In order to have a measure that enables us to distinguish two point sources of light (i.e., two stars) from one, C. M. Sparrow defined a resolution limit equal to 80% of the Rayleigh criterion. At this angular distance, centers of two Airy disks can be connected via a line of constant and equal intensity as shown in Figure 1.3. This means that in the example above, we will still be able to count the image as two stars if there are 0.48 light years apart from each other.

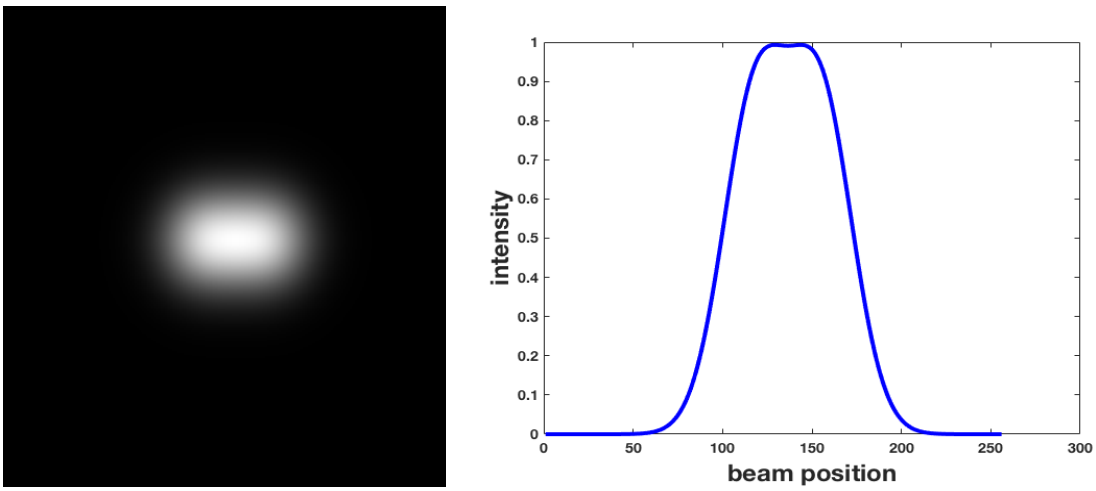

Figure 1.3: Sparrow limit for two emitters: on the left are two emitters separated by the Sparrow distance and on the right is intensity profile for the horizontal bisection of the left image.

The Abbe criterion is the definition for the diffraction limit which is used extensively in microscopy. In the Rayleigh and Sparrow limits, the definition of criterion is based on resolving two point emitters but the Abbe criterion emphasizes on a spatial frequency cut off created by the diffraction limit as shown in Figure 1.4. This cut off appears in the Optical Transfer Function (OTF), which is the Fourier transform of the Point Spread Function (PSF) of an optical system. The PSF describes how a point source of light will look like when imaged by the optical system.

The Abbe diffraction limit states that resolution of a lens is proportional to the wavelength of the emitter and to the inverse of the numerical aperture (N_a), where $N_a = n\sin(\theta)$, n being the refractive index of the medium between the lens and the sample and θ is the half angle of the cone of light into the lens.

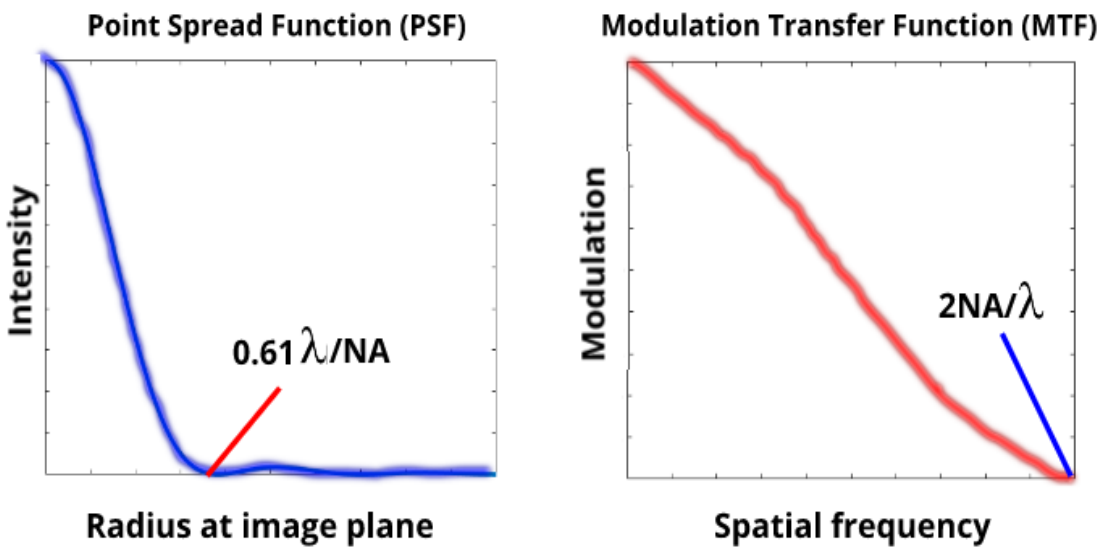

Figure 1.4: Abbe diffraction limit: Airy pattern for a single emitter (left) and Modulation Transfer Function (MTF) which is the amplitude of the Fourier transform of the Airy beam (known as Optical Transfer Function or OTF), showing the cut off on spatial frequency.

In microscopy we use objective lenses to gather the emitted light from the sample plane []. Common immersion media between objective and coverslip are water, air, and more recently silicon oil. One way of categorizing objective lenses would be to put them in three separate groups of oil objectives, water objectives, and air objectives. Among these three groups, oil objectives have the highest numerical aperture. Based on the Abbe criterion, for a light source of $\lambda = 600$ nm and an oil objective with a high numerical aperture of N_a=1.5, the Abbe diffraction limit in the lateral direction will be $\lambda/2N_a$=200 nm and in the axial direction $2n\lambda/N_a^2$=800 nm which is almost four times the resolution in lateral direction.

1.2 Super-resolution Techniques

Calculations in the previous section show there exists a limit for the resolution of a conventional optical microscope. Super-resolution techniques were developed to overcome the diffraction limit and achieve high enough resolution to investigate nanometer scale. All current methods that break the diffraction limit make use of the independence of individual emitters. Super-resolution techniques can be further classified into those that make use of stochastic independence or structured independence[18]. Commonly the independent behavior is the ability for each emitter to switch between two states, such as a dark and fluorescent state.

An example of a technique that are based on structured switching is Stimulated Emission Depletion (STED)[19]. The fundamental principle behind STED is a method to reduce the fluorescent emission from the outer section of an excitation volume by switching molecules in this region to a ground state. STED decreases the fluorescence emission volume by using an auxiliary laser beam that creates a doughnut-like illumination on the excitation volume, as seen in Figure 1.5.

All fluorescence emission from the outer section of the excitation volume is depleted through sending fluorophores to the ground state via stimulated emission, using the second laser beam [20]. The light from stimulated emission is separated from the emission by wavelength.

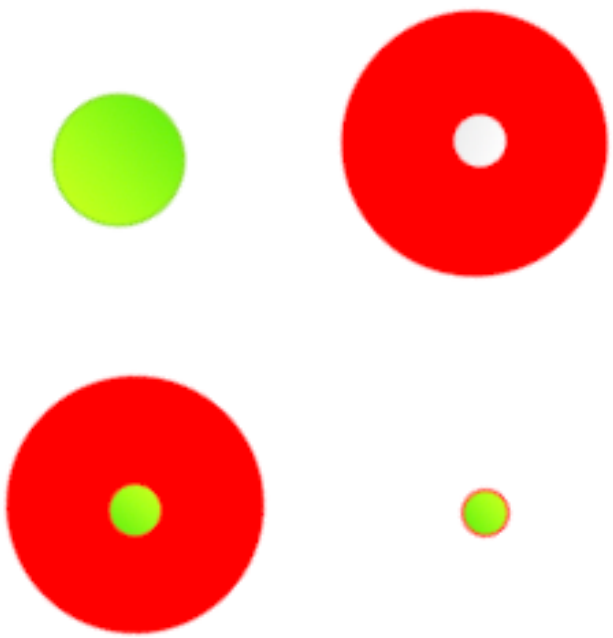

Figure 1.5: STED principle: Two synchronized laser pulses are focused on the sample, one to excite and one to deplete the fluorescent molecules, to achieve single molecule localization. The focal spots produced by the STED laser and the depletion laser are shown as green and red circles, respectively. As a result of the doughnut shaped beam, only the molecules at the center of the doughnut will be on and localized accurately, while all the neighboring molecules are off.

The shape of the STED beam at the sample plane is determined by the phase pattern in a phase mask. In the most common approach, the laser intensity is highly concentrated at the doughnut ring and drops at the center. Molecules at the center emit light. Continuing advances have helped to simplify implementations of STED, for example less complicated alignment, continuous wave (CW) laser, number of available dyes across the visible spectrum, and 3D live cell imaging [21, 22].

Single-molecule localization microscopy (SMLM) techniques use the stochastic switching and/or activation of fluorescent labels to localize in each frame, a small percentage of the total number of emitters, and use these localizations to reconstruct

a super-resolution image.

SMLM techniques include photo-activated localization microscopy (PALM), fluorescence photoactivation localization microscopy (FPALM), stochastic optical reconstruction microscopy (STORM), and direct STORM (dSTORM). With each of these techniques, only a well separated small subset of fluorophores emits fluorescence light at each frame so we can localize the position of a single fluorophore.

The principle behind (f)PALM is that a sparse subset of photo-activatable fluorescent proteins (PA-FP), that are attached to proteins of interest and then fixed within a cell, are activated by a laser pulse at λ_{act} and imaged at λ_{exc} until most are bleached. This process is repeated until the population of inactivated molecules that are not bleached gets depleted. After localizing all the FPs, by summing all the frames, on can create a super-resolution image.

The (f)PALM method is illustrated in Figure 1.6. If the location of each molecule is first determined by fitting the expected molecular image given by the PSF of the microscope, each molecule can be plotted as a Gaussian that has a standard deviation equal to the uncertainty σ_{xy} in the fitted position.

Repeating with all molecules across all frames and summing the results yields a super-resolution image in which resolution is dictated by the uncertainties as well as by the density of localized molecules. This process is repeated until a sufficient number of emitters is recorded to reconstruct the super-resolution image [23].

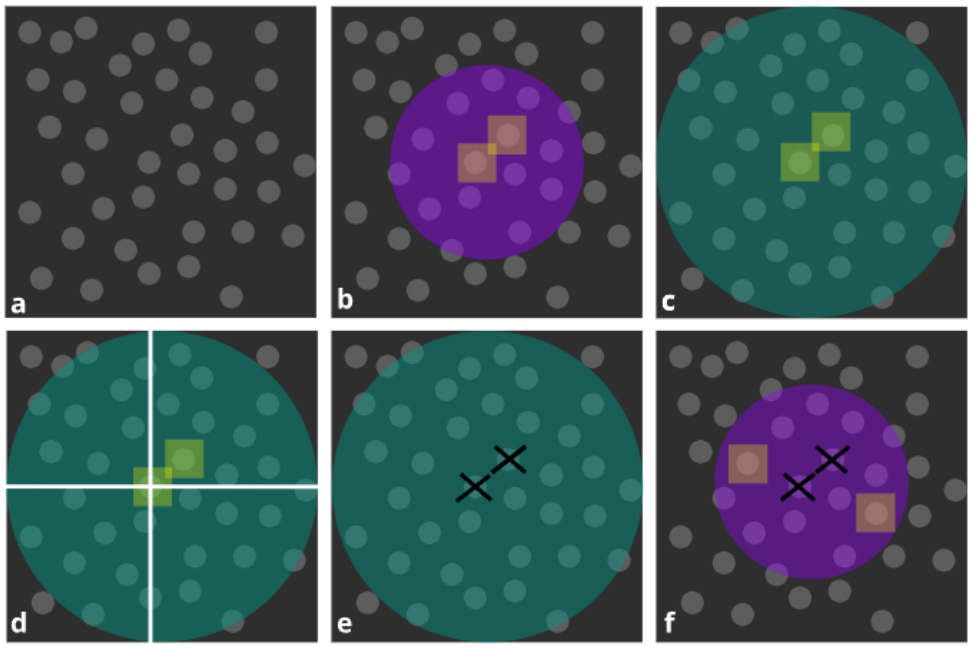

Figure 1.6: PALM principle: (a) Initially all molecules in the specimen are inactive (dark circles). (b) A sufficiently low intensity 405 nm laser photoactivates a small number of molecules. Photoactivation of the molecules occurs stochastically. (c) The 561 nm readout laser is used to detect the position of the photoactivated molecules within the illuminated area. (d) Digital images of the photoactivated molecules are analyzed to identify and localize molecules that remain fluorescent. (e) Photoactivated molecules spontaneously photobleach. (f) A new set of molecules is photoactivated.

STORM is based on stochastically switching of single molecule optical switches based on two dyes in close proximity on and off using light of different colors. The use of a photo-switchable cyanine dye, Cy5, is demonstrated in [24]. Cy5 can both fluoresce and switch to a stable dark state under a red laser illumination [**?**]. It can be converted back to the fluorescent state by exposure to a green laser, but the recovery rate depends critically on the close proximity of a secondary dye, Cy3. Therefore, the target proteins are labeled with Cy5-Cy3 dye pairs, in which Cy3 acts as an activator, which influences the activation of the reporter, Cy5. During data acquisition,

the sample is alternately illuminated by an excitation laser and an activation laser. The excitation laser has relatively high intensity, which excites activated reporter fluorophores to an excitation state, switching most of them into a dark state, while the activation laser is used to switch a fraction of the reporter fluorophores from the dark state to the active state. However, in the STORM imaging technique, a STORM imaging buffer, which consists of an enzymatic oxygen scavenging system and a reducing agent, is critical for reducing the oxidation and enhancing the photo-switching ability for the fluorophores. Thus, the fluorophores can be switched on and off hundreds of times before being permanently photo-bleached [25, 26].

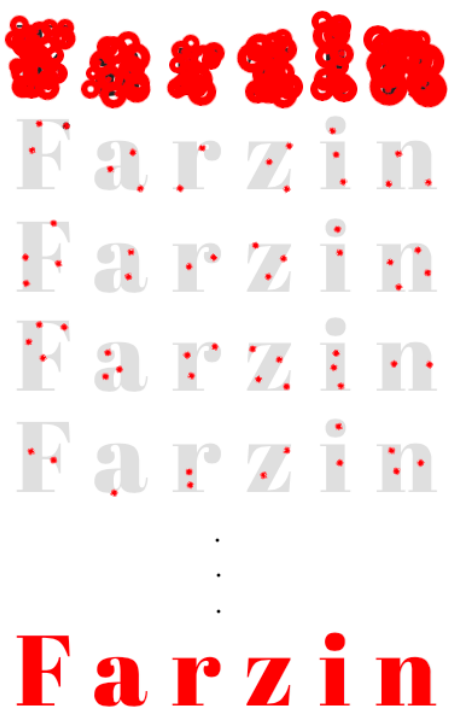

Figure 1.7: dSTORM scheme: if all molecules that bear fluorescent tags are on at the same time, we will get a blur since each molecule is seen with the size of a PSF. With dSTORM, 99% of molecules are off, while 1% comes out of the dark state stochastically; one is able to fit a Gaussian and then find its center. After tens of thousands of frames, reconstructing the final image, we get a sharp Farzin.

dSTORM simplifies the STORM technique by labeling samples with only one type of fluorophore, while the sample is simultaneously illuminated, one for excitation and one for activation. In dSTORM dyes like Cy5 and the structurally similar cyanine derivative, AlexaFluor647, can be reversibly switched for hundreds of cycles between a fluorescent state and a dark state without the need of an activator fluorophore. The dSTORM scheme can be seen in Figure 1.7.

1.3 Multi-Target Sequential Imaging

Many biological questions of interest are related to the organization of multiple structures with respect to one another inside a single cell. For example, investigation of proteins involved in signaling cascades plays an essential role in understanding complicated mechanisms of different types of cancer and allergies. To investigate such problems one needs to image multiple structures in a single cell.

There have been various efforts to come up with useful strategies for multi-target super-resolution imaging. Bates et al.,[27] showed results on dual-color STORM by using a family of fluorescent labels such as Cy2-AlexaFluor647 and Cy3-Alexa-647 in an activator-reporter scheme. In this scheme, there is a molecule called reporter which is a photo-switchable fluorophore, and a molecule that helps the reposter to get photo-activated, and is called the activator.

Shroff et al.,[28] showed results on dual-color PALM by using pairs of endogenously expressed photoactivatable fluorescent proteins tdEos- Dronpa/PSCFP2 with the advantage of being able to be viewed in live cell by conventional epi-fluorescent techniques before fixation. Andresen et al.,[29] introduced two bright green fluorescent proteins, bsDronpa and Padron, generated by extensive mutagenesis of the reversibly switchable fluorescent protein (RSFP) Dronpa, with unique absorption and switching characteristics. Whereas bsDronpa features a broad absorption spec-

trum extending into the UV, Padron displays a switching behavior that is reversed to that of all green fluorescent RSFPs known to date. These two RSFPs enable live-cell fluorescence microscopy with multiple labels using a single detection color, because they can be distinguished by photoswitching. This paper also studied an alternative approach to multi-color measurements based on the use of spectrally closely spaced probes to be assigned to a specific color based on the ratio of the photons detected for each emitter in each of the spectral channels and for this purpose they used bsDronpa and Dronpa whose emission maxima are separated by less than 20 nm. Subach et al.,[30] reported implementing red PAFPs allowing for simultaneous imaging using PAGFP as a green partner. They specifically developed PAmCherry1 with excitation/emission maxima at 564/595 nm to use along GFP for PALM dual-color imaging. Baddeley et al.,[31] approach was to combine 3D and spectral super-resolution simultaneously with readily available fluorochromes as well as operating in a wavelength range where biological autofluorescence is minimised. They used a combination of conventional near-infrared dyes, such as Alexa 647, Alexa 680 and Alexa 750, all excited with a 671 nm and separated them in emission path.

Wilmes et al.,[32] showed 3 color live cell super-resolution imaging by using HaloTag in dSTORM. Endnesfelder et al.,[33] produced a review on fluorescent probes that can be photoswitched/photoactivated and suited for single-molecule localization based super-resolution microscopy and showed that a combination of a suitable organic dye and fluorescent protein would allow dual-color imaging using both organic fluorophores and fluorescent proteins. Lampe et at.,[34] developed a technique for multi-target dSTORM. The search for the ideal dye pairs suitable for dual−color dSTORM has been compromised by the fact that fluorophores spectrally apt for dual?color imaging differ with respect to the optimal buffer conditions required for photoswitching and the generation of prolonged non−fluorescent (OFF) states. They present a variant of dSTORM that combines spectral demixing with the buffer compatible blinking properties of red emitting carbocyanine dyes and call

it spectral demixing dSTORM or SD-STORM.

Jungmann et al.,[35] reported Exchange-PAINT based on formerly developed DNA-PAINT [36] approach that allows sequential imaging of multiple targets using a single dye and a single laser source. They showed four-color two-dimensional (2D) imaging and three-color 3D imaging of proteins in fixed cells. Zhang et al.,[37] synchronously obtained the fluorescence spectra and positions of about 10^6 single molecules in labeled cells in minutes, which consequently enabled spectrally resolved, true-color super-resolution microscopy. The method, called spectrally resolved stochastic optical reconstruction microscopy (SR-STORM), achieved cross-talk-free three-dimensional (3D) imaging for four dyes 10 nm apart in emission spectrum. Excellent resolution was obtained for every channel, and 3D localizations of all molecules were automatically aligned within one imaging path. There have been other PAINT-like variations for example in Chapter 5, we used a DNA-strand-displacement scheme where antibodies are pre-conjugated to a protector strand of ssDNA. After cellular labeling and before imaging, a complementary template strand, which is labeled with the dye, is added to the sample to bind and label the protector. This approach is shown with complete details in Chapter 5 of this dissertation.

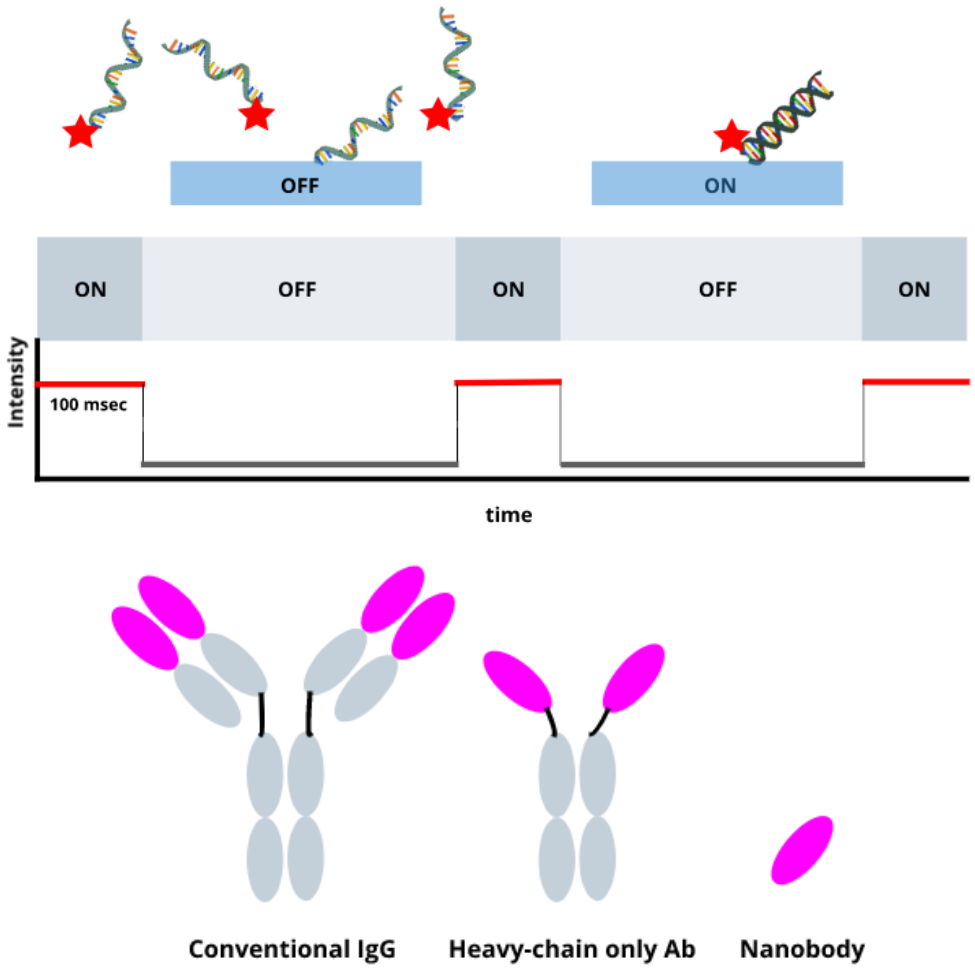

Figure 1.8: Various labeling strategies for super-resolution imaging. (top) DNA-PAINT: in this method, we have the imaging strand, which are DNA strands conjugated to a dye, and docking strands, which are the complimentary single DNA strands that can bind to the target molecule we want to image and also can bind to the imaging strands to create a blinking mechanism through binding/unbinding events. (bottom) IgG, antibody, and nanobody are proteins of different sizes that can be conjugated to dyes and are designed to attach to specific targets.

A strategy for investigating the organization of multiple structures in a single cell is to label different structures at the same time with various structure-specific agents, in the same imaging buffer where each structure-specific agent has a fluores-

cent tag with well-separated emission spectra. Since the excitation wavelengths of these tags would be different, several excitation lasers are necessary as light sources in the optical system, which implies the need for multiple optical paths at the excitation and emission side of the microscope. There are two main problems related to the strategy above. First, different dyes have different photo-physical properties so having them at the same time in the same dSTORM imaging buffer will result in different imaging resolutions for each group of dyes, since we can only optimize the oxygen scavenging condition and mercaptoethylamine (MEA, which works best for xanthene dyes) or β-mercaptoethanol (BME, which works best for cyanine dyes) concentration for one type of dye. Second, multiple optical paths in the emission side will result in differential aberrations which are important when investigating the organization of various structures in nanometer scale. To solve these problems, one must pay attention to two essential properties of a fluorescent dye, i.e., duty cycle and the number of photons per emission [38]. A comparison of three different dyes is shown in Figure 1.9 trying to image a ring-like structure, like a 2D cross-section of a clathrin-coated pit.

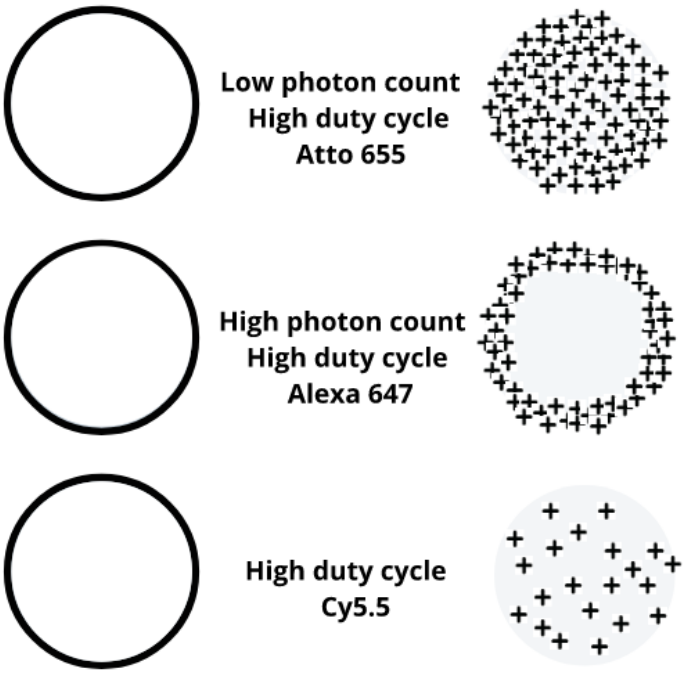

Figure 1.9: Duty cycle and photons per emission for different dyes: (top) Atto655, (middle) AlexaFluor647, (bottom) Cy5.5.

In a paper published by our lab, Valley, et al. [1] shows that by using the fluorescent dye with the most desirable photo-physical properties (i.e., AlexaFluor647), problems related to different photophysical properties of the dyes that are used for imaging, can be solved. They showed that one could take advantage of AlexaFluor647 photo-physical properties for multiple structures if we image them, not at the same time on various cameras or different regions on the same camera, but to image them sequentially. Figure 1.10 shows how sequential imaging works.

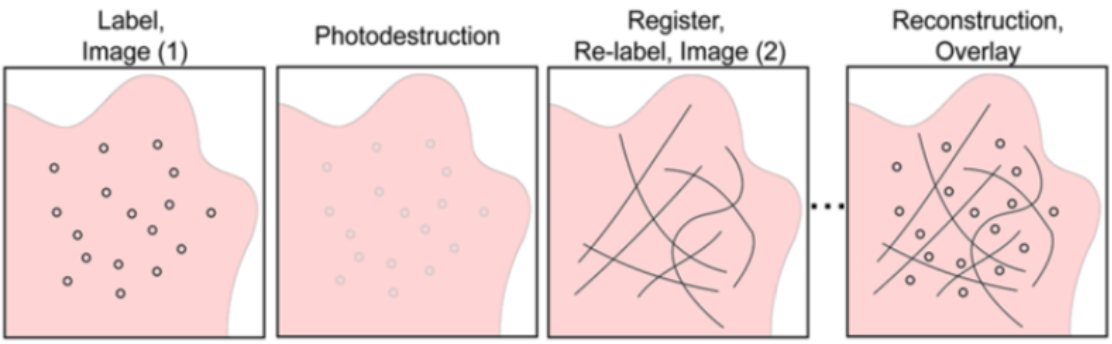

Figure 1.10: Sequential imaging scheme. Adapted from figure.1 of Valley et al [1].

There are several advantages in designing a dedicated microscope for sequential imaging. The main benefits are to have an optimized optical path for AlexaFluor647 and to automate the imaging workflow which decreases the labor needed from the user in imaging multiple cells. Drift correction algorithms are also used to correct for drift as imaging is taking place. In this dissertation, the details of the design of the microscope and all the calibration needed for the hardware to make the imaging system work correctly will be provided. This dissertation also shows some of the sortware written to get all parts of the device to work together. The graphical user interface (GUI) designed for automation of taking the data was described in detail, then a repositioning reliability test by imaging α-tubulin and β-tubulin in the same cell will be performed to show the microscope works appropriately. Finally two biological questions of interest will be investigated.

Chapter 2

Sequential Microscope Design

As discussed in Chapter 1, the goal of the instrument described herein is to perform automated high-throughput sequential imaging on fixed cells to image multiple targets. The specific design of the system should embody the following characteristics:

1- Multi-Target super-resolution imaging.
2- Single fluorophore imaging.
3- Automated data acquisition.
4- High-throughput data acquisition.
5- Drift correction while imaging.

Now we can go through them them one by one.

1- Multi-Target super-resolution imaging:

Multi-Target super-resolution imaging techniques and history of their development were reviewed briefly in Chapter 1, and we mentioned some of the advantages and disadvantages of these methods. Sequential imaging helps the user to avoid many of the major problems of the traditional multi-color methods. Sequential labeling and imaging allows the imaging of multiple structures in the same cell using a single

fluorophore species, which is beneficial since in super-resolution applications, the optimal dye suited to the method can be chosen, the optical setup can be simpler and there will be no chromatic aberrations between images of different structures and no registration method will be needed between imaging channels on the detector. In Chapter 5, we will also describe a labeling method based on DNA strand displacement that is beneficial to our sequential imaging scheme, to quickly and easily perform the labeling and removal of the fluorophores during each sequence.

2- Single fluorophore imaging:

Imaging multiple targets with a single fluorophore has benefits over imaging them with various fluorophores. When we image each unique structure with its specific fluorophore (as we image all targets at the same time and in multiple emission channels), different photo-physical properties of the dyes cause the resolution of each structure not to be the same as the other structures [33]. Since we want to have the same resolution for different structures, it is better to use a single fluorophore for all of them.

There are two options when choosing a dye; Photoswitchable fluorescent proteins and organic fluorophores. The first option has the advantage that they can be genetically attached to a protein of interest and provide stoichiometric labeling. In addition, fluorescent proteins do not require specific imaging buffers and can be used for live-cell imaging. One disadvantage of fluorescent proteins is their lower brightness, which decreases the localization accuracy and the optical resolution. In addition, experiments that aim to follow dynamic processes require multiple read-out cycles of photoswitchable fluorophores, and only few photoswitchable fluorescent proteins are available for this purpose so far. Bright and at the same time reversibly photoswitchable fluorescent proteins are thus rare, and organic fluorophores are sometimes an attractive alternative choice.

A key factor affecting the quality of dSTORM images is the choice of the proper

switchable probe. The reversibly switchable probes, which include many of the organic dyes, can be converted between fluorescent (on) and dark (off) states multiple times upon excitation by light either of the same or different wavelengths. Two properties of switchable probes crucial to super-resolution image quality are, first, the number of photons detected per switching event, and second, the on/off duty cycle (or the fraction of time a fluorophore spends in the on state).A fluorophore with good characteristics isis AlexaFluor647[38], but then we will need to image the structures sequentially, otherwise they can not be recognized on the detector from one another if labeled with the same dye.

3- Automated data acquisition:

User interactions with the microscope can create errors in the measurement process. One crucial user related error happens in the cell repositioning process. Cell repositioning is necessary when the user needs to image multiple labels (i.e., various structures) in a single cell, as shown in Figure 2.1. To do this, after imaging the first round, she needs to take the sample off the microscope, put the new label on, and put the sample back on the microscope and find the same cell she imaged in the first round. In microscopes that don't use a motorized stage with a home position (i.e., a fixed reference position), this error can be avoided. We use the idea in the design of our sequential microscope. We want automated data acquisition for multiple cells for each round of imaging, whereby each round of imaging we mean imaging multiple cells for the same labeled target structure.

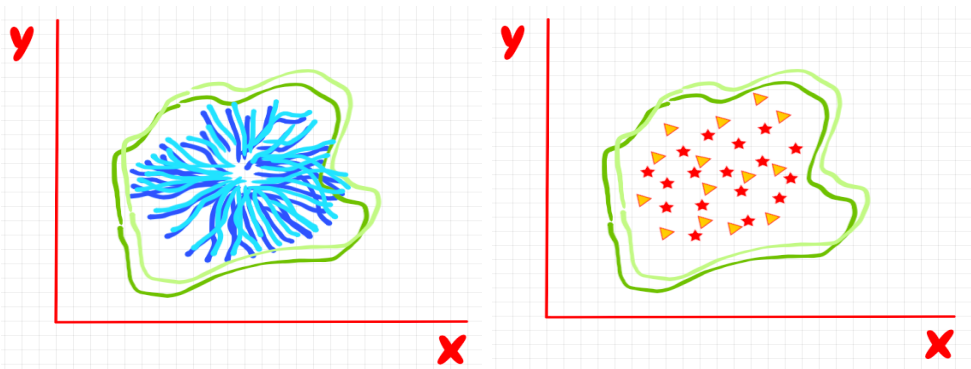

Figure 2.1: Cell repositioning: on the left we see a cell repositioning failure by a user that has done it manually. If we image the same structure (shown in blue) we can see the shift after reconstruction. On the right, user is imaging two different structures, so if an unwanted uncorrected shift happens, the resulting overlay between two structures can not be trusted.

4- High-throughput data acquisition:

When the user wants to image one or more structures on multiple cells, he/she would benefit if the imaging system can collect high-throughput data, meaning a large number of cells per cover slip, This means that at each round of imaging, a high number of cells are imaged by the microscope without the intervention of the user.

High-throughput data acquisition has different meanings in different contexts. In electron microscopy or wide-field imaging in a clinical environment for pathology purposes, one might expect tens of coverglasses imaged within minutes. This type of high-throughput imaging requires pattern recognition where having only a widefield image of a cell or a group of cells is enough for the related analysis. In our context, by high-throughput imaging we mean between 40-50 cells per cover slip and the goal is to have super-resolution data of all these cells. Although in typical biological applications, this term points to thousands of cells being imaged in few minutes with conventional microscopy techniques, but for super-resolution imaging

modalities, imaging 40-50 cells per round in few hours is high enough to justify using the term high-throughput. Here we make a rough calculation of data acquisition time-scale for our scheme, we need around 40,000 frames with about 10 milliseconds data exposure time to reconstruct a super-resolution image with enough data points. This calculation results in about 4 and a half hours of imaging time. In addition to the imaging time, we need some time for repositioning each cell and also for saving the data to the hard drive. For multiple structures, we need to count in the photo-bleaching, quenching and relabeling time. So the best interest of the user is to be able to automatically image a high number of cells without being physically present at the microscope while taking the data. For imaging multiple structures, high throughput imaging saves not the only time of user but has the benefit of cutting out the user induced errors.

5- Drift correction while imaging:

Drift correction or active stabilization is an important topic in microscopy. There are different sources for drift, like relaxation of stepper motor gears, stage settling, and temperature. Temperature control is not always possible in an experimental setup and if the experiments are lengthy, taking several hours, due to the temperature change during the day/night cycle, one needs to have a strategy for dealing with temperature induced drift of the sample/sample holder. By automating the microscope and using two stages to combine long range and good precision, we can perform live drift correction as the experiment is running. The benefits of doing live correction will be explained in the drift section of this chapter. We need an optical system that has all the five qualities mentioned above. Furthermore, we need a code that runs all the hardware in harmony, preferably through a graphical user interface (GUI) at the user's end and provides automated data acquisition with minimal intervention. All the code used is home written with object-oriented programing via classes designed to control devices and data flow. Now, we will discuss all steps needed in the design and then in the next sections will go through the details of characterizing each step.

First of all, to image multiple cells sequentially for various labels, we need to be able to go back accurately to the initial position of each imaged cell in order to image the next label for that cell. The accuracy we need for replacing the cells is on the order of few nanometers. This ability is provided by using a motorized stage that has a home position. The stage we use to provide such ability is a Thorlabs's three-axis stepper motor with the minimum step size of 100 nm, accompanied by a Thorlabs's 3D piezo stage with positioning accuracy of 5 nm. These two stages, together, are called NanoMax Flexure Stage (MAX341/M by Thorlabs).

2.1 Hardware and Optical Design

Here I show the final result of the optical design of the microscope in Figure 2.2. In subsequent sections I will go over the details of each major section of the microscope and why it is designed the way it is.

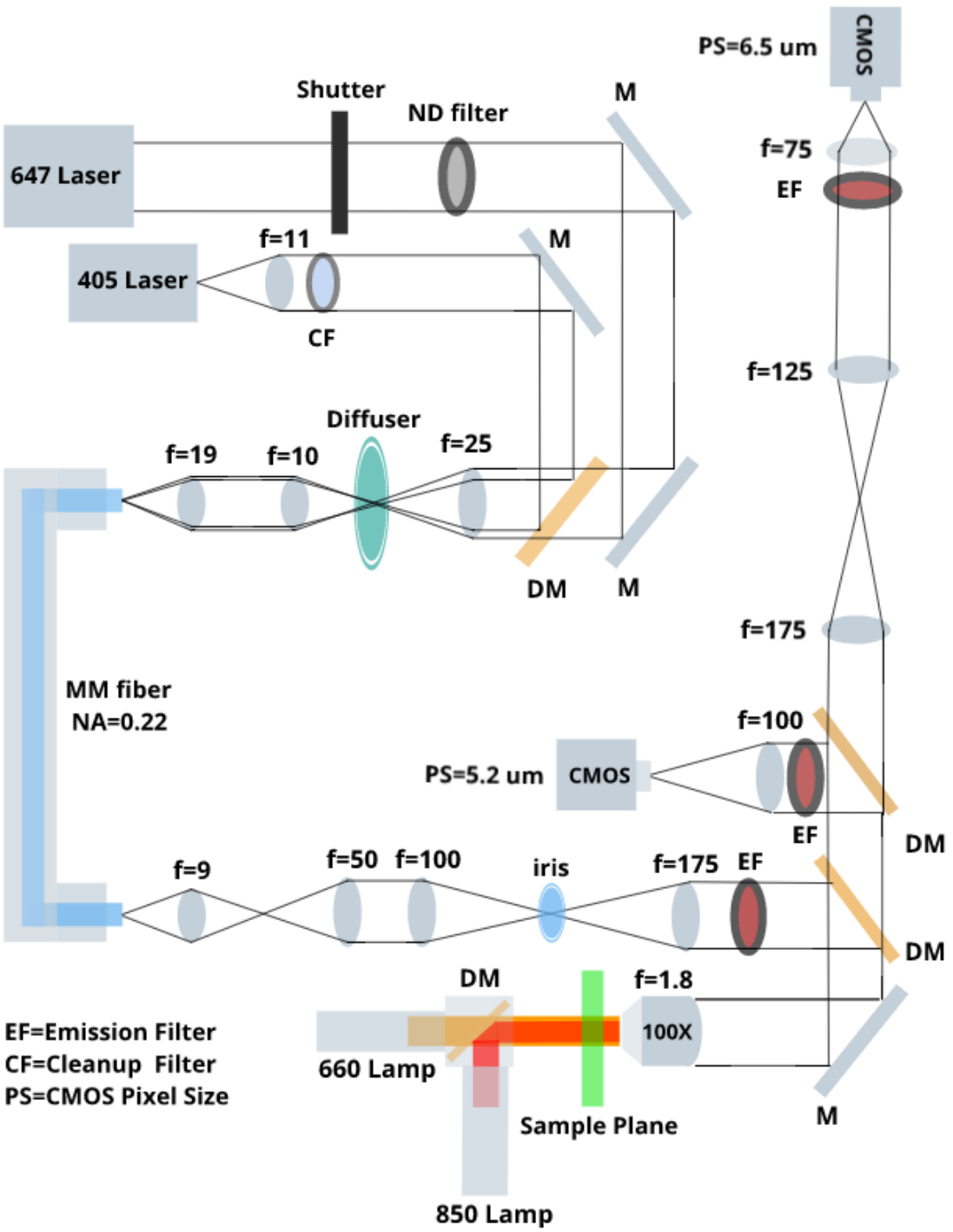

Figure 2.2: Overall optics of the microscope

2.1.1 Excitation Path Optics: from Laser to Fiber

Excitation path design is explained in two pieces. In this section we have the final design of the excitation path from laser to fiber. I will explain in detail the motivation of this design.

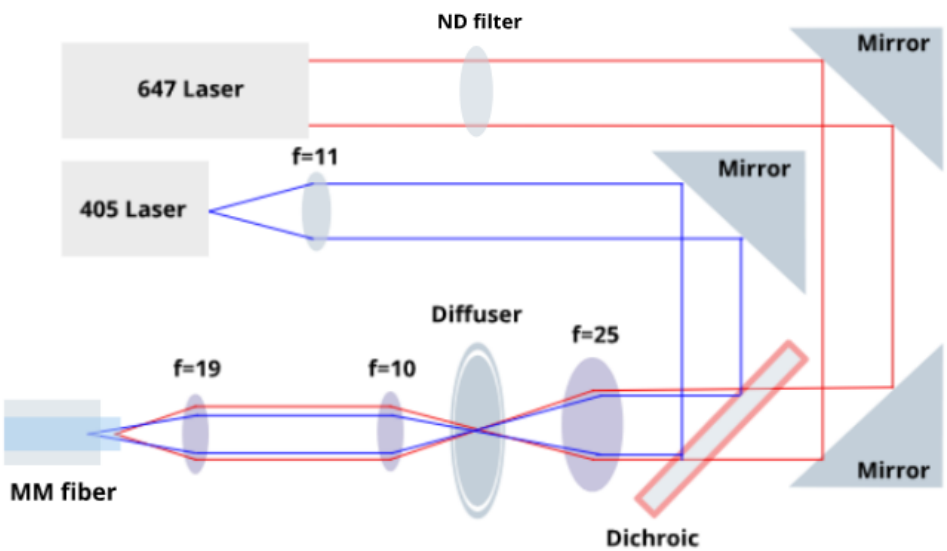

Figure 2.3: Optical path for coupling light into the multi-mode fiber. Input power to the fiber can be adjusted with a combination of electronic control of the laser (50 mW-500 mW) and a flip-mount neutral density (ND) filter.

There are four different and critical elements in this section of the excitation path. Here we name them one by one and explain their role in the sequential microscope, thus explaining why they should be in the setup and how they work with elements before and after them:

1-MPBC Fiber laser:

We need an excitation laser to excite our dye AlexaFluor647. We can pick from a range of lasers. Before we get into why we pick this specific laser, it is good to take

a look at the excitation spectrum of the dye; see Figure 2.4.

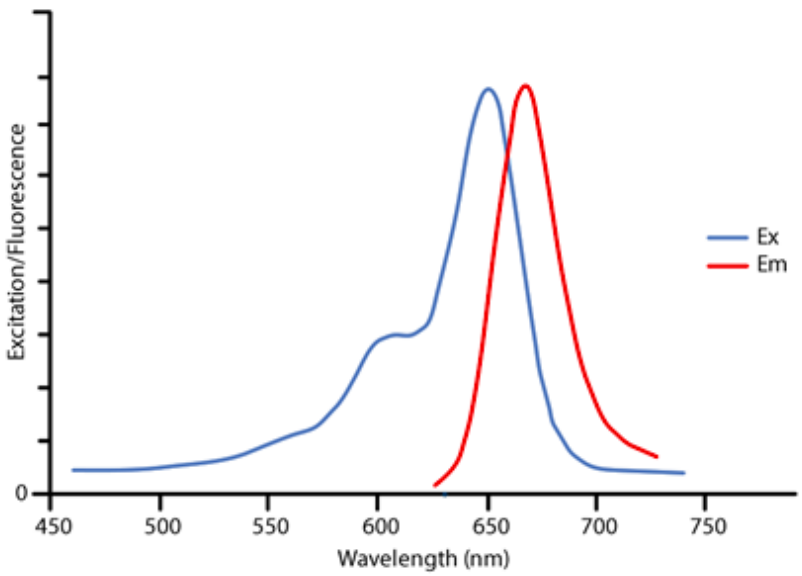

Figure 2.4: Excitation and emission spectrum for AlexaFluor647 by Jacksonimmuno.com

Based on the excitation spectrum in Figure 2.4, we can pick a laser line anywhere between 635 nm to 655 nm to excite the dye before the peak of excitation falls too low (less than the full width half maximum i.e., the FWHM) but now other factors come to play like wavelength stability, power stability for long term use, having a narrow linewidth, tunability of the output power, and a well defined clean beam shape. The MPBC laser is chosen based on these considerations. Here are the qualities of the product we use:

1- Ellipticity on average is 7% which means the beam is very close to a circle in a cross-section with respect to the axial direction of propagation.
2- M^2 beam quality: a low M^2 value indicates the ability to be focused to a tight spot. M is the ratio of the beam angle of divergence to that of a Gaussian beam with

the same waist width. Here M=1.08.
3- Emission Linewidth (FWHM) is 0.1 nm so we have a narrow accurate spectrum.
4- Active Power Stabilization to ensure long term power stability smaller than 2%.
5- Wavelength stability to ensure spectral purity (0.02 nm).
6- 99% linearly polarized light in TEM_{00} mode with polarization direction vertical to the base.
7- CW collimated beam with tunable power between 50 mW and 500 mW.

Some of these qualities are of more importance and some are not a key factor in why we chose this laser. We want a CW beam with tunable power that can go up to few hundred milliwatts, we also want a stabilized power for long term which is not provided by many diode lasers. Emission linewidth is of importance but having a 0.1 nm for FWHM is better than needed, and the same can be said for wavelength stability. Other factors (ellipticity, M^2 factor, and linear polarization) are only important to the degree that we can have a relatively good beam shape to put through optical diffuser and multi-mode fiber, other than that, for example we do not require linear polarization in our current system.

2- Diode laser with 405 nm wavelength:
Now we will consider the second part of the excitation path which is the activation laser line.

We need a laser line with wavelength of around 400 nm for taking the emitters out of their dark state. This duty is specifically needed when photobleaching the sample after taking the data and can also be used to accelerate data collection of sparse structures. Since we don't need high intensity to take the fluorophores out of their dark state (less than 0.1 kW/cm^2), a diode laser that can produce few milliwatts at the output of the fiber is enough.

Therefore, we choose an inexpensive diode laser and controller, a laser mount

that is temperature controlled, a cleanup filter, and an aspherical lens to collimate the output beam of the diode laser into the excitation path of the microscope. The laser mount is shown in Figure 2.5.

As mentioned in the caption of Figure 2.5, the laser mount needs to be connected to the laser controller. The laser controller is itself connected to the computer by a USB connection so the user can control the on/off mode and power of the diode laser by the code from computer. Figure 2.5 shows the laser controller and how it functions.

Figure 2.5: Laser mount LDM9T/M. Number 1 is the temperature control knob, number 2 is the on/off switch, number 3 is the connection port from the diode laser power controller to the laser mount, number 4 is the power supply, and Number 5 is the mount plate that the user needs to put the three pins of the diode into the correct order to produce laser light. This figure is taken from [2].

3-Optical Diffuser (also known as laser speckle reducer):

Once the decision for lasers is made, we need to decide on a strategy for taking excitation light from the lasers to the sample plane. One way is to take the light

directly from laser output. This way, we will have two Gaussian beams on the sample plane. These Gaussian beams need to be magnified each by a specific amount (based on their initial beam size) to have the right size on the sample plane to provide the proper intensity needed for imaging and for photobleaching.

The problem with this approach is that there will be speckle patterns and the Gaussian beam profile present at the sample plane which is not ideal for imaging. Gaussian beam profile causes a non-uniform illumination of the sample plane, thus the structures that are imaged will receive different intensity as a function of their position with respect to center of the Gaussian beam. The speckle patterns are random and change the uniformity of illumination for each location randomly as a function of time. We need to eliminate these two problems and have a uniform non-random pattern over the area we are imaging. One approach to solving this problem is using a combination of multi-mode fiber and a speckle reducer [39].

An optical diffuser is a glass with random roughness designed on the surface to scatter incoming light into a specific output angle. An effective addition is to have a motorized system to vibrate the glass with a high frequency through an oscillating electric current, which will provide smoother output since the average of the scattered patterns over time will look smoother. In Figure 3.1 we see the principle of how the diffuser works.

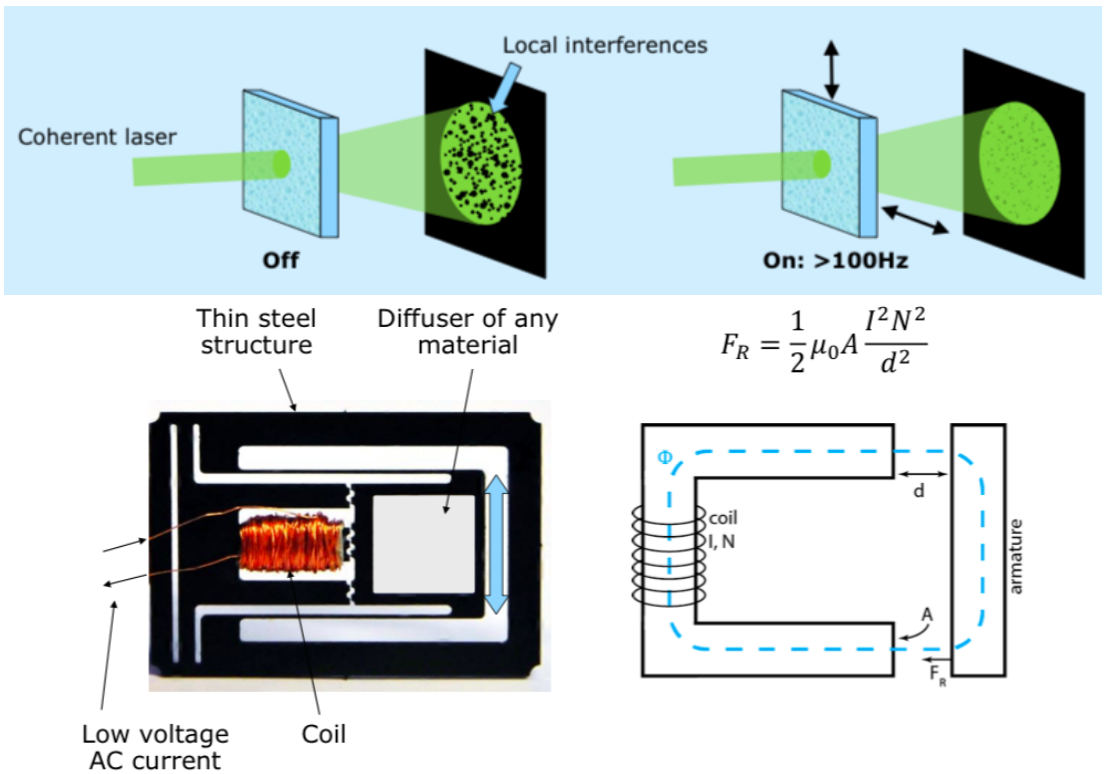

Figure 2.6: How a diffuser works: Top figure shows how a vibrating diffuser reduces speckle patterns. Bottom figure shows the vibration mechanism (Optotune.com).

Now that we have shown the principle behind diffuser function, we will take a look at the Gaussian profile of the beam after using the diffuser to see if we have the flattened beam profile we need on the sample plane. See Figure 2.7

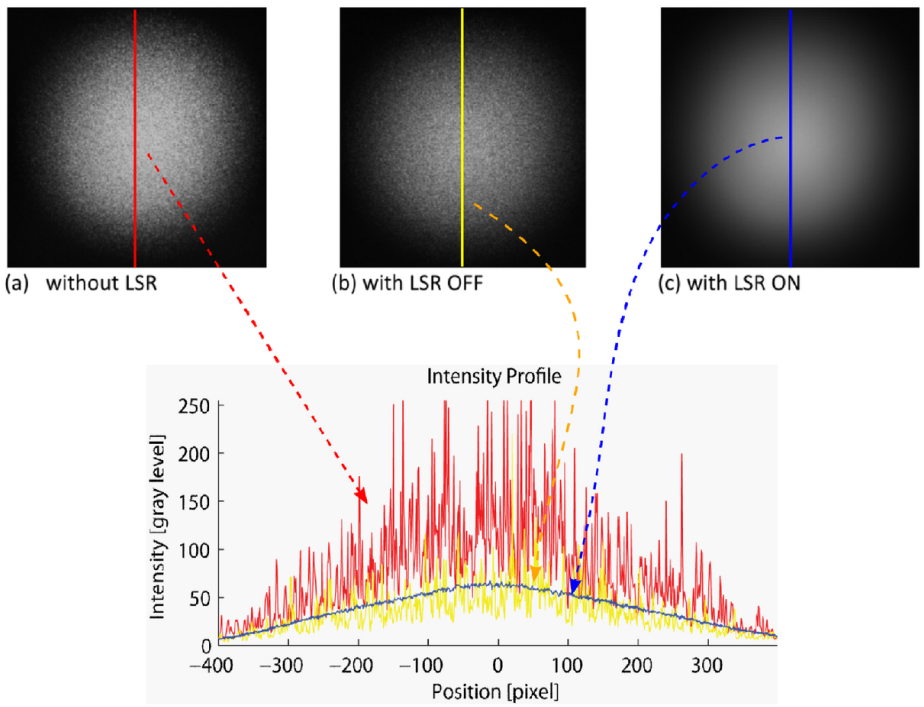

Figure 2.7: Effect of the diffuser on a Gaussian beam: (a) Gaussian beam without diffuser (b) Gaussian beam after a static diffuser (c) Gaussian beam after a vibrating diffuser, where it shows the least fluctuation of the spatial region across the detector. Image is reproduced from Optotune.com

As we see in Figure 2.7, using a vibrating diffuser significantly improves the speckle problem but doesn't deliver a flattened beam profile. An effective way to solve this problem is to use an aspheric lens to focus the light onto the diffuser and then a multi-mode fiber to take the laser light and transfer it to the second part of the excitation path. This way we will put the beam profile coming out of the multi-mode fiber tip onto the sample plane, where the profile is a top-hat (looks like the flat top of a pork pie hat) and not a Gaussian. Such a scheme is shown in Figure 2.8.

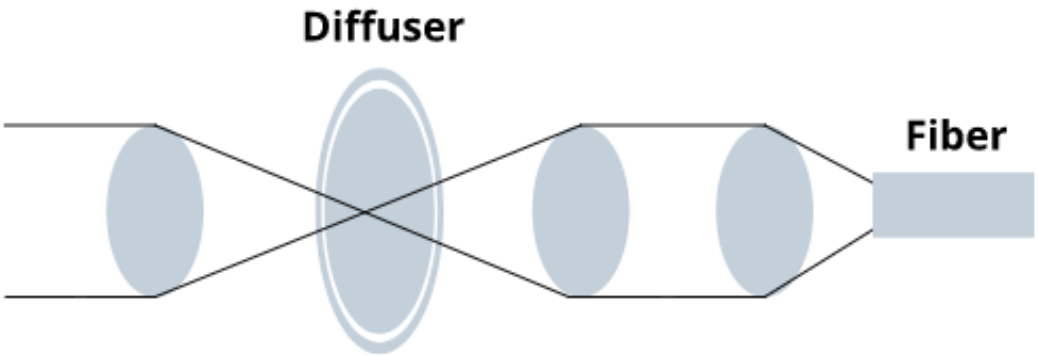

Figure 2.8: Optical design for a flat coupling excitation beam profile into the fiber.

4- Multi-Mode Fiber:

Optical fibers use total internal reflection (TIR) to confine light and guide it within their solid structure. Optical fibers are used in various fields and applications from telecommunications to spectroscopy to illumination.

A common type of optical fibers is a step-index fiber. In step-index fibers, the inner core is made from a material with a refractive index higher than the cladding layer. In such a fiber, a critical angle of incidence exists where the incident light will reflect off the core/cladding interface rather than refract into the surrounding medium. For the incident light to be able to travel through the fiber, a specific condition needs to be fulfilled. This condition is called Total Internal Reflection (TIR), where the angle of incidence must be less than a certain angle, which is defined as the acceptance angle, θ_{acc}. In such a fiber, Snell law can be used to calculate the critical angle:

$$\sin(\theta_c) = \cos(\theta_t) = \frac{\mathrm{n_{clad}}}{n_{\mathrm{core}}}$$

Here θ_c is the critical angle for TIR to happen, θ_t is the transmission angle into the core, n_{clad} is the refraction index of the clad material, and n_{core} is the refraction index

of the core material of the fiber. These angles are all shown in Figure 2.9.

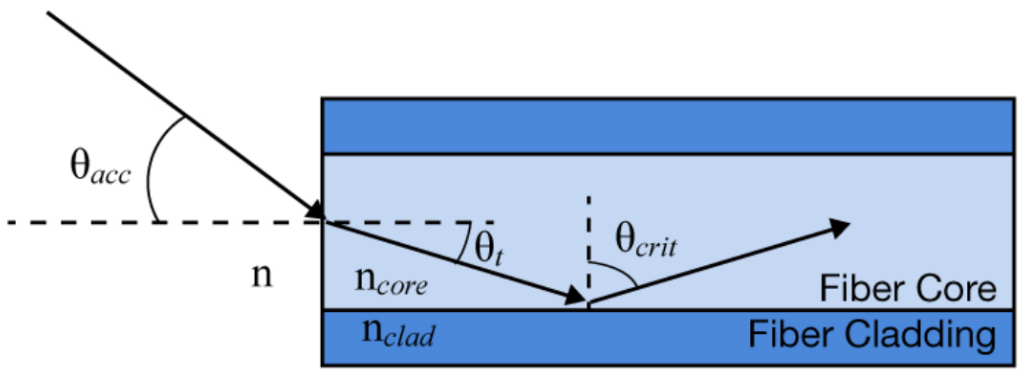

Figure 2.9: Propagation of light in a step-index optical fiber.(Thorlabs.com)

Now we can find the Numerical Aperture of the fiber (in this dissertation we address it everywhere as N_a), which defines the half angle of acceptance from the incoming light (θ_{acc}) into a fiber tip, from the following equations.

$$n\sin(\theta_{acc}) = n_{\text{core}}\sqrt{(1-\cos(\theta_t)^2)} = \sqrt{(\text{n}_{\text{core}}^2 - \text{n}_{\text{cladd}}^2)}$$

$$N_a = n\sin(\theta_{\text{acc}}) = \sqrt{(\text{n}_{\text{core}}^2 - \text{n}_{\text{cladd}}^2)}$$

In fibers with a large core, the N_a can be calculated directly using this equation (i.e., in Multi-Mode fibers).The N_a can also be found experimentally by tracing the far-field beam profile and measuring the angle between the center of the beam and the point at which the beam intensity is 5 % of the maximum. However, based on manufacturers' data, calculating the N_a directly provides the most accurate value.

Now we need to choose between using a single mode fiber with the diffuser or a multi-mode fiber. The main question here is if both these fibers are able to create a uniform profile across the sample plane. Figure 2.10 shows the difference between these choices based on [39].

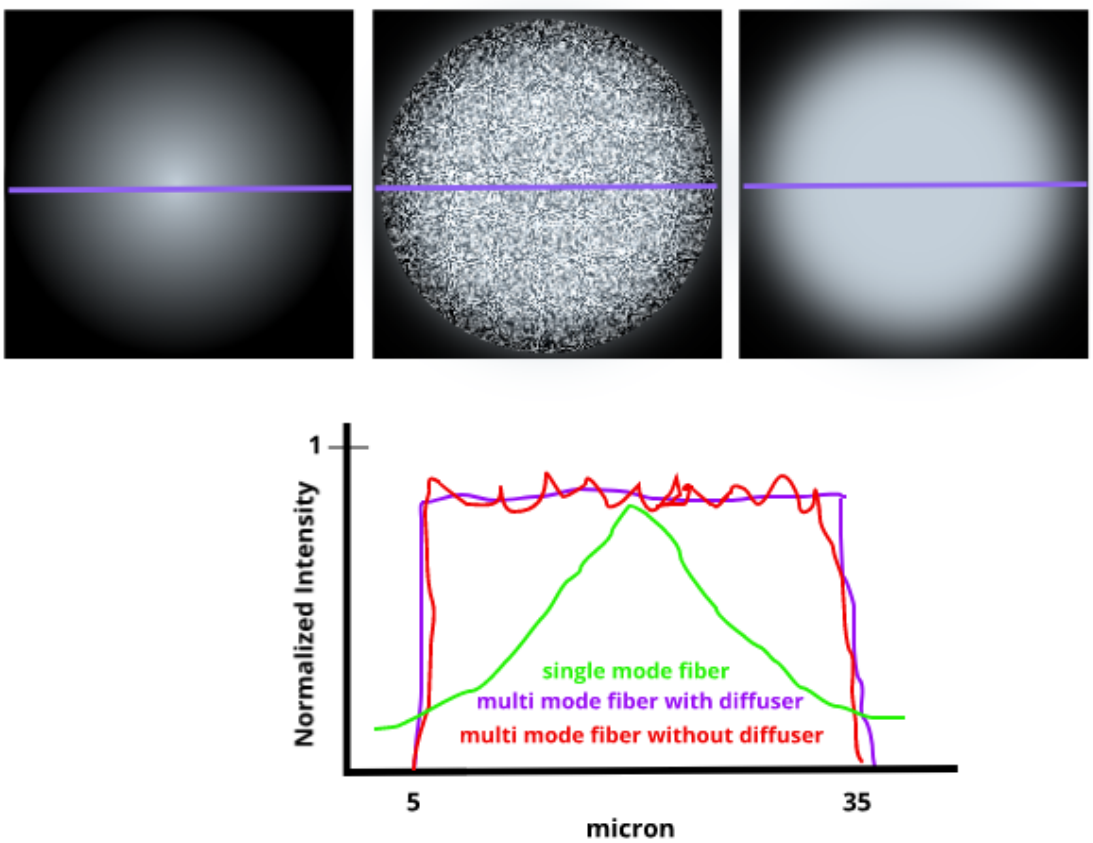

Figure 2.10: Beam profile of different types of fiber. On the top, left image shows a single mode fiber, middle image shows a multi-mode fiber without optical diffuser, and the right image shows multi mode fiber with the diffuser. On the bottom, normalized intensity of the cases above are compared.

Another important aspect to consider is that the light from a single-mode fiber, when focused inside the objective lens, can cause optical damage. Based on all the information provided above, the decision was made to use a multi-mode fiber after the diffuser to have the benefit of a top-hat beam profile on the sample, providing the same resolution uniformly across the region of interest on the sample plane. The fiber we choose was M105L02S-A - 105 m, 0.22 N_a by Thorlabs.

For the multi-mode fiber we chose, we need to calculate the input acceptance

angle and see what beam size is proper for such an acceptance angle so we know if there is a need for beam expansion for any of the laser beams. This calculation is shown in Figure 2.11 to compare two different lenses immediately before the light is directed into the fiber.

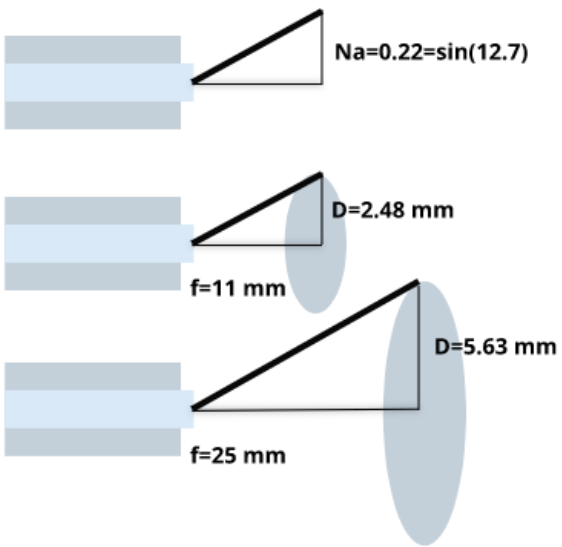

Figure 2.11: Numerical Aperture of multi-mode fiber for two lens choices. On top, we have a multi-mode fiber with N_a=0.22 which means the acceptance angle is 12.7 degrees. In the middle we have an aspheric lens of f=11 mm in front of the same fiber which focuses all of the collimated light into the fiber with the acceptance angle θ_{acc}. To do this, we need a beam waist of 2.48 mm at the lens, and at the bottom we have an achromat doublet of f=25 mm which shows a beam waist of 2.48 mm is needed at the lens.

Now we need to make a design based on the calculations and information we have. Our goal is to send both laser lines into the multi-mode fiber with high efficiency. Since the core size of multi-mode fibers is big in comparison with a single mode fiber, as long as we have a small enough focusing half-angle into the fiber, we will have good coupling efficiency. Lens choices are based on two points: first, we need to focus the beams on the diffuser. Here, the lens choice before the diffuser is dependent on

the beam-size we want to achieve after it.

Based on the need to make the beam-size after the diffuser almost half of the beam-size before the diffuser (to have the proper beam-width for sending it into the fiber by an aspheric lens) and also to keep the optical path reasonably compact, we pick a lens with 25 mm focal length before the diffuser and a lens with 10 mm focal length after the diffuser. The latter lens choice is also limited due to the choice for the lens that focuses the beam into the fiber, which in turn is dependent on the numerical aperture of the fiber. We can't go much higher than 19 mm for the last lens and we do not want to lose light by choosing a very small lens in size instead of the 10 mm lens. So there are limitations when coupling into a fiber that come from different practical aspects. A choice of 11 mm focal length for a collimating 405 laser light is due to the fact that we have a point source and can't afford to lose very much light by having a spread out focal point.

At this point we add two auxiliary parts to have more control over the 647 laser beam intensity without changing the output power of the laser. This idea will allow for automation.

These two pieces are a shutter SHB1T and its controller that let us block the laser beam by TTL signal and through a DAQ card, and a flipper mount MFF101/M by Thorlabs, that we can mount a neutral density filter into and put it in front of the beam to get low laser intensity if needed, controlled again through a DAQ card. Both of these components are shown in Figure 2.12.

Figure 2.12: Flip mount and shutter for 647 laser beam control. Number 1 shows two SMA connectors, marked DIG I/O 1 and DIG I/O 2, for use in applications requiring an external trigger in form of a TTL signal to toggle flipper position. Number 2 is power supply connection. Number 3 is USB connector for the computer. Number 4 shows the TTL connector for the shutter controller. Number 5 is mode button to enable the shutter controller for either manual or computer based control. Number 6 is the interlock. This figure is taken from [3].

2.1.2 Excitation Path Optics: from Fiber to Sample

In this section our goal is to achieve the design in Figure 2.13. I will discuss in detail how we get to this design.

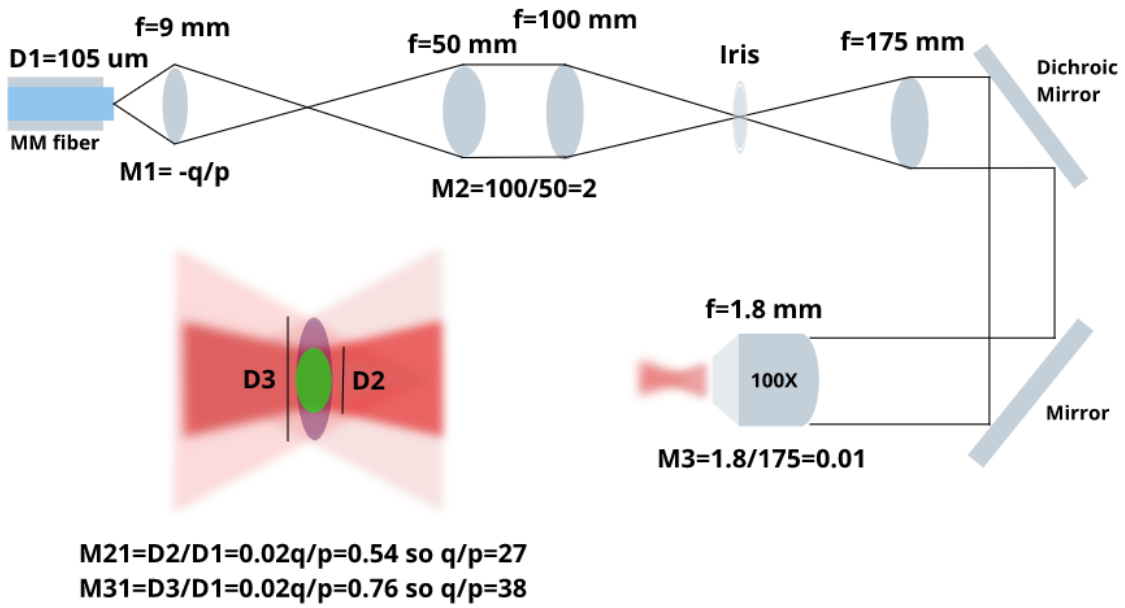

Figure 2.13: Optical setup between fiber and sample plane. p and q distances are calculated for two different beam sizes that represent the circles inside and outside a square region of 256 × 256 pixels.

To design this part of the optical system, we need to pay attention to the general goal of the excitation part for the sequential microscope, which is to have a top-hat excitation beam profile on the sample, maintaining an intensity of 5 kW/cm^2 on the illumination region, to maintain a reasonably fast blinking rate for the AlexaFluor647 dyes. To find out what size the illumination region needs to have, we calculate an approximation for the amount of power we need to take out of the 647 fiber laser as a function of the illumination region size. This calculation is based on the simple following equations where P is power and I is the intensity we want to maintain on the sample plane. The 1.25 factor is to compensate for 80% efficiency of the multi-mode fiber. The resulting plot is shown in Figure 2.14.

$$P_{laser\ out} = P_{on\ sample} \times 1.25$$

$$P_{on\ sample} = I \times \pi r^2$$

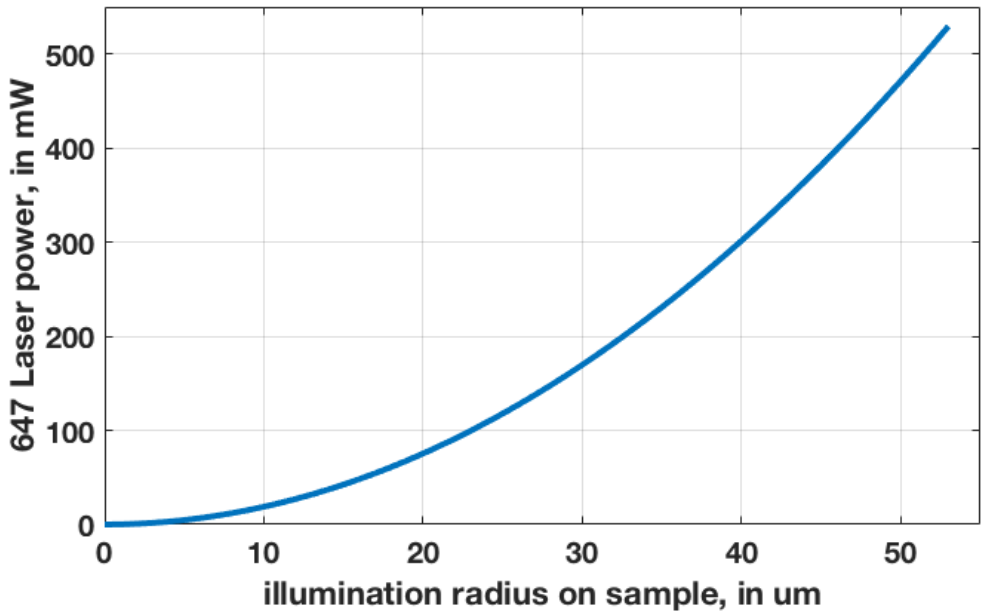

Figure 2.14: Laser output power needed to have 5 kW/cm^2 on circles of radius r on the sample plane, with a increasing areas of illumination.

Theoretically, since our 647 nm laser can have an output up to 500 mW, we should be able to have a circular illumination region on the sample plane with a radius as big as 52 microns. There are some limitations, though, that take away this freedom and we need to pay attention to them.

First, we have a limit on the amount of light we can enter into the back of the objective lens. The reason is that although the optical components in the objective body can tolerate this amount of power, but in the case any small particle of dust sits on the surface of any of the lenses involved, the dust particle becomes heated and creates a very hot spot that in a matter of seconds will result in lens damage which will be seen on the camera as a big dark spot. Due to possible damage, we put an upper limit for the power we can get out of the 647 fiber laser, here using 350 mW. We hardcode this limit into our control codes so that limit is not adjustable by

the microscope user later.

Second, for proper sampling we desire a back projected pixel size of 100 to 120 nm on the sample plane. Three standard ROI sizes on the camera are 512×512 , 256×256, and 128×128 pixels, but we can also create an arbitrary ROI size on the sensor for imaging. Now if we take the back projected pixel size from the main imaging camera to the sample plane to be 110 nm, we can approximate the size of the ROIs on the sample plane and see if they imply any limitations. A 512×512 ROI on the camera translates to a $512 \times 0.110 = 56.32$ um radius on the sample plane, which means that based on Figure 2.14, our laser will not have enough power to maintain an intensity of 5 kW/cm^2 over a region of this size, so choosing an ROI of 512×512 is not feasible. An important point to make is that we can adjust the blinking rate by using different laser intensities on the sample plane. For example, we can have the excitation intensity of 1 kW/cm^2 maintained on the sample and by increasing the exposure time of the camera, get still good results. There are practical limitations though, for example we are not interested in an ROI of 128×128 pixels since the size of such a ROI on the sample plane is approximately a circle with radius of $128 \times 0.110 = 14.08$ um while most of the cells we use (HeLa, RBL, etc.) have dimensions bigger than this. Thus, using such an ROI will result in imaging only part of the cells although it can be done faster through having an excitation intensity of higher kW/cm^2 which needs smaller exposure times, therefore our most reasonable choice will be an ROI of 256×256 pixels which contains approximately a radius of $256 \times 0.110 = 28.16$ um. Now we have two choices: one is to image the inner circle of a 256×256 region, or to image the outer circle. A comparison is made in Figure 2.15.

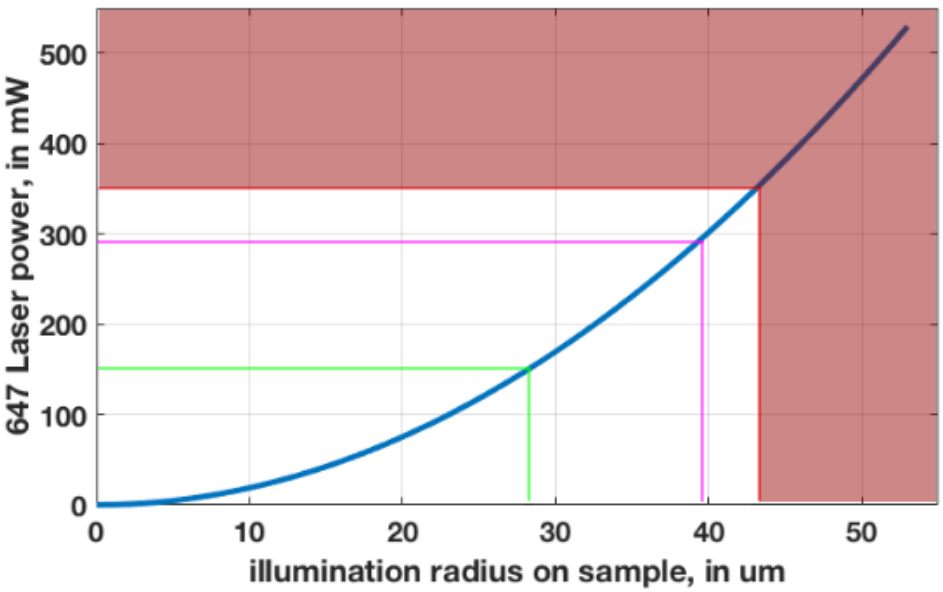

Figure 2.15: Limitations on laser output power needed to have 5kW/cm^2 on the sample. Red region creates optical damage. The pink line shows the power needed to illuminate the outer circle of a 256×256 region and the green line shows the power needed for the inner circle.

Based on Figure 2.15, both pink and green sizes are achievable. The obvious choice between the two is the pink line which represents the outer circle of a square the size of 256×256 pixels. The reason is shown in Figure 2.17 as the way each circle covers the square. The inner circle does not cover the corners of the square while the outer circle will cover the whole square. Since on the camera we can choose ROIs of a square shape, the outer circle has the advantage. So we need to test the top-hat profile for both cases and if we can extend the illumination profile to cover both circles and remain top-hat, we will use the outer one. Also we have assumed that when coupling the light into the multi-mode fiber, adjusting the illumination top-hat profile to cover regions of different size (by adjusting the lenses before and after the fiber) will not have any power drop. In case there is not any power drop, again our choice will be the outer circle. We will investigate these experimental conditions in

Chapter 3.

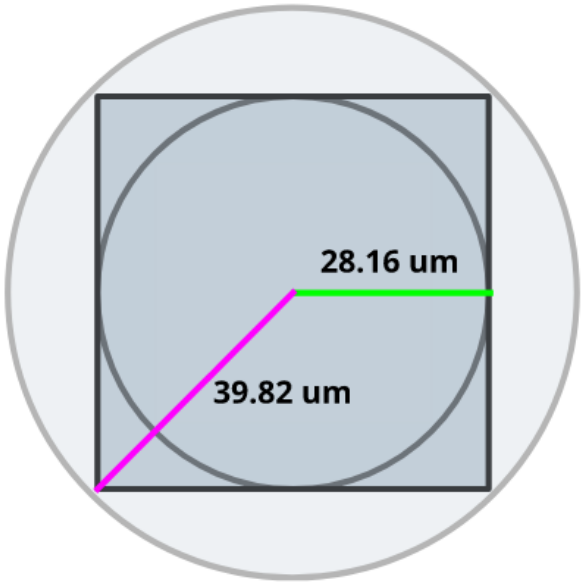

Figure 2.16: Comparison of possible ROIs for a square shaped 256×256 imaging region on main sCMOS camera with two circular ROIs of illumination on the sample. The green line shows the radius of the inner circle and the pink line shows the radius of the outer circle. Only the outer circle covers the square corners.

After finding the limitations due to optical damage, physical sample size, and back projected pixel size, now we can calculate the magnification needed between the tip of the multi-mode fiber and sample plane. Knowing the magnification helps us to design the optical elements needed for this part of the excitation path.

Our goal is to image the tip of the fiber onto the inner or outer circle of a 256×256 region with an approximate back projected pixel size of 110 nm, which means we want the final size of the radius of the circular image to be either 28.16 um or 39.82 um. This results in a magnification range between 0.54 to 0.76 between the fiber tip of 105 um size and the sample plane, as shown is Figure 2.17.

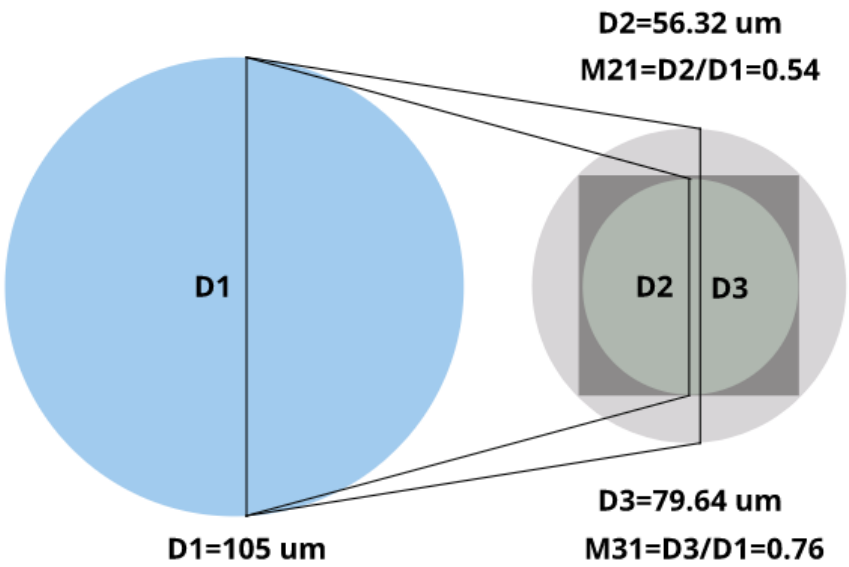

Figure 2.17: Magnification between fiber tip and sample. D1 is the multi-mode fiber diameter, D2 is the diameter of the circle inside the square region of 256 pixels, and D3 is the diameter of the circle outside that square.

Now based on the magnification information, we can make a design from the multi-mode fiber tip to the sample plane. The components needed are three:

1- An infinity corrected objective plus tube lens. Our objectives are 60X and 100X; we use a tube lens with 175 mm achromat doublet. Calculations here are done for the 100X objective.

2- A beam expander (in this case beam shrinker) to focus light before the tube lens in order to use an iris and to compensate for magnification adjustment purposes. We use a two achromat doublet lenses with focal lengths of 50 mm and 100 mm.

3- For the last part of the design there are two options. The first to use two lenses as a beam expander (in this case beam shrinker) which here they need to have a big focal length difference to compensate for a 20 to 40 magnification making the lens choices hard. A better option is to use a single lens with a small focal length and create the magnification needed by using the principal lens equation $\frac{1}{f} = \frac{1}{p} + \frac{1}{q}$ which

leads us to $M = -\frac{q}{p}$ where we can adjust p (distance between tip of the fiber and the lens) and q (distance between the lens and image of the tip of the fiber after the lens). This choice does not require too much space on the optical table. Design based on these three choices is shown in Figure 2.13.

As seen in Figure 2.13, using the equation for magnification, we can move the 9 mm lens back and forth in front of the fiber tip to find the desired magnification. Experimental check for that would be to look at the size of the circle (image of tip of the fiber on the sample plane) on the camera and check the size of it in units of the back projected pixel size. We will do this check is Chapter 3.

2.1.3 Emission Path Optics: from Sample to sCMOS

In this section our goal is to design the optics between the sample plane and the main imaging camera, which is an ORCA-Flash4.0 V2 digital CMOS camera, model C11440 by Hamamatsu [4].

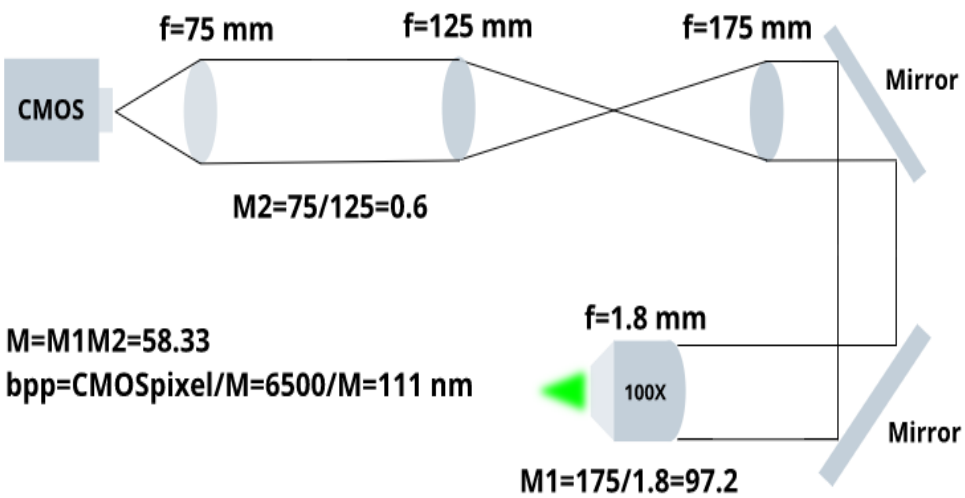

Figure 2.18: Optics between sample plane and sCMOS.

To be able to have a correct design we need to know the camera, we first get into the properties of the digital sCMOS we tend to use, then will design the proper optics to image using such a camera.

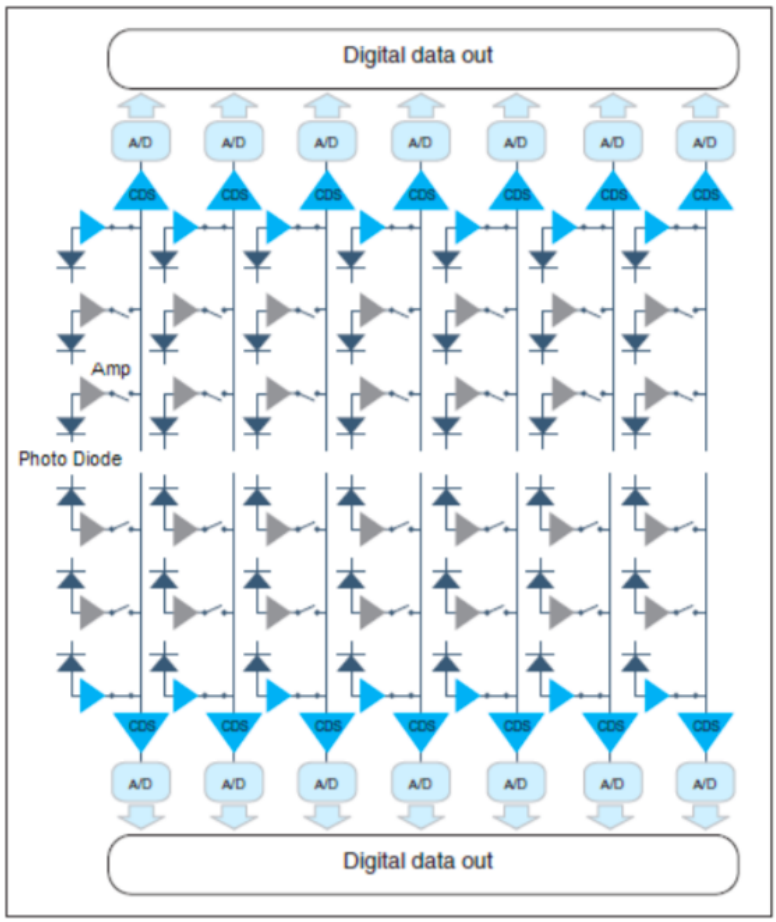

Figure 2.19: Structure of sCMOS image sensor. The top and bottom of the sensor work independently. In each part, photodiodes and the amplifier convert the photons to voltage in a pixel. CDS circuits lower the noise and A/D s convert the analog result to digital output. This figure is taken from [4].

The pixel of a sCMOS image sensor is composed of the photodiode and the amplifier that converts the charge into voltage. Entered light is converted to charge and then to a voltage in the pixel. The voltage of each pixel is output by switching

the switch one by one is shown in Figure 2.19. The sensor used in this camera has an on-chip CDS (correlated double sampling) circuit, which plays an important role in achieving low noise. In addition, the sCMOS image sensor has a split readout scheme in which the top and the bottom halves of the sensor are read out independently; the data of each horizontal line is read by 2 lines of column amplifier and A/D in the top and the bottom in parallel and simultaneously. This camera uses a rolling shutter method for the readout. In the rolling shutter, the exposure and readout are done line by line as shown in Figure 2.20. But even if the object moves during the exposure, the effect of the rolling shutter is very small. The camera read out the image sensor from the center line to the top and from the center line to the bottom simultaneously.

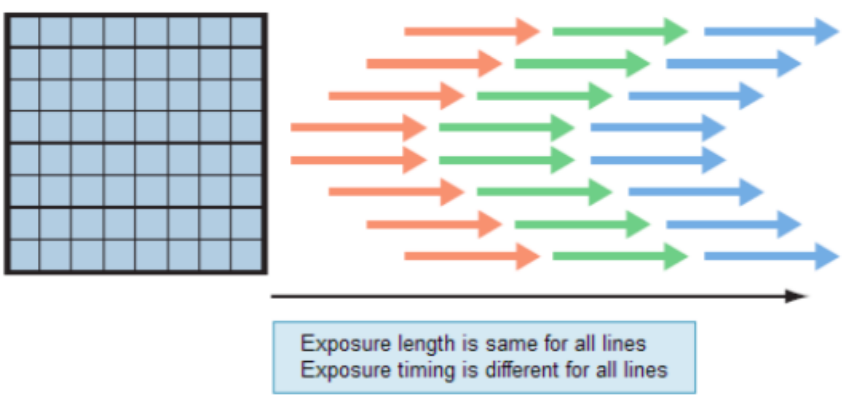

Figure 2.20: sCMOS sensor readout method and direction. This figure is taken from [4].

Setting the readout mode of a sensor is the way to extract data from the experiment. sCMOS has three readout modes:

1- Normal readout: reads the charge individually for all pixels. This is the mode we usually use to take the data.

2- Binning readout: adds the signal of adjacent pixels in the digital domain. This method achieves high sensitivity in exchange for losing resolution. 22 binning readout

and 44 binning are possible on sCMOS.

Interface	Binning	Settings			
		Horizontal		Vertical	
		Size	Position	Size	Position
Camera Link	Regardless of binning	---	---	4 lines steps	
USB 3.0	1×1 (Normal readout)	512 pixels	32 pixels	8 lines	4 lines
	2×2 binning readout	256 pixels	16 pixels	4 lines	2 lines
	4×4 binning readout	128 pixels	8 pixels	2 lines	1 lines

Figure 2.21: sCMOS sensor readout modes. This figure is taken from [4].

	Binning	Horizontal / Vertical		Calculation formula
Free running mode	1×1	1024	---	1/ (int(Vn/2048/30/1H)×1H)
		1536		
		2048		
	1×1	512	---	1/ (int(Vn/2048/100/1H)×1H)
	2×2	---	---	
	4×4	---	---	

Vn = Number of vertical line (The center of the set area is the middle of the sensor.)
1H = 9.744 36 × 10^{-6}
int () = The decimal point is rounded down.

	Binning	1×1 (Normal readout)		2×2 / 4×4
	Horizontal / Vertical	1024 / 1536 / 2048	512	---
Free running mode	2048	30	100	100
	1024	60	200	200
	512	120	400	400
	256	240	801	801
	128	481	1603	1603
	64	968	3206	3206
	8	7894	25 655	25 655

Figure 2.22: Frame rate calculations for USB3.0 connetion. This figure is taken from [4].

3- Sub-array readout: Here only a specific region of interest is scanned. The

benefit is to reduce the frame rate by reducing the number of vertical lines processed. Fastest readout would be for regions at the center of sensor. Possible options for this mode are shown in Figure 2.22.

Now we shall find the frame rates for the normal readout used as our main data taking mode. The needed formula and the results are shown in Figure 2.22. Calculating frame rates in free running mode and in the normal readout case gives another reason why we need to choose 256×256 pixels as the size of our region of interest on the camera. We mentioned that blinking rate can be adjusted by excitation intensity, and we can adjust the exposure time of the sCMOS based on the blinking rate. These factors can be changed to work with the limitations of a specific microscope and/or experiment. Our limitation is to have almost the whole cell inside our region of interest and to image with a reasonably fast speed since we want to use the microscope in a high-throughput capacity. For these reasons we pick the frame rate of 100 frame/sec. To achieve frame rates of 100 frame/sec and higher, we have to go to regions on the camera that are smaller than 512×512 pixels in size. Finally, the exposure times accessible in sCMOS are as shown in Figure 2.23.

	Standard scan
Free running mode	1 ms to 10 s
Free running mode (at Sub-array)	38.96 µs to 10 s

Figure 2.23: Available exposure times for USB3.0 connetion. This figure is taken from [4].

The free running mode has two options: normal readout mode (in which the exposure time is longer than the 1 frame readout time) and electrical shutter mode (in which the exposure time is shorter than the 1 frame readout time). These two readout modes are automatically switched depending on the exposure time setting.

We use the normal readout mode when taking data.

The exposure time can be extended to collect more signals and increase the signal-to-noise ratio. In the normal readout mode, the frame rate depends on the exposure time as frame rate = 1/exposure time. Figure 2.24 shows the exposure time data readout related to the free running mode.

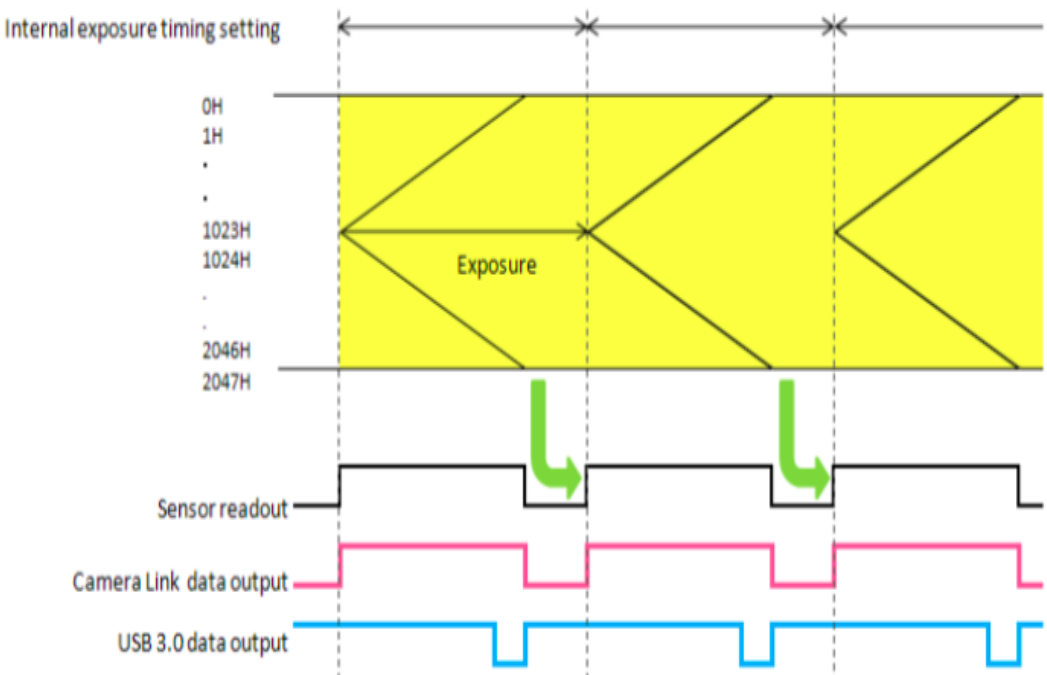

Figure 2.24: Exposure time readout by the sCMOS sensor vs USB3.0 data output in free running mode. Exposure time in this mode is calculated as 1/frame rate. This figure is taken from [4].

Finally, Quantum efficiency (QE) of sCMOS shows the percentage of incident photons turned to electric charge. This is important when imaging in low-light conditions. The QE of the sCMOS sensor is shown in Figure 2.25.

2- Lamp of Wavelength 660 nm:

To be able to find the cells in wide-field, to focus on them, to pick them up for

imaging, we need a lamp. The lamp we pick for this purpose is M660L4 from Thorlabs.This lamp is positioned directly above the sample plane.

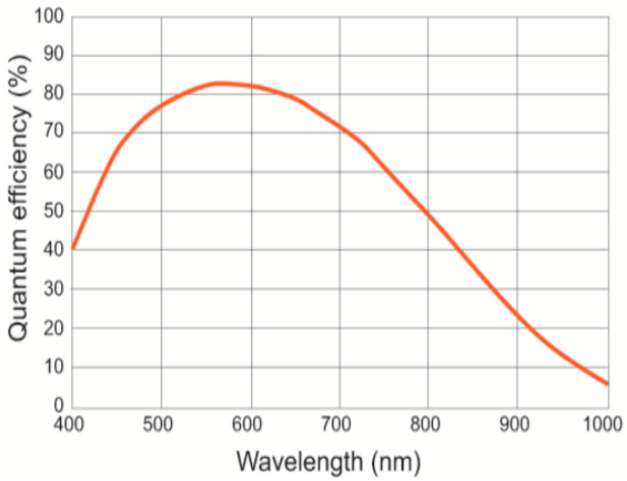

Figure 2.25: Quantum efficiency of the sCMOS sensor. This figure is taken from [4].

	Camera Link	USB 3.0
Imaging device	Scientific CMOS image sensor	
Effective number of pixels	2048 (H) × 2048 (V)	
Cell size	6.5 µm (H) × 6.5 µm (V)	
Effective area	13.312 mm (H) × 13.312 mm (V)	
Full well capacity (typ.)	30 000 electrons	
Readout noise (typ.)	1.0 electrons (median) 1.6 electrons (r.m.s) at standard scan 0.8 electrons (median) 1.4 electrons (r.m.s) at slow scan	
Dynamic range	37 000 : 1	

Figure 2.26: Characterisitcs of the sCMOS sensor. This figure is taken from [4].

3- Emission Path Optics Design:

After going over the camera and lamp parameters and characteristics, we now design the optical path from the sample plane to the sCMOS sensor. The first parameter to consider is the back projected pixel size (bpp) from the sensor onto the sample

plane. We previously mentioned that we like to have a bpp between 100 nm to 120 nm, so if we do the calculations for bpp=110 nm we can use the physical pixel size in Figure 2.26 to find the total magnification as shown in Figure 2.27.

The magnification between sample plane and sCMOS camera comes from two parts: the magnification of the infinity corrected objective-tube lens system, and the rest of the optics between the tube lens and the camera. We will use a 100X objective with an achromat doublet of f=175 mm as tube lens, so till here we have a magnification of 97.2 (=175/1.8). If we call this part of the magnification as M_{obj} and the total needed magnification as M_{tot}, the missing part M_{rest} we will satisfy the following equation:

$$M_{rest} = M_{tot}/M_{obj} = 59.09/97.2 = 0.61$$

One reasonable option is to provide M_{rest} out of a two-lens system that plays the role of a beam expander. In this case, we can write $f_2/f_1 = M_{rest}$ or $f_1/f_2 = 1/M_{rest}$=1.64

.

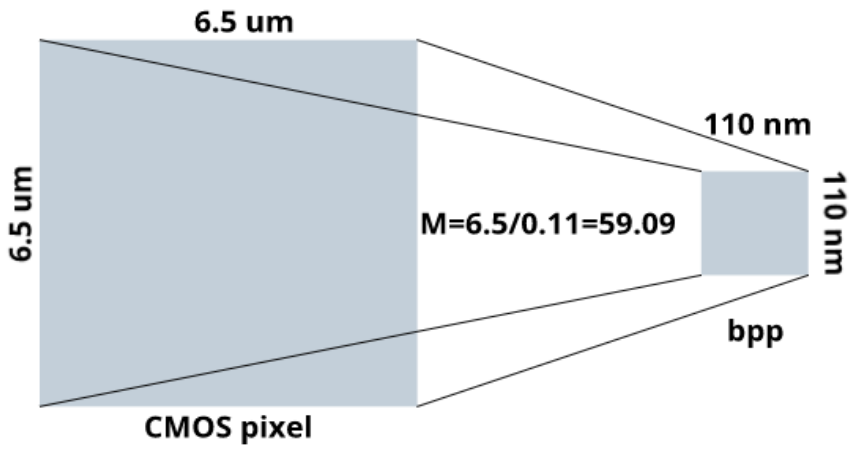

Figure 2.27: Magnification between the sCMOS pixel and the sample plane pixel (bpp).

What lens choices do we have to create such an expander? There are many possible choices but for practical reasons we describe the following two: first, two lenses of focal lengths 125 mm and a 75 mm which produce an M_{rest}=1.66; the second choice is two lenses of focal lengths 200 mm and 125 mm that produce a M_{rest}=1.6. The first choice clearly is better due to occupying less space on the optical table. Calculating the back projected pixel size based on such a lens choice gives us bpp=111 nm which is acceptable. The design for such an optical system is shown in Figure 2.18.

2.1.4 Emission Path Optics: from Sample to IR sCMOS

Up to this section, we have designed the complete optics needed for a sequential microscope. We can stop right here and build our system and an experiment, but there is one remaining aspect of the microscope: how to deal with drift. In order to do that, I designed the optics from sample plane to IR sCMOS as follows.

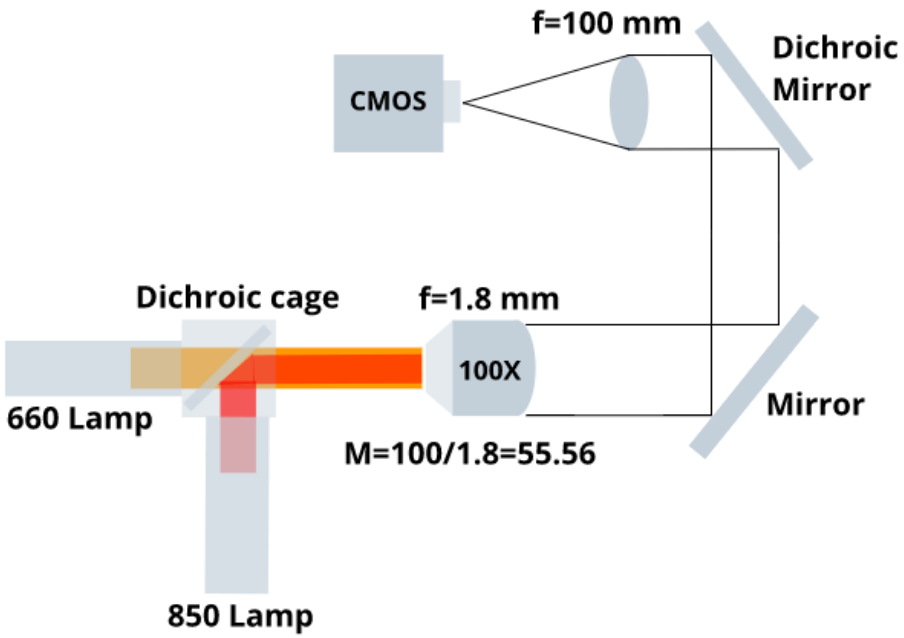

Figure 2.28: Sample plane to second sCMOS optics. Both lamps are shown.

We will discuss in more detail to this aspect in a drift specific section later but to state briefly, we decided to implement drift correction while imaging. To do this, we need a second camera and a second lamp, and this means we need an extra emission optical path. In this section we design a second emission path that is used only for the purpose of monitoring the cell being imaged live in a wide-field mode. There are three parts in this optical path that we need to describe before we get to the optical design: the lamp, the camera, and the dichroic.

1- Lamp of Wavelength 850 nm:

Here we use another LED driver (LEDD1B) and a DAQ to control the lamp as mentioned before. Since all parts of the controller will be shown in section 2.3, we show the spectrum of the lamp in Figure 2.29.

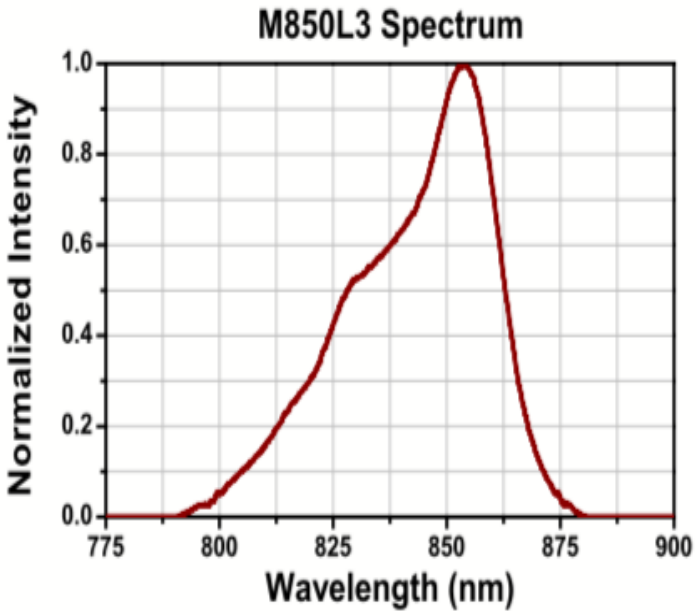

Figure 2.29: IR lamp spectrum.

2- sCMOS Camera:

We use a DCC1545M sCMOS camera from Thorlabs. Properties of the camera can be seen in Figure 2.30. Note that we don't need high QE here since we are not doing super-resolution with this camera and this camera doesn't collect emission photons from single molecules of the sample, but it collects the light of the 850 nm lamp and images the whole cell.

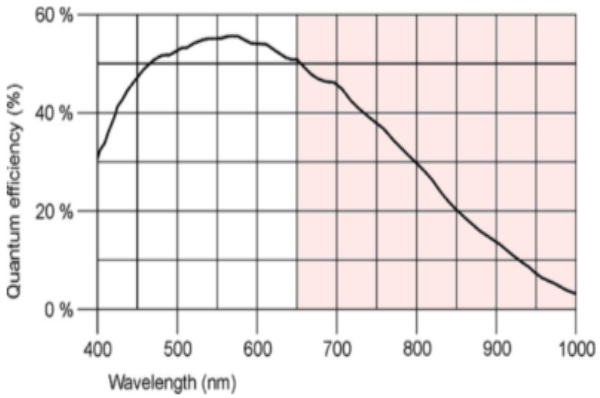

Sensor specification		
Sensor type	CMOS	
Shutter system	Electronic rolling shutter	
Readout mode	Progressive scan	
Resolution	1280 x 1024 pixels (1.31 Megapixel)	
Pixel size	5.20 µm, square	
Sensor name	Aptina MT9M001 (monochrome)	
Gain		
Monochrome model (master gain)	13x	
Analog gain boost	1.5x	
Frame rate (freerun mode)	fps	25.0
Frame rate (trigger mode, 1 ms exposure)	fps	25.0
Exposure time in freerun mode	ms	0.037 to 983
Exposure time in trigger mode	ms	0.037 to 983

Figure 2.30: sCMOS camera for live monitoring of the cells in wide-field. Number 1 shows the sensor and mount ring. Number 2 shows the area to attach a USB3 connection in the back of the camera. Other end of the USB connects to the computer in order to provide direct control. This figure is taken from [**?**].

3- Dichroic Mirror:

Since we have a lamp with 660 nm wavelength for the first sCMOS, we need a dichroic mirror to be able to use the second lamp with an IR wavelength for the second sCMOS. We use a FF750-SDi02-25x36 from Semrock inside a dichroic cage CM1-DCH/M - 30 mm cage cube with a dichroic filter metric mount from Thorlabs

that is connected to the lamp directly. The cage and dichroic spectrum are shown in Figure 2.31.

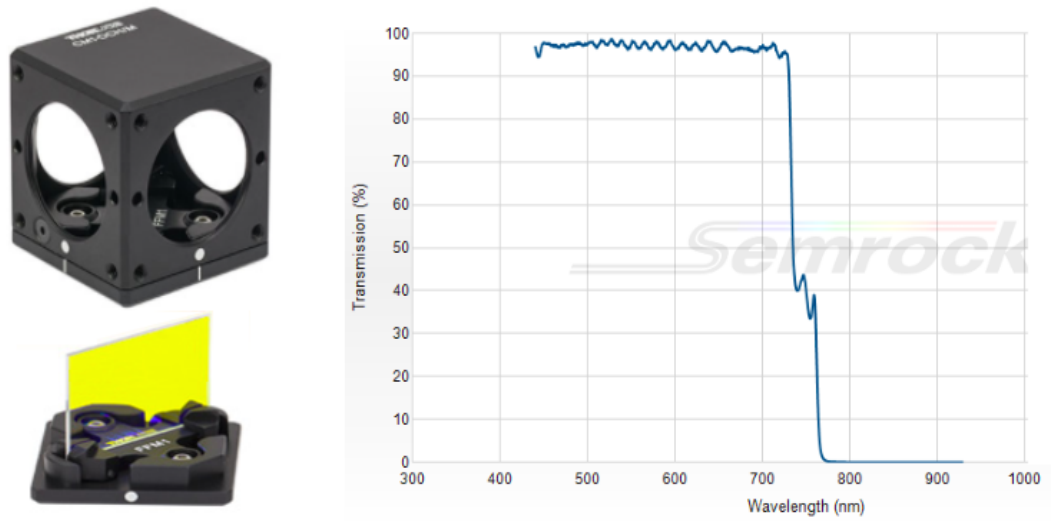

Figure 2.31: Dichroic cage and mirror.

Now we can design the optical path. To have a 100 to 120 nm back projected pixel size we needs a demagnification of 43.3 to 52 as seen in Figure 2.32.

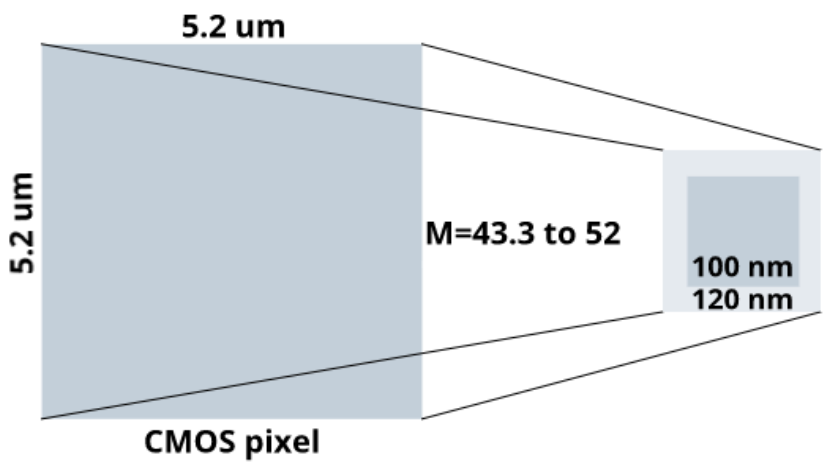

Figure 2.32: Magnification between IR sCMOS and the sample plane.

For this range of magnification, we are limited to a tube lens with a focal length of 78 to 94 mm, so a reasonable choice would be a lens with f=100 mm which will produce a magnification of 55.6 and a back projected pixel size of 93.6 nm. We use a 100 mm achromat doublet for this case. The design is shown in Figure 2.21.

2.2 Sample Stage

We now have the optics of the microscope designed. Next, we design a stage to hold and position the sample. We need to move the sample from one cell to another, as well as to automate the imaging process, so the stage has to have a reference position so we can save the position of each cell in the first round of imaging to go back to later. We choose a BSC203 Bench-top stepper motor controller from Thorlabs, a three axis stepper motor. In Figure 2.33, we show how the stepper motor works.

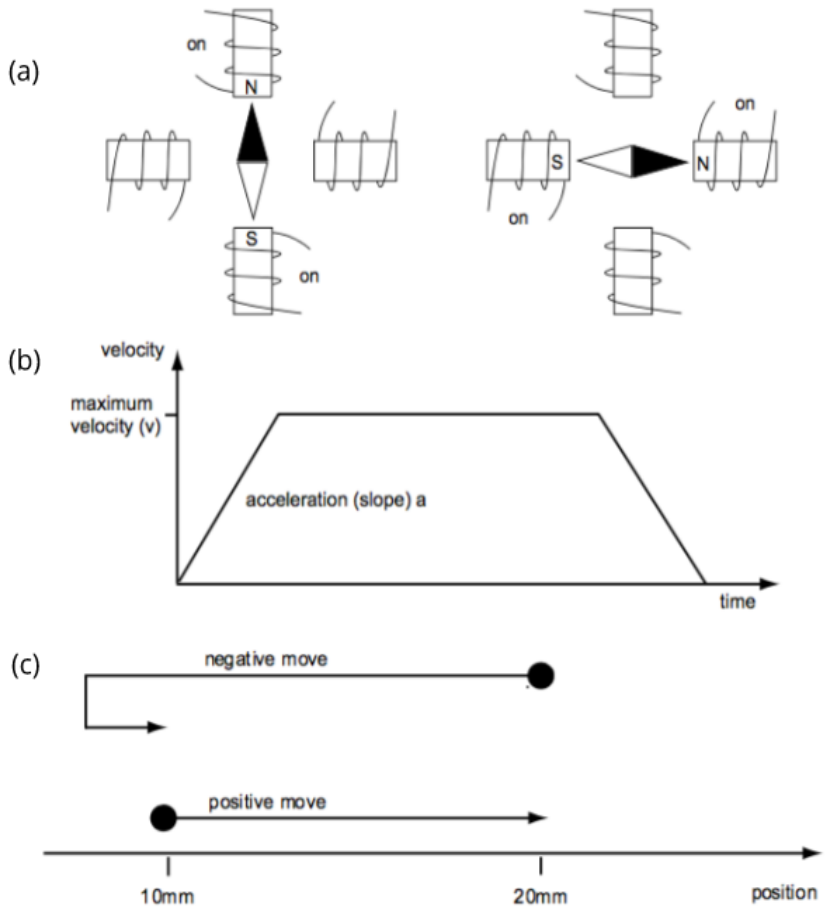

Figure 2.33: Stepper motor principle of working. (a) Producing the movement by magnets, (b) each step as a function of time, (c) stepper error correction scheme. This figure is taken from [5].

The physical stage that is connected and controlled by this controller is the model MAX341/M by Thorlabs which is called NanoMax flexure stage and contains a 3-axis stepper motor plus a 3-axis piezo motor. For the piezo motor, we need separate controllers. The NanoMax flexure stage is shown in Figure 2.34. We have to adjust the physical position of the NanoMax on the optical table with respect to our optical setup since the sample holder is sitting on the top plate. We need to have the sample

plate at a very specific position with respect to the objective lens. We will go into detail of this positioning at the end of this section.

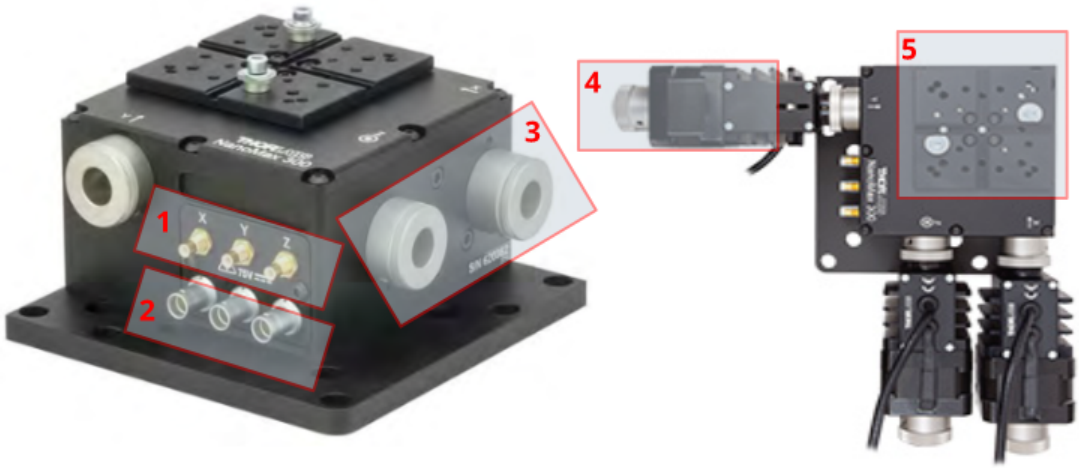

Figure 2.34: NanoMax Stage. Number 1 is SMC coaxial connectors for piezo movement control. Number 2 is 7-pin LEMO connectors for piezo feedback channel. Number 3 is the motor drive connector, Number 4 is the NanoStep motor drive. Number 5 is the connection plate that we mount the sample holder onto. This figure is taken from [5].

We need to mount the sample on top of the plate that resides on top of the NanoMax. We need a design that let the sample be locked on top of the NanoMax so movement of the stepper motors and piezo stages can be transferred directly to the sample. On the other hand, the sample needs to stay between the objective lens in the bottom and the lamps on the top. We designed a two piece sample holder that can be removed for relabeling the sample after each round of imaging. This sample holder on one end is fixed on top of the NanoMax by screws and on the other end has a round opening to mount 25 mm round metal coverslip holder. The latter also has two spring-loaded removable pieces on the side of the opening that can put pressure on top of a 25 mm coverslip holder to keep it fixed during experiment. Figure 2.35 shows the design.

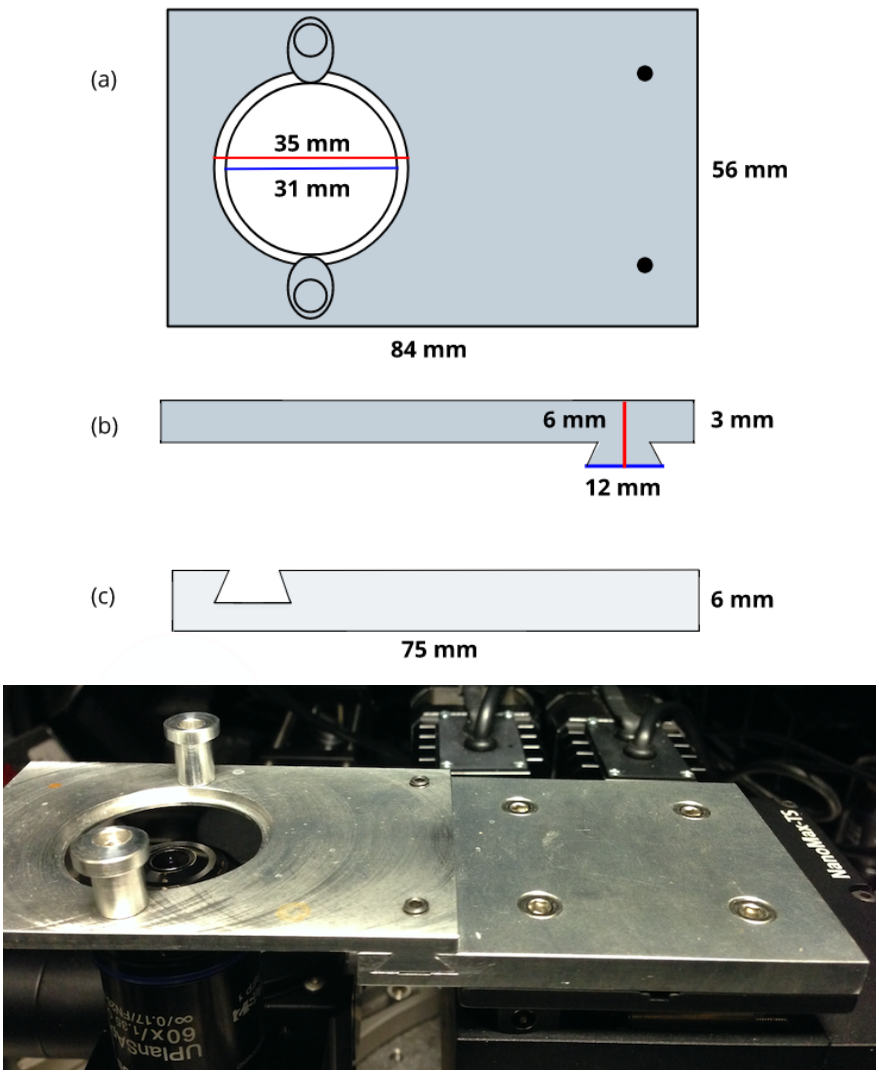

Figure 2.35: Sample holder design. (a) Sample holder from above with two spring loaded pieces that keep the sample fixed in position, (b) sample holder from side, (c) the piece that connects the sample holder onto the stage.

We need to have a design for positioning the NanoMax on the optical table to serve the optical alignment correctly. The method to do this is described in the alignment section which is presented in the appendix A of the dissertation.

2.3 Instrument Control

Instrument control is composed of MATLAB Instrument Control codes (MIC) for controlling devices, and the hardware control. Hardware connections are shown in Figure 2.36.

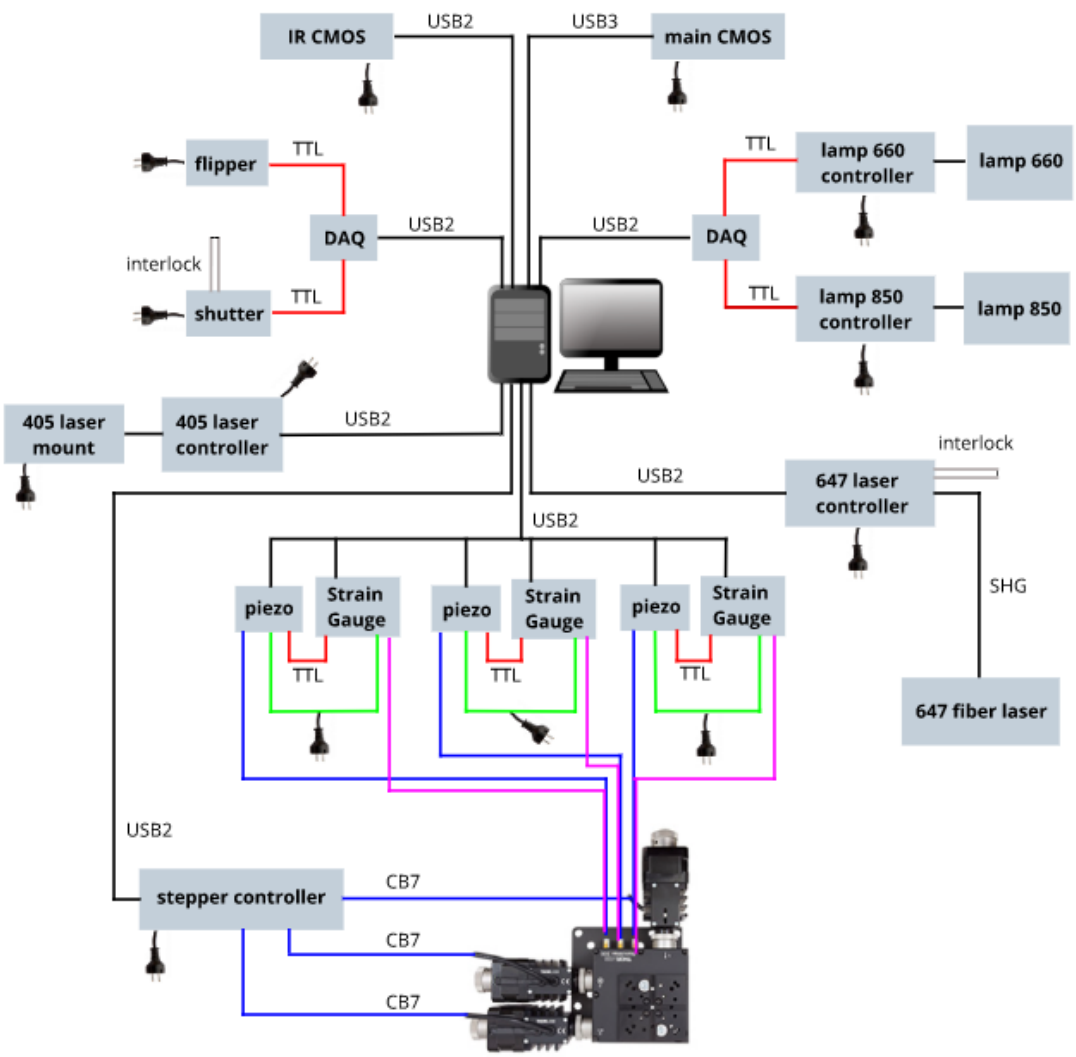

Figure 2.36: Control scheme and hardware connections.

2.3.1 Hardware Control

1- 647 fiber laser controller: MPBC fiber laser controller box and its parts can be seen in Figure 2.37.

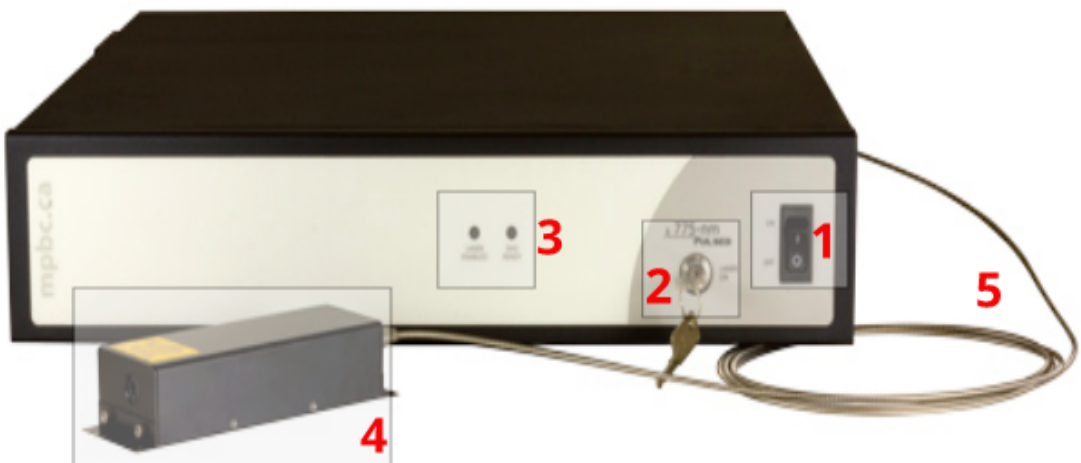

Figure 2.37: MPBC laser. Here is the laser controller box. Number 1 is the switch which needs to be on position 1 for the laser to be on. Number 2 is a safety key. Number 3 shows LEDs that indicate steps of turning on and sending out the light. Number 4 is the collimation box that sends out the collimated laser light. Number 5 is the emission fiber.

There are some physical connections needed for this laser. These connections are made through the panel at the back of the controller box as can be seen in Figure 2.38. I only indicate the ones that are used for setting up the laser in the current setup.

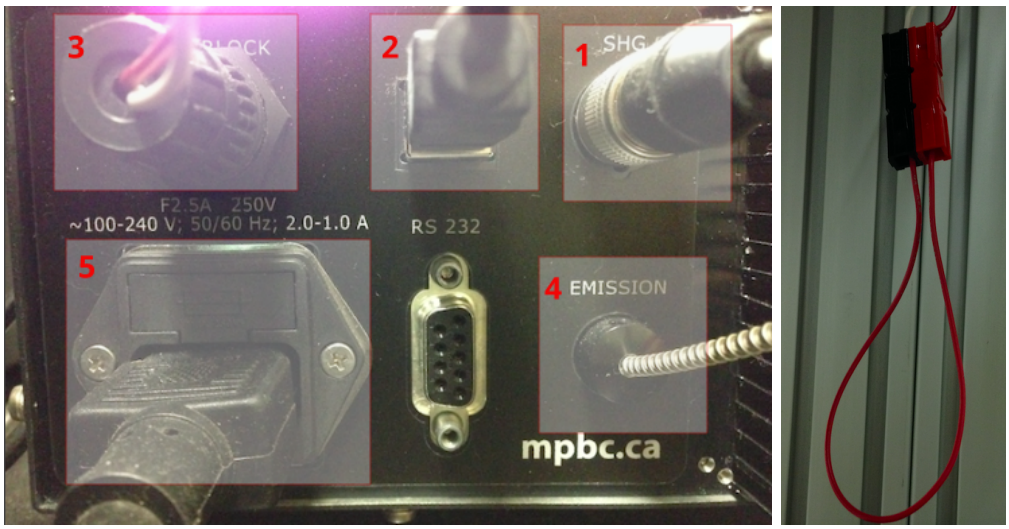

Figure 2.38: MPBC laser box, back panel. On the left: Number 1 connects the control box to the collimation box and produces the control signals. Number 2 connects the control box to the back of the computer and is a USB connection for computer-based control. Number 3 is the interlock, number 4 is the emission fiber, and number 5 is the power strip. On the right: the interlock from the left figure. Interlock needs to be connected as shown here. The wires at the top of the figure are the same ones that come out of the interlock in the left image.

2- 405 nm laser diode control:

To use the laser controller, we need to be able to control the controller functions and connections through computer.

Figure 2.39: Laser controller TLD001. Number 1 is the power connection, number 2 is the output potentiometer and is used to set the output intensity (power) of the laser, number 3 switches between constant power and constant current modes, number 4 can be set to show one of 4 operating parameters as follows: I_{LIM} for the maximum drive current limit, I_{LD} for the laser diode drive current in mA, P_{LD} for the laser diode optical output power in mW, and I_{PD} for the photo diode current in mA. This figure is taken from [6].

We do this using Kinesis software developed by Thorlabs. This software is downloadable from the Thorlabs website and can be used to check the connection status and functionality for all Thorlabs devices. The panel designed for the T cube laser

controller is shown in Figure 2.39.

3- digital sCMOS for fluorescence imaging:

Each camera has physical and software specifications. We are using a digital sCMOS camera from Hamamatsu (C11440-22CU). This camera has the following parts as seen in Figure 2.40, and then described briefly afterwards.

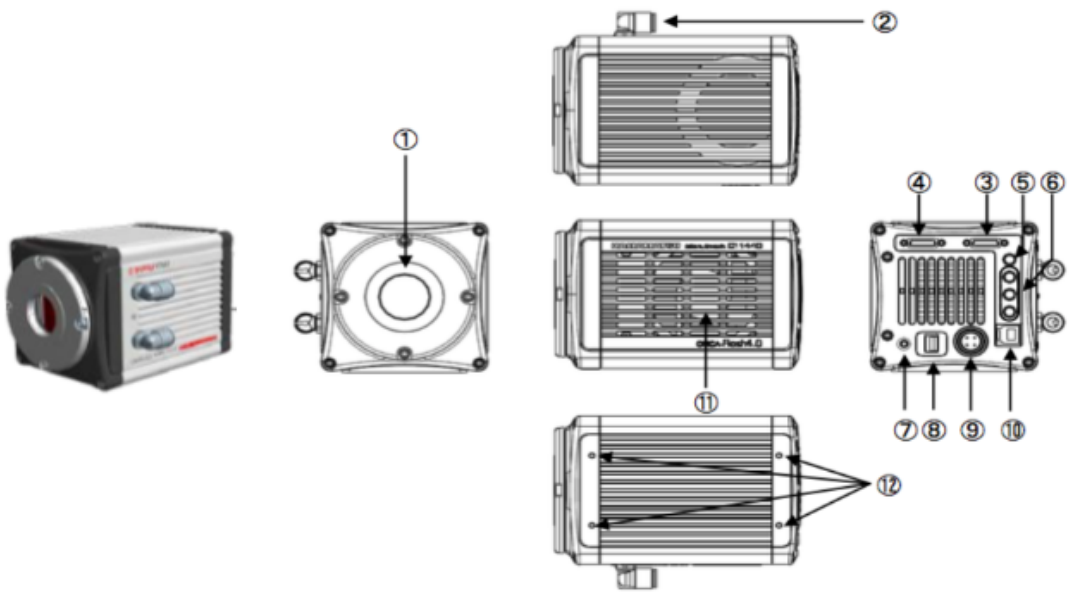

Figure 2.40: sCMOS camera parts. This figure is taken from [4].

Here we go through the sCMOS parts as numbered in the figure:

1- Lens mount: can be attached to C-mount lens or an optics system.

2- WATER connector: It connects the camera and the circulating water cooler with the cooling water hoses. We do not use this part in our setup.

3- Camera Link interface connector1: This is connected to the Camera Link interface connector 1 on the computer. We don't use this connection currently.

4- Camera Link interface connector2: This is connected to the Camera Link interface

connector 2 on the computer.

5- Trigger input connector: This is used when the camera is being operated using external synchronization. Input impedance is 10 kOhm. When an external trigger is input, the trigger is activated at the falling or rising edge of the signal.

6- Timing out connector 1,2,3: This is used when peripheral device(s) require synchronization with the camera. Output impedance is 33 Ohm.

7- Status Lamp: The LED indicates status of camera as shown in Figure 2.41.

Lighting color	Status of power distribution
Turn off (no color)	Power off
Green (Blinking)	Initialization
Green (lighting)	Power on
Orange (lighting)	Data transfer
Red (lighting)	Heat up

Figure 2.41: sCMOS status lamp modes. This figure is taken from [4].

8- Power switch: The power is turned on/off. When the power switch is set to ON, the camera turns on, starts initialization and the lamp blinks in green. When the initialization is completed, the lamp color stays green. When the camera transfers data, the lamp color is orange. When the power switch is set to OFF, the camera returns to the power off state and the lamp turns off.

9- DC power input connector.

10- USB 3.0 interface connector. We use this connection in our current setup.

11- This is the inlet for the heat ventilation.

12- Screw holes for attaching the option: to attach adjusting pole or plate, etc.

4- Lamp control:

To control the lamp we need a LED driver (LEDD1B) which is a controller by

Thorlabs, and a DAQ card for direct control of the voltage by computer. Figure 2.42 shows all the parts needed for setting up the lamp. The list of parts is discussed after the figure.

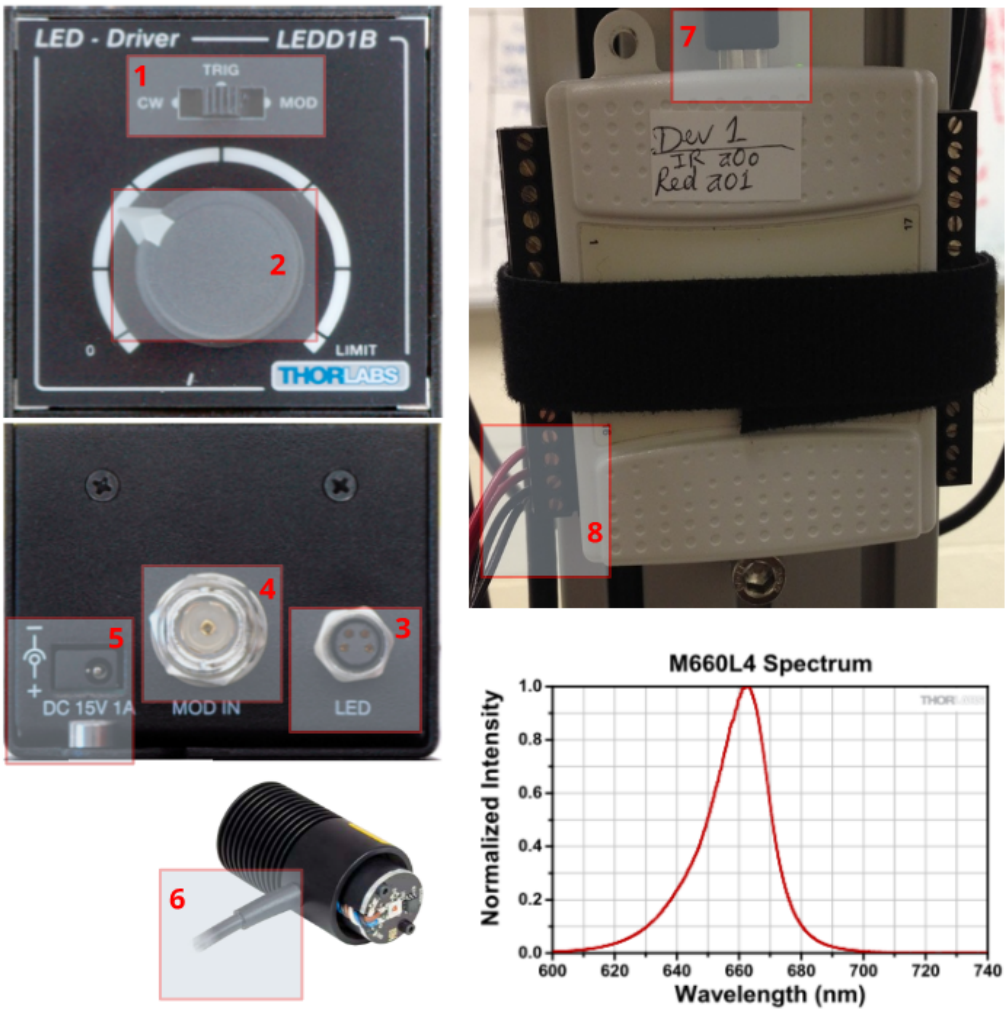

Figure 2.42: Lamp of wavelength 660 nm and related parts. List of parts and their function is discussed bellow the figure. This figure is taken from [7].

Here we discuss the list of parts and how they work:

1- MODE Switch - Used to switch between CW, Trigger and Modulation modes. The CW (continuous wave) mode provides a constant non-modulated LED current.

In Trigger Mode, the brightness of the LED can be adjusted using the control knob, and an externally applied TTL signal is used to switch the LED current on and off. A high level will enable the LED current and a low level will switch the LED current off. Note the brightness can be set manually. To turn on the LED switch to Trigger mode and a computer controlled TTL signal will switch the LED on for a predefined period of time, while the camera is triggered to take pictures. In Modulation mode, the LED is controlled completely by an external voltage. 0V corresponds to off and 5V represents the maximum LED current. All values in between correspond to the LED current. The LED current can be arbitrary modulated, e.g., sine wave modulation. This setting is what we currently use.

2- Control Knob: Used to switch on the unit, and to adjust the intensity of the associated LED when operating in CW mode.

3- LED connection: The LED head cable is connected here.

4- BNC connector: A standard BNC connector allows an externally generated signal (0 to 5V) to be applied to the unit (center pin: V+, housing: Ground). This provides an external control of the LED device. This is the place we connect to the DAQ card side board.

5- Power supply and On/Off switch.

6- This is the wire that connects the lamp to the LED connection on the controller.

7- USB connection between the DAQ and back of the computer to control the DAQ operation by computer.

8- DAQ connection board to number 4 on this lists which is the lamp controller.

5- Stepper motor control:

As we can see in the figure, stepper motor movement occurs by using magnets in the on/off position two at a time. Stepper motor movement between two points is consisting of three phases: acceleration, constant velocity, and deceleration. It is necessary to allow the movement in the negative direction, towards the reference

position, since the stage moves more than it should; there is a small plus step added to correct this error and proceed to the wanted position. To use the stepper motor we need a controller. The controller and details on the front and back panel are shown in Figure 2.43. Parts are listed after the figure.

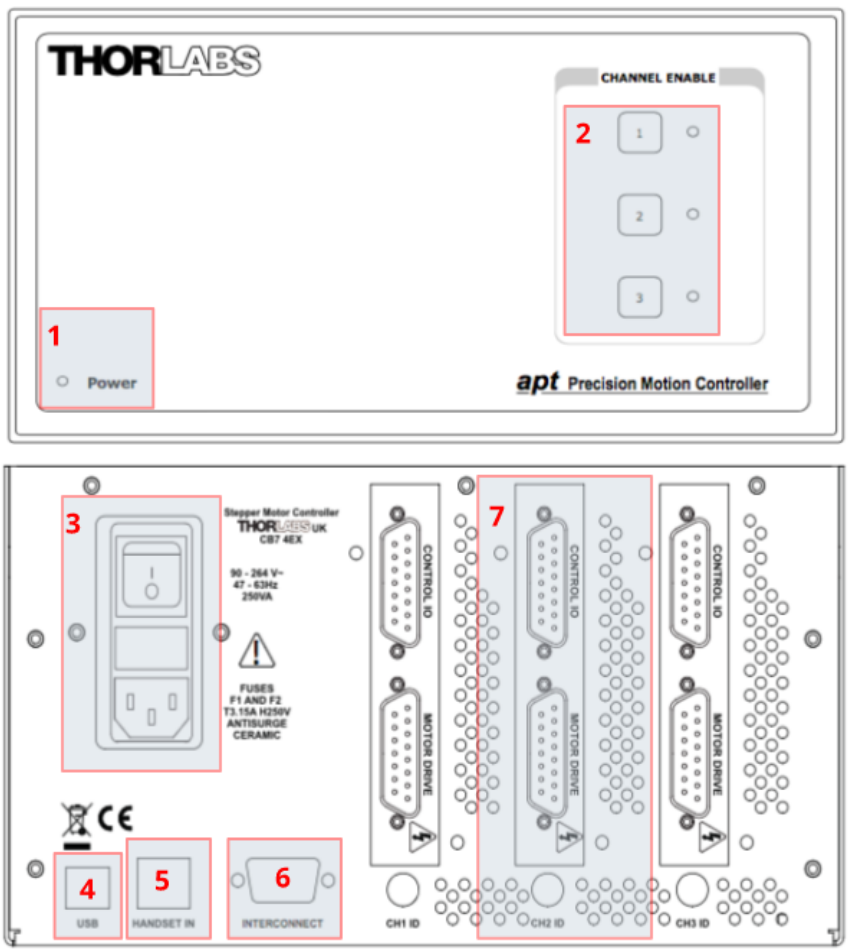

Figure 2.43: Stepper motor principle of working. (a) Producing the movement by magnets, (b) each step as a function of time, (c) the stepper motor's error-correction scheme. This figure is taken from [8].

Here is the controller part list:

1- Power LED: Indicates that power is applied to the unit.

2- CHANNEL ENABLE buttons: Used to enable/disable channel functionality. The associated LED is lit when the channel is enabled. Disabling the channel allows the motor actuator to be moved manually.
3- Power connection and on/off switch.
This connector provides all the current and encoder feedback connections to drive a range of encoded and non-encoded stepper motors.
4- USB port: for system communications.
5- HANDSET IN: Provides connection for the MJC001 Joystick. We do not use this socket.
6- INTERCONNECT: (9-Pin D-Type, Male) For Future Use. No function at present.
7- MOTOR DRIVE (bottom row): (15-Pin D-Type, Female) Provides connection to the actuator.
CONTROL I/O (top row): (15-Pin D-Type, Female) The CONTROL I/O connector exposes a number of electrical signals useful for external control. It is possible to configure a particular controller to respond to trigger inputs, generate trigger outputs, or both respond to and generate a trigger output.

6- Piezo stage control:

The Stepper motor has a 4 mm range in each of X,Y, and Z direction with 100 nm accuracy. The piezo stage that we use in the closed loop condition has 20 um range in each direction with a resolution of 5 nm as the smallest step size, although even a 1 nm step is possible but it will not be accurate. Combined together in the NanoMax stage, they allow us to reach nanometer precision movement. We use the stepper motor for finding the position of our target cells and the piezo stage for small range adjustments. We continue movement using the piezo stage and control mechanism via T-Cube Strain Gauge Reader of TSG001 and a T-Cube Piezo Driver unit TPZ001 by Thorlabs. TSG001 is a single channel reader equipped with a SMA position monitor output generating an analog voltage (0-10V) proportional to the strain gauge signal. When operated with TPZ001, high precision closed loop positioning is possible using

feedback equipped piezo actuators. A low voltage output connector allows for easy monitoring of the strain gauge signal. Figure 2.44 shows the piezo control scheme.

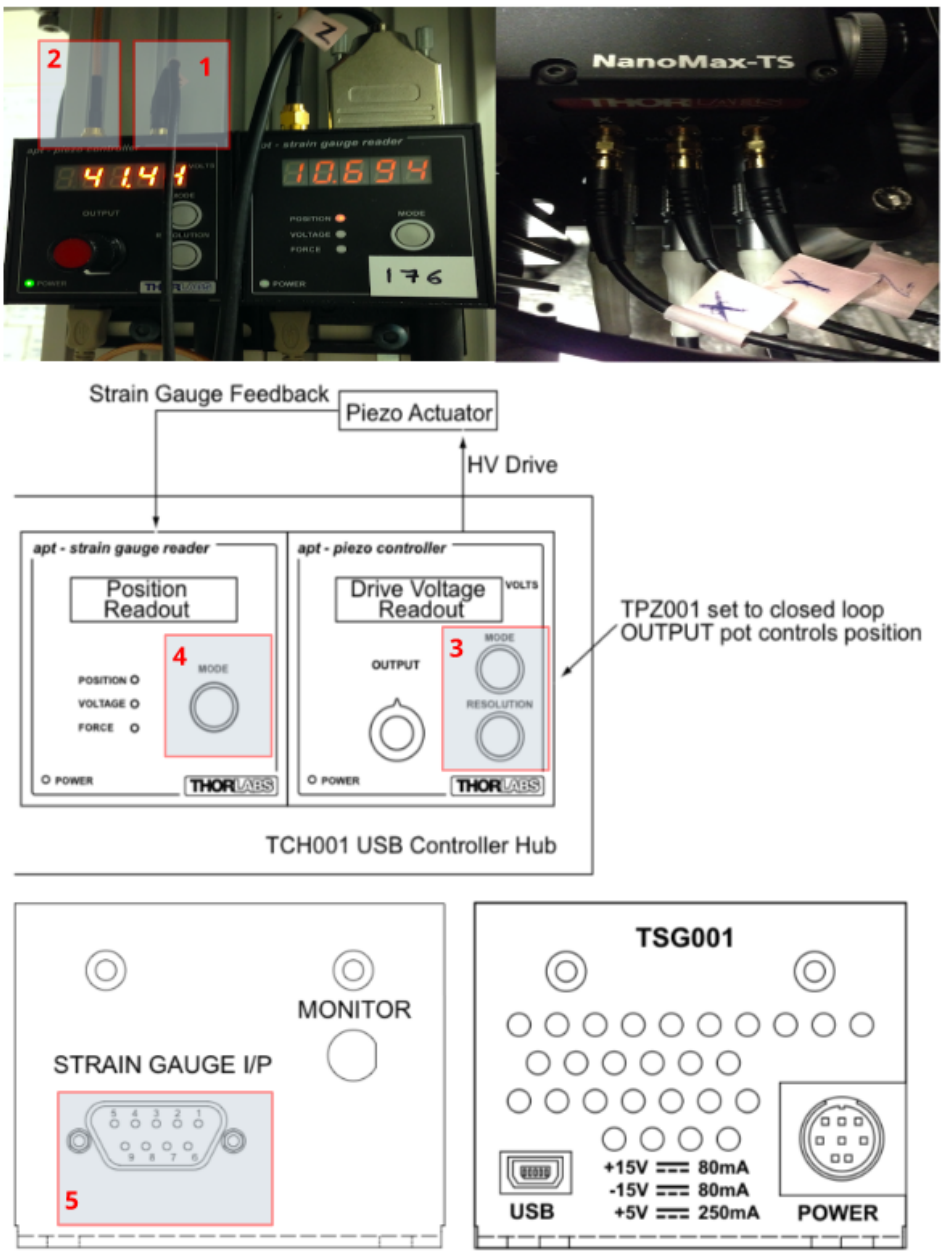

Figure 2.44: Piezo Actuator and Strain Gauge Reader: Number 1 is the connection between the stage and the piezo actuator. Number 2 is the connection between the piezo actuator and the strain gauge reader for feedback. Number 3 is the mode button to set the device to close/open loop for the control purposes .Number 4 is a mode button which releases the switch between display modes of position, voltage, and force on the strain gauge. Number 5 is the strain gauge I/P (9 Pin DIN connector) that receives the signal from the strain gauge to provide the feedback for the control loop. This figure is taken from [9].

2.3.2 MATLAB Instrument Control (MIC)

MIC is a collection of programs written by the Lidke lab group in MATLAB that facilitates automated data collection of complex, multi-component microscopy systems. MIC uses object-oriented programming where a class defines the capabilities of each instrument. Each instrument class inherits from a common MIC abstract class and therefore has a basic common interface.

Common component types (laser, camera, etc.) have their own further abstract sub-classes to give common interfaces and to facilitate the development of control classes for specific new instruments. Export methods, unit tests and graphical user interfaces are provided for each of the instrument components. Control of multi-component instruments can be by scripting or creating functions or classes that make use of individual components. Use of the MATLAB environment allows immediate access to data and image analysis even during data collection and one can easily extend or modify any of the control classes.

We show the hierarchy of the classes and the different categories they can belong to in order to create the class to control the sequential microscope in Figure 2.45 where the upper level is the general abstract class which then proceeds to the device abstract class and from there goes to the device class which contains methods and properties specific to that model. Some classes can be grouped under the same category and some can not. For example all the light sources, from laser to lamp, are grouped under a single abstract class. The same happens for cameras, but stages do not have the same abstract class since the qualities and characteristics of them are not easily gathered under the same category. Finally all these are gathered under a single class are named MIC_SEQ_SRcollect.m.

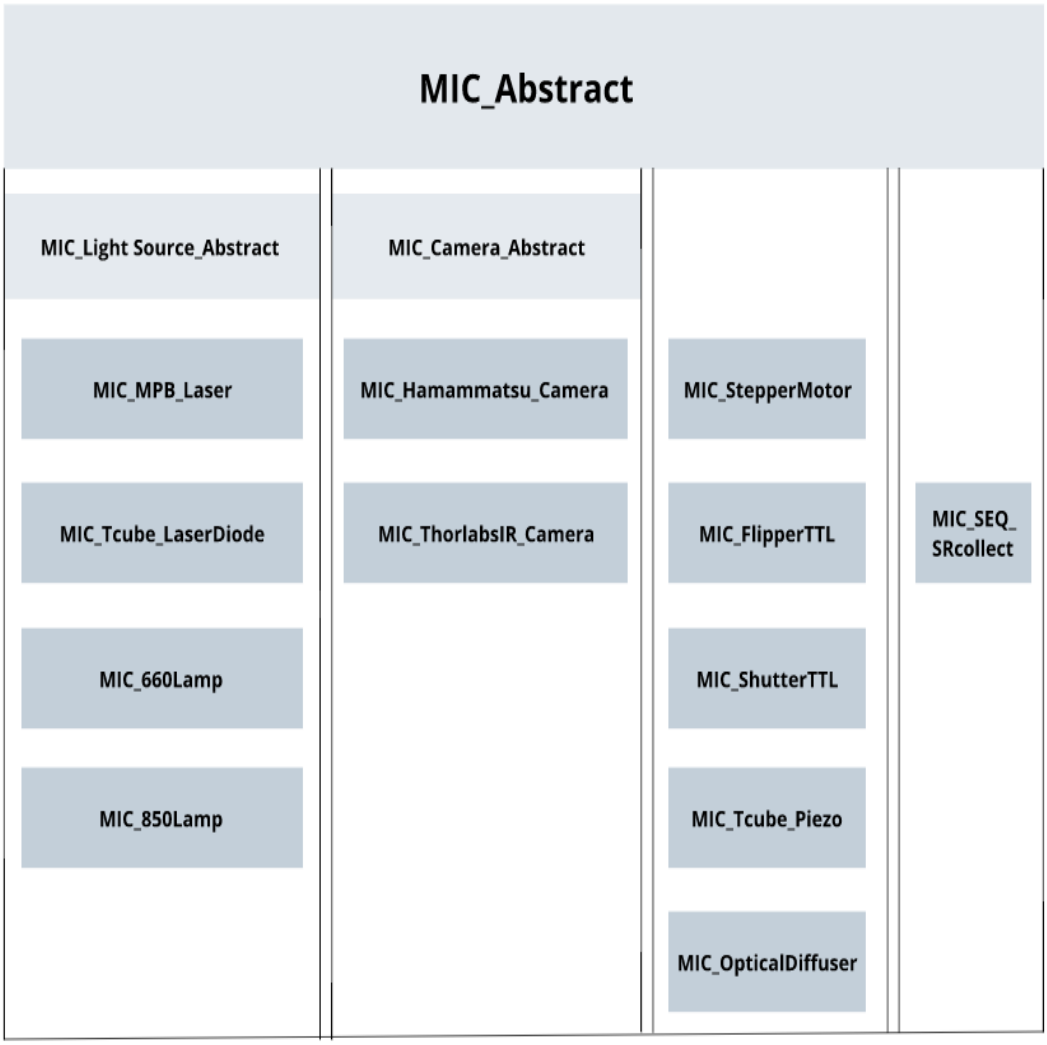

Figure 2.45: MIC inheritance scheme.

2.3.3 Graphical User Interface (GUI)

In order to make taking data and interaction with microscope easy for the end user, we design a graphical user interface (GUI). This GUI implements every light source, camera, stage, and mechanical device used by the microscope.

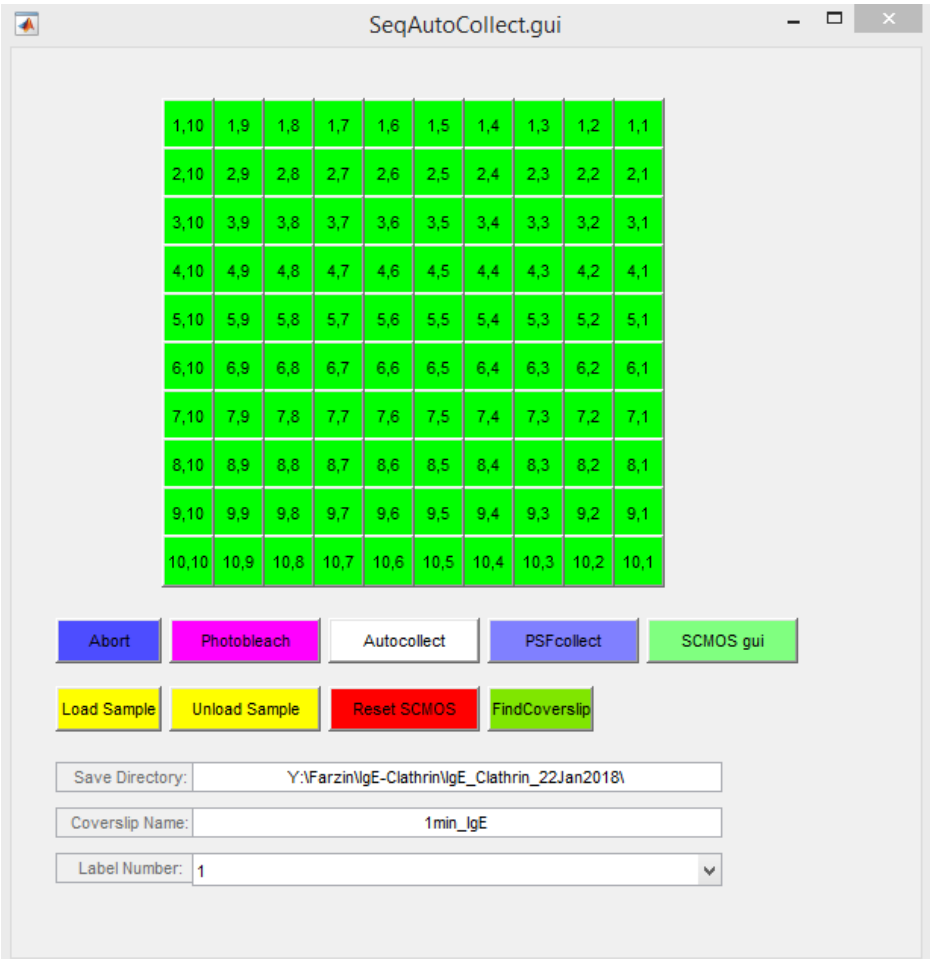

Figure 2.46: Sequential microscope GUI. Each green button on the grid takes us to a specific location on use of the stepper motor.

The GUI has three main parts: stage-indicator push buttons (100 green buttons inside the square), horizontal push buttons that have multiple different functions and, fill-ins that accept an address to a file or register a label number. Each of the stage-indicator push buttons takes us to a specific position with respect to home position (zero position) of our stepper motor.

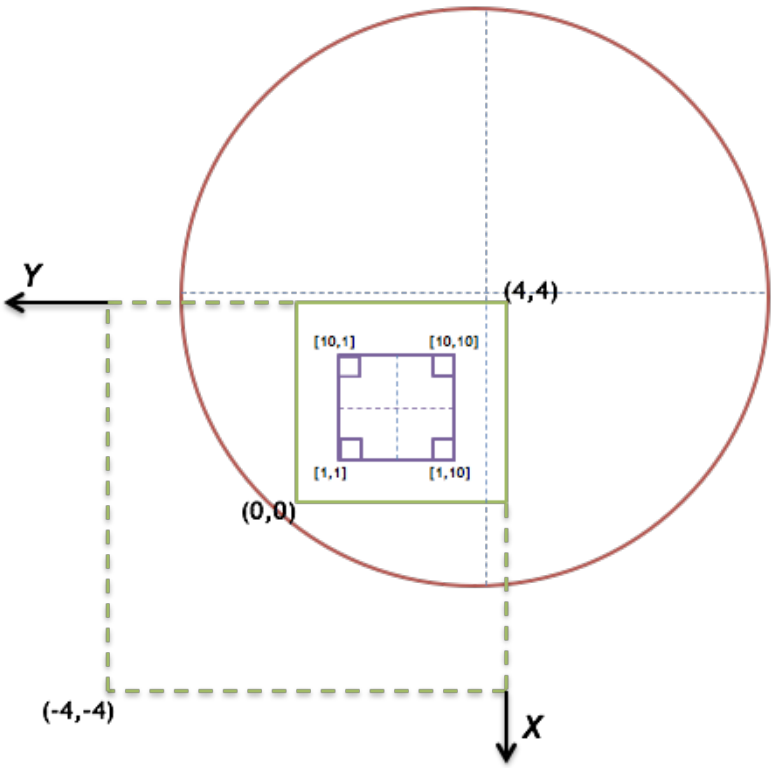

Figure 2.47: Available range of motion for the stepper motor through sequential microscope GUI. Red circle shows the size of sample holder. Objective lens is placed beneath the center of the red circle. Green square with solid lines shows the total range of movement for stepper motor in XY plane. Sequential microscope's GUI's range, shown by a purple square, only uses about %25 of the whole available area to the stepper motor. We prefer the center of the purple square to be at the center of the red circle.

The other push-buttons on the GUI facilitate various functions as indicated by the labels. On the top row we have from right to left: sCMOS GUI (brings us the imaging camera GUI), PSFcollect (bring up a GUI to test the point spread function (PSF) of the microscope), Autocollect (by pushing this button, the user orders the microscope to start taking data from formerly registered reference cells), Photobleach (starts photobleaching, i.e., starts both the main 647 laser and 405 laser and doesn't save any images; photobleaching mode usually runs for half the number of frames we

use when taking super-resolution data), Abort (stops the imaging process without deleting any of the MATLAB classes used for taking data), and on the lower row we have from right to left: Find Coverslip (brings up a large 2048 by 2048 region so user can change the z position of the sample and bring cells into focus), Reset sCMOS (to get rid of a rare bug when main camera stops working and needs re-initialization), Unload Sample (moves stepper stage and thus the sample upward to the initial position so it does not touch the objective tip anymore) Load Sample (moves stepper stage and thus the sample downward to a specific distance from the tip of the objective. It is not touching, and a distance of 1 mm is kept as caution for not breaking the sample or making a scratch on the front lens of the objective.) The GUI pops up as the main code of the microscope starts running, i.e., obj=MIC_Seq_SRcollect, and each of the devices is built in the constructor of the class and later, using the GUI, we can use all these codes together. Figure 2.48 shows the flow of the experiment.

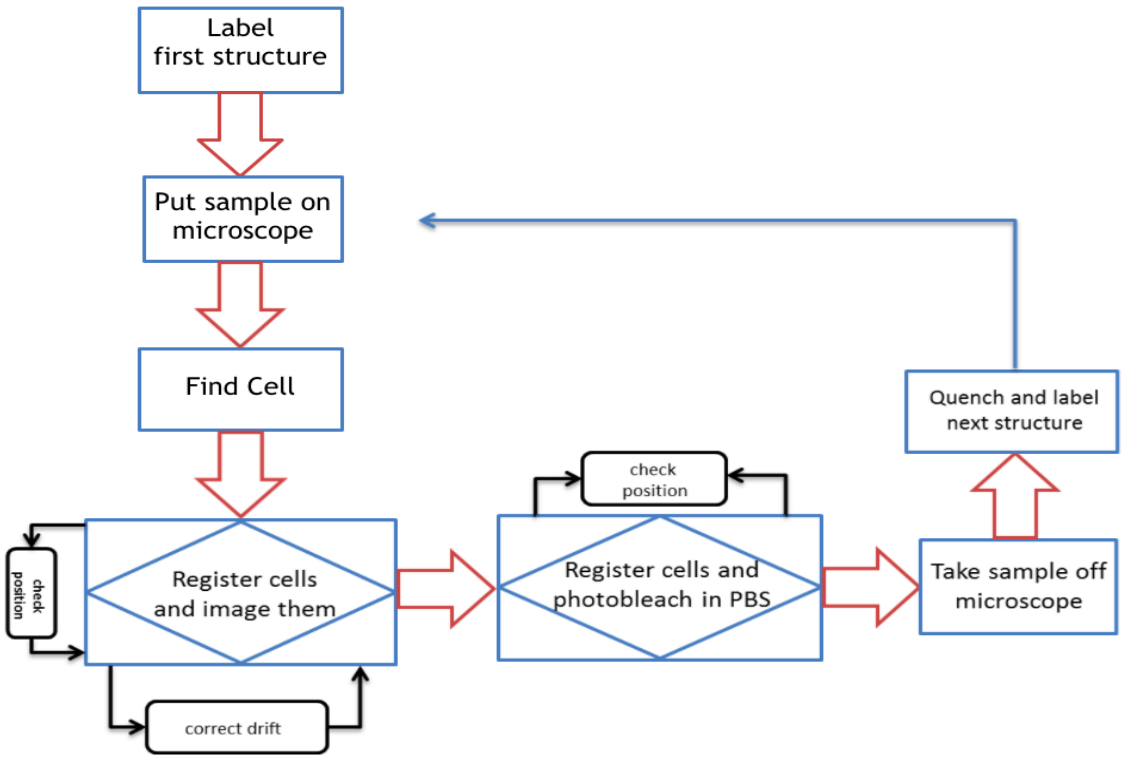

Figure 2.48: Flow of the experiment

2.4 Drift Correction

Relaxation of stepper motor gears, stage settling, and change in room temperature during an experiment are among different causes of drift. Change in room temperature causes thermal expansion of the coverglass and the coverglass holder mounted on top of the objective lens, which results in relative movement of the sample with respect to the objective. Depending on what kind of material is used for the coverglass holder, different amount of expansion will happen for 1 degree change in temperature.

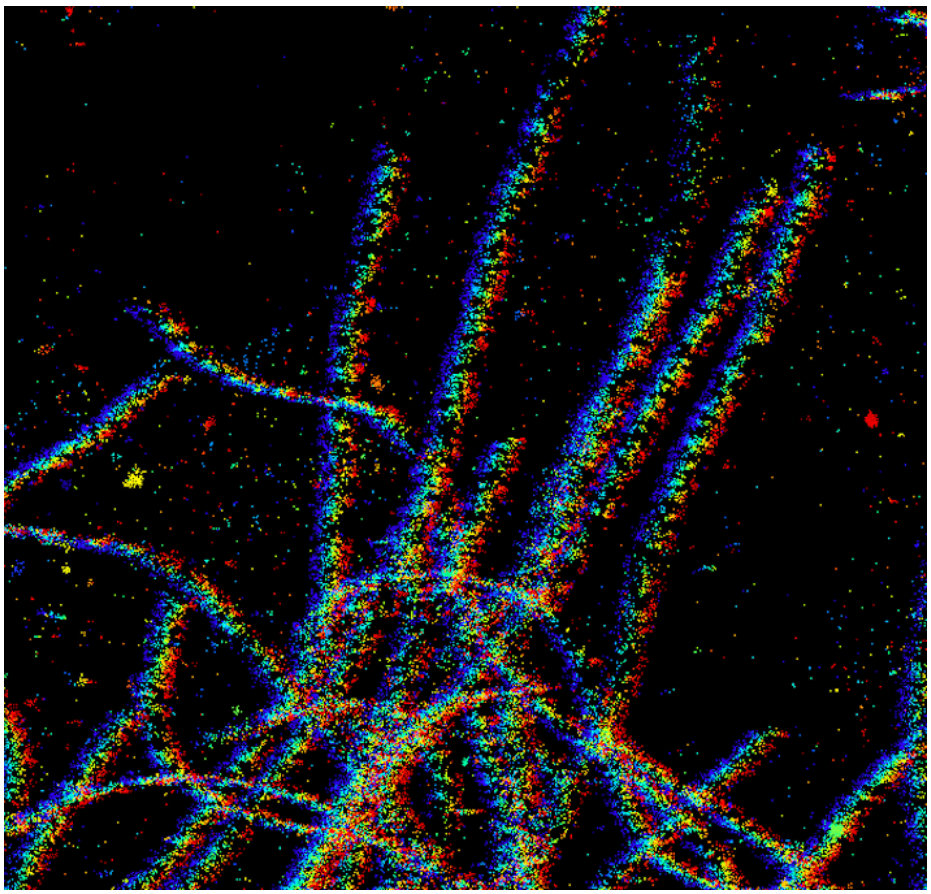

Figure 2.49: Drift in microtubule imaging due to temperature during an experiment of 400 seconds. By color coding localizations in time, the drift is seen as a rainbow. Here we show a drift of 1 nm/sec.

It would be interesting to have a rough estimate of the drift due to the thermal effects by considering the possible sources, so here we do a simple calculation to get an idea of the amount of the drift we should expect with respect to the materials we use for our holder and coverglass. The first calculation is based on the linear expansion coefficient. The main equation is:

$$\Delta L = \alpha L \Delta T$$

where L is the length of the sample holder in each direction, T is the room tempera-

ture, and α is the thermal expansion coefficient of aluminum. For Y direction, L_1=84 mm, and for X direction, L_2=56 mm, ΔT=1 C in 4 hours (based on measurement during a working day) and α=22.5$\times 10^{-6}$ m/mC, the result will be: ΔL_1=1932 nm and ΔL_2=1288 nm. Since we used ΔT=1 C in 4 hours, in one second we will have 0.1342 nm of drift in the Y direction of the NanoMax and 0.0894 nm of drift in the X direction. In a single cell super-resolution experiment we have 40,000 frames with 100 frames/second, so the whole period of taking data will be 400 seconds. The theoretical amount of drift during such experiment will be 53.67 nm in the Y direction and 35.78 nm in the X direction.

A second calculation is to find ΔL based on the amount of power absorbed by only the coverglass (not the sample holder) due to the 647 laser power during imaging a single cell for 40,000 frames. It is important to notice that we are not considering the heat transfer from coverglass to surrounding material (water, oil, and aluminum) which cause the thermal effects of the absorption to decrease. If the change in temperature is solely by absorption of power, we can use the following equations:

$$Q = mc\Delta T$$

so

$$\Delta L = \frac{\alpha L Q}{mc}$$

Our coverslips are BoraSilicat with a thermal expansion coefficient of α=3.3$\times 10^{-6}$ m/mC, L=12.5 mm is the radius of a 25 mm round coverglass of thickness of 0.2 mm, m=256 mg is the average mass of a single coverglass and C=0.84 J/g-K is the specific heat capacity of the glass, so if the intensity of laser is maintained at 5 kW/cm^2, the energy through the coverglass surface in 400 seconds will be: 2×10^6 J/cm^2. If we take the size of the focus on the coverglass to fill the inner circle of a 256 by 256 region, we will get 12.45 J. If we consider 1% of this energy absorbed, ΔL in the X and the Y directions will be 46 nm. We assume the worst case scenario that no heat dissipation to other materials have happened here. The Y direction is most

important since the sample holder is connected at one end to the plate on top of the NanoMax and at the other end is free, so the main drift will happen in the positive Y direction. The effect of both these sources will approximately produce about 100 nm per 40,000 frames of data on 0.25 nm/sec. The experimental measure of the actual drift will be done in chapter 3, and as we will see is around 1 nm/sec, but we can already see by this simple approximation that drift will play an important role in our experiments and needs to be controlled.

There are multiple ways to deal with drift. First, you can design the microscope to drift very small. This is the best way to deal with the drift problem. For this approach, one needs to find out all possible causes of drift in the optical system (e.g., mirror springs, dichroic cage caps, sample holder) and take care of them by using solid pieces that are not adjustable (e.g., fixed mirrors), and by building the sample holder from a material that shows least possible thermal expansion (Invar) which will drift only a very few nanometers in a few hours. Invar produces the best result.

The second way to correct drift is to do a post correction on the localization positions and reconstruct the final super-resolution images after the experiment is done. To do a post correction, one needs to use a drift marker [40] in order to be able to trace the direction and amount of drift from the first frame to the last. A bright fluorescent bead adhered to the coverglass can be used as a drift marker. After collecting all the data from the bright bead, by correcting the drift for the bead we can correct drift simultaneously for our main structure. There are two problems with this method of drift correction. First, this method doesn't work well for correcting drift in the axial direction (Z) when using a 2D imaging mode, and second, a bright bead will effect localization of less bright single molecules in the vicinity, making that part of the data unusable.

Third, are methods that compute the drift from the trace that localizations create through frames. The most common drift correction technique using point localization

data has been image cross-correlation, in particular, a fast implementation using fast Fourier transforms (FFTs) known as phase correlation [41, 42].

Fourth, are methods that identify and track features in the final image through a dataset to correct the drift [43]. Others in the Lidke lab have been developing a method that divides the problem into intra-dataset and inter-dataset drift correction, both using a cost function that is simply the weighted sum of the nearest neighbor distances for all the points in a frame (or dataset) with respect to the sequentially next frame (or dataset).

Our approach of dealing with drift is live drift correction, which is called active stabilization, performed as the experiment takes place. We implement the strategy described by McGorty et al.[44].This approach is able to correct for correcting drift in the axial direction when using a 2D imaging mode, and there is no need to use bright beads to mark the position of the sample for post-correction.

2.4.1 Active Stabilization

To use live drift correction one needs a motorized stage that can be moved with respect to a fixed position. We use two stages, one a 3-axis stepper motor to move to the position of the cell, and a 3-axis piezo stage to control and correct the drift accurately. Having these stages enables us to design a control method for live drift correction. Our control method is to take a Z-stack of reference images right before we start imaging a cell, and then during the experiment at each 5 seconds interval we take a current wide-field image and cross-correlate with the Z-stack to check on and correct for any change in X, Y, and Z positions. The correction scheme that we apply after calculating the cross-correlation is PI-control (proportional integral control) which will be discussed in the next section.

When cross-correlating a Z-stack of reference images to a current image, noise

plays an important role in estimating the deviation from reference position and can be misleading since noise levels might be higher than the accuracy we need to correct the position of the sample with, which means any try to move the sample from current position to its reference position directly (proportional control) will not work properly due to the existing noise level in reading the position. We need a proportional-integral control scheme to deal with this problem.

2.4.2 Proportional Integral Control

PI-controller is the method we use to get better feedback signal for our control scheme. In order to understand the concept of a Proportional Integral controller for drift control and correction, it will help to start with a simple example, a mass-spring-damper system used for closing doors. However an important difference between our PI-control scheme and what explained in this section is that in our system, we are not trying to control the movements of the sample holder (control of the movements of the sample holder is done through a similar PID-scheme which is part of our stepper motor and piezo stage movement scheme and can be tuned) but we are trying to control the efficiency of our feedback information based on noise related error in our cross-correlation-based distance measurement. This means that we have a zero-mass system in analogy with the mass-spring equations that will explain how a PID damping system works. Now that we cleared this issue, we can go on to see how a PI-controller works.

The equation that governs such a problem can be written based on Newton's second law, simply as the following:

$$m\ddot{x} + b\dot{x} + kx = F$$

Here F is the external force. Now if we take the Laplace transform of this equation and find the transfer function between the external force and the displacement, we

get to the following equations (where $U(s) = \frac{X(s)}{F(s)}$):

$$ms^2X(s) + bsX(s) + kX(s) = F(s)$$

$$U(s) = \frac{1}{ms^2 + bs + k}$$

Our goal is to obtain fast rise time, minimal overshoot, and zero steady-state error. Now let's use a real example. Take $m = 5kg$, $b = 20\frac{Ns}{m}$, $k = 20\frac{N}{m}$, $F = 1N$, and by plotting the step response as the right side of the last equation, we will have Figure 2.50.

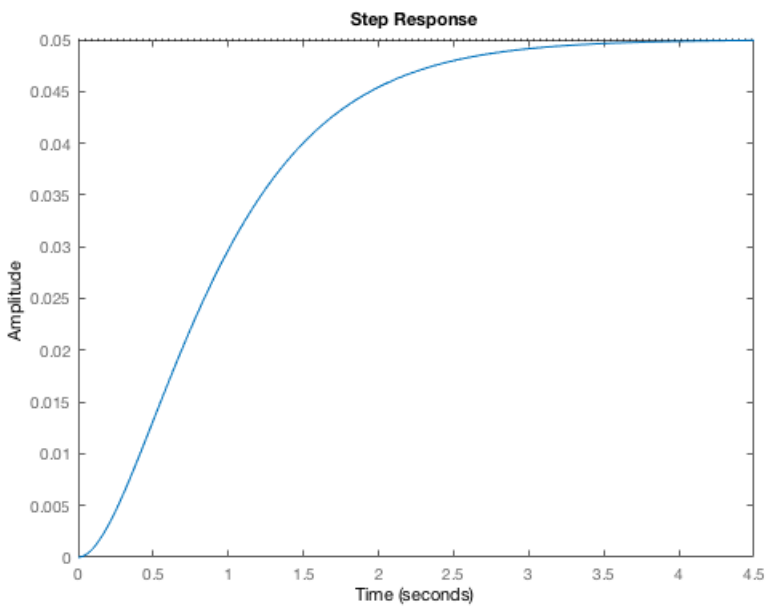

Figure 2.50: Step response of the mass-spring-damper system with constants of $m = 5kg, b = 20\frac{Ns}{m}, k = 20\frac{N}{m}, and F = 1N$.

Here, an amplitude of 0.05 (1/20) is the final value of the output to a unit step input which means there is a 0.95 difference between input and output (i.e., error). The rise time is about 2 seconds and the settling time is about 3.5 seconds. We now introduce three different types of controller with closed loops to increase the qualities

of the plot, and then we pick the best approach among these three to control the drift of the microscope:

First, we consider the proportional controller which can be formulated by the following equation:

$$U(s) = \frac{K_p}{5s^2 + 20s + (20 + K_p)}$$

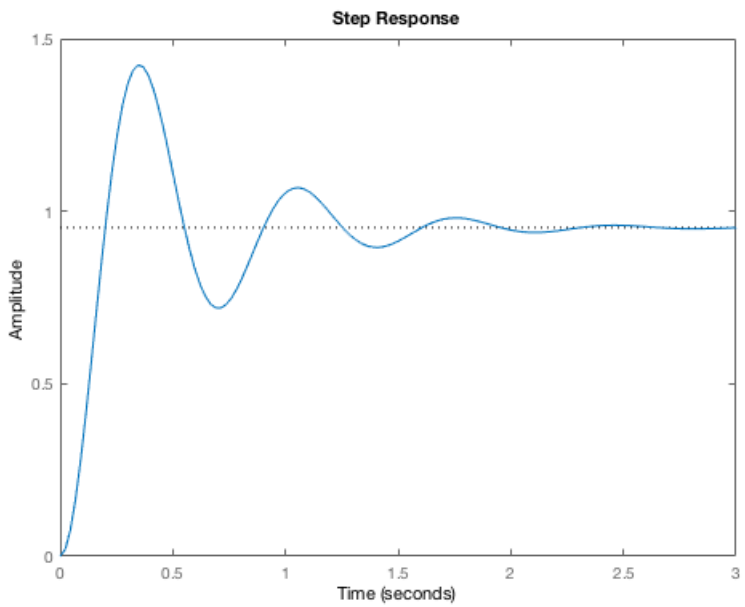

Figure 2.51: P-only control scheme with $K_p = 400$.

Figure 2.51 shows that by applying a proportional control scheme we reduced the rise time, the steady-state error and the settling time while creating a large overshoot. So some of the problems are fixed but other issues like overshoot are raised that need to be handled by a drift correction scheme. Next, we look at Proportional Derivative controller (PD) which mathematically can be implemented by the following equation with $K_d = 30$ for the derivative term, meaning we are now sensitive to changes in

error vs time:

$$U(s) = \frac{K_d s + K_p}{5s^2 + (20 + K_d)s + (20 + K_p)}$$

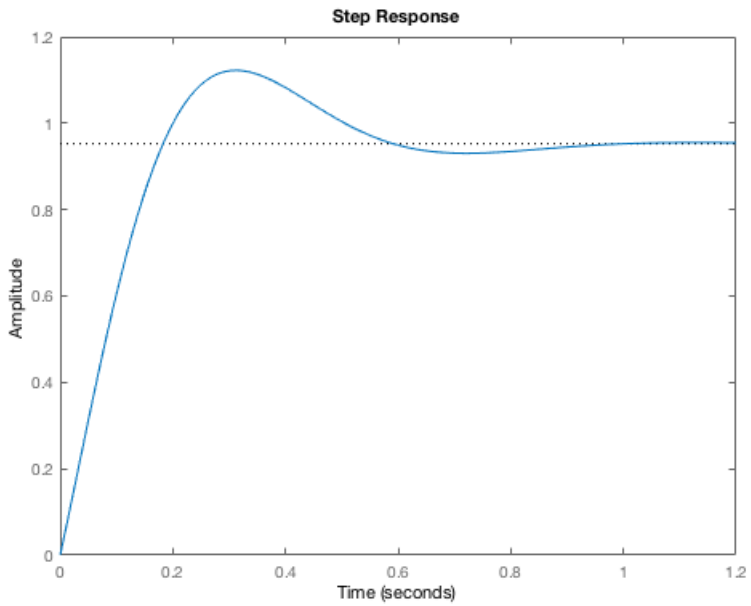

Figure 2.52: PD control scheme with $K_p = 400$ and $K_d = 30$.

Figure 2.52 shows that by applying a proportional derivative control scheme we reduced overshoot and settling time in comparison with the proportional control scheme, and had some small effects of rise time and offset, but is this controller appropriate for a drift correction scheme? The answer is no and we will say more below. Finally, we look into a proportional integral controller (PI), where instead of the derivative term we have the integral of time, so the equation will be rewritten as follows:

$$U(s) = \frac{K_p s + K_i}{5s^3 + (20)s^2 + (20 + K_p)s + K_i}$$

We need to reduce the proportional gain because the integral term reduces the rise time as well and increases the overshoot and we do not want to have same effect

from proportional and integral terms at the same time.

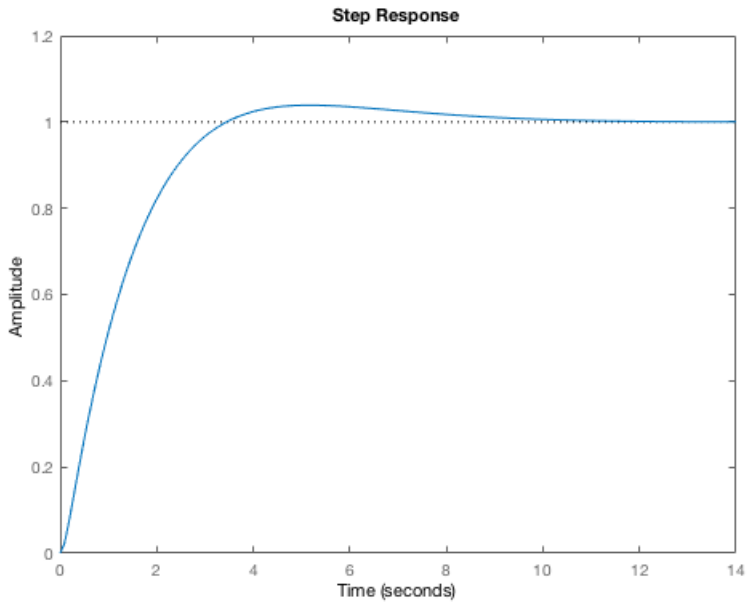

Figure 2.53: PI control scheme with $K_p = 40$ and $K_i = 20$.

Between these three control schemes and a fourth scheme of proportional derivative integral controller (PID), the best for active stabilization is an optimized PI controller.

The reason for this is related to the nature of the error in the experiment. We find the offset by calculating the difference between the current cell positions while taking data, at 5 second intervals, and saved cell positions at the start of the experiment. Since the positioning error is random, following it directly and in the opposite direction (as the proportional controller scheme does) is problematic since if the size of error is big, due to the offset we might get far from the correct position which means going out of focus. On the other hand, following the changes in error in time (as the differential scheme does) is problematic since we have very fast changes in

error due to the random nature of it and following these changes is meaningless and non-correlated with the true position of the target cell. With the proportional integral scheme, allowing these two problems are taken care of. The error is not taken care of immediately, but when tuned for the microscope at hand, it does provide a trustable scheme and can keep the range of drift within 10 nanometers. Figure 2.54 shows the comparison between P-only and PI-control simulation for our microscope, based on actual noise and drift.

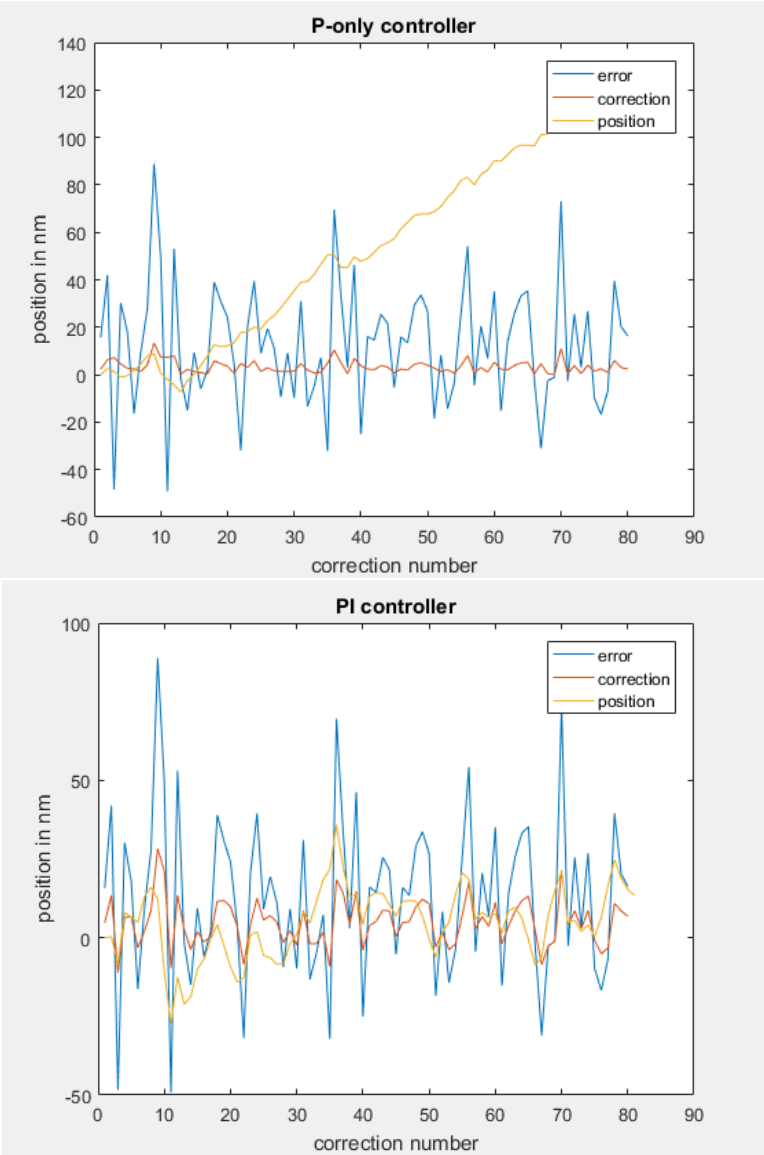

Figure 2.54: Simulation to compare a P-only vs. a PI-control scheme for our piezo stage. Here in each figure we have three plots. Blue plot shows the error in reading the current position, every 5 seconds, where numbers are based on real experimental values. Red plot shows the correction of error every five seconds. Yellow plot shows the actual current position at each 5 seconds. (top) P-only control scheme. In this scheme we follow the error by commanding the piezo to move fast in the exact opposite direction. (bottom) PI-control scheme. In this scheme we don't follow the error, but we try to keep the sample always at its initial position.

2.5 Conclusion

In this chapter, we designed a sequential microscope. Our design has different parts: optics, hardware, and software. For the optics part, we calculated and designed excitation and emission path and payed attention to details needed for the system to satisfy our needs. For the hardware part, we described all the needed components and how to connect them and what modes we should use them in. For the software part, we described the MIC class and codes written to control the hardware and to run the experiments. We also mentioned our strategy to deal with drift and how we actively stabilize the sample during experiment. In Chapter 3, we will go over the experimental necessities and limitation as well as investigating the characteristics of our design.

Chapter 3

Calibration and Characterization

In Chapter 2 we introduced the concepts needed in the design of the sequential microscope, then we designed the optics around those concepts. This design included excitation and emission path as well as considerations related to mechanical stages and cameras, control by Kinesis, MIC, and microscope GUI. In this chapter, we test and calibrate the design by doing measurements for different parts of the microscope and fine tune or change some of the details to achieve the needed super-resolution quality.

3.1 Measurements Related to the Design

3.1.1 Excitation Path Optics: from Laser to Fiber

There are two main areas we need to test the system for in the region from laser to fiber. These two areas are first, to measure the amount of power we can get out of the fiber and second, to measure the effect of diffuser on a beam profile. We get to these issues respectively.

1- Measuring the power out of the fiber:

In Chapter 2 we mentioned that we had limited our laser power to the upper limit of 350 mW to prevent optical damage to the objective lens. On the other hand, we need to have the desired intensity for dSTORM technique on the sample plane (i.e., between 5 and 10 kW/cm^2 although we set our designed value to 5 for practical reason of laser output power limitations) inside or outside a 256 by 256 square region (26.7 um $\times$ 26.7 um) as our imaging ROI. For the outer part of the circle, based on calculations shown in Figure 2.15 we need to have at least 85% efficiency of coupling into the fiber (while the actual measured coupling efficiency is about 80%) to be able to maintain at least 5 kW/cm^2.

We have a significant limiting factor that lowers the amount of power entering the fiber and that limiting factor is the presence of optical diffuser along the optical path. Reason for this decrease is that we need to focus the collimated laser beam onto the diffuser and collimate it again before coupling it into the fiber, but by passing the beam through the diffuser we lose some of the power due to scattering. Measuring the amount of power right before the diffuser and right before the fiber entrance shows around 7% loss of initial laser power when the diffuser is off and up to 25% when it is on. This means that with the highest allowable power of 350 mW out of the 647 laser, considering the 80% coupling efficiency of the multi-mode fiber, we will get a power of 260 mW (diffuser off) or 210 mW (diffuser on). This shows that for having a top-hat beam profile and an intensity of 5 kW/cm^2 we need to illuminate the circle inside the square of the 256 $\times$ 256 pixels.

Another limiting factor is the adjustment needed to achieve a top-hat beam profile. By adjusting the position of the lens right before the diffuser and the diffuser itself, we can change the shape of the beam profile toward a better top-hat profile. This will in turn effect the coupling into the fiber. Experimentally it causes an average of extra 5% drop in the power into the fiber. So we get about 80% of the

scattered light transferred by the fiber which is 260 mW out of the initial 350 mW. Effect of the diffuser on power out of the fiber is shown in Figure 3.1.

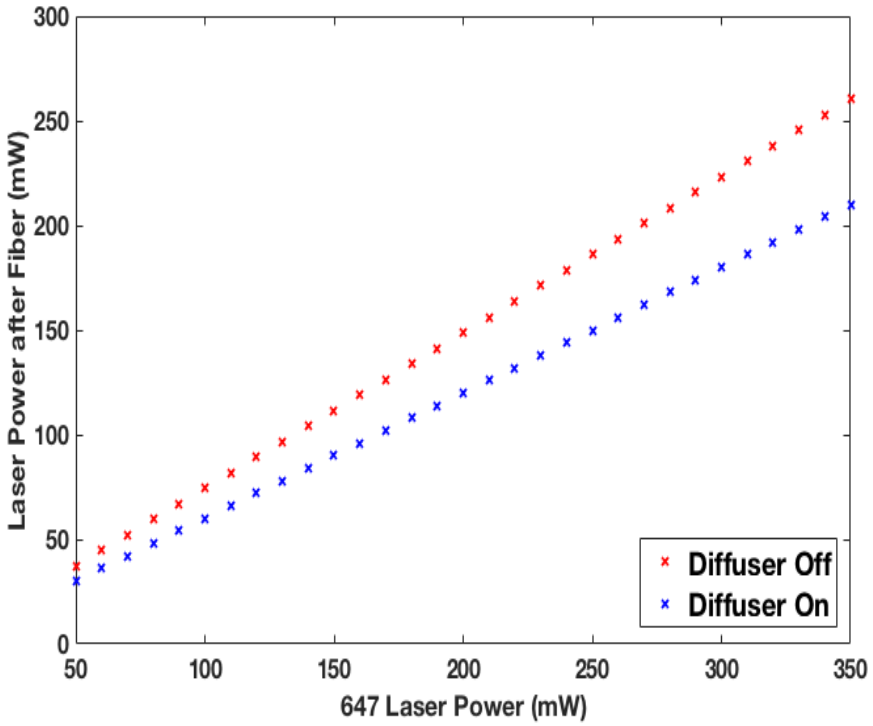

Figure 3.1: Effect of the diffuser on the power out of the multi-mode fiber.

2- Measuring the beam profile of the diffuser:

Since the physical place of the diffuser is on the path between the lasers and the multi-mode fiber, we will introduce the top-hat beam profile in this section although it could be placed in other sections as well. Here the diffuser is tested in two conditions: when it is off and when it is on (i.e., vibrating). For both cases we need a fluorescent sample on the microscope so we can measure the beam profile on the main sCMOS camera. The best way to perform this test is to image a planar sample with high density of labeling. This sample can be fluorescent beads or AlexaFluor647 dyes on glass. Labeling density shouldn't be too high that creates a 3D effect due to dyes adding

up on top of each other in multiple layers. In such case, by moving in Z direction for few hundred nano meters, image of the fluorescent sample on the sCMOS camera will not go out of focus which means the 3D effect of floating dyes in the few micron-thick layer of DiH2O trapped between two coverglasses causes a rather smooth transition between the edge of the fluorescent area and the background. Here I used 15 uL of 11 uM AlexaFluor647 on a 25 mm coverglass under 18 mm coverglass glued on top to seal the sample. The result can be seen at Figure 3.2.

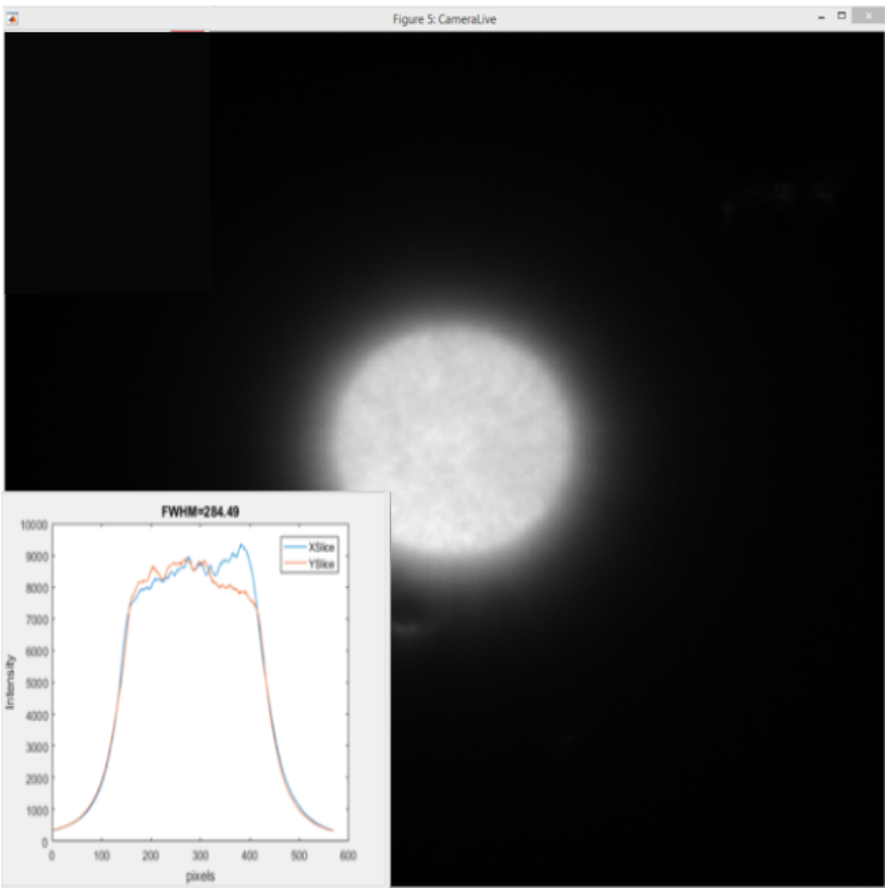

Figure 3.2: 3D effect of AlexaFluor647 dyes floating in the DiH2O trapped between the two coverglasses, on softening the top-hat beam profile edges.

We prepare 3 uL of AlexaFluor647 dyes in 11 uM of DiH2O, on glass which is low

enough concentration that gives almost a single layer of fluorescent dyes so creates sharp edges when in focus, and at the same time it is high enough concentration to give a uniform surface full of dyes so we can detect any speckle or other pattern due to multi mode fiber. The result can be seen at Figure 3.4 for both cases when the diffuser is off and when it is on. As we can see, in comparison with Figure 3.2 the edges drop 2 to 3 times faster, which means the image of the tip of the fiber on camera has sharper edges.

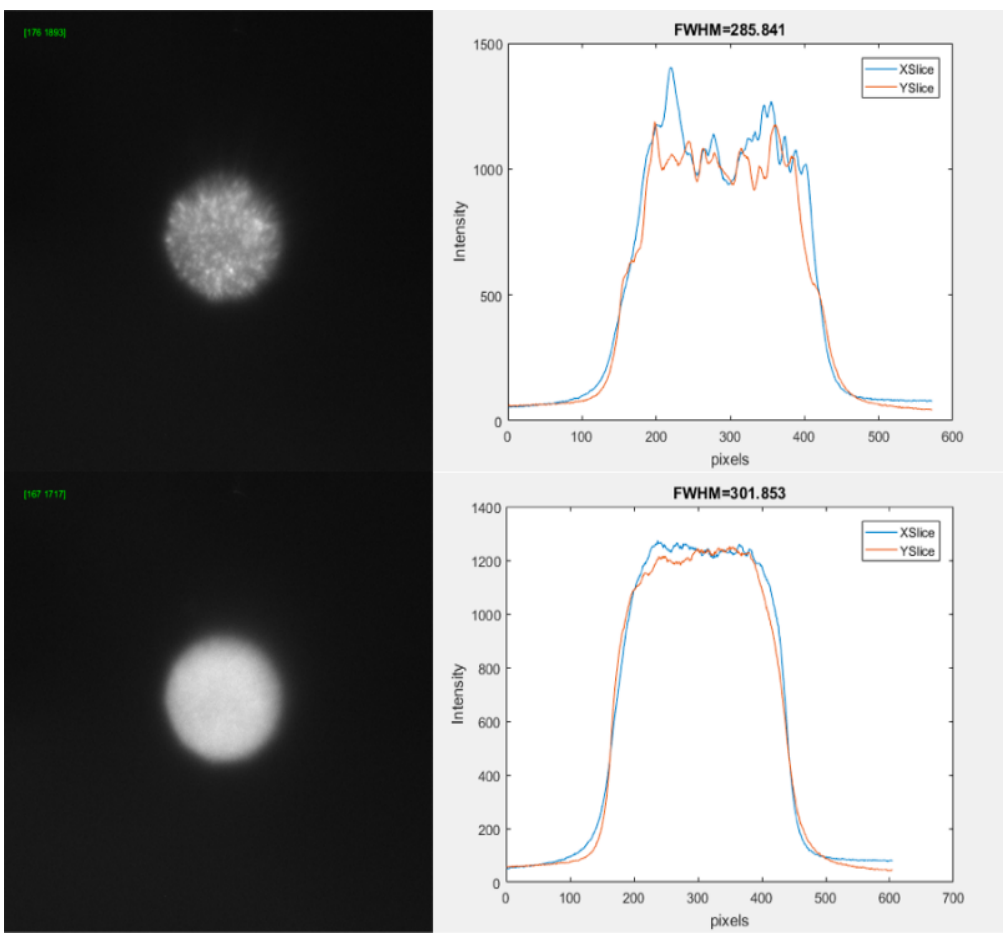

Figure 3.3: Comparing effect of the diffuser between on and off states, by imaging a thin layer of AlexaFluor647 on glass.

3.1.2 Excitation Path Optics: from Fiber to Sample

For the excitation path of the microscope, we image the tip of the multi-mode fiber onto the sample plane. Based on design considerations of Chapter 2, the image of the tip of the fiber on sample plane is a circle with the radius of 128×0.11 um=14.08 um. We need to tweak two of the lenses to get the required result on sample plane.These two lenses are the lens with f=9 mm focal length that is placed immediately after the tip of the fiber, and the lens after this one which has f=50 mm. Placement of these two lenses can be seen in Figure 3.4.

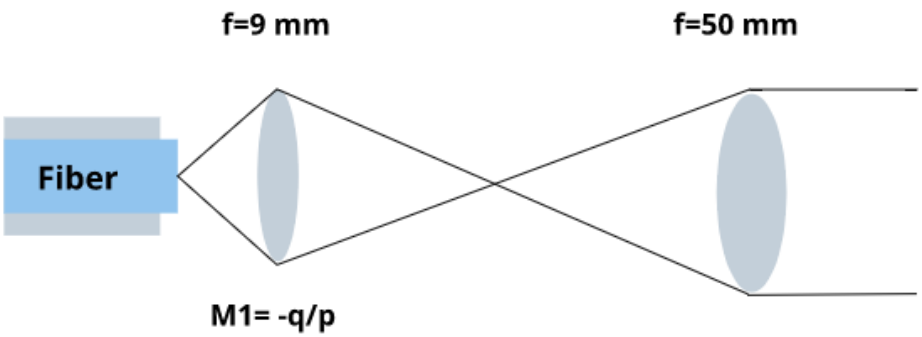

Figure 3.4: Lenses that need tweaking to create a top-hat beam profile of the right size and sharpness. Here p and q are defined as the distance between the 9 mm lens and the tip of the fiber (as the object), and from the 9 mm lens to the image of the tip of the fiber. p and q simply can be found by using 1/f=1/p+1/q where f is 9 mm.

In Chapter 2 we calculated the q/p ratio to be between 27 to 38. Based on laser power considerations talked about in Chapter 2 and experimental results shown already in this chapter, we have to tweak the distance between tip of the fiber and the 9 mm lens to be closer to 27, but the exact amount will be the one that produces the image with the sharpest edge so the intensity can be confined only to the circle inside the square of size 256×256 pixels. The result of the correct lens placement is

shown in Figure 3.5

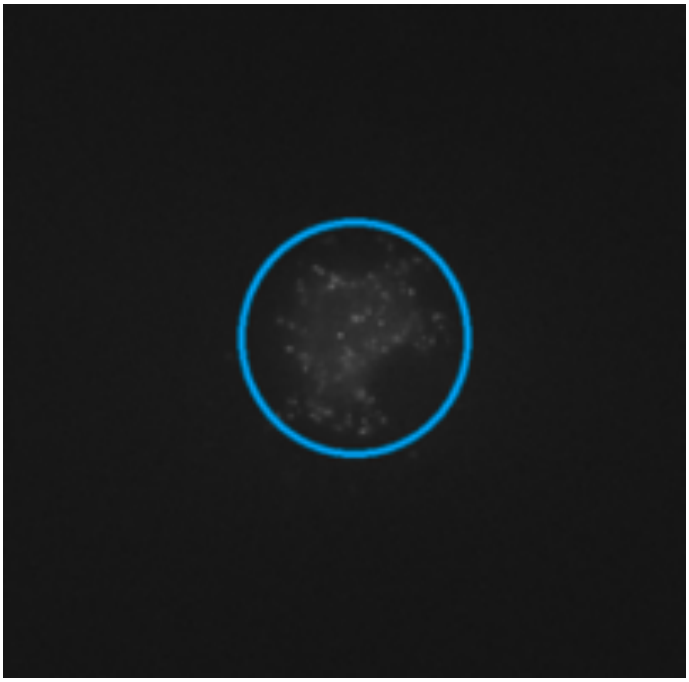

Figure 3.5: Effect of top-hat profile on imaging a single cell. The blue circle shows the circle inside the square of size 256×256 pixels. The area outside the circle is crowded with cells but shows no cell, which means the edges of the excitation region are sharp and our excitation beam is confined within this region.

3.1.3 Emission Path Optics: from Sample to sCMOS

In this section, we want to find the magnification between the sample plane and each of our sCMOS cameras.

We are setting up and testing with an inexpensive 60X objective before making a change to a 100X silicon immersion oil objective. Also, we decided to change the design to accommodate a Spatial Light Modulator (SLM) to the design later for enabling the microscope for PSF engineering in the emission path. Before we get more into the details of emission path, we need to present the modified design here.

This new design is shown in Figure 3.6.

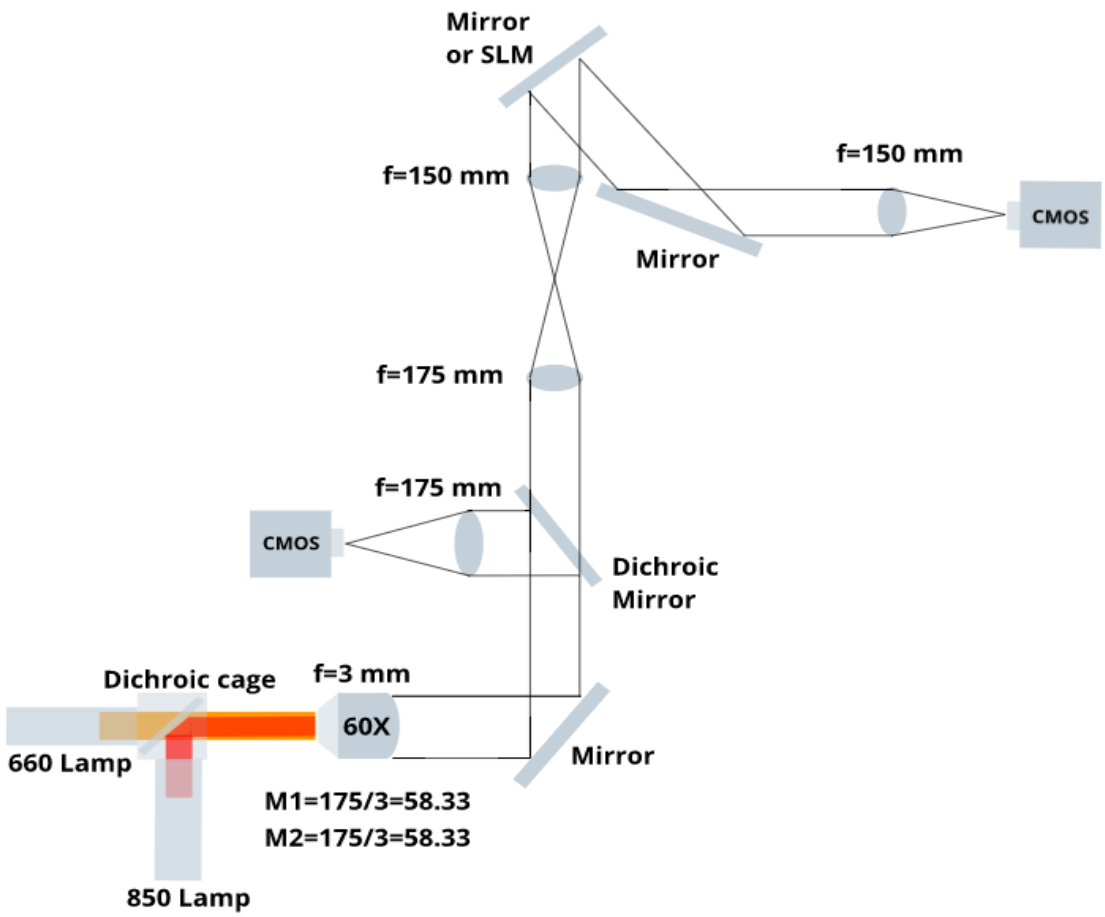

Figure 3.6: Modified emission path for a 60X objective. Spatial Light Modulator (SLM) enables the setup for PSF engineering. Here the angle of SLM is shown in exagerated manner.

To check for correct magnification in both arms of the emission path, we use a Thorlabs standard grid ruler (R1L3S3P). This ruler has different fine spacings etched on it in the form of separate squares. Each square is made up of a grid with a specific period. Periods are 200 um, 100 um, 50 um, 10 um, and 1 um. We use the 5 um period for our measurement on the sample plane. Such ruler is shown in Figure 3.7.

Figure 3.7: Thorlabs grating ruler. Each square shows a grating with specific period etched on one side of glass.

We first drop an oil drop on the top surface of the oil objective then we put the ruler on the oil and clamp it down to stay fixed during the magnification related measurements. After that we turn on both lamps, then by using the stepper motor in the Z direction (by moving the sample holder toward the fixed objective), we bring the ruler to focus, so the grid lines look sharp and show good contrast on both cameras at the same time.

A complication is that we do not get both live images of the grid to have the same sharpness at the same time. One of them is usually few hundred microns out of focus. In this case, we slide the lens back and forth to solve the problem. But the best way to approach this is first to adjust Z position of the grid to have the image on main sCMOS camera in perfect focus, then to tweak the lens that focuses light onto IR sCMOS sensor to bring the image of the grid to focus.

Figure 3.8 shows this measurement for both cameras on their live mode. The main sCMOS is not using the whole size of the sensor but adjusted to image on a square region with the size of 512×512 pixels, and the IR sCMOS is imaging on the

full sensor which is 1280×1024 pixels. Based on the value of magnification for each case (M=58.33 for main sCMOS and M=58.33 for IR sCMOS), the back-projected pixel size (bpp=6.5/M=0.111 um for main sCMOS and bpp=5.2/M=0.089 um for IR sCMOS), and by knowing the size of the region of sensor used on each camera, we calculate the number of 5 um-periods we should see in each case: 11.4 for main sCMOS ($512 \times 0.111/5 = 11.36$) and 22.8 for IR sCMOS ($1280 \times 0.089/5 = 22.78$).

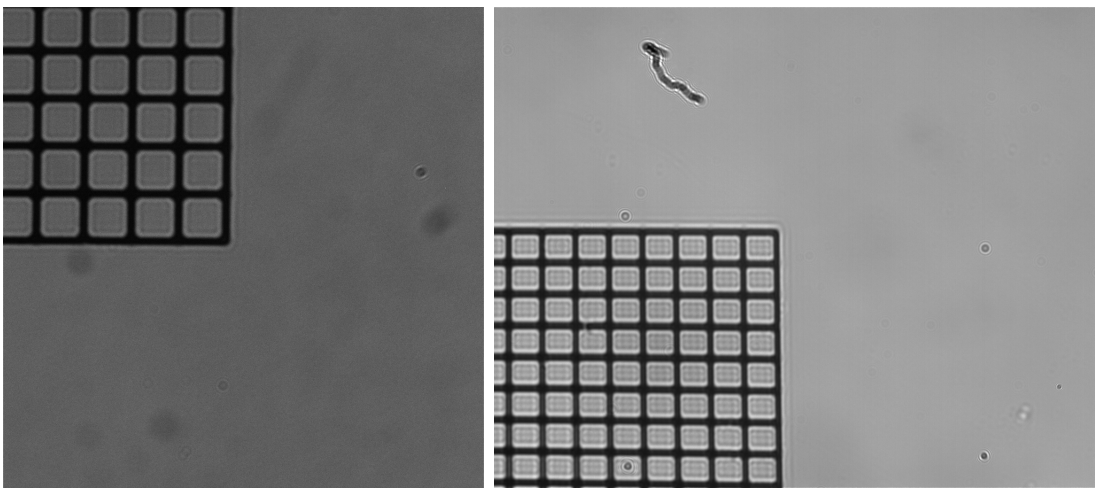

Figure 3.8: Image of grating with 5 um period on a 512×512 pixels region on main sCMOS (left) and on a 1280×1024 pixels region on IR sCMOS (right). Due to different optical path elements, images are seen rotated in comparison, and while the left image is focused, the image on the right is few hundred microns out of focus although the lens is positioned in the correct assumed distance from the sCMOS; all it needs is a bit of tweaking around its position to get into focus.

Another factor we need to check is the signal to noise ratio for sCMOS and IR sCMOS captured images. As we set the exposure time to higher values, we can create an image with higher amount of signal. The reason we have to do this check is that we need to calculate the cross-correlation of the reference image taken with the main sCMOS at the start of each experiment (when we pick up the target cells) with the image that is taken with the IR sCMOS every 5 seconds as the experiment is going on. Value of cross-correlation coefficient decreases as the exposure time decreases due

to the decrease in the signal to noise ratio. The main sCMOS at the exposure time of 10 milliseconds produces a wide-field image of higher contrast. For IR sCMOS the exposure times smaller than 1 second have a low signal to noise ratio thus the cross-correlation coefficient is lower. Comparison between two cases for IR sCMOS exposure time is shown In Figure 3.9.

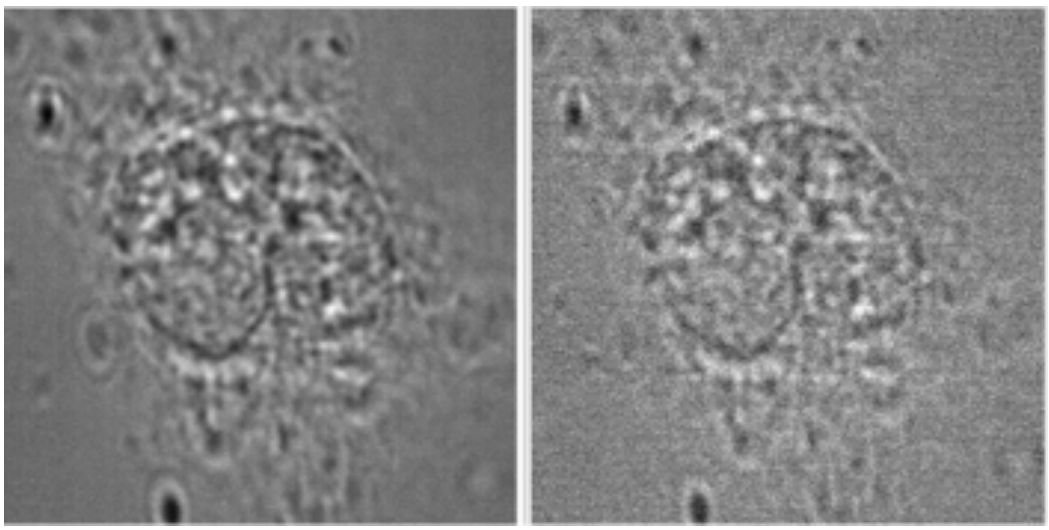

Figure 3.9: IR camera comparison between exposure times 1 sec (left) and 100 msec (right).

We take 40,000 frames of data with ten millisecond exposure time on the primary sCMOS camera, for each cell so the whole length of taking data on a single cell will be 400 seconds. To monitor and stabilize the changes in the cell and its environment actively, we image the cell every 5 seconds with the IR sCMOS and create a movie out of these frames. This movie is created when analyzing the data for each cell, for each label, so it can be used as a useful tool to check for any environment induced a decrease of cross-correlation coefficient due to a floating object during an experiment.

3.2 Sample Stage Measurements

As mentioned in Chapter 2, we don't use the whole range of the stepper motor since our design is based on 100 square regions, each of the size of 2048 by 2048 pixels, which means 2048×111 nm= 0.22 mm, so ten squares that make the range we want to travel in X or Y direction is equal to 2.2 mm. Now, to align the emission paths correctly with respect to excitation path, we need to align the NanoMax in a way that places the objective precisely in the middle and underneath the sample holder. We also want to image around the center of the cover glass and at the same time, by not moving toward the edges, we prevent sides of the cone of the objective lens from getting into physical contact with lower edges of the sample holder since it can cause damage to the lens surface. We will stay in the operational range of stage is shown in Figure 3.10.

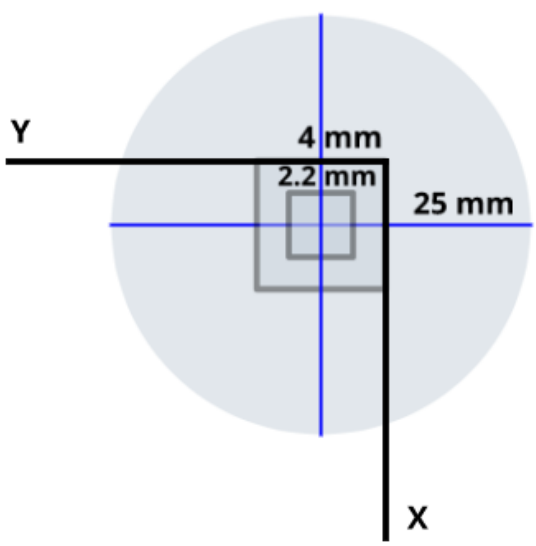

Figure 3.10: Stepper motor range of motion. The circle shows the coverglass, and the surrounding square shows the range of motion for the stepper motor in XY plane and small square shows the range of motion to contain 100 regions of the size 2048 by 2048 pixels where each back-projected pixel size is 111 nm. X and Y axes indicate the home position and positive direction of the stepper motor.

We saw in Figure 2.43 that stepper motor has a correction scheme for moving in the negative direction (i.e., toward reference) that is the impulse response for forward and backward movements are different for the stepper motor. But the critical factor while imaging is not the stepper motor since it is only used to move to the position of each cell before the imaging starts. The critical factor is the piezo stage and to find its impulse response since we are going to correct for drift by moving the piezo stage incrementally while we take single molecule data. We need to measure the movement of piezo when it is told to start from the current position and finish at a specific location in both positive and negative directions. To do this, we put 50 uL of 40 nm dark red beads by Sigma in DiH2O to achieve 10 millimolar concentration and put a 40 uL drop on top of a 25 mm round coverglass by ThermoFisher (number 1.5 coverglass which has 17 to 21 mm thickness) and cover it by a round cover glass of size 12 mm, then seal it with nail polish on the edges and let it dry.

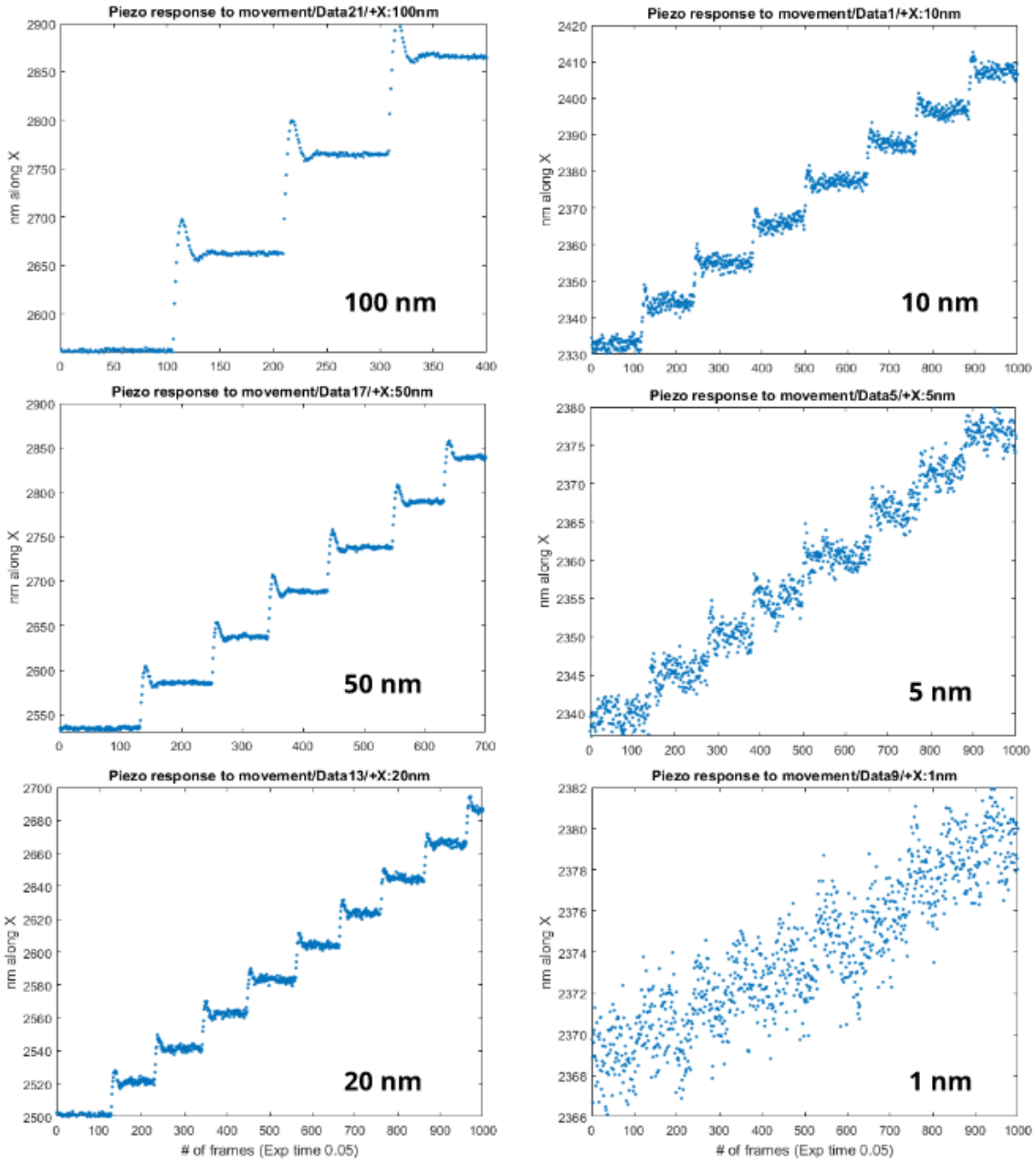

Figure 3.11: Piezo stage impulse response, nm in $+X$ direction for 1000 frames with exposure time of 5 msec.

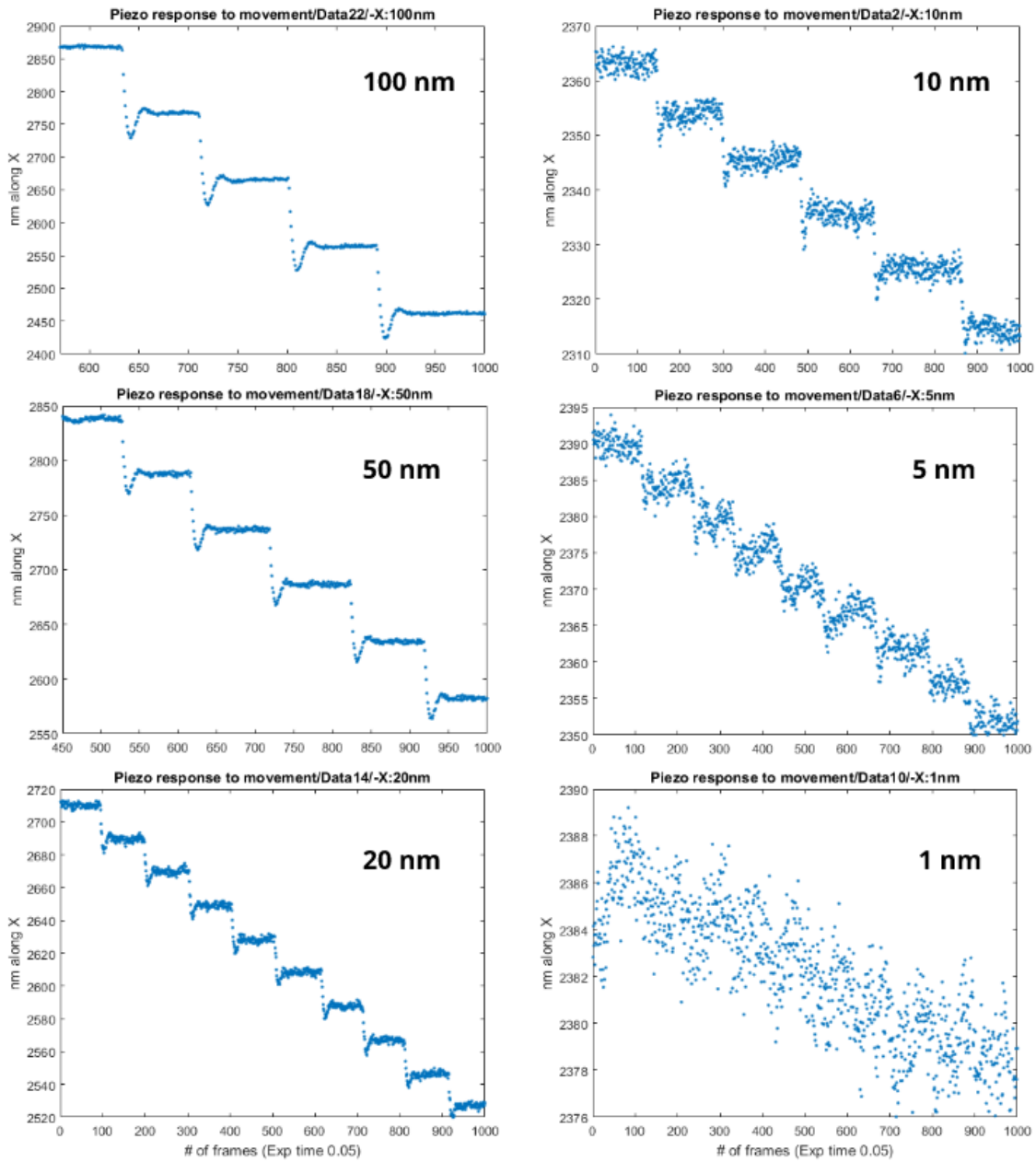

Figure 3.12: Piezo stage impulse response, nm in -X direction for 1000 frames with exposure time of 5 msec.

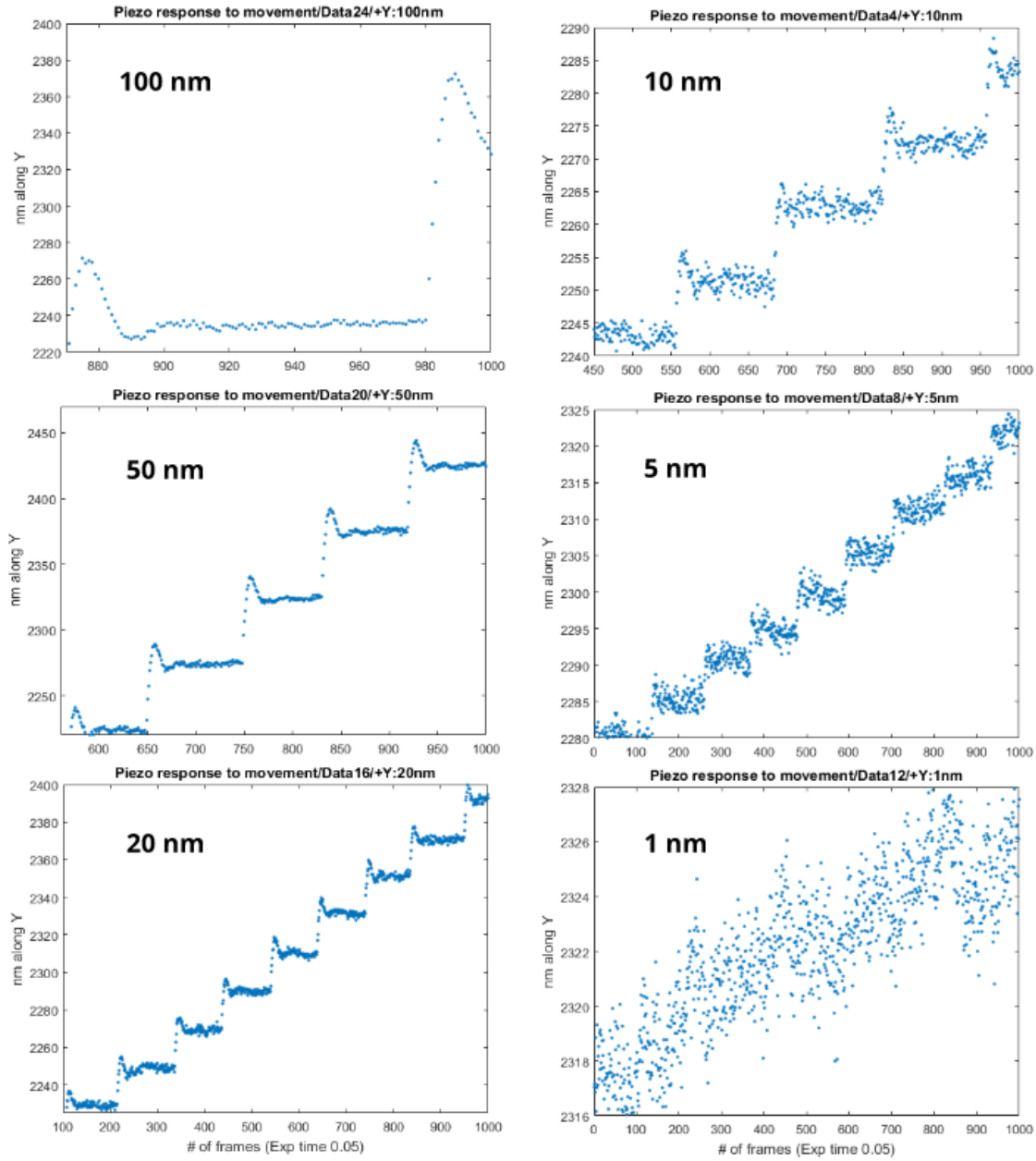

Figure 3.13: Piezo stage impulse response, nm in $+Y$ direction for 1000 frames with exposure time of 5 msec.

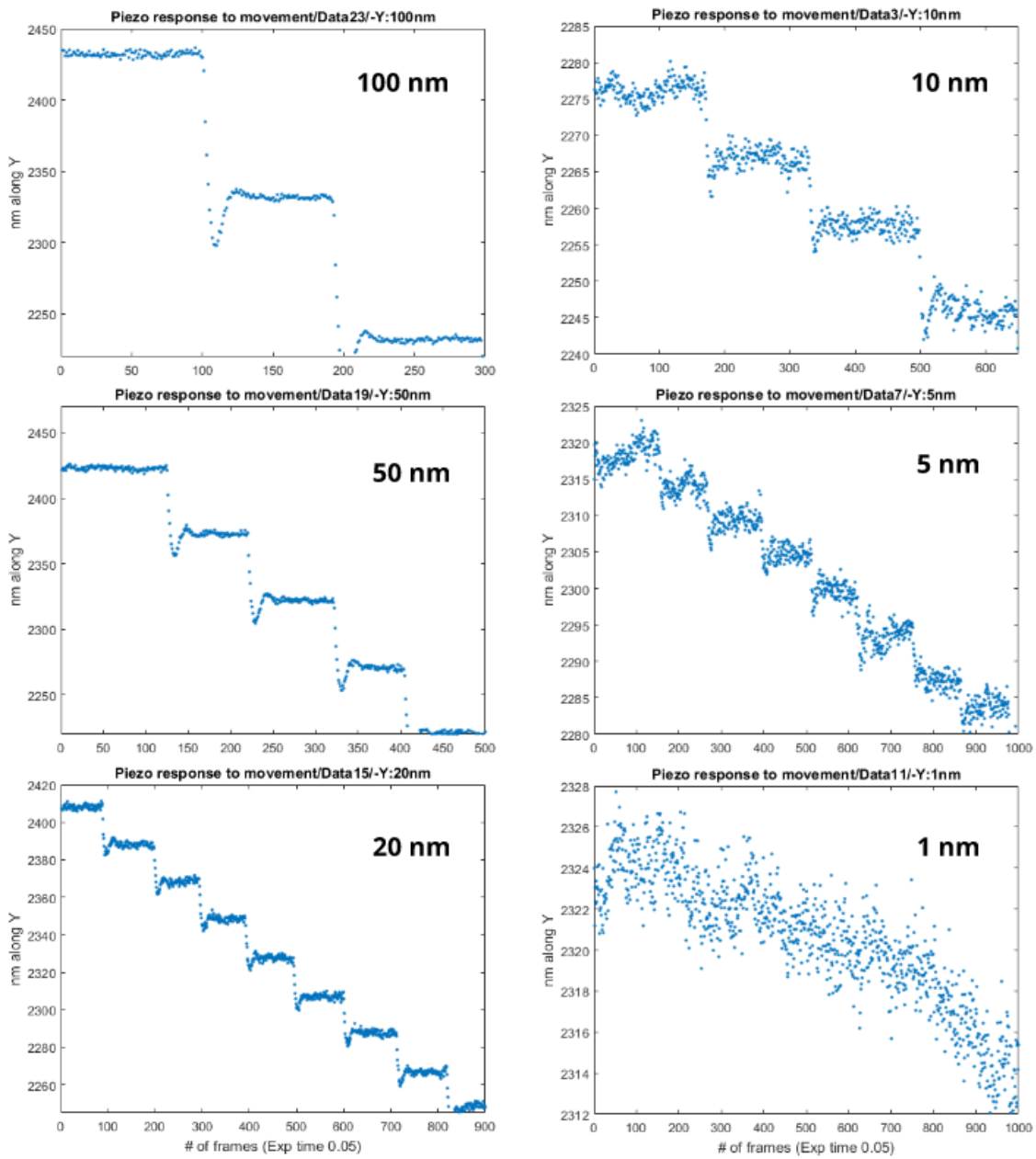

Figure 3.14: Piezo stage impulse response, nm in -Y direction for 1000 frames with exposure time of 5 msec.

Now that we know how the piezo and the stepper respond to movement, we

need to check the way a stage movement (doesn't matter if it is the movement by the stepper or piezo stage since their X,Y,and Z directions are the same) will be shown on main sCMOS camera. Here we investigate the relationship between a finite step mechanical shift on piezo stage in the lateral plane (XY plane) and the resulting image shift. This is a necessary test since we need to be able to replicate the directional change in position calculated in MATLAB between a reference and a live image, and move the piezo mechanically in reverse direction to correct the drift while imaging.

To perform this test, we use RBL cells plated on 25 mm round coverglass that are adhered to the coverglass overnight and fixed, so they are immobile during the experiment. RBL cells are small enough to be framed completely inside a square region of the size 256 by 256 pixels. Fixation is done by the instructions present in the appendix C of this dissertation. After fixing the cells, a single cell is picked and placed at the center of the imaging region, and we take a wide-field image as a reference image. We then use the piezo to shift the cell in the lateral plane and take an image and to find the shift between this new image with the reference image and then we use the piezo to move the cell back to the reference position, so the shift is zero. This is done in two steps:
1- We perform v=shift(u,δ) in MATLAB, where u is the reference image, δ=[ΔX,ΔY] is the shift, and v is the shifted image.
2- After we have created the shift, we put the cell back to the center and then we use piezo with same steps of the size of δ and try different signs for ΔX and ΔY to recreate the same shift by piezo again.

Shift function in MATLAB creates all images on the left side of each section through creating an overlay between the reference image (center) and shifted image. All images on the right side of each section are generated by the movement of the piezo motor in try to duplicate the left image. The line that appears in all sCMOS

images is due to directly adding an image and the shifted version of it and showing them by using *dipshow* in a single image. X-axis of the piezo is in the same direction as X-axis of live sCMOS image while Y-axis in piezo is the opposite direction of Y-axis of a live image. Result of this experiment is shown in Figure 3.15.

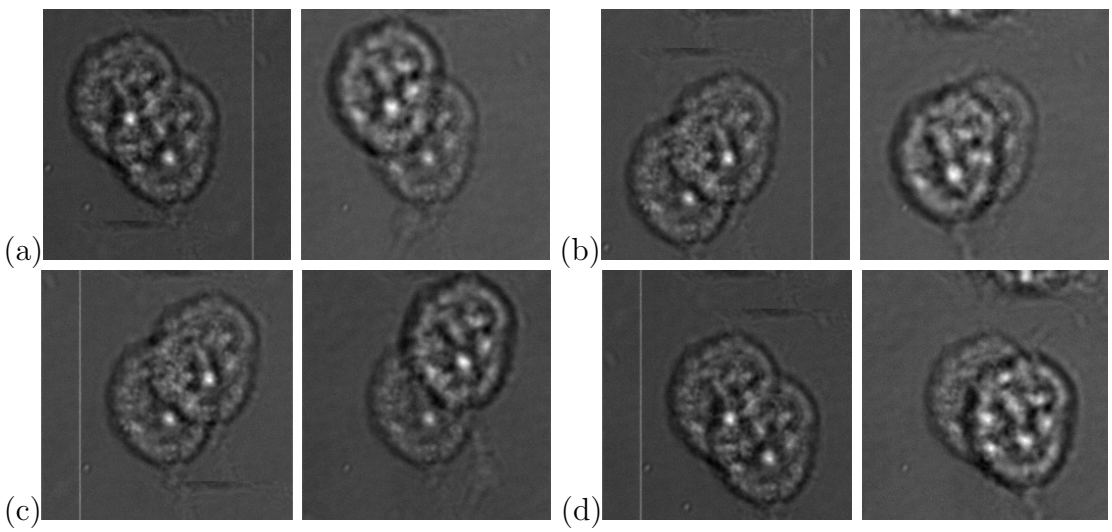

Figure 3.15: Creating a mechanical shift by piezo stage then applying "shift" in MATLAB to put the sample back at its initial position. Images on the left, all with a vertical white line on them, are created by overlaying the image of the cell in initial position with the image of the cell shifted through MATLAB function "shift". Images on the right are created by overlaying the image of the cell in initial position, with the image of the cell shifter mechanically by piezo. Direction of the shift in MATLAB that recreates the same piezo shift, is different for each case, and is calculated in the following: (a,left) shift=[$-\Delta$X ,$-\Delta$Y], right: shift=[$-\Delta$X ,$+\Delta$Y] (b-left) shift=[$-\Delta$X ,$+\Delta$Y], right: shift=[$-\Delta$X ,$-\Delta$Y] (c-left) shift=[$+\Delta$X ,$-\Delta$Y], right: shift=[$+\Delta$X ,$+\Delta$Y] (d-left) shift=[$+\Delta$X ,$+\Delta$Y], right: shift=[$+\Delta$X ,$-\Delta$Y]

3.3 Choosing Cells to Image

Another test we need to perform is to pick a target cell and save its position to go back to it later for imaging. In this process, two aspects are checked, and necessary

corrections are taken care of:

1- the relation between each green push button on the GUI and the home position of the stepper motor.

2- the relationship between live sCMOS ROI mode and the image taken from this live ROI with the home position of the stepper.

When the user pushes a green location-button on the GUI, stepper motor puts a specific part of the sample in front of the objective lens. Then an image pops up that shows a 2048 × 2048 pixels region on main sCMOS with many cells inside to pick from, as can be seen in Figure 3.16.

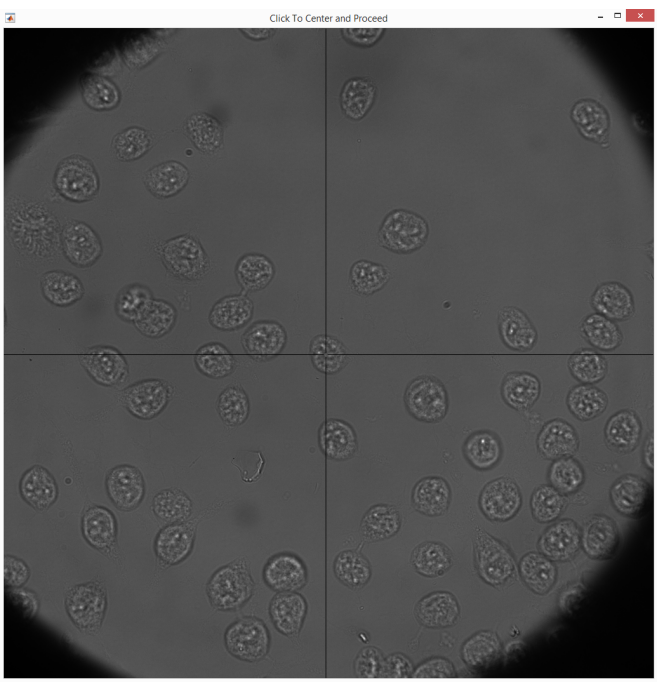

Figure 3.16: Choosing cells to image, step 1. Choosing a target cell from a 0.2 mm by 0.2 mm region containing many cells, is the first step of target cell imaging.

When the user clicks on a cell, the click location is calculated with respect to the top left corner of the image (point 0,0 of image in MATLAB) and stepper motor moves in a way to bring the picked cell to the center of sCMOS sensor, then another

smaller image pops up of size 256×256 pixels with the picked cell at its center. Our goal is to bring the picked cell to the center of the sensor the way shown in Figure 3.17.

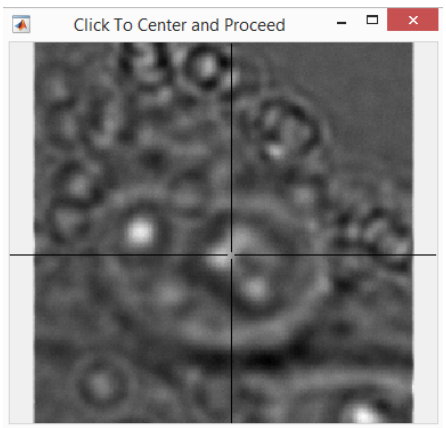

Figure 3.17: Choosing cells to image, step 2. In this step, a 26.7 um×26.7 um region around the cell we chose in step 1 is shown.

We need to calculate the relation between the click position and the stepper home position, in both live ROI and image ROI. Figure 3.18 explains the issue.

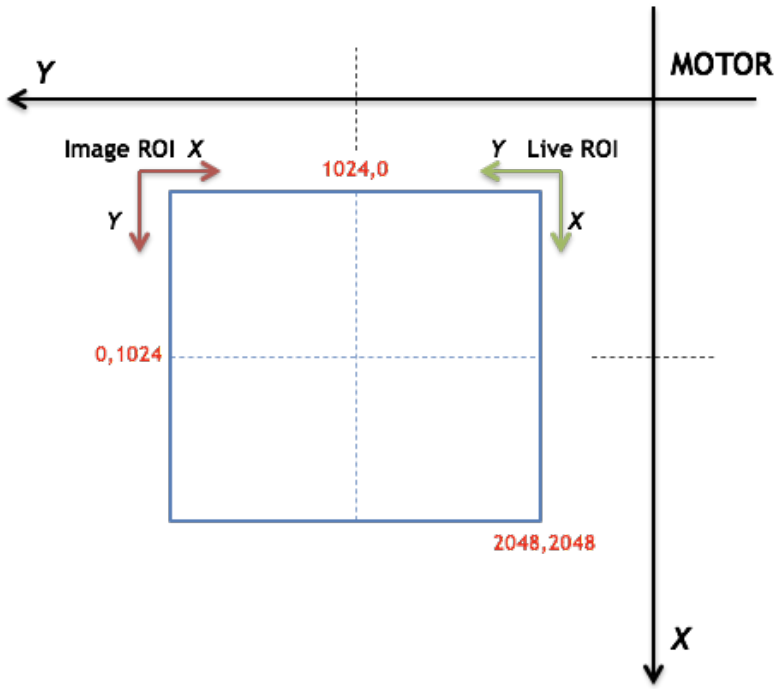

Figure 3.18: Relation between the ROI of the main sCMOS and stepper motor home position.

Here we show how the details of the math work by clicking a button on the GUI and then bu picking up a cell in the popup image. Figure 3.19 shows this situation.

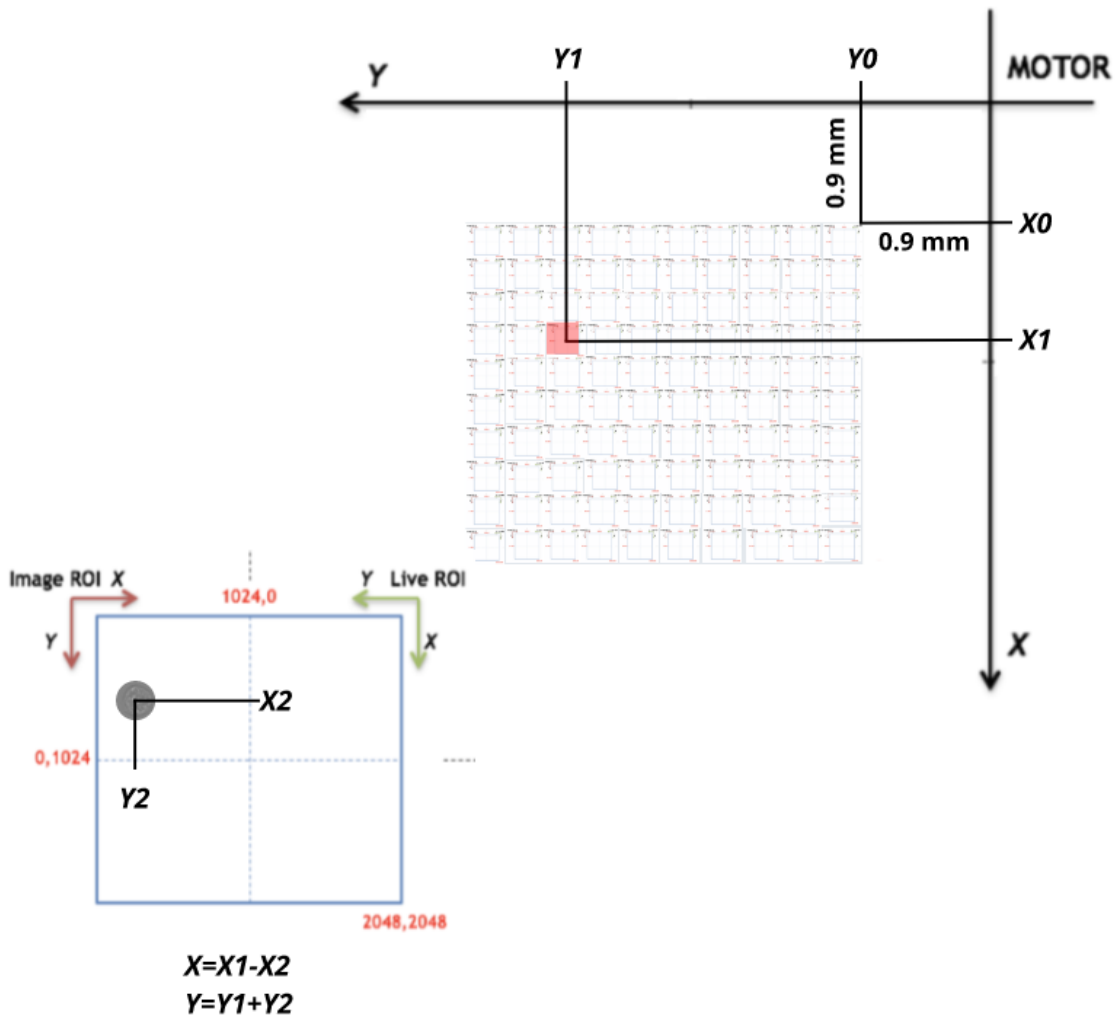

Figure 3.19: ROI on main sCMOS vs stepper Motor home position. Here the red (chosen) button is expanded in form of a 2048×2048 region and position of a clicked cell on this region is calculated with respect to home position of the stepper motor to move the cell to the center and appears a 256×256 region around it.

Next step is to look at the structure at low laser intensity (by putting the flip-mount that contains an ND filter in front of the laser beam), so we can make sure if we are in the proper axial distance from the surface of the cell or not. If the structure we want to image is not in focus, we can change the axial position using the stage GUI

as shown in Figure 3.20. Based on the usual place of appearance of each structure in the cell, we need to change the distance between the sample and objective lens in the z-direction to be able to see if the target structure is labeled efficiently and if it is in focus. For example, if our target structure is a receptor protein, we should look for it on the surface of the cell, so we can change the z distance to go to the cover glass or to go to the top surface of the cell or if we want to image the cell nucleus, we need to focus somewhere in the middle of the cell, etc.

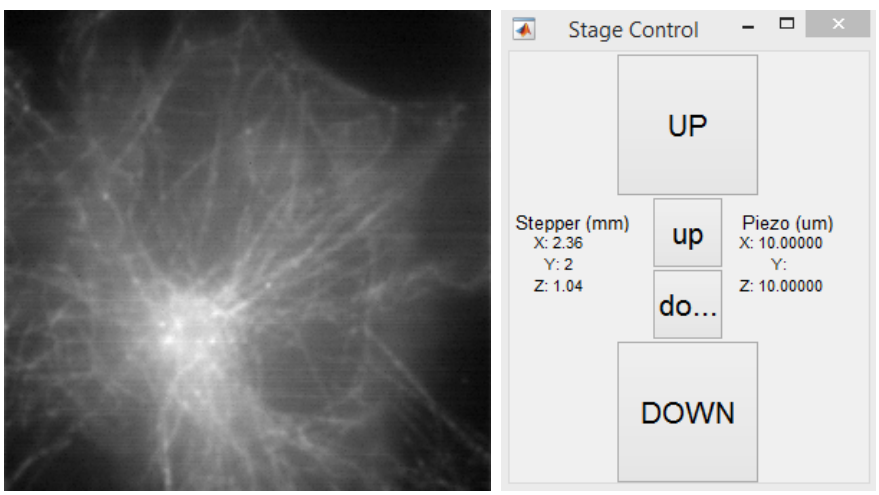

Figure 3.20: Pick up a cell, step3. Here user can check the structure in low laser light and change the z-position by the stage GUI

After changing the z position using the stage GUI buttons, the user closes this image, and upon closing it, she will be asked if she wants to save this image. She can click on "Yes" or "No" buttons presented. By clicking on "Yes," a wide-field image and the location of the X,Y, and Z of the stepper motor for this cell will be saved for later use.

3.3.1 Imaging Cells

We calibrated the movement of the piezo stage and formulated the relation between live ROI and image ROI with the reference position of the stepper motor. There is another crucial aspect of the experiment that needs paying attention to and needs correction. That aspect is the error of stepper motor is going back to saved positions. This error happens from time to time, and few microns of misplacement is observed by comparing the current position of stepper motor after finding the cell with the reference position of the cell saved before. In this case, we need a strategy to make sure we are in the position we intend to be. A good solution to this problem is presented by McGorty et.al.[44].

This solution is based on performing iterative cross-correlation between a saved wide-field reference image of a cell and a z-stack of 21 images (50 nm apart from one another, to cover a 1 um range total) that are taken from that cell after the stepper motor has moved to the saved reference position as shown in Figure 3.21.

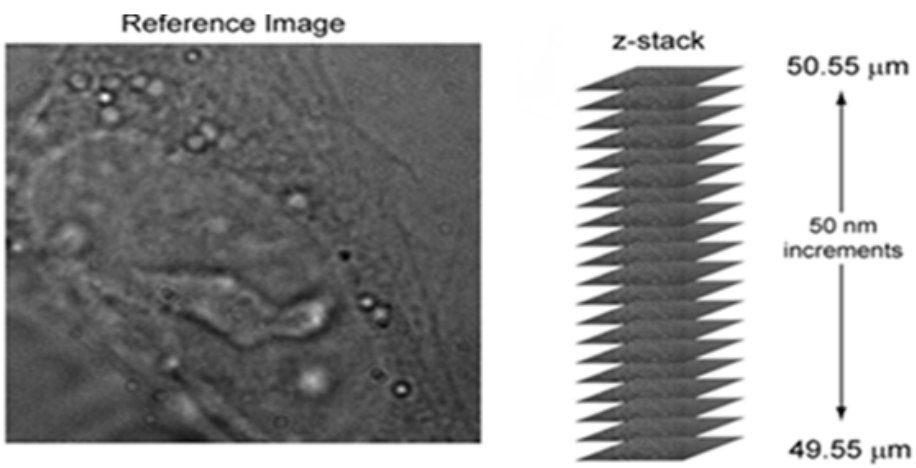

Figure 3.21: Taking a z-stack of 21 images to compare with the reference image [1].

The way this method works is: we calculate the cross-correlation coefficient be-

tween the initial reference image and each of the 21 images in the Z-stack. Cross-correlating two images yield an image with the same size and with a maximum whose position depends on the relative shift between the two images and whose intensity depends on their likeness. This can be roughly formulated as:

$$C_{a,b} = \int\int I_a(x,y) I_b(x-x', y-y') dx' dy' = FT^{-1}[FT(I_a) FT^*(I_b)]$$

Where I_a is the reference image, I_b is each of the 21 images in the Z-stack, and FT is the Fourier Transform. By plotting the peak position of the correlation function vs. defocus (Z-position of any of the 21 images), we can determine the focus position since a shift perpendicular to the image plane causes a decrease in the peak height of the correlation function. We should beware though that this decrease by itself does not indicate the direction of the defocus (positive or negative in z). This process is shown in Figure 3.22.

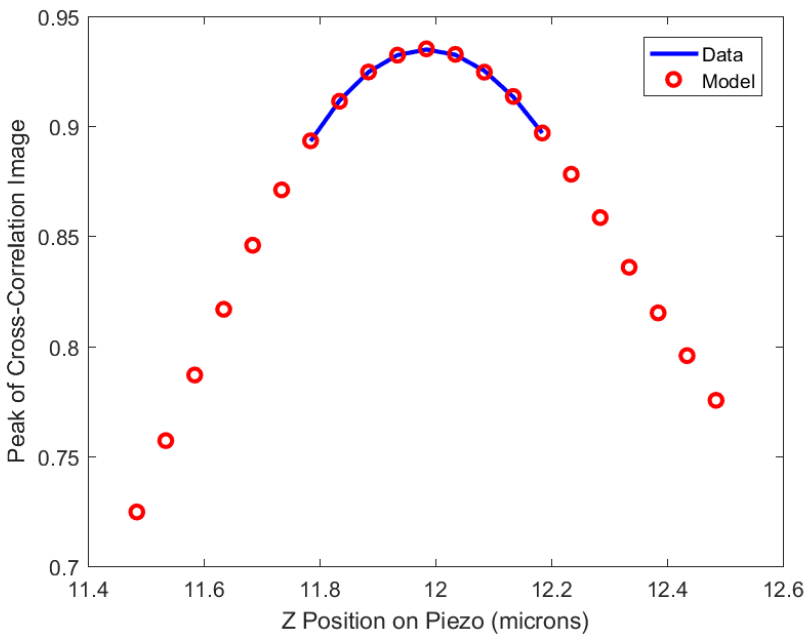

Figure 3.22: Cross-correlation plot to find the best z-position.

At each iteration round, we find the z-position of the peak of cross-correlation plot; then we find the difference between the X,Y,and Z position of the peak, with the X,Y, and Z-position of the reference cell. If this difference is not smaller than a specific amount, we go for another round of cross-correlation and do this check again. The iteration loop breaks when this condition is satisfied. At this point, the shutter in front of the 647 laser beam opens, and the microscope starts taking the data.

3.3.2 Testing the Repositioning Ability of the Microscope

At this point, a reliability test is needed to show that we can go back to a cell and image it for a second time without being shifted from the reference position and without having uncorrected drift during the experiment. Best structures inside a cell for such a test are microtubule strands due to their structure. As shown in Figure 3.23, microtubule strands are formed by two type of proteins; α-tubulin and β-tubulin that sits next to each other in a specific way. To show α-tubulin and β-tubulin molecules fall precisely on top of each other for every single strand in a cell, is a good test for our purpose.

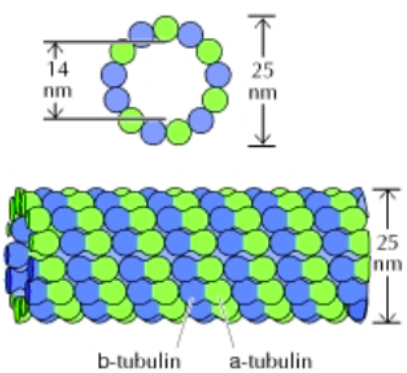

Figure 3.23: Structure of a microtubule strand [10].

To perform this test RBL cells are fixed with the fixation protocol in the appendix section and labeled with 2.5 ug/mL of monoclonal anti β-tubulin antibody produced in mice by Sigma-Aldrich (T8328-100UL) for 1 hour then washed for three 5 minutes in a blocking buffer (395 uL of 1X-PBS, 100 uL of 10% BSA, 5 uL of 10% Triton) and 40 cells are imaged for 40,000 frames of 100 frames/second. Imaging buffer consists of an enzymatic oxygen-scavenging system and primary thiol: 50 mM Tris, 10 mM NaCl, 10% (wt/vol) glucose, 168.8 U/ml glucose oxidase (G2133; Sigma-Aldrich), 1,404 U/ml catalase (C9332; Sigma-Aldrich), and 20 mM 2-aminoethanethiol, pH 8. The chamber is sealed by placing an additional coverslip over the chamber, and the oxygen-scavenging reaction allowed to proceed for 20 min at room temperature before the imaging started.Figure 3.24.

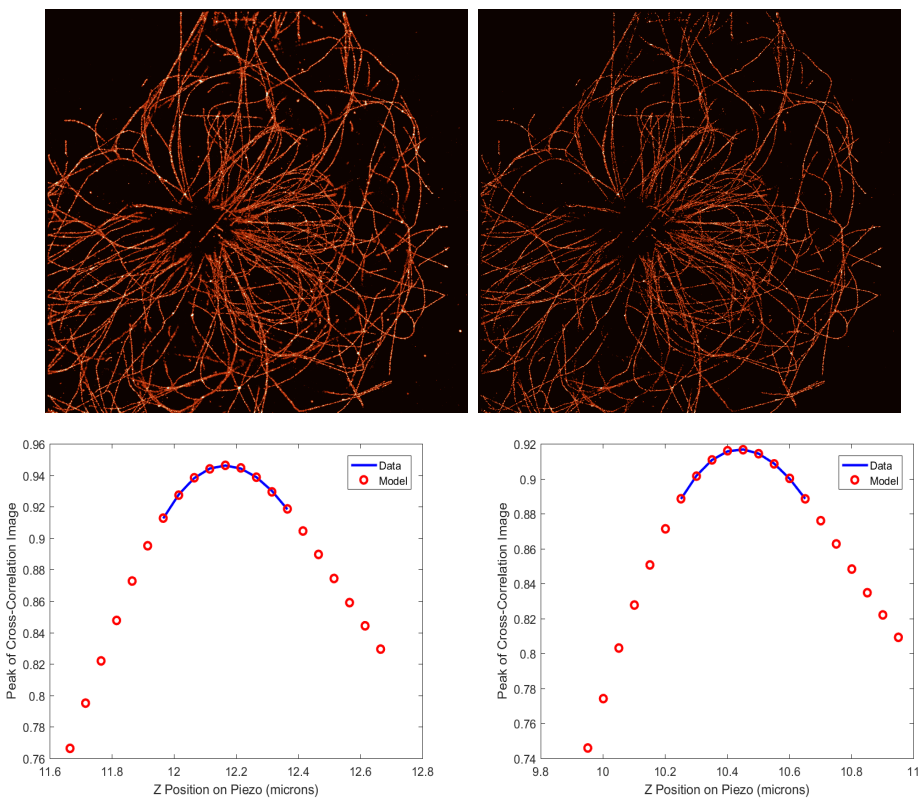

Figure 3.24: beta tubulin (left), alpha tubuin (right), and second label.

Then the imaging buffer is taken out, and cells are photobleached in PBS, by using both 647 and 405 lasers for half the imaging time. Then cells are taken off the microscope and quenched in 1mM NaBH4 for 15 minutes before the second label is put on for imaging α-tubulin with the same condition as β-tubulin for 1 hour. Then three 5 minutes of blocking is done, and cells are imaged in a freshly made imaging buffer. After the experiment is done, image reconstruction is done to create separate super-resolution images for each cell at each label as well as the color overlay of the labels for each cell, as shown in Figure 3.25.

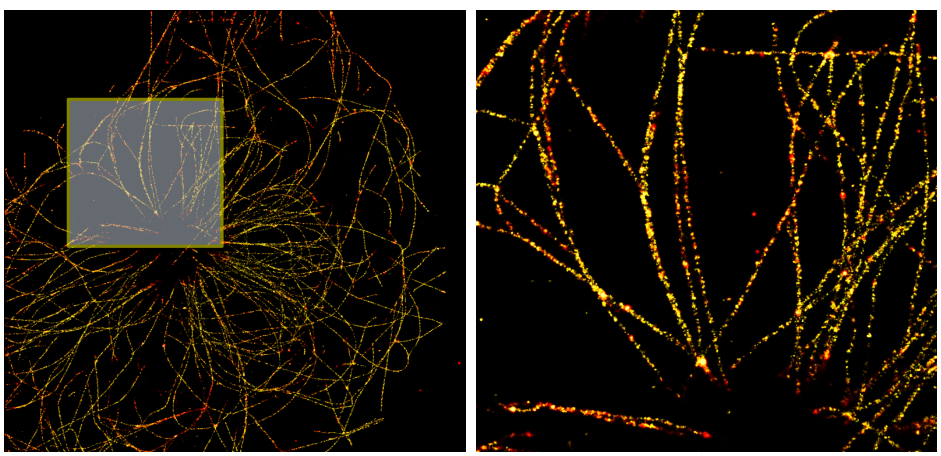

Figure 3.25: Overlay of β-tubulin in red and α-tubulin in green, in a single RBL cell (left) zoomed in (right).

There are 40 RBL cells imaged for reliability test to show the high-throughput capability of the microscope.

3.3.3 Imaging Multiple Labels

We showed that the reliability test for repositioning of the cells on sequential microscope works nicely for tens of cells, so now we image four different structures on a single cell sequentially and overlay the structures to produce a four-color image.

Chosen structures are IgE receptor aggregates, clathrin-coated pits, alpha tubulin sites on microtubule strands and mitochondria. All these structures are imaged in a single HeLa cell near the apex of the cell as shown in Figure 3.26, are not in TIRF mode.

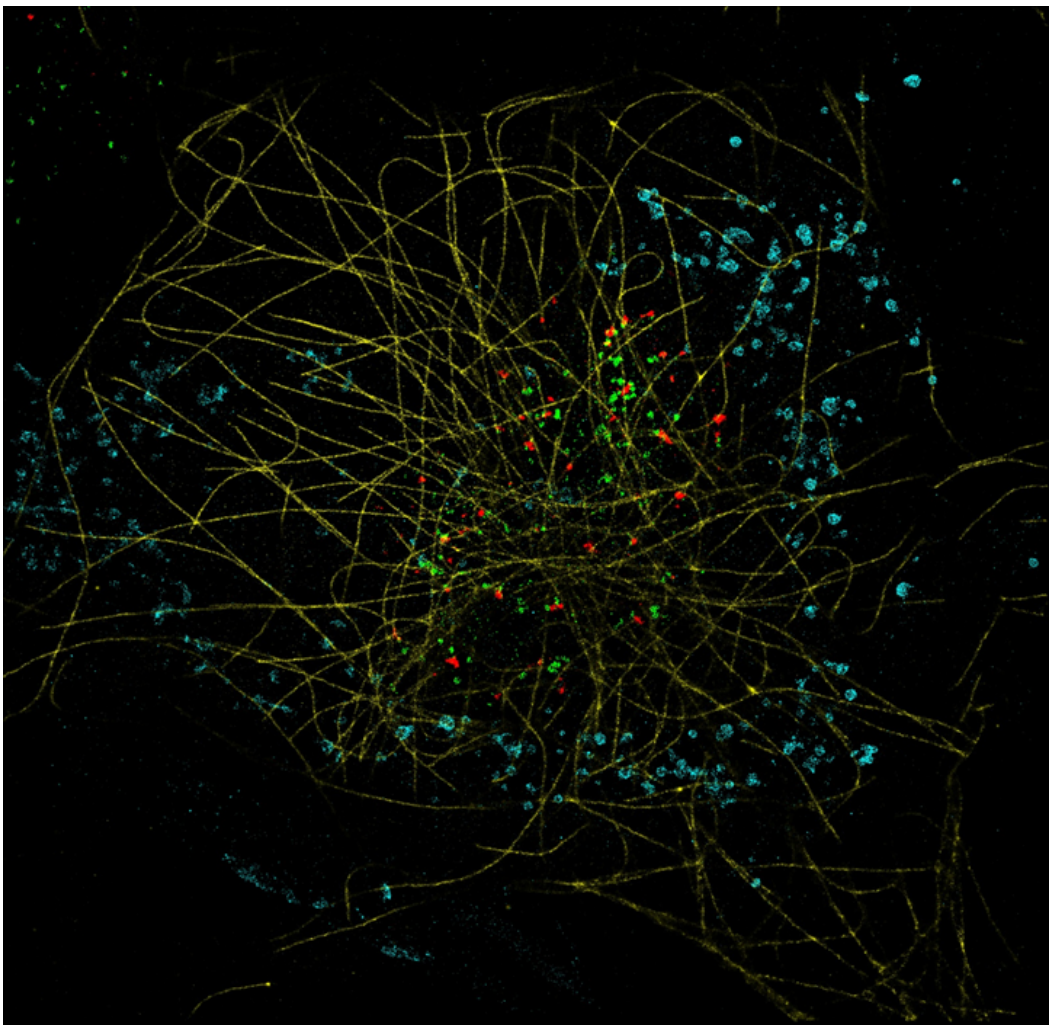

Figure 3.26: Four structures imaged sequentially in a HeLa cell. Yellow is tubulin, Blue is mitochondria, Red is IgE aggregates after 2 minutes of activation with DNP24-BSA, and Green is clathrin-coated pits.

3.3.4 Image Analysis and Statistics

We use multiple steps for image analysis. There are two types of information we gain from image analysis. The first type is visual information which consists of two subgroups: images and plots. Images are reconstructed through specific functions that take structured collected data as inputs. There are four functions to produce the following images: super-resolution image (which is the final result image), drift image (which shows the drift through color coding localizations in time), histogram image (which can be used to get a sense of the number of localizations per emitter visually), and sum image (which is a wide-field image of the target structure under laser light) as shown in Figure 3.27.

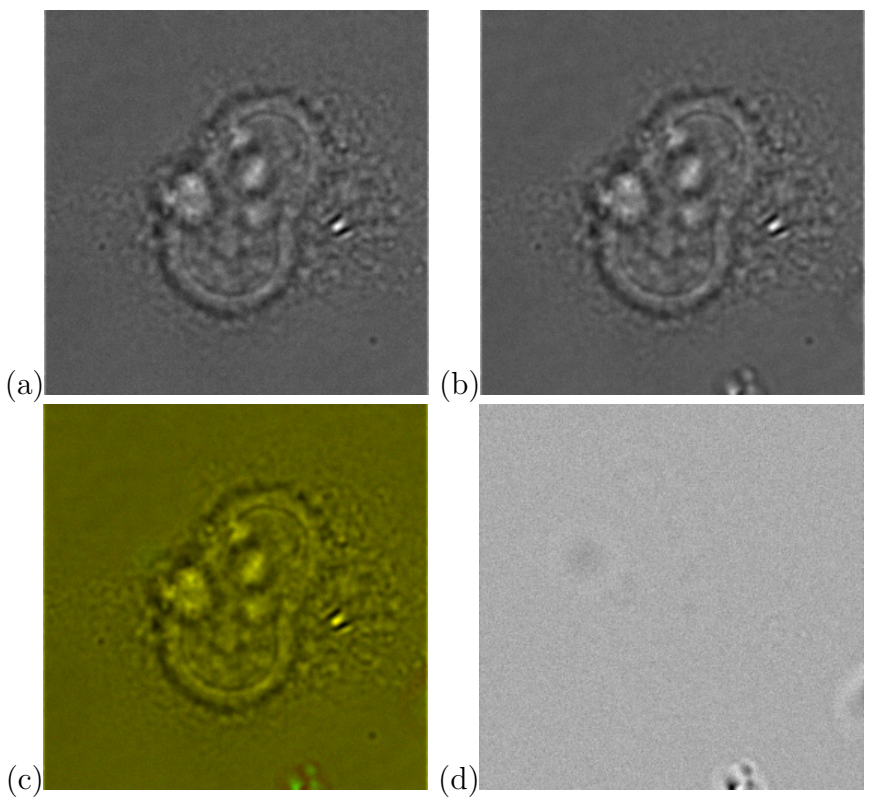

Figure 3.27: Overlay and difference for a single cell. (a) reference image of the cell, (b) current image of the cell, (c) difference image, (d) color overlay image.

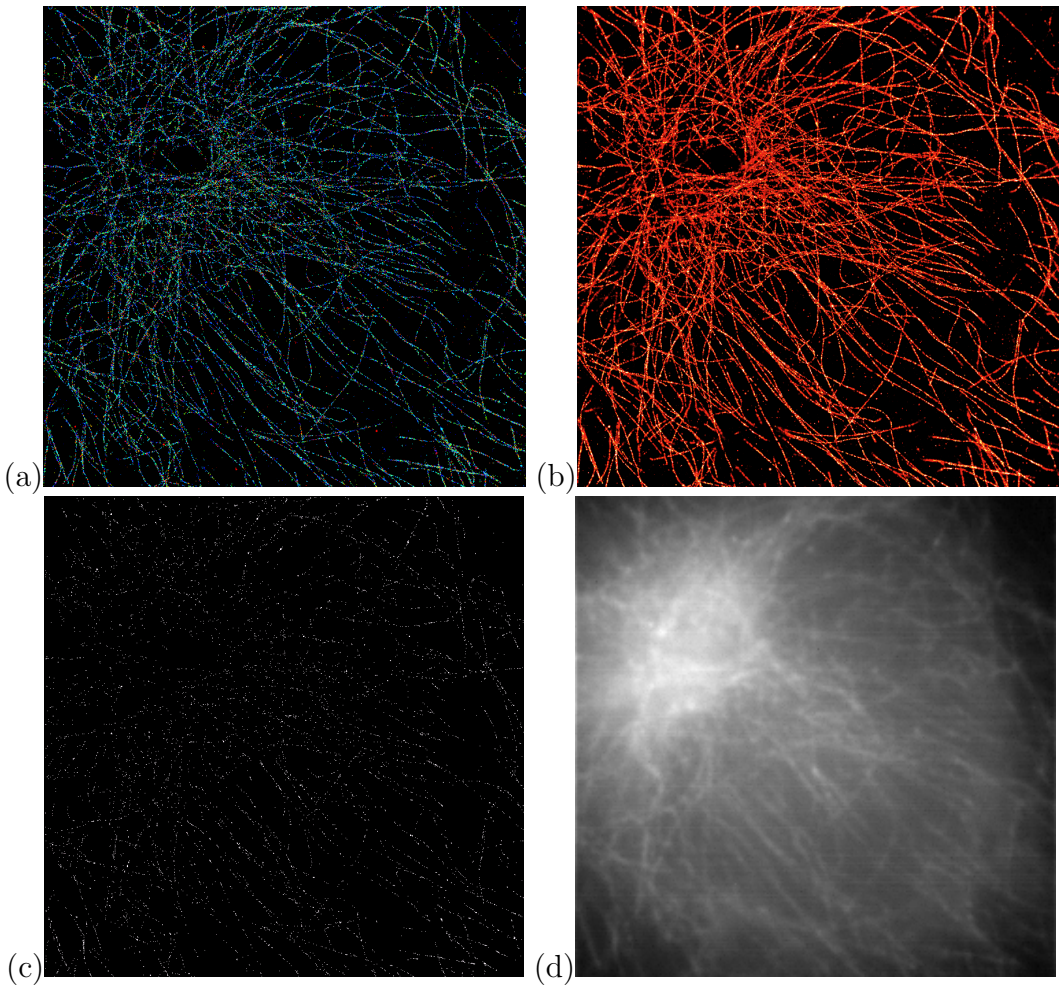

Figure 3.28: Reconstructed images. (a) drift image, (b) super-resolution image, (c) histogram image, (d) sum image

The second subgroup of visual information are plots that bring different details to our attention. Four of the most critical plots are the following: fit per frame plot (shows the number of fitted emitters per frame vs. time, through the whole experiment) which can provide information about the effectiveness of the buffer and give a feeling about emitter density of the sample fitted with a single emitter model. Duty cycle, on/off emitter lifetime plot, and background as shown in Figure 3.29.

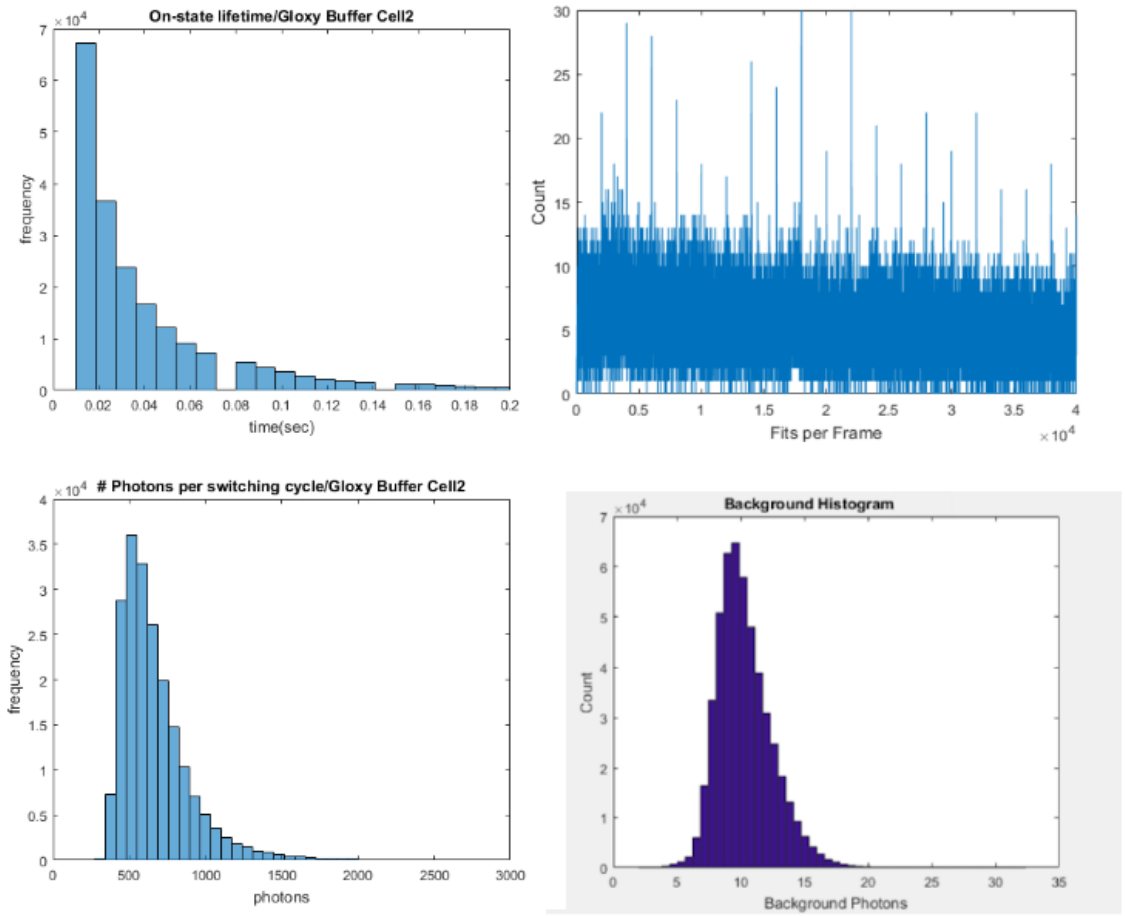

Figure 3.29: Analysis on the emitters. (a) on/off emitter, (c) duty cycle, (c) fit per frame, (d) background.

3.3.5 Cluster Analysis

To analyze the super-resolution images in more detail, for problems that involve two or more structures of interest that have globular forms, and to investigate spatial organization between these structures, we use clustering techniques to gain more information. Two primary methods we use are the following: First method is Density-based spatial clustering of applications with noise (DBSCAN) [45] which groups

points in space that are closer than an arbitrary distance set by the user based on nature of the problem at hand. The group of points that get clustered are called core point, and the points that get outcasted are called outliers. Outliers can't be reached from any other points. There are two parameters needed in DBSCAN. First is a characteristic distance ϵ which roughly represents the size of the expected neighborhood and second is the minimum number of points required to form a cluster, as shown in Figure 3.30.

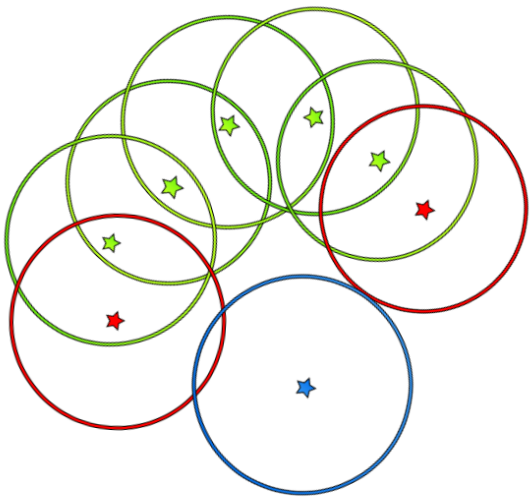

Figure 3.30: DBSCAN: clusters and outlier points are chosen based on radius size ϵ and how points at the center of circles fall into each others neighborhood. Green stars have all two points in their radius so these are core points. Red stars fall into the cluster although only have one star in their radius. Blue star is considered as noise.

After finding all the clusters for different rounds of sequential imaging (i.e., for different structures) we can calculate the center to center distance between clusters of structure A and structure B and plot a histogram to see if we find a characteristic distance between the structures under investigation or not (This method is not appropriate for filamentous structures and only works fine for globular structures).

The second method we use for cluster analysis is pair correlation. Here the goal is to figure out if the pairs we see in the super-resolution image have random distance or do they have a characteristic distance.

The pair auto-correlation function (or radial distribution function) g(r) of a system of particles describes how density varies as a function of distance from a reference particle. If a given particle is taken to be at the origin O, and if ρ is the average number density of particles, then the local time-averaged density at a distance r from O is ρg(r). This simplified definition holds for a homogeneous and isotropic system. In simplest terms, g(r) is a measure of the probability of finding a particle at a distance of r away from a given reference particle, relative to random.

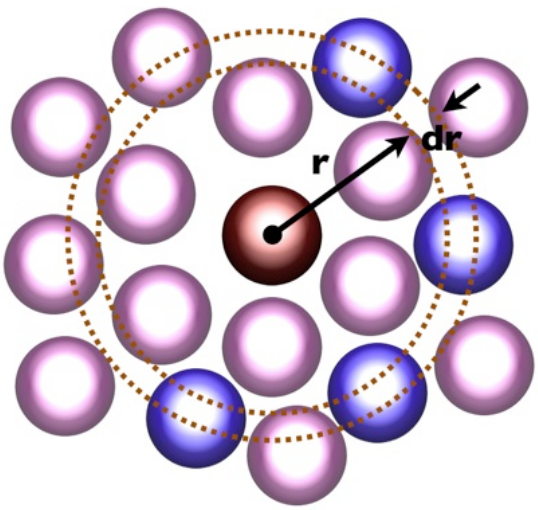

Figure 3.31: pair correlation [Lidke Lab Wiki].

The general algorithm involves determining how many particles are enclosed within a shell or inner radius r and outer radius r+dr from the particle. This general theme is depicted below, where the red particle is the reference particle and blue particles are those which are within the circular shell, dotted in orange. The pair correlation is usually determined by calculating the distance between all particle pairs

and binning them into a histogram. The histogram is then normalized with respect to a random distribution. The pair cross-correlation function c(r) is similar to g(r), except that now the density distribution is calculated for particles of one color (or label) with respect to particles of a second color (or label) as shown in Figure 3.31.

3.3.6 Conclusion

In conclusion, in Chapter 3, we built and characterized different parts of our microscope based on the design we provided in Chapter 2. We tested different parts in excitation and emission path and tuned them. We then tested the microscope repositioning ability by imaging α-tubulin and β-tubulin as test structures and by overlaying the super-resolution reconstructed images. We then imaged four structures sequentially. At this point, sequential microscope is ready to be used in biological research of interest.

Chapter 4

Biological Applications of Sequential Super-resolution Imaging

Parts of this chapter are taken directly from our two collaborative papers on Autophagy [46, 12, 13].

In Chapters 2 and 3 we showed the ability of sequential microscope to image multiple structures, automatically and with high-throughput performance. Sequential microscope enables us to investigate the spatial organization between different structures that play essential roles in biological questions of interest. In this chapter, we will briefly look into two specific biological problems that sequential microscope has been used for so far i.e., clathrin-mediated endocytocis and autophagy.

4.1 Clathrin-mediated Endocytocis

Endocytosis is an essential phenomenon for some functions at the cell level and beyond, for example, to control the concentration of receptors on the surface of the cell and to bring the nutrients inside.

This phenomenon happens through different and distinct mechanisms that enable the cell to internalize external objects within a wide range of sizes and shapes. The size range starts from the scale of small molecules and moves upward to the range of micron. Since most chemicals are polar molecules that cannot pass through the hydrophobic plasma membrane by passive means, an active form of transport and internalization is required by the cell so it can bring important material inside.[47] Endocytosis happens in four categories: receptor-mediated endocytosis (known as clathrin-mediated endocytosis), caveolae, macropinocytosis, and phagocytosis. In this section, we only talk about the first category.

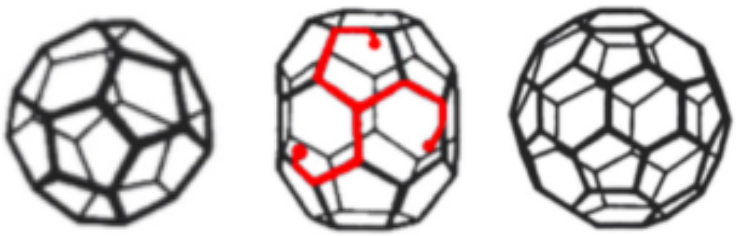

Figure 4.1: Possible clathrin basket shapes. Three different possible clathrin basket shape and sizes. (left) mini-coat 28 triskelia, (middle) single clathrin skeleton in a Hexagonal barrel 36 triskelia, (right) football 60 triskelia.[11]

Clathrin is a cytosolic protein that can form vesicles of up to few hundred nanometers coated with these proteins. These vesicles can be found in all types of cells. They are created from pits at the plasma membrane where they pick up their cargo, and they are called clathrin-coated pits. Usually, it's thought that aggregation of receptors on the plasma membrane signals for formation of the pits to internalize the

stimulated receptors or cargo and once the cargo is inside the cell, the clathrin coat disassembles back into clathrin proteins and the uncoated vesicle is trafficked to its destination, as shown in Figure 4.2

To understand clathrin endocytic machinery we need two types of information: first, we need to know different types of molecules involved in the formation of clathrin-coated vesicles and cargo selection, and second, we need to know the size of protein formations, so with utilizing both these parameters we can understand the machinery for endocytosis. Clathrin is a trimeric assembly of three heavy chains each with an associated light chain, and it is this three-legged structure or triskelion, that is the assembly unit of a clathrin coat [48]. Clathrin cages can assemble in different formations with different sizes. Three of possible configurations are shown in Figure 4.1.

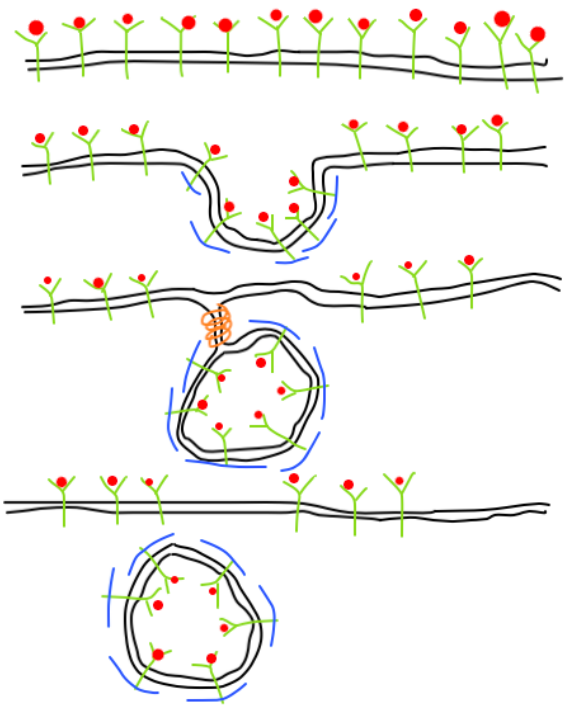

Figure 4.2: Clathrin-mediated endocytosis concept. In this figure we have FcεR1 receptor (green) on the plasma membrane (black) of RBL cells. We see four stages of endocytosis: antigen (red) detection by the receptors on the surface of the cell, clathrin pit formation (blue), invagination and cut the pit by dynamin molecule (orange), internalization of the pit.

4.1.1 Statement of the Problem

We investigate the relation between the size of IgE receptor aggregates and the internalization mechanism. There are two primary possible internalization mechanisms to investigate: through clathrin-mediated endocytosis or Arf6-mediated endocytosis. Literature shows a correlated presence of these two proteins in the vicinity of the endocytic pit [48]. In this dissertation, we only work with clathrin though. This project is still ongoing and is part of a bigger project that looks into the clathrin-mediated

endocytosis as well as Arf6-mediated endocytosis of IgE receptor aggregates in live and fixed cells. For the purpose of benefitting the project, RBL cells are genetically engineered by Dr. Cedric Cleyrat, our collaborator at Dr. Bridget Willson's lab to have GFP attached to the formation and surfacing of pits and the internalization and dynamic of them can be watched in in-vivo experiments.

4.1.2 Endocytosis Experiments

We have done extensive experiments on the microscope on clathrin-mediated endocytosis of activated IgE receptor aggregates on the surface of fixed Rat Basophilic Leukemia (RBL) cells.

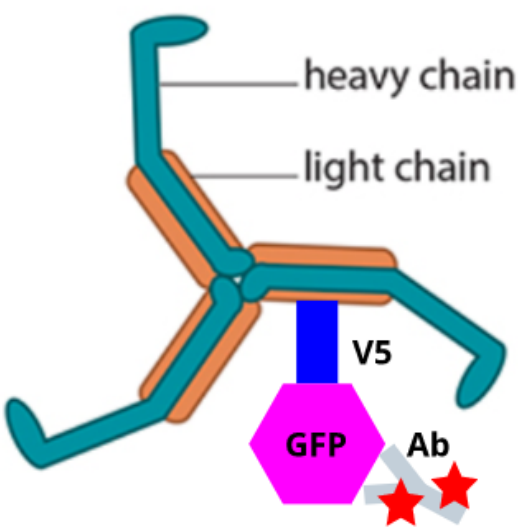

Figure 4.3: Clathrin labeling schemes. Clathrin labeling can be done via labeling different molecules of CLC, V5, and GFP, with antibody or nanobody.

These cells were all engineered to express GFP. First step was to investigate the best labeling strategy to image clathrin. We tried four possibilities as shown in

Figure 4.3: 1- Imaging heavy-chain clathrin with anti-heavy-chain antibody conjugated to AlexaFluor647, 2- Imaging light-chain clathrin with anti-light-chain antibody conjugated to AlexaFluor647, 3- Imaging GFP with anti-GFP-nanobody conjugated to AlexaFluor647, 4-Imaging GFP with anti-GFP-antibody conjugated to AlexaFluor647. These strategies are shown in Figure 4.4 and Figure 4.5

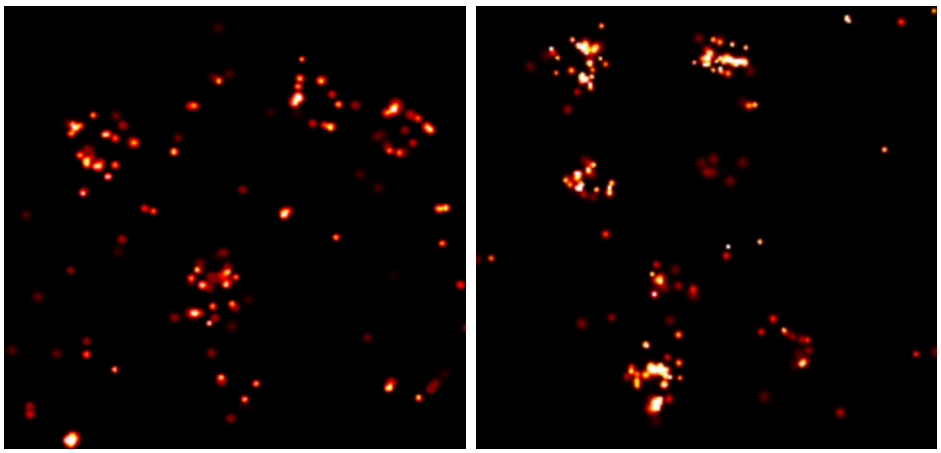

Figure 4.4: Clathrin labeling strategies in RBL cells. (left) nanobody labeling against clathrin light chain, (right) antibody labeling against clathrin light chain. Both strategies do not show effective labeling of clathrin.

IgE receptors were activated by adding synthetic agent DNP24 to induce aggregation, then cells were fixed after 1 and 2 minutes. Cells were imaged on sequential microscope in STORM buffer (1350 uL of TNG, 150 uL of OSB, and 50 uL of MEA) and in a sealed chamber under 5 kW/cm^2 excitation intensity. Cells then were photobleached in PBS, then washed with 6 drops of signal enhancer (Thermo Fisher Scientific, I36933) for 30 minutes and quenched for 15 minutes in NaBH4, then labeled with 2.5 ug/mL of anti-GFP-AlexaFluor647 (Life Technologies, A31852) for 2 hours. Afterwards cells were washed for 3 times five minutes (596 uL of 1X-PBS, 150 uL of 10% BSA, and 3.5 uL of 10% Triton) before imaging in the STORM buffer. Of the four strategies we tested, two showed much better results in providing the proper

concentration of dyes for imaging, on clathrin cites when tested for different labeling concentrations. From these two, we pick the anti-GFP-alexa647 labeling due to the usefulness of the engineered GFP in live imaging of endocytosis. Two color super-resolution imaging results for three different activation time-points of IgE receptors are shown in Figure 4.6.

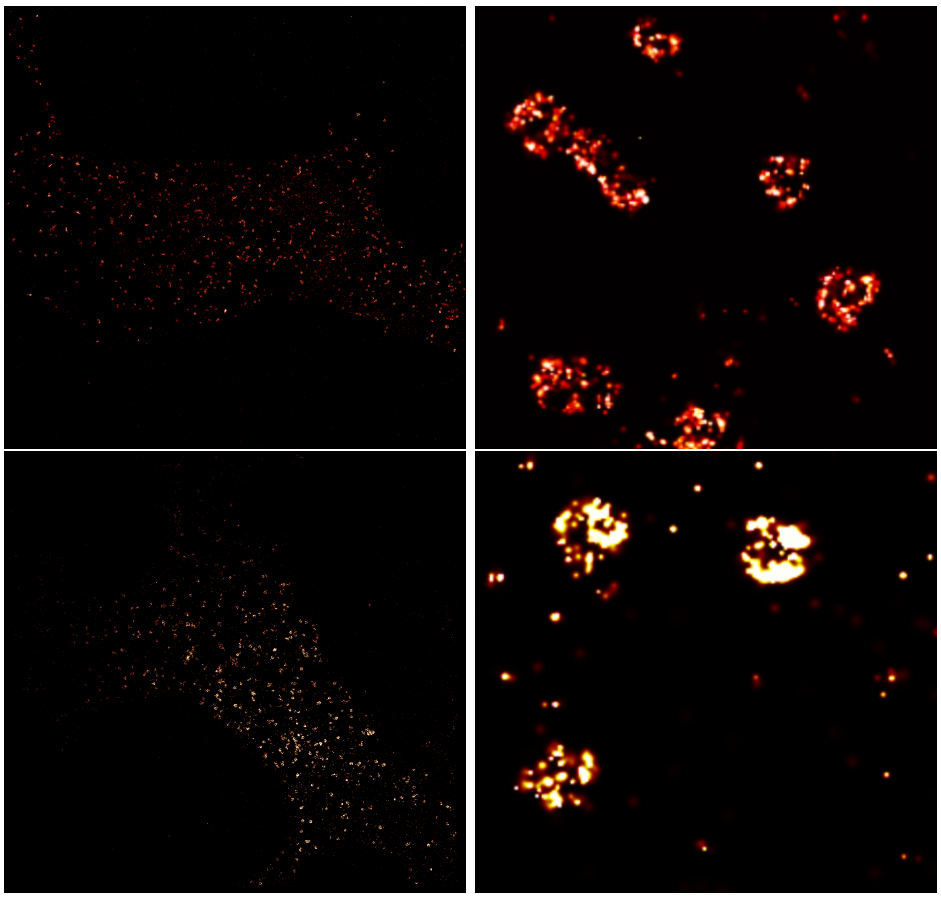

Figure 4.5: Clathrin labeling strategies in RBL cells. Images on the left show the whole cell and images on the right show the zoomed version. (top) antibody labeling against clathrin heavy chain, (bottom) antibody labeling against GFP. Both strategies are effective.

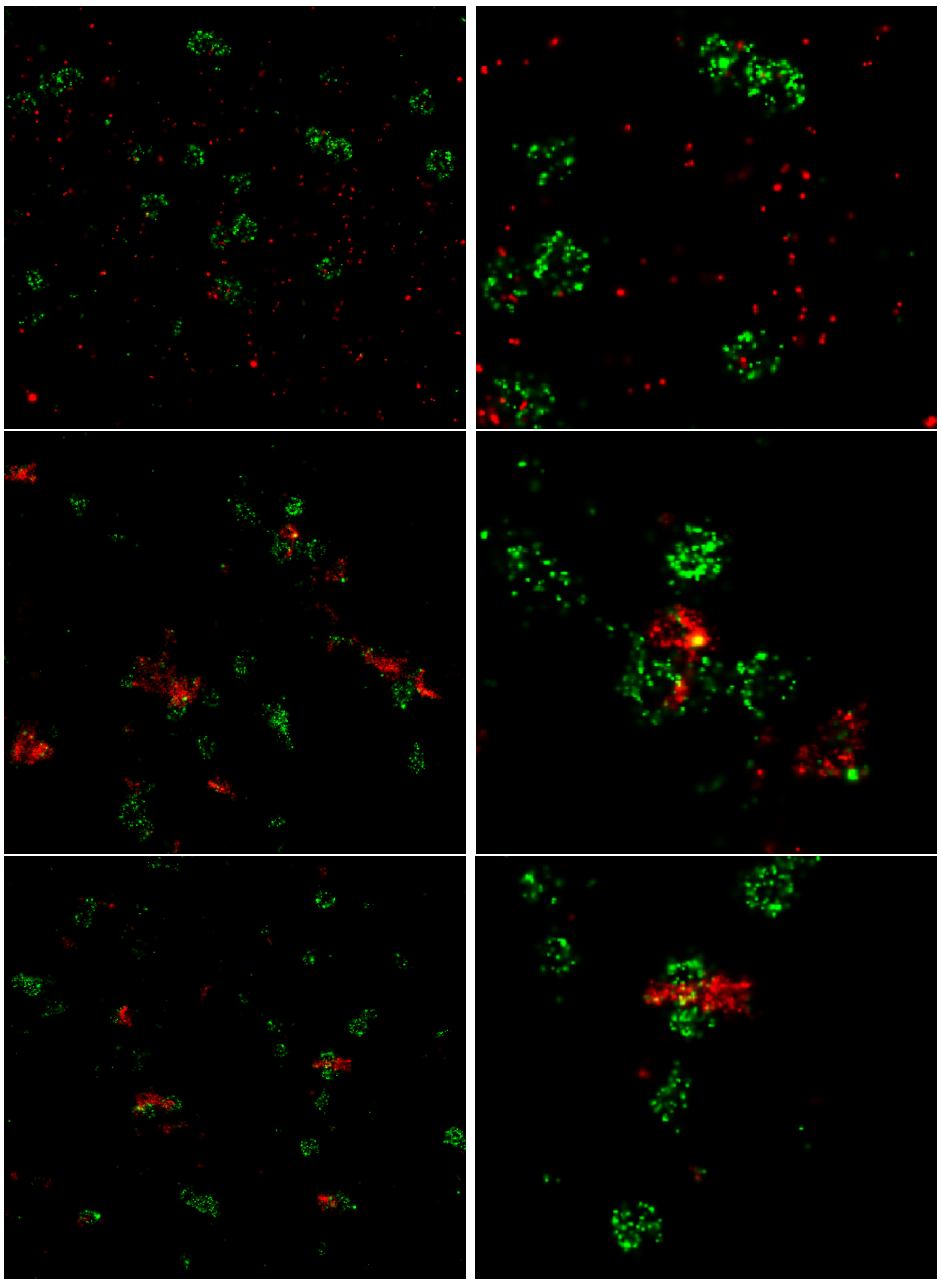

Figure 4.6: Imaging IgE receptor endocytosis by clathrin-coated pits. IgE receptor aggregates are activated by DNP24-BSA for 0, 1, and 2 minutes, before fixing the cell. Images show the overlay of IgE (red) with clathrin-coated pits (green) labeled with anti-GFP antibody. Images on the right are zoomed version of images on the left.

Cluster analysis is done on the super-resolution results for each label. As discussed in Chapter 3, we use DBSCAN for analysis of such data, which creates clusters out of nearby localizations based on a characteristic distance (set by user's expectation of the size of the clusters) and the minimum number of localizations required to form a cluster. After using this method for both labels, we overlay the structures and find the center to center distance between the clusters of label 1 and label 2. An example of an overlay is shown in Figure 4.16.

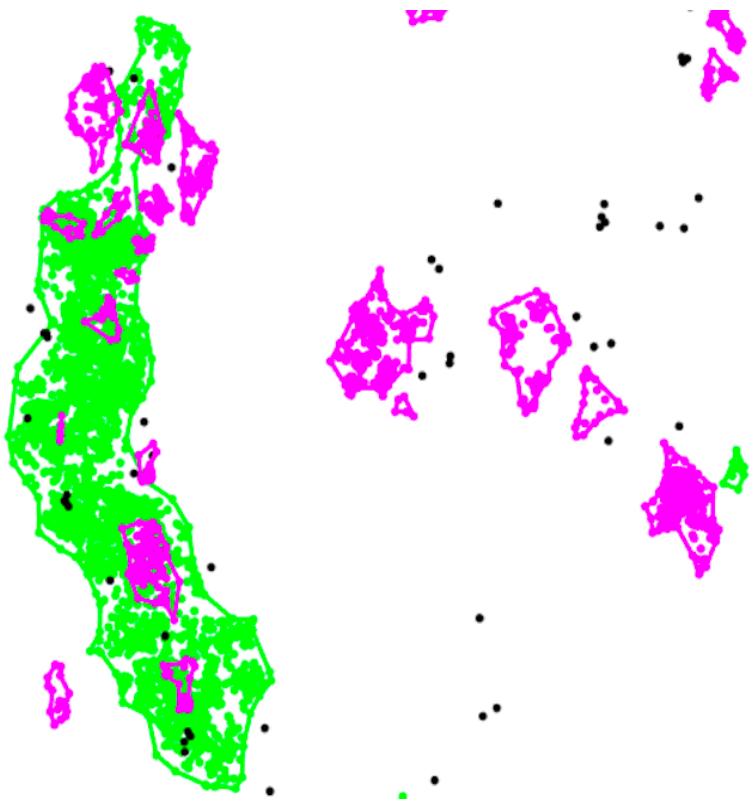

Figure 4.7: Clustering analysis of IgE receptor endocytosis by clathrin-coated pits. IgE receptor aggregates (green) with activation time of 2 minutes are clustered, and clathrin-coated pits (red) appear around them. Black dots show the unclustered localizations of both labels.

Figure 4.16 shows two important concerns. First, using the center to center distance between clusters of IgE and clathrin can be a bad idea if the IgE cluster

is elongated in one direction or if it has a curvy structure. Second, some of the clathrin localizations will not be visualized in super-resolution reconstructions due to staying under the IgE cluster, but can be seen in the overlay above. Figure 4.8 shows a super-resolution overlay of the IgE-receptor aggregates with clathrin-coated pits, where each structure is imaged for 40,000 frames of 10 msec exposure time.

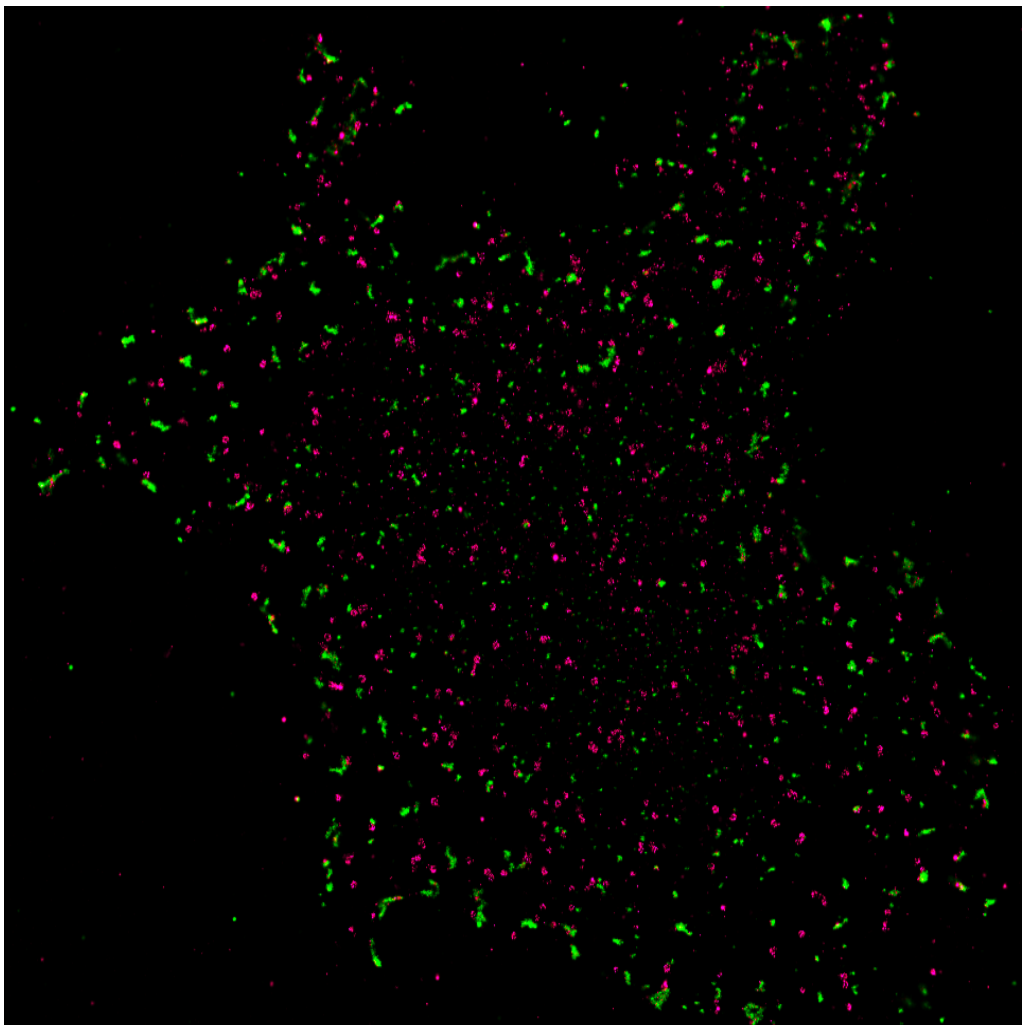

Figure 4.8: Imaging IgE receptor endocytosis by clathrin-coated pits. IgE receptor aggregates in an RBL cell (green) for activation time of 1 minute, and clathrin-coated pits (red) carrying endogenous GFP, tagged with anti-GFP-AlexaFluor647 dye. Clathrin-coated pits form near the IgE-receptor aggregates.

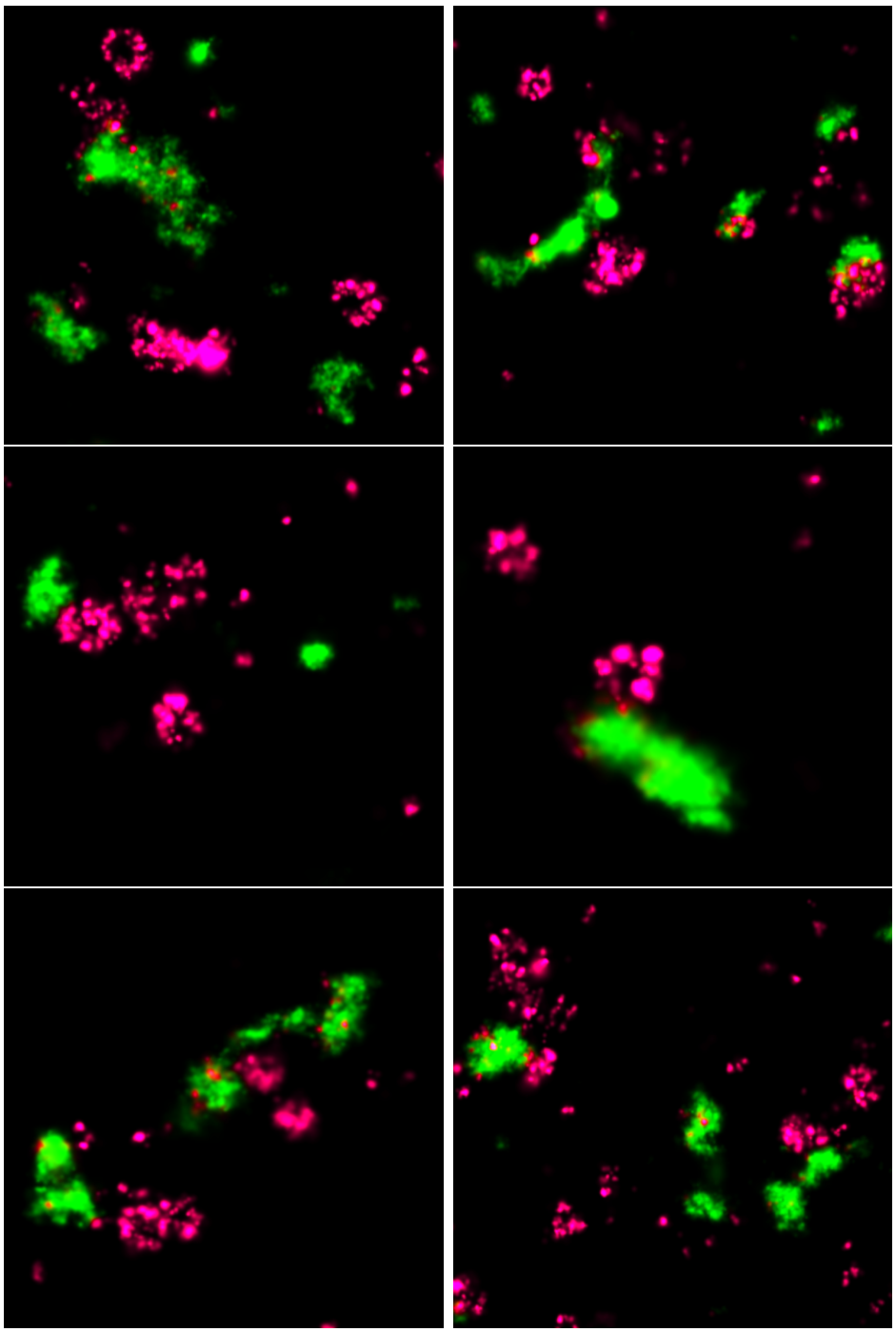

Figure 4.9: Imaging IgE receptor endocytosis by clathrin-coated pits. These images are zoomed version of Figure 4.8. Clustering of IgE receptor aggregates in an RBL cell (green) for activation time of 1 minute, and clathrin-coated pits (red) carrying endogenous GFP, tagged with anti-GFP-AlexaFluor647 dye.

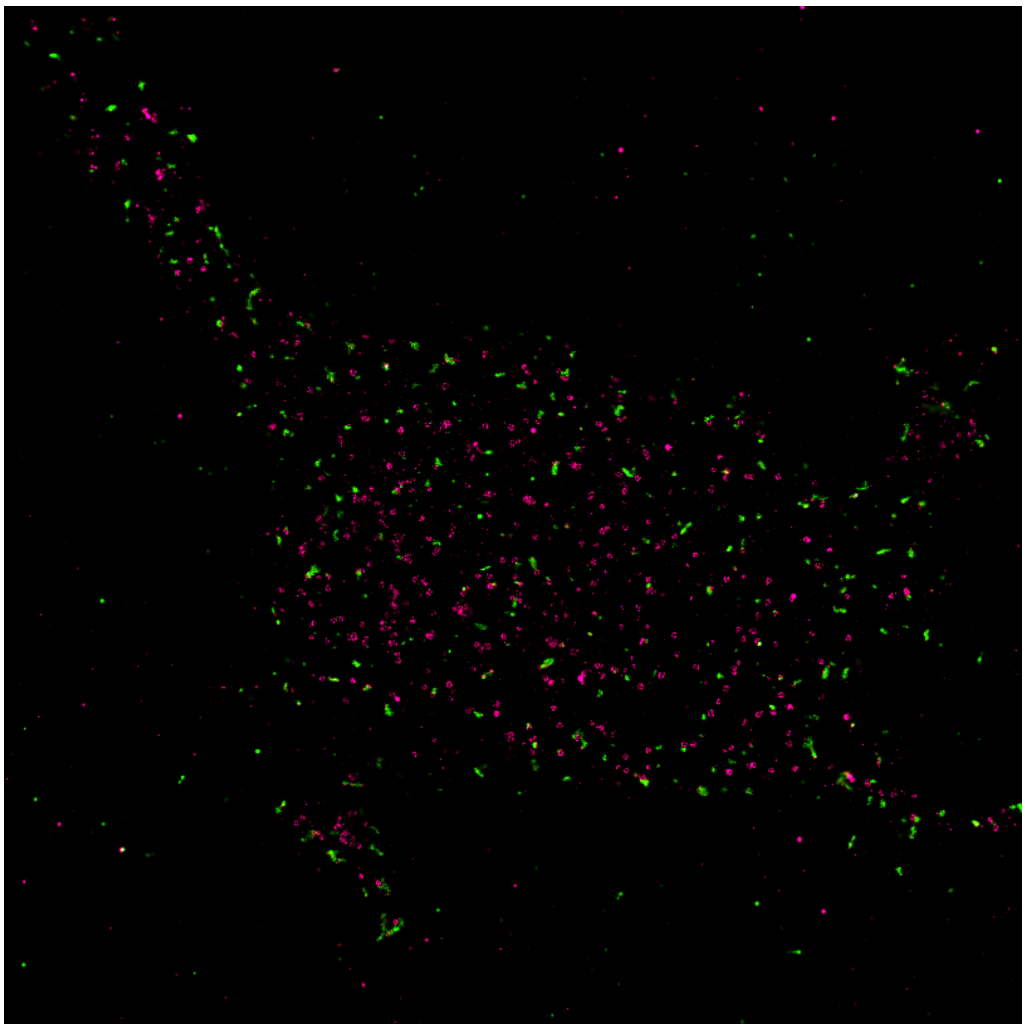

Figure 4.10: Imaging IgE receptor endocytosis by clathrin-coated pits. IgE receptor aggregates in an RBL cell (green) for activation time of 2 minutes, and clathrin-coated pits (red) carrying endogenous GFP, tagged with anti-GFP-AlexaFluor647 dye. Clathrin-coated pits form near the IgE-receptor aggregates.

An interesting observation shown in Figure 4.9 and Figure 4.11 is the appearance of clathrin-coated pits next to the IgE receptor aggregates in many occasions, for both 1 minute and 2 minutes of activation on RBL cells. Our initial expectation is to see the clathrin-coated pits right under the IgE receptor aggregates, but these images clearly show that this expectation might not be completely correct.

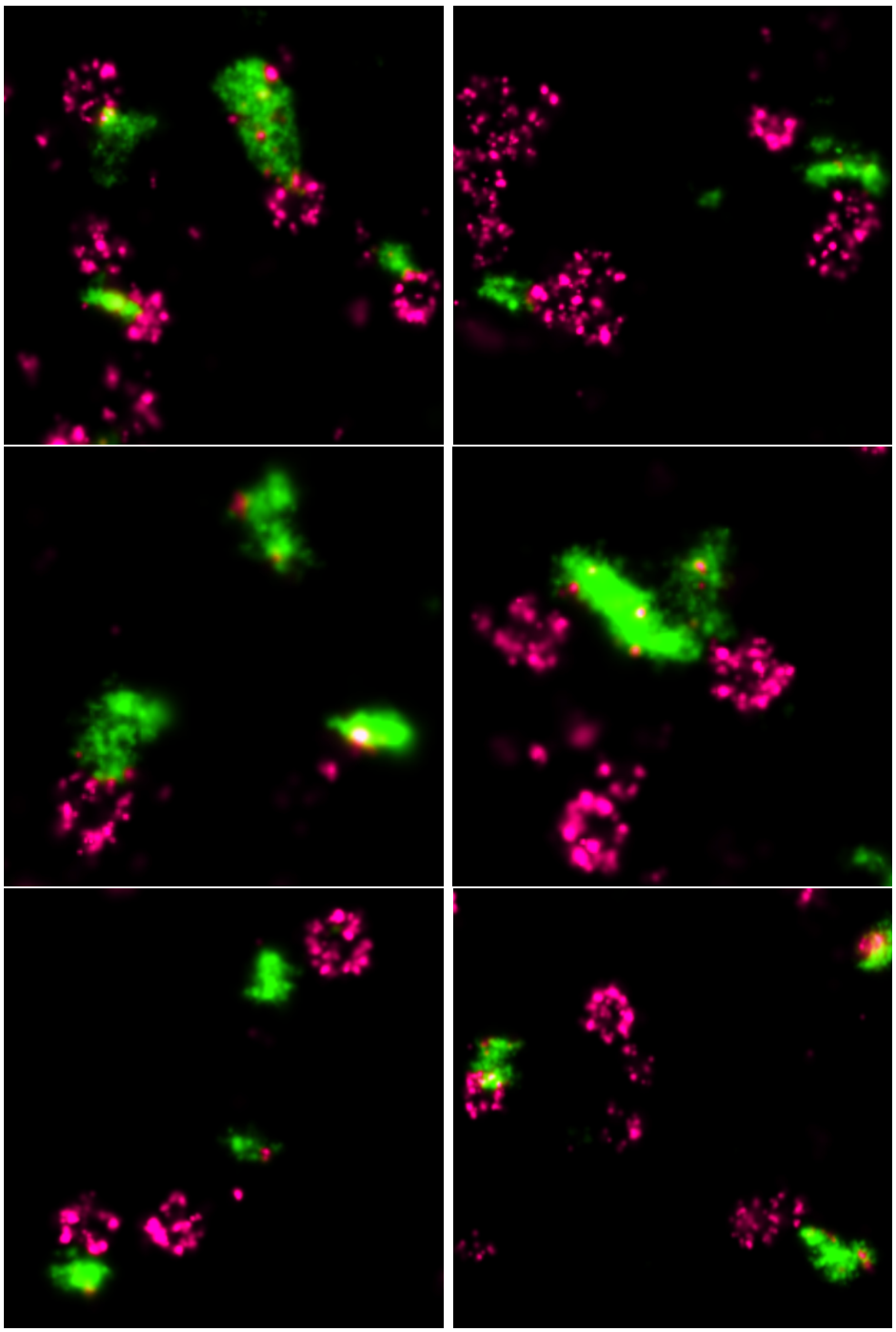

Figure 4.11: Imaging IgE receptor endocytosis by clathrin-coated pits. These images are zoomed version of Figure 4.10. Clustering of IgE receptor aggregates in an RBL cell (green) for activation time of 1 minute, and clathrin-coated pits (red) carrying endogenous GFP, tagged with anti-GFP-AlexaFluor647 dye.

4.1.3 Conclusion and Outlook

Our observations suggest that there might be another internalization pathway for IgE-receptor aggregates. Next step would be to find the percentage of the IgE-receptor aggregates that have clathrin-coated pits next to them. Based on our data, I have the following suggestions for future experiments on this subject:

1- using cluster analysis to: first find the number of clusters for each label, then to find the percentage of IgE-receptor aggregate clusters that have one or more clathrin-coated pit cluster next to them.

2- to find the relation between the size of IgE-receptor aggregates and the number of clathrin-coated pits around them.

3- to investigate the relation between activation time and percentage of IgE-receptor aggregate clusters that have one or more clathrin-coated pit cluster next to them.

4- to perform three label experiment for IgE-receptors, clathrin-coated pits, and the protein ARF6, and do all 3 analysis suggested above on the final results.

4.2 Autophagy

Autophagy is a collection of intracellular homeostatic processes with roles in cytoplasmic quality control and metabolism impacting a broad spectrum of degenerative, inflammatory, and infectious diseases. Autophagy related organisms in the cell are shown in Figure 4.12. [49]

In cancer, autophagy acts in tumor suppression by removing damaged organelles and possibly growth factors, and reduces chromosome instability. On the negative side, autophagy helps cancer cells resist anti-cancer treatments and survive in conditions of low nutrient supply. In infection and immunity, intracellular bacteria and viruses are removed from host cells by autophagy, and antigens are processed. Autophagy may prevent auto-immune and inflammatory decease. On the negative side, some microbes have evolved to subvert autophagy. In heart disease, autophagy may be protective during pressure overload. On the negative side, it is harmful during reperfusion. In liver disease autophagy can alleviate endoplasmic reticulum stress by degrading portions of the organelle containing misfolded proteins. On the negative side, excessive autophagy may cause liver damage. Autophagy removes damaged organelles and can limit production of reactive oxygen species so it is pro aging.

Autophagy prevents aggregate-prone protein accumulation that lead to physiological dysfunction. On the negative side, it may contribute to muscle wasting, and defective autophagosome clearance may interfere with cellular function. Basal autophagy prevents intracellular proteins from accumulating to toxic levels. On the negative side, inefficient lysosomal clearance results in intracellular accumulation of autophagosomes, which may process the amyloid precursor protein into toxic forms.[49]

The best-studied form of autophagy, macroautophagy, depends on the autophagy-related gene (Atg) factors in yeast, where this system has been genetically delineated [50].

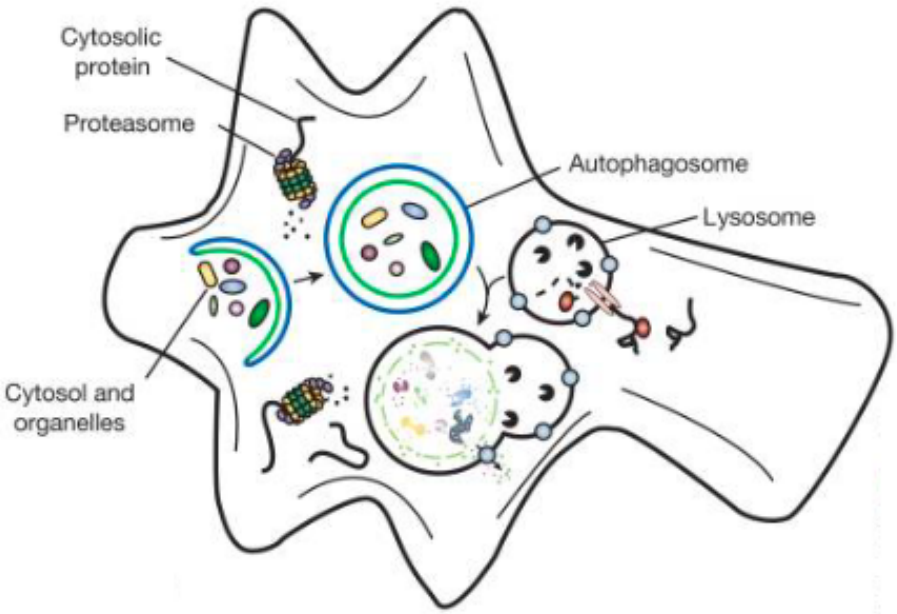

Figure 4.12: Autophagy related systems in a cell.

The many similarities of the core Atg machinery in yeast and mammalian cells are complemented by qualitative and quantitative differences between how mammalian and yeast cells execute autophagy. This extends but is not limited to an expanding spectrum of mammalian receptors [51] and receptor regulators [52] for selective autophagy. Perhaps the most intriguing differences are the roles of unique regulators of autophagy such as, among prominent others recognized early on as associated with genetic predispositions to diseases, the immunity-related GTPase M (IRGM), which bridges the immune system and the core Atg machinery to control autophagy in human cells. The core autophagy machinery in mammalian cells has several subsystems interconnected via specific molecular interactions into a unifying apparatus [50]

as shown in Figure 4.13. During autophagy, the cytoplasmic cargo is sequestered by specialized organelles termed autophagosomes, which are characterized by the presence of LC3B, one of the mammalian paralogues of yeast Atg8. Although autophagy is primarily known as a tributary to the degradative lysosomal pathway, functionally different terminations have been considered for autophagocytosed cytosolic material, leading to secretion of cytokines or small molecular weight immune mediators. In particular, autophagy has been examined for its potential in unconventional secretion of leaderless cytosolic proteins that cannot enter the conventional secretory pathway but play extracellular functions. How IL-1β is secreted instead of being degraded in autophagic organelles remains unknown. In collaboration with Dr.Tomo Kimura from Dr.Vojo Deretic group, I designed and performed the super-resolution tests needed to investigate the key elements of the pathway for unconventional protein secretion through autophagy that separates it from degradative autophagy.

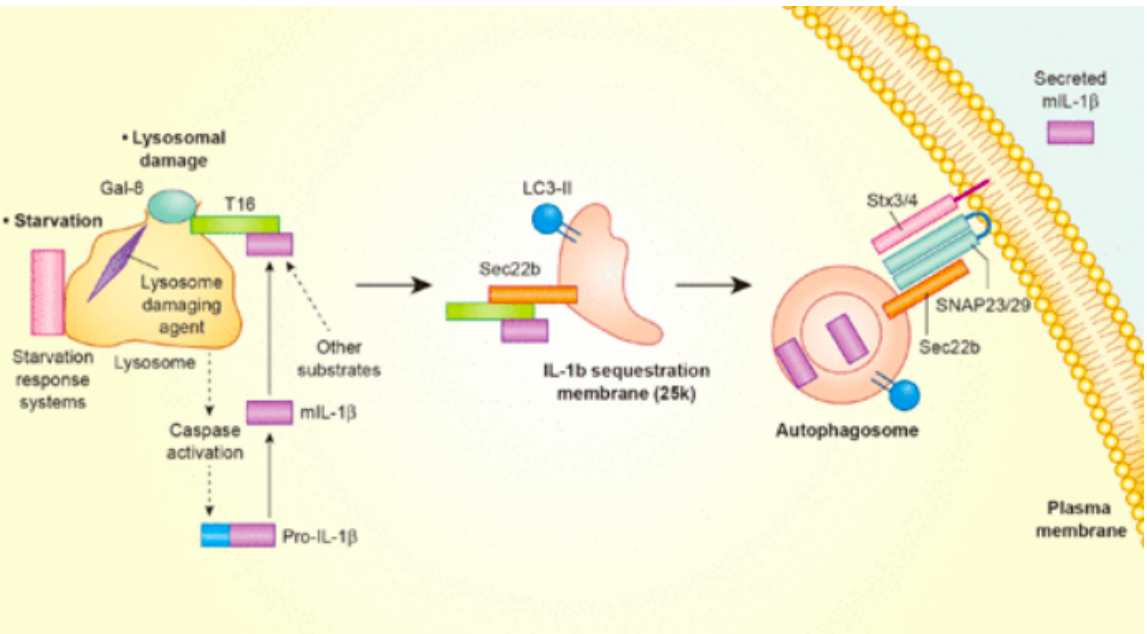

Figure 4.13: Secretory autophagy, an unconventional secretion pathway for cytosolic proteins, diverges from degradative autophagy by utilization of specialized SNAREs and cargo receptors. Secretory autophagy delivers unconventionally secreted cytosolic cargo including in response to lysosomal damage and signaling. TRIM16 acts as a specialized secretory autophagy receptor for IL$-\beta$. Secretory autophagy requires different SNAREs than degradative autophagy.[12]

This pathway, termed secretory autophagy, requires a specialized receptor recognizing the cytosolic cargo. It also relies on cooperation of this receptor with the R$-$SNARE present on LC3$-$type2+ERGIC$-$ derived membranes whereupon the cargo is sequestered. Finally, secretion of the cargo depends on plasma membrane syntaxins instead of delivery to lysosomes via syntaxin17. The secretory autophagy pathway utilizes a specialized cytosolic cargo receptor regulator from the TRIM family and a dedicated ERGIC R$-$SNARE Sec22b that both interacts with the receptor regulator and engages the plasma membrane Qa$-$SNAREs. This system is utilized by a subset of unconventionally secreted leaderless cytosolic proteins.

4.2.1 Co-clustering of flag-TRIM16 and GFP-Sec22b

Several experiments were done to investigate the co-clustering of flag-TRIM16 and GFP−Sec22b. Since secretory autophagy is not the main autophagy pathway, number of cells that give a clear representation of this phenomenon was very low in percentage so tens of experiments were required to find a single proper cell, which was frustrating at times.

After fixation as described in supplement of this dissertation, cells were labeled with anti-flag-AF647 at 5 ug/ml in PBS + 2% BSA + 0.05% Triton X-100 (PBS/BSA/TX) overnight and washed in PBS/BSA/TX. Then, cells were mounted in 1% agarose gel for sample stabilization. 1% gel was made from 4% gel heated to 80C and mixed with heated 1X-PBS at 80C then brought down to 40C. 75 uL of 1% gel was added on coverslip and the resulting sample placed in a refrigerator at 4C for 5 minutes to solidify. The coverslip was mounted on an Attofluor cell chamber (A-7816, life technologies) with 1.1 ml of the imaging buffer. Imaging buffer consisted of an enzymatic oxygen scavenging system and primary thiol: 50 mM Tris, 10 mM NaCl, 10% w/v glucose, 168.8 U/ml glucose oxidase (Sigma G2133),1404 U/ml catalase (Sigma C9332), and 20 mM 2-aminoethanethiol (MEA), pH 8. The chamber was sealed by placing an additional coverslip over the chamber and the sample the oxygen scavenging reaction was allowed to proceed for 20 min at room temperature before the imaging started.

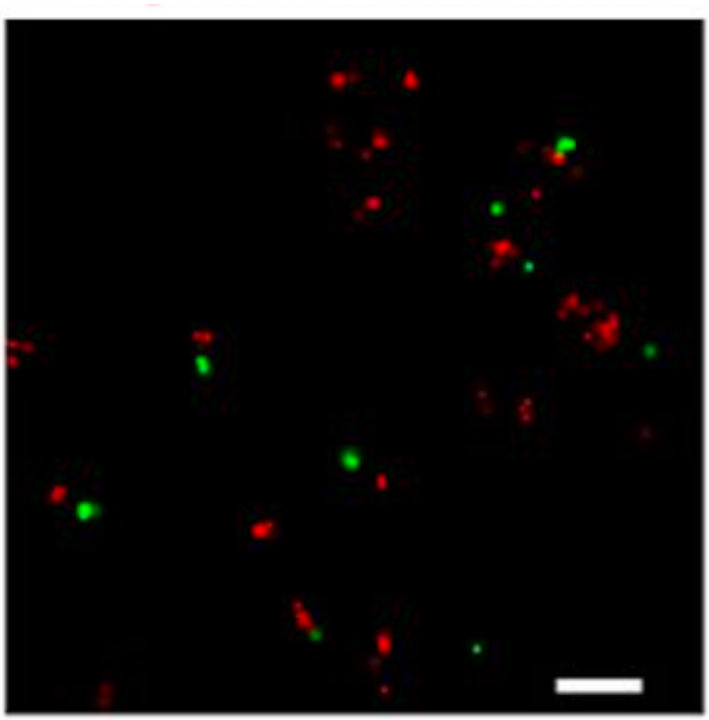

Figure 4.14: Two color super-resolution, showing co-clustering of flag-TRIM16 (red) and GFP−Sec22b (green). Scale bar, 200 nm.

Imaging was performed by our sequential microscope. The IR camera at the time of these experiments was DMK 31AU03- imagingsource. A 642 nm laser (80 mW-HL6366DG-Thorlabs) was used as the excitation laser, not the current 647 fiber laser, and a 405 nm laser (40 mW-DL5146-101S-Thorlabs) was used to accelerate the dark to fluorescent state transition. The objective was NA=1.49 (APON 60XOTIRF-Olympus) and the filters consisted of a 835/70 nm (FF01-835/70-25-Semrock) for IR stabilization emission path, 708/75 nm (FF01-708/75-25-Semrock) for SR image emission path, and 640/8 nm (LD01-640/8-12.5-Semrock) laser diode clean up filter.

During the data acquisition, the 642 nm laser was used at 1.5 kW/cm^2 to take 20 sets of 2,000 frames at 20 Hz. After imaging all cells on the coverslip, the dye was removed using bleaching and NaBH4 for quenching. GFP-Sec22 was labeled by first

blocking the cell with Signal Enhancer (136933-Molecular Probes, Life Technologies) for 30 minutes followed by relabeling with GFP binding protein (gt- 250-Chromotech) conjugated with AF647 at 1 ug/ml for 2 hours. For the second round of imaging, each cell was re-aligned using the saved brightfield reference image as described in Chapter 3.

Data were analyzed via our 2D localization algorithm based on maximum likelihood estimation (MLE) [53]. The localized emitters were filtered through thresholds of a maximum background photon counts at 200, a minimum photon counts per frame per emitter at 250, and a minimum P value at 0.01. The accepted emitters were used to reconstruct the super-resolution image. Each emitter was represented by a 2D-Gaussian with σ_x and σ_y equal to the localization precisions, which were calculated from the Cramr-Rao Lower Bound (CRLB). Resulting two color overlay image can be seen in Figure 4.14.

For cluster analysis, the data was first processed by H-SET (Hierarchical Single Emitter hypodissertation Test), a top-down hierarchical clustering algorithm designed to collapse clusters of observations of blinking fluorophores into single estimates of the true locations of the fluorophores using a log-likelihood hypodissertation test [54]. Next, the pairwise cross- correlation function was computed from this data via a reconstructed histogram image using a pixel size of 10.4 nm, as described in Chapter 3. The two-dimensional pairwise cross-correlation function was averaged over eight 3000 nm x 3000 nm regions of interest chosen to emphasize the co-clustering of the two proteins. The results were then angularly averaged to produce the figure displaying g(r) versus r and the results can be seen in Figure 4.15 where a characteristic distance is observed.

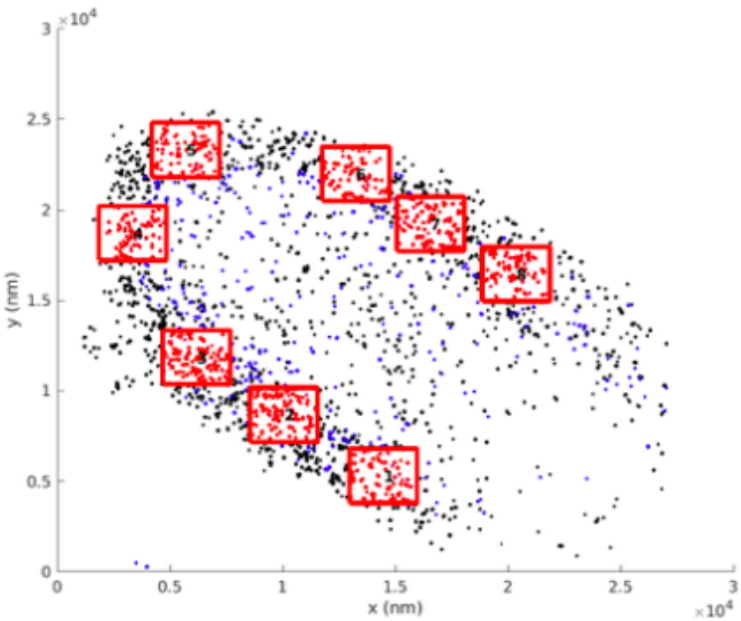

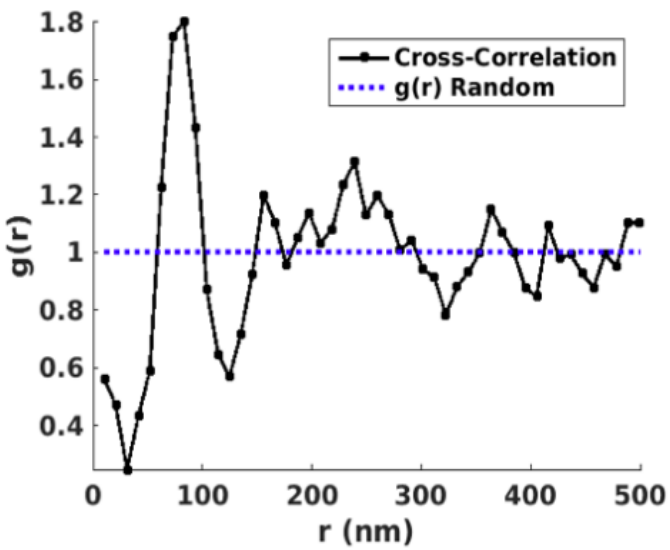

Figure 4.15: Cross-correlation analysis of flag−TRIM16 and GFP−Sec22b super?resolution data showing a characteristic separation of 70 nm. In the top figure, blue and black dots show the recognized clusters by DBSCAN for the first and the second label.

4.2.2 Co-clustering of LC3 and Syntaxin17

In this work I collaborated with Dr.Suresh Kumar from Dr.Vojo Deretic lab, to study a specific co-clustering. During the experiment I got lucky and was able to image, for the first time ever, different phases of autophagosome formation, in a single super-resolution image in a single cell, which created huge excitement among collaborators.

Superresolution (SR) microscopy of endogenous LC3 in cells expressing GFP-Stx17 revealed an array of profiles representing different stages along the autophagosomal pathway and indicated a separation of smaller than 25 nm for 75% of the Stx17 and LC3 cluster centers within the arms of type I profiles that are defined to represent fully shaped phagophores. This proximity suggested the possibility of direct or very close interactions between Stx17 and LC3 as shown in Figure 4.16. Thus, is considered the simplest model that mammalian paralogs of yeast Atg8, e.g., LC3B as an mAtg8 commonly used to visualize autophagosomes, may play a role in controlling recruitment of Stx17 to conventional autophagosomes. HeLa cells were plated on 25 mm round Number 1.5 coverslips and allowed to adhere overnight. After fixation with the protocol mentioned in the appendix section of this dissertation, cells were incubated with anti−rabbit-LC3 antibody overnight and washed with PBS followed by labeling with AlexaFluor647. The coverslip was mounted on an Attofluor cell chamber with 1.1 ml of the imaging buffer. Imaging buffer consisted of an enzymatic oxygen-scavenging system and primary thiol: 50 mM Tris, 10 mM NaCl, 10% (wt/vol) glucose, 168.8 U/ml glucose oxidase, 1,404 U/ml catalase, and 20 mM 2-aminoethanethiol, pH 8. The chamber was sealed by placing an additional coverslip over the chamber, and the oxygen-scavenging reaction was allowed to proceed for 20 min at room temperature before the imaging started. Imaging was performed using the same sequential system that was used before in collaboration with Dr.Kimura, above but the main laser was replaced with the 647 fiber laser nm. During the data

acquisition, the 647-nm laser was used at 15 kW/cm^2 to take eight sets of 5,000 frames (a total of 40,000) at 100 Hz. After the dye was removed using bleaching and NaBH4 as described in Chapter 3, GFP-Stx17 was labeled by first blocking the cell with signal enhancer for 30 min followed by relabeling with GFP- binding protein (A31852; Thermo Fisher Scientific) conjugated with AlexaFluor647 at 10 ug/ml for 1 h.

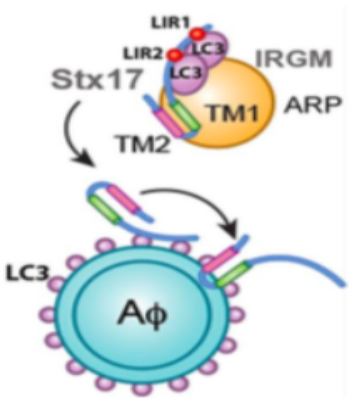

Figure 4.16: ARP delivering Stx17 to autophagosomes. First, ARP (IRGM; Stx17 with its LIRs bound by LC3 or other mAtg8s) allows insertion of Stx17 into the autophagosomal membrane through exchange interactions with LC3/mAtg8s on autophagosomes. Then, the SNARE domain, occupied by LC3/mAtg8s, is released.[13]

Data were analyzed via a 2D localization algorithm based on maximum likelihood estimation. The localized emitters were filtered through thresholds of maximum background photon counts of 200, minimum photon counts per frame per emitter of 250, and a minimum P value of 0.01 as before. Each emitter was represented by a 2D Gaussian function with σ_x and σ_y equal to the localization precisions, calculated from CRLB. Clustering analysis was performed. 28 regions of interest (ROIs) were selected from the image. Clustering was then performed separately for each label in each ROI using the density-based DBSCAN algorithm (Daszykowski2001) choosing a maximal nearest neighbor distance of 40 nm and requiring clusters to contain at

least 10 observations. In all cases, the vast majority of observations for each label in each ROI formed a single cluster. Cluster boundaries were produced via the MATLAB boundary function, from which cluster areas were computed. Finally, the center-to-center distances between LC3 and GFP-Stx17 cluster centroids per ROI were tabulated. Results are shown in Figure 4.17

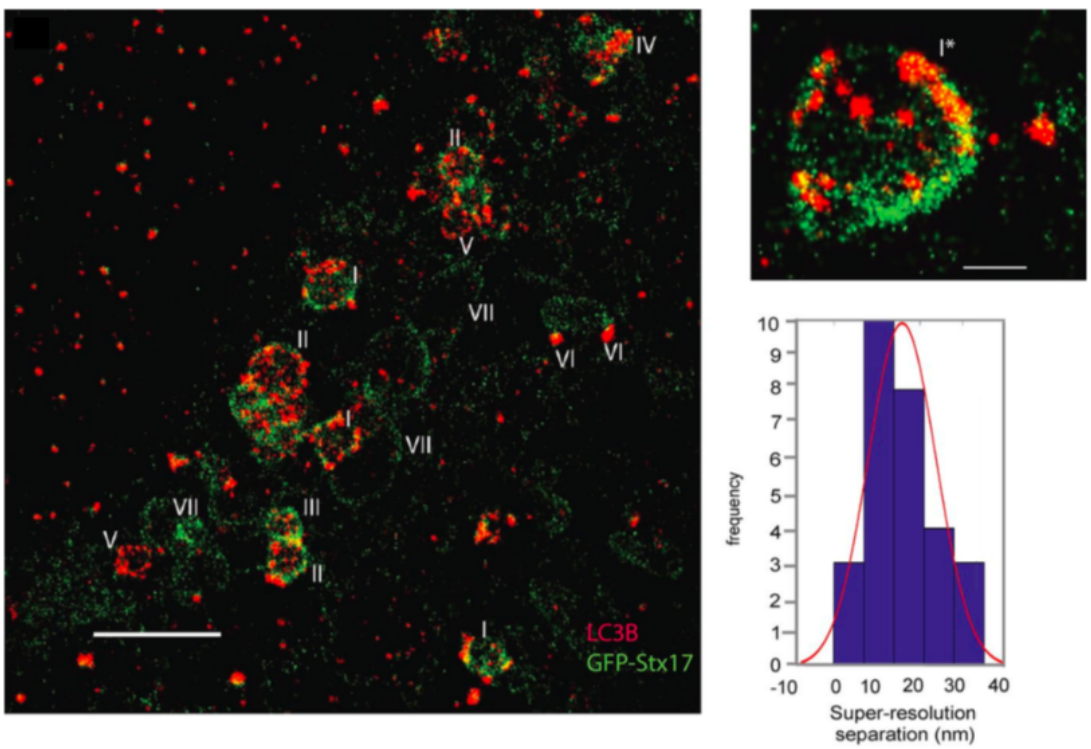

Figure 4.17: SR microscopy of GFP-Stx17 and endogenous LC3. HeLa cells were transfected with GFP-Stx17 and induced for autophagy with pp242 for 2 h in the presence of ba lo- mycin A1 to allow for accumulation of interme- diates, and then endogenous LC3 (rabbit anti-LC3) and GFP-Stx17 were sequentially imaged at 647 nm as detailed in the SR mi- croscopy and analysis section in Materials and methods. Shown is a section of the whole- cell scan in Fig. S1. Pseudocolors: green, GFP-Stx17; red, endogenous LC3. A key to different autophagic profiles (marked I−VII) is given in the Fig. S1 legend. Bar, 1 um. (top right) Type I profile enlarged and marked as I*. Bar, 200 nm. (bottom right) Graph showing a plot of center-to-center distances between LC3 and GFP- Stx17 cluster centroids from five type I profiles.

Chapter 5

Labeling Strategies for Sequential Super-resolution Imaging

Parts of this chapter are taken directly from our paper on DNA-strand-displacement [ ].

Sequential labeling and imaging in fluorescence microscopy allows the imaging of multiple structures in the same cell using a single fluorophore species. In super-resolution applications, the optimal dye suited to the method can be chosen, the optical setup can be simpler and there are no chromatic aberrations between images of different structures. In first section of this chapter, we describe a method based on DNA strand displacement that can be used to quickly and easily perform the labeling and removal of the fluorophores during each sequence, and in the second section we compare methods for labeling actin filaments.

For DNA strand displacement, site-specific tags are conjugated with unique and orthogonal single stranded DNA. Labeling for a particular structure is achieved by hybridization of antibody-bound DNA with a complimentary dye-labeled strand. After imaging, the dye is removed using toehold-mediated strand displacement, in

which an invader strand competes off the dye- labeled strand than can be subsequently washed away. Labeling and removal of each DNA-species requires only a few minutes. We demonstrate the concept using sequential dSTORM super-resolution for multiplex imaging of subcellular structures.

A key advantage in fluorescence microscopy is the ability to specifically label and image multiple targets within a cell. This is typically achieved through labeling of targets with spectrally distinct dyes with emissions that can be easily separated by filter-based detection. While this approach is achievable for many or the super-resolution imaging methods, the photo-physical requirements of the dye for each technique and the available dyes are not always ideally matched, placing limitations on multi-color super-resolution. For example, in single molecule localization microscopy (SMLM) it is desired to have low duty cycle and high number of photons per switching cycle. The best fluorophores for this are similar in spectra to AlexaFluor647/Cy5 [38]. Additionally, the differential aberrations between spectral channels must be carefully accounted for in super-resolution imaging.

One approach for overcoming limitations in multi-color labeling is the use of sequential imaging, where the same fluorophore is used to image multiple structures in a label-image-remove process that is repeated for each target. This strategy has been demonstrated in several SMLM methods. Tam et al [55] used sequential labeling of antibodies and NaBH4 to quench remaining dyes while imaging using STORM [24]. Yi et al [56] used sequential antibody labeling and elution paired with dSTORM imaging [57]. Our own group demonstrated the use of sequential antibody labelling with bleaching and NaBH4 quenching for dSTORM imaging [1]. Each of these techniques requires a lengthy process between imaging steps to remove (photobleach or chemically quench) the fluorophore before labeling the next target. Another method, DNA-Exchange-PAINT [35] relies on transient binding of a dye-labeled imaging strand to a complementary docking strand to produce blink-

ing. Sequential labeling can be done quickly by replacing the imaging strand in the buffer. However, DNA-PAINT suffers from high background due to the fluorescence imaging strand in the buffer, thus requiring TIRF or other selective illumination schemes. Also, the frame rate must be low, typically 100-300 ms, a factor approximately an order of magnitude lower than dSTORM imaging. An alternate strategy based on this approach uses semi- permanent binding of imaging strands to docking strands, allowing unbound imaging strands to be removed from the sample, thereby reducing background fluorescence [8]. A low salinity buffer with high concentrations of formamide is used to break hybridization for removal of the imaging strand.

5.1 DNA Strand Displacement

Here we describe and evaluate a new sequential dSTORM labeling approach that allows for fast exchange of fluorescent labels while maintaining the inherent advantages of dSTORM - low background and higher data collection speeds. The concept relies on DNA strand displacement, which is a powerful method for designing enzyme-free reaction pathways to enable programmable, autonomous manipulation of DNA. Strand displacement has been used in a broad range of applications, including biological computing, molecular machinery, and in vivo biosensing [58, 59, 60, 61, 62]. Here we take advantage of the toehold-method of DNA strand displacement to sequentially add and remove the AF647 dye for multiplex dSTORM imaging without the need for enzymes or chemical treatments. We show that strand-displacement is an efficient and rapid means to exchange fluorescent dyes for sequential dSTORM imaging.

Taking advantage of the properties of DNA interactions, we developed a labeling scheme for sequential dSTORM based on the method of toehold-mediated strand displacement. This is shown schematically in Figure 1. Using click chemistry, we

directly conjugate the azide-modified protector strand to the secondary antibody. Upon addition of the complementary AF647-labeled template strand, the two DNA strands will hybridize, forming an AF647-labeled antibody. The template strand is removed by addition of the invader strand, which binds to the exposed toehold on the template strand and thereby nucleates a subsequent displacement reaction that displaces the template from the complex. In addition, the formation of additional base-pairs between the invader and the template strand provides a thermodynamic bias toward completion of the displacement process. Crucially, in our system this displacement reaction removes the AF647 label from the antibody as part of an inert waste complex that can then be washed away. After imaging and removal of the AF647 strand, the sample is relabeled with an orthogonal AF647-oligo that recognizes a different antibody via sequence-specific hybridization to its template strand, and the process can then be repeated. In this work, we describe two orthogonal DNA gate and invader strand sets that enable multiplex imaging. However, many more DNA sets could be constructed to allow for essentially any number of targets to be labeled.

The limiting step in sequential dSTORM is the potential for residual fluorescence from an initial target that could result in cross-talk artifacts for subsequent targets. We first established the ability of the invader strand to displace the AF647-template strand. HeLa cells were fixed and labeled with either anti-clathrin or anti-tubulin primary antibodies followed by the appropriate protector-labeled secondary antibody. Upon addition of AF647- template DNA, the oligo binds to the protector and robust labeling of the cells is achieved. To determine the kinetics of strand displacement, the cells are imaged over time during addition of the invader and the AF647 intensity for each cell was monitored. A rapid loss of AF647 is observed for both oligo sets with a greater than 95% reduction in intensity. To quantify the amount of residual cross-talk in sequential imaging, we compared dSTORM images of the same cell before and after invader addition. Cross-talk, as determined by the total number of

localizations, is found to be 2% and 5% for Set A and B, respectively.

Since the two DNA sets are orthogonal (that is, none of the strands from set A will interact with strands from set B, and vice versa), they can be used to label distinct targets within the same cell. Figure 3 demonstrates the use of DNA strand displacement for sequential dSTORM. Cells were first labeled concurrently with clathrin and tubulin primary antibodies, followed by the appropriate protector-labeled secondary antibodies. The template for the first target is added and a super-resolution image acquired. Upon completion of the first round of imaging, the invader strand is added to remove the AF647-template from the first target and cells are washed. Next, the template strand to the second target is added and imaging of the second target is performed. We also performed the template labeling and imaging in the reverse order with similar results. A representative image from both labeling directions is shown in in Figure 5.1

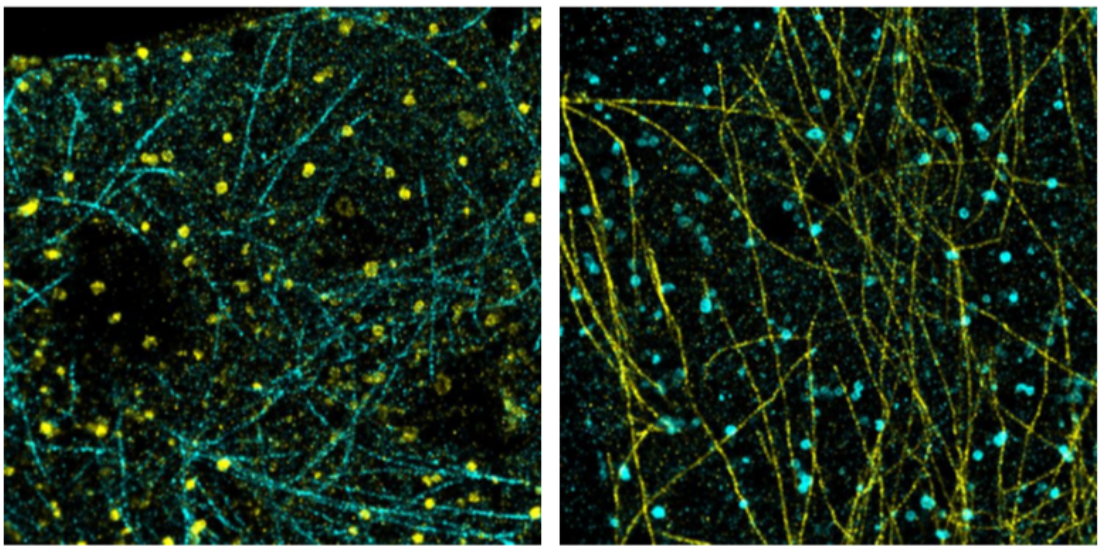

Figure 5.1: DNA strand displacement labeling strategy

We have shown the potential for DNA-strand displacement in providing a rapid

and efficient labeling for multiplex sequential super-resolution. The exchange of labels requires about 10 minutes when performed by hand on the bench, although this could be reduced by approximately a factor of two using automated fluidics. This approach has the advantage over previous methods in that no enzymes, chemical treatments or photobleaching steps are required. The strand-displacement step, shown in Figure 5.2, is rapid thanks to the 8 nucleotide toehold, dramatically reducing the overall imaging time to the point where the total imaging time for dSTORM is dominated by the data collection. This is a significant improvement over our previous sequential dSTORM method [1] that required photobleaching, quenching by NaBH4, and an immunofluorescence labeling step between sequences, which resulted in approximately 2 hours for the complete removal and re-labeling steps per each structure.

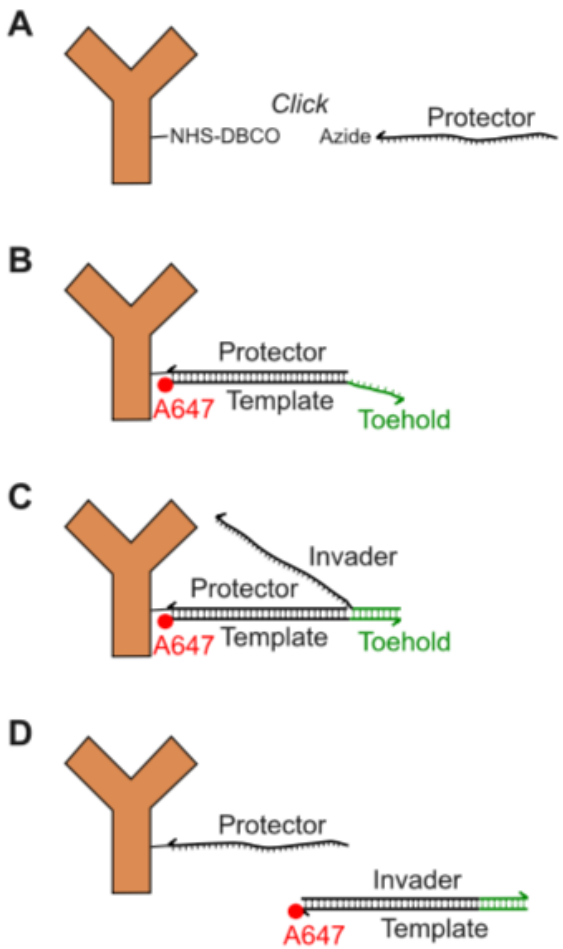

Figure 5.2: DNA strand displacement labeling strategy

The observed residual from strand displacement when applied to dSTORM imaging was as low as 2%. The residual cross-talk and speed of removal is similar to that of the denaturing approach used by Schueder et al.[63]. Whereas strand displacement requires an extra reagent, the invader stand, the denaturing approach uses a buffer with the odorous and suspected carcinogen, formamide. For applications that require even further reduction is cross-talk, strand displacement could be complemented by either photobleaching or dye quenching at the cost of a few minutes per cell for photobleaching or about 10 minutes per coverslip when quenching with

NaBH4.

Since the DNA sets do not cross-react, sample preparation time is reduced by the ability to incubate all antibodies simultaneously and distinct targets are individually labeled at the time of imaging by addition of the corresponding AF647-template strand. While we have demonstrated this approach with two-target imaging, many more orthogonal DNA sets could be generated to increase multiplex capacity. Direct conjugation of the template strand to the primary antibody would allow for essentially limitless target combinations.

DNA Design: Four sets of non-interfering invader strand and gate sequences were designed using the NUPACK secondary structure prediction and design software [64, 65, 66] in conjunction with custom scripts to test and report any cross-reactivity between sets. Each strand displacement gate consists of a 38mer template strand and a 30mer protector strand. When hybridized this structure forms a 30 base pair duplex and an 8 nucleotide single-stranded toehold (using a long toehold promotes rapid nucleation of the strand displacement reaction). Each invader strand is a 38mer single strand that is complementary to the corresponding template strand. The super-resolution dye AlexaFluor647 is attached to the 5' end of each template strand, and the azide group for conjugation to the antibody is attached to the 3' end of each protector strand. The two sets of nucleotide sequences, listed 5' to 3', are as follows:

Protector (This is bound to Antibody)
Template (This has AlexaFluor647 for SR imaging)
Invader (Removes dye-labeled template)

Set A:
GCCTGCTTTATCTCTGTTCTACTATTTCCG TT/3AzideN/

5Alex647N/CGGAAATAGTAGAACAGAGATAAAGCAGGCAAA
CGAAA TTTCGTTTGCCTGCTTTATCTCTGTTCTACTATTTCCG

Set B:
GGGTCAAGTCAAAGTCAAGTATCAAGTCGG TT/3AzideN/5Alex647N/
CCGACTTGATACTTGACTTTGACTTGACCCTTGATATT AATATCAA
GGGTCAAGTCAAAGTCAAGTATCAAGTCGG

DNA oligonucleotides purchased from Integrated DNA Technologies(Coralville,IA). Anti-alphaTubulin (Cat. T6074) primary antibody purchased from Sigma Aldrich (St. Louis, MO). Anti-Clathrin (Cat. ab21679) antibody was purchased from Abcam (Cambridge, United Kingdom). Affini-Pure Donkey Anti-Mouse (DAMIG, Cat. 715-005-150) and Affini-Pure Donkey Anti-Rabbit (DARIG, Cat. 711-005-152) secondary antibodies were purchased from Jackson Immunoresearch (Westgrove, PA). 25mm number 1.5 coverslips (Cat. CS- 25R15) were from Warner Instruments (Hamden, CT). Bovine Serum Albumin and Triton X-100 were purchased from Sigma Aldrich (St. Louis, MO). Paraformaldehyde and glutaraldehyde were obtained from Electron Microscopy Sciences (Hatfield, PA). Image-iTTM FX Signal Enhancer (Cat. I36933) was purchased from Life Technologies (Carlsbad, CA).

Protector DNA strands were coupled to antibodies through a two-step process. First, antibodies (1 mg/mL) were reacted with dibenzocyclooctyne (DBCO)-sulfo-NHS Ester at a 6:1 ratio in PBS + 100 mM NaHCO3 for 30 min at room temperature with gentle mixing. Unreacted DBCO-sulfo-NHS ester was removed using a Pro-Spin Column (Cat. CS-800, Princeton Separations) according to manufacturer instructions. This resulted in close to 3:1 DBCO:Ab final ratio. Second, 3-azide-modified DNA is covalently bound to the DBCO group via a Cu-free click reaction. DNA-azide was added to Antibody-DBCO at a 4:1 ratio and allowed to incubate overnight at 4C. The next day, the sample volume was adjusted to 500 ul with PBS

and unreacted DNA was removed using an Amicon Microcentrifuge Filter (100 kDa, Cat. UFC510024, Millipore) according to manufacturer instructions. This resulted in a final Protector:Ab ratio of 1.5-2. The final sample was stored at 4C for up to one month.

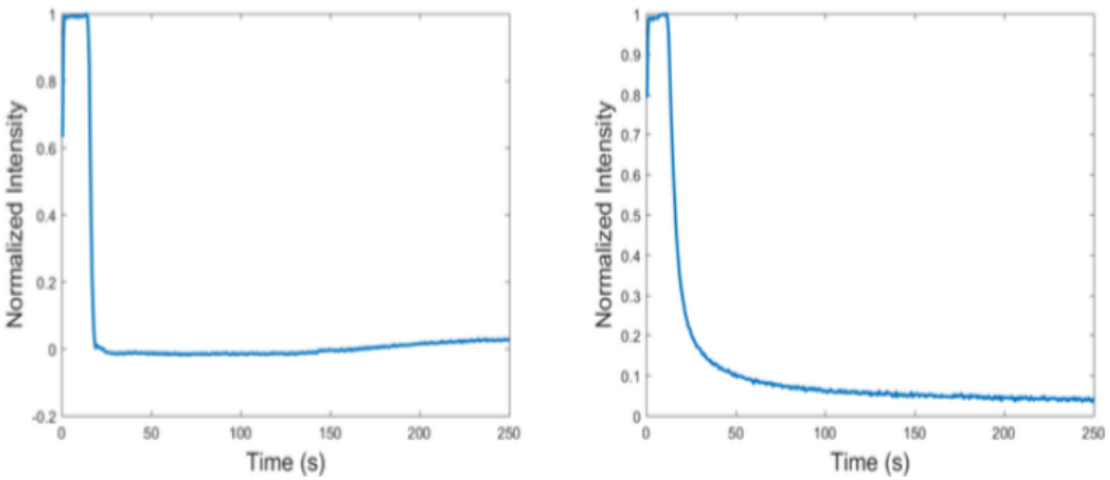

Figure 5.3: Effect of Invader on the detected intensity from the sample over time. As can be seen in both cases, after adding the invader, the intensity drops very fast due to unbinding mechanism.

HeLa cells were cultured in Dulbecco Modified Eagle Medium (DMEM) with 10% fetal calf serum and pen/strep. For imaging, cell were cultured on piranha-cleaned 25 mm coverslips within a 6-well plate at 200,000 cells per well. Cell were allowed to adhere to the glass for 12-16 hr before fixation as described in Valley et al [1]. Briefly, cells were fixed with 0.6% Paraformaldehyde-0.1% Glutaraldehyde-0.25% Triton X-100 for 1 min and immediately followed with 4% Paraformaldehyde-0.2% Glutaraldehyde for 2 hr. Cells were then incubated with 0.1% NaBH4 for 5 min, washed with 10 mM Tris in PBS, and blocked with 4% BSA-0.1% Triton X-100 in PBS for 1 hr. Finally, cells were incubated with Signal Enhancer for 15 min. For labeling, antibodies were diluted in 2% BSA-0.05% Triton X-100 in PBS. Cells were incubated with primary antibodies at 10 ug/mL for 1 hr, followed by extensive

washes then incubation with appropriate oligo- conjugated secondary antibodies at 5 ug/mL for 1 hr. Cells were again washed and post-fixed with 2% PFA for 15 min. Final washes of 10 mM Tris-PBS and then PBS were performed and coverslips were stored in PBS at 4C until imaging. Fixation and antibody labeling was performed at RT.

Each coverslip was mounted on an Attofluor cell chamber (A-7816, life technologies) and washed four times with 1 mL of PBS. To label target structure with AlexaFluor647, 400 uL of template solution (4.87 uM template in PBS) was added to the coverslip for 5 min. Excess template was removed by four washes with 1 mL of PBS and the coverslip was covered with 1.2 mL of dSTORM imaging buffer. Imaging buffer consisted of an enzymatic oxygen scavenging system and primary thiol: 50 mM Tris, 10 mM NaCl, 10% w/v glucose, 168.8 U/ml glucose oxidase (Sigma G2133),1404 U/ml catalase (Sigma C9332), and 32 mM 2-aminoethanethiol (MEA), pH 8. The chamber was sealed by placing an additional coverslip over the top. To remove template after imaging a specific structure, the cell chamber was removed from the microscope and the coverslip was washed four times with 1 mL of PBS, followed by incubation with 4.87 uM invader in 400 uL of PBS to remove the template. To image the next structure, cells were washed four times with PBS, followed by addition of the template specific to the new target for 5 min, four washes with PBS and final addition of imaging buffer. Effect of adding the invader on the intensity on sample is shown in Figure 5.3

The imaging system is custom-built from an inverted microscope (IX71, Olympus America Inc.). A XYZ piezo stage (Mad City Labs, Nano-LPS100) mounted on a x-y manual stage is installed on the microscope for cell locating and brightfield registration. The trans-illumination halogen lamp equipped with the microscope is used for collecting the brightfield images. The trans-illumination lamp power supply is connected to an analog/digital I/O board and controlled by a NI-DAQ card that

allows the computer to adjust the lamp intensity by sending an analog output voltage from 0 V to 5 V to the lamp power supply. A 642 nm laser (collimated from a laser diode, HL6366DG, Thorlabs) is coupled into a multi-mode fiber (P1-488PM- FC-2, Thorlabs) and focused onto the back focal plane of the objective lens with 1.45 NA (UAPON 150XOTIRF, Olympus America Inc.) for data collection. A quad-band dichroic and emission filter set (LF405/488/561/635-A; Semrock, Rochester, NY) was used for sample illumination and emission. Emission light was filtered using a band-pass filter (685/45, Brightline) and collected on an iXon 897 electron-multiplying charge-coupled device (EM CCD) camera (Andor Technologies, South Windsor, CT). The EMCCD gain was set to 100, and frames were 256 256 pixels (for each channel) with a pixel size of 0.1067 um. The emission path includes a quad band optical filter (Photometrics, QV2-SQ) with 4 filter sets (600/37, 525/45, 685/40, 445/45, Brightline) and the EM CCD camera mentioned above. All of the instruments are controlled by custom- written software in MATLAB (MathWorks Inc.).

When imaging each label, a brightfield reference image was acquired in addition to the position of each cell imaged. During data acquisition, the 642 nm laser was used at 1 kW/cm^2 to take 20 sets of 2,000 frames at 60 Hz. After imaging all target cells, the coverslip chamber was removed from the microscope and exchange of label was performed as described above. After labeling, the coverslip holder was placed back on the microscope and each cell was located and re-aligned using the saved brightfield reference image as described in [1]. Imaging was performed as described in Microscopy and Optical Setup. Data was analyzed via a 2D localization algorithm based on maximum likelihood estimation (MLE) [53]. The localized emitters were filtered through thresholds of a maximum background photon counts at 200, a minimum photon counts per frame per emitter at 250, and a data-model hypodissertation test [67] with a cutoff P value at 0.01. The accepted emitters were used to reconstruct the SR image. Each emitter was represented by a 2D-Gaussian with σ_x and

σ_y equal to the localization precisions, which were calculated from the Cramr-Rao Lower Bound. Measurement of invader time course: Cells were labeled and template bound to the protector as described above. Imaging was performed in PBS buffer to match the typical conditions used for strand displacement. Data was collected at 2 Hz using low laser intensity to prevent photobleaching. Images were collected for 20 s to establish a photobleaching rate and then invader strand was added to a final concentration of 4.87 uM during the time series acquisition. Time course plots were generated from the raw image data by subtracting from each frame a scalar background offset using the DipImage [68] function backgroundoffset. The sum intensity of each frame was calculated and normalized to the highest value in the intensity trace.

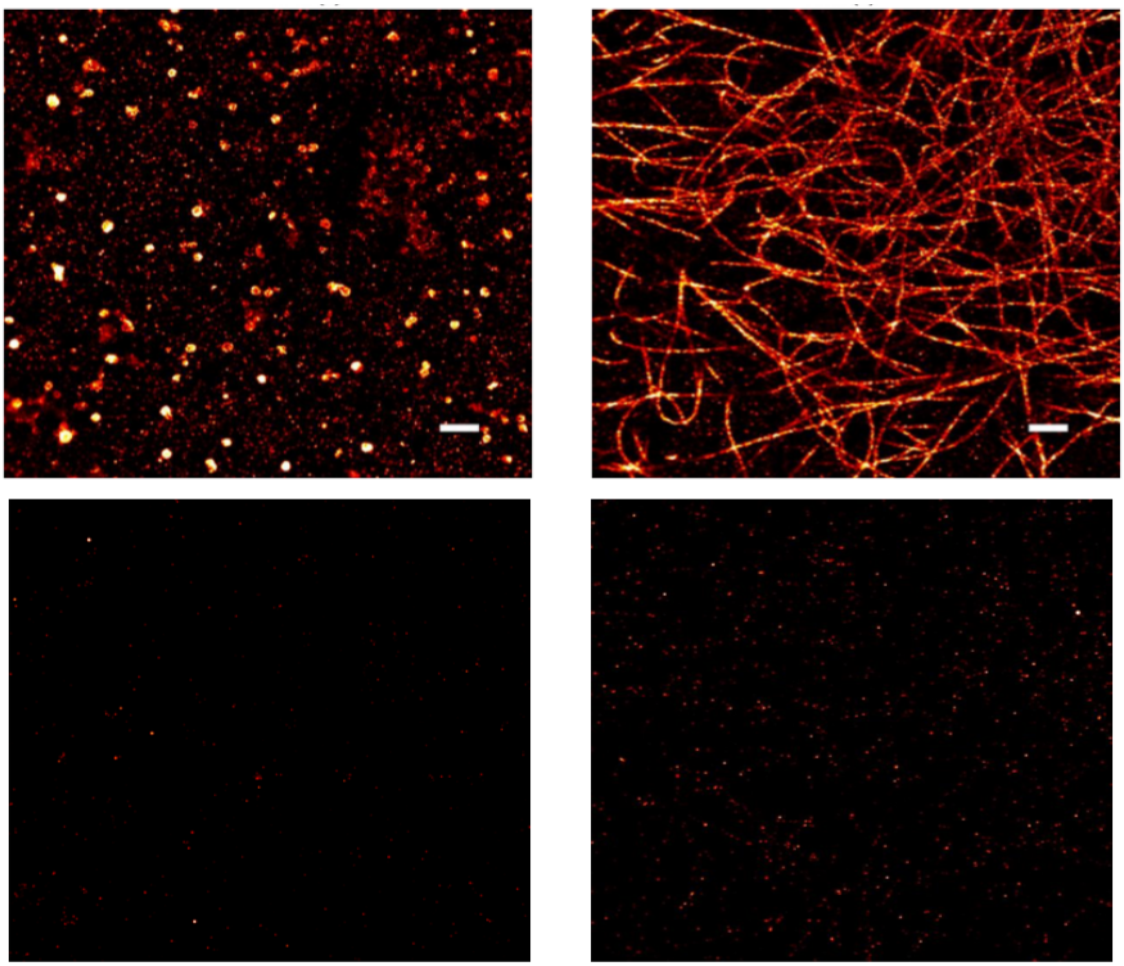

Figure 5.4: Effect of Invader on removing clathrin (left), and microtubules (right) labels.

Calculation of cross talk Super-resolution imaging was performed on template-labeled cells, before and after treatment with invader. The measured data was then analyzed to determine the number of localizations. The ratio of number of localizations after treatment with invader to that before invader was determined as a measure of crosstalk. A crosstalk in the range of 2% to 5% was detected for the experiments reported here. The effect is shown in Figure 5.4

5.2 Imaging Actin

Imaging actin in live and fixed cells is important for investigation of many biological problems. There are different methods developed to image actin. Three main methods are as follows:

1- Injection of fluorescently labeled actin.
2- By fluorescently labeled phalloidin, an F-actin-binding compound [69].
3- By expression of actin-GFP fusion proteins.
4- Peptide labeling known as lifeact.

Each of the methods above have their own limitations. First one is technically demanding, third one relies on non-tagged actin to buffer the defects [70], and the comparison of the second and last method are the topic of this section, so we do not go into detail on other two methods. Phalloidin is a toxin found in the death cap mushroom. It is a lethal heptapeptide. It destroys the liver cells. It functions by binding and stabilizing filamentous actin (F-actin) and prevents the depolymerization of actin fibers. Phalloidin containing fluorescent tags is used in microscopy. lifeact, a 17-amino-acid peptide, which stained filamentous actin (F-actin) structures in eukaryotic cells and tissues. lifeact does not interfere with actin dynamics in vitro and in vivo and in its chemically modified peptide form allowed visualization of actin dynamics in nontransfectable cells [71]. We can get efficient staining with even 4 nM F-lifeact. The F-lifeact peptide can be used as a cheap and nontoxic alternative to phalloidin.

With only 17 amino acids, lifeact can be synthesized cost-effectively, either as an oligonucleotide or as a chemically labeled peptide. lifeact can be used for actin imaging as an alternative to phalloidin. However, although the low affinity of lifeact to F-actin reduces unwanted perturbations, it also limits its use for the measurement

of intra-filament dynamics. The most important advantage of lifeact is its lack of interference with cellular processes. This is consistent with lifeact's low binding affinity to F-actin in vitro, its lack of effects on actin polymerization and depolymerization, and its lack of competition with major actin-binding proteins.

In the context of super-resolution imaging, the localization accuracy is limited by the label density [70, 72]. According to the Nyquist-Shannon sampling theorem [73], a distribution feature smaller than twice the distance between two labeled targets cannot be resolved. The labeling density of a fluorescent protein and an antibody on their targets may be limited due to the expression level and the antibody size (larger than 10 nm). A major problem is the difficulty of fully labeling the structure using antibodies and photoactivatable fluorescent proteins. Because actin subunits and antibodies are 6 and 12 nm wide, respectively, a single actin filament composed of 360 subunits/um can be labeled by an antibody at a maximum density of only 180 molecules/um. Solution to this problem is addressed by using lifeact in context of IRIS method [71].

In this section my goal is to design and perform and series of experiments to compare between imaging with phalloidin and imaging with lifeact. I will investigate strength and limitations of each method for fixed cell imaging. Part of the fixation and imaging is done by Hanieh Mazloom Farsibaf, who I thank here.

5.2.1 Experiments

We know that phalloidin dissociates from its binding sites after about 30 to 60 minutes of imaging (200,000 to 300,000 frames×0.01 sec/frame=2000 to 3000 sec= between 30 minutes to 1 hour) which causes the excess fluorescent dyes to float around gradually in the imaging buffer and among the cells. This excess amount of dyes causes too much out of focus background since the excitation laser light even in

total internal reflection (TIRF) mode, causes too much excitation from the emitters hence it radically decreases the number of good fits in time. As a result of this dissociation, number of fits should decrease in time so it would be a good test to compare phalloiding and lifeact in a scenario where we image a single cell for a long time and plot the fits/frame vs. time. We know that the affinity of lifeact for F-actin is low which causes the peptide to unbind and bind in a matter of few mili seconds, which is a totally different mechanism than how phalloidin works. Theoretically it means that we should be able to image with lifeact for as long as we want, but would there be any factor that might cause a drop in fit/frame vs. time?

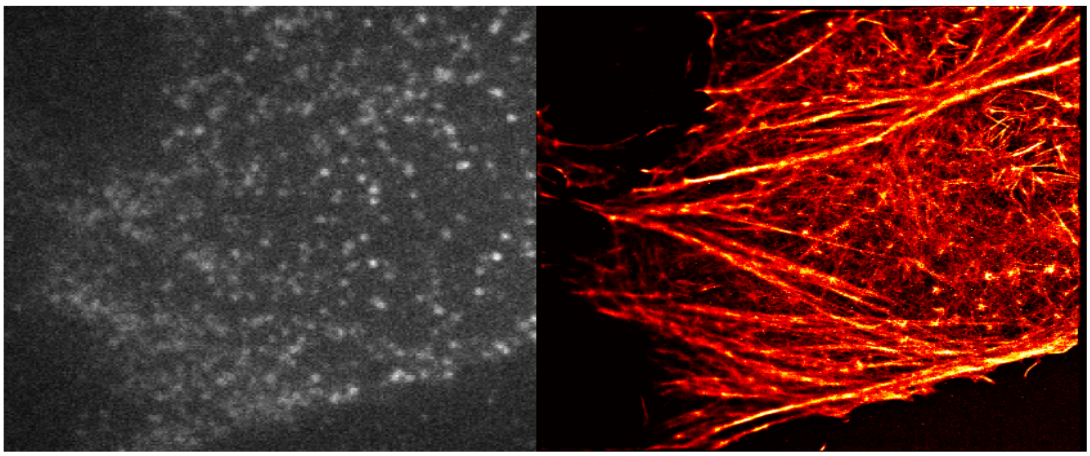

Figure 5.5: Super-resolution reconstruction (right) and a single frame of the raw data showing emitters (left) of a dataset of 100,000 frames, with exposure time of 50 msec, labeled with 6.5 nM LifeAct-Atto655, on normally fixed HeLa cells.

But there are two problems related to our optical system that result in a less than optimal super-resolution reconstruction image. First, our detector can not go faster than 10 msec for exposure time (practically 12 to 14 msec) which is not short enough to overlap with lifeacts bounding-unbounding time, which experimentally is between 3 to 5 msec. Second problem is the laser power on TIRF setup which does not provide more than 20 mW at the back lens of the objective. If we can get 50%

higher power, we will have brighter emitters. Since we use Atto655 with LifeAct, we will have most of dyes come on once and then die, so we need to extract as many photons as possible from that single event which means to have brighter dyes. Figure 5.5 shows a single frame of the data on TIRF microscope where we do not have bright enough emitters along with a non-uniform excitation pattern.

On the TIRF microscope we checked the fit/frames for lifeact experiment of 22 sets of 40,000 frames to find the fit/frame from the start, till saturation (when there are too many dyes floating around, so too many emitters are next to each other to be able to fit them by the single emitter fitting code). Related results are shown in shown in Figures 5.6, 5.7, and 5.8.

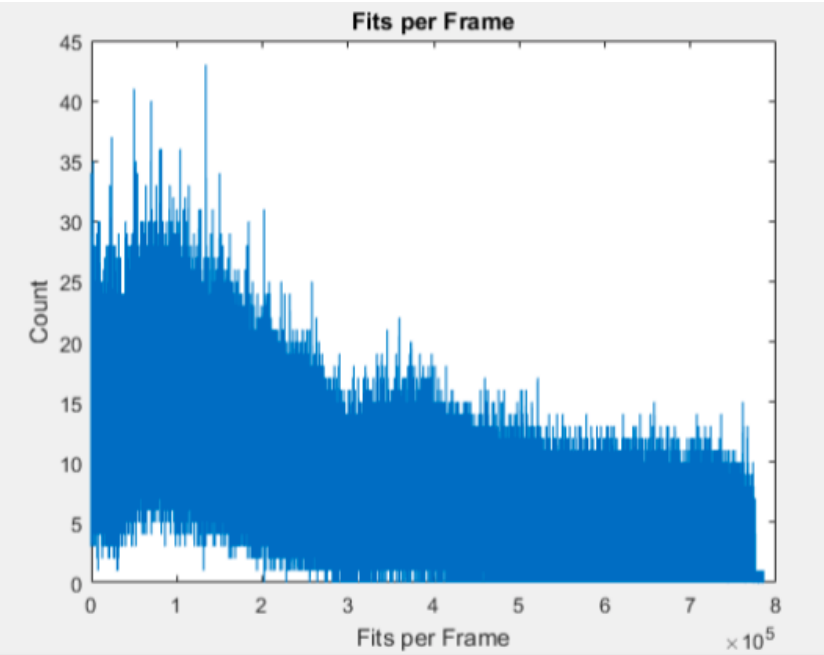

Figure 5.6: Fit per frame of HeLa cells imaged for 22 sets of 40,000 frames, with exposure time of 20 msec, labeled with 6 nM LifeAct-Atto655.

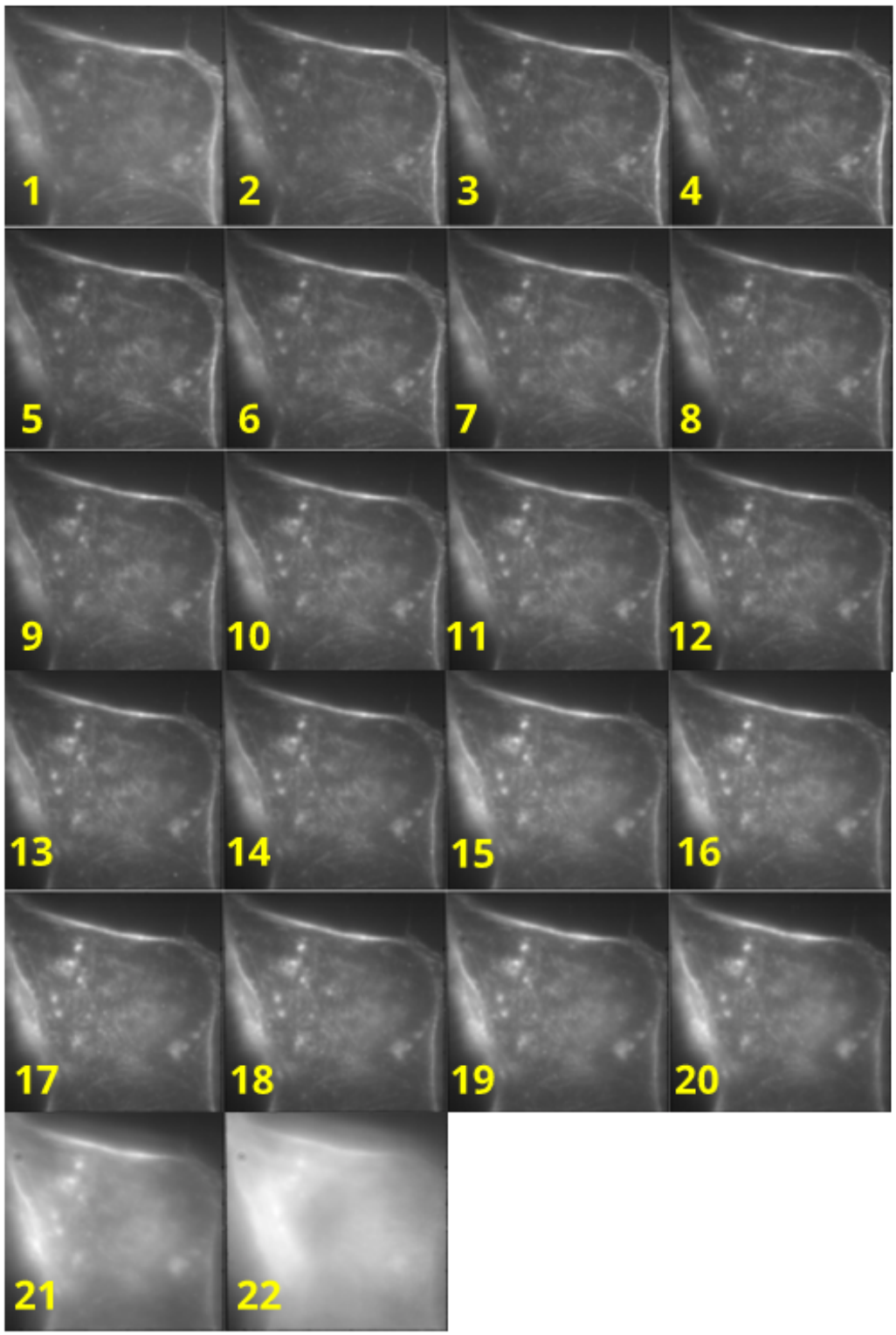

Figure 5.7: Sum image of HeLa cells imaged for 22 sets of 40,000 frames, with exposure time of 20 msec, labeled with 6 nM LifeAct-Atto655.

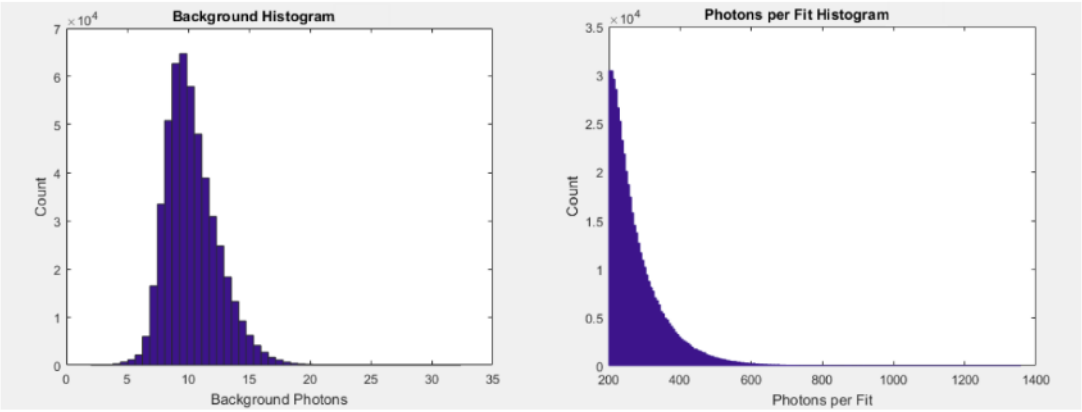

Figure 5.8: Background (left) and photons/fit (right), of HeLa cells for a single 40,000 frames dataset, with exposure time of 20 msec, labeled with 6 nM LifeAct-Atto655.

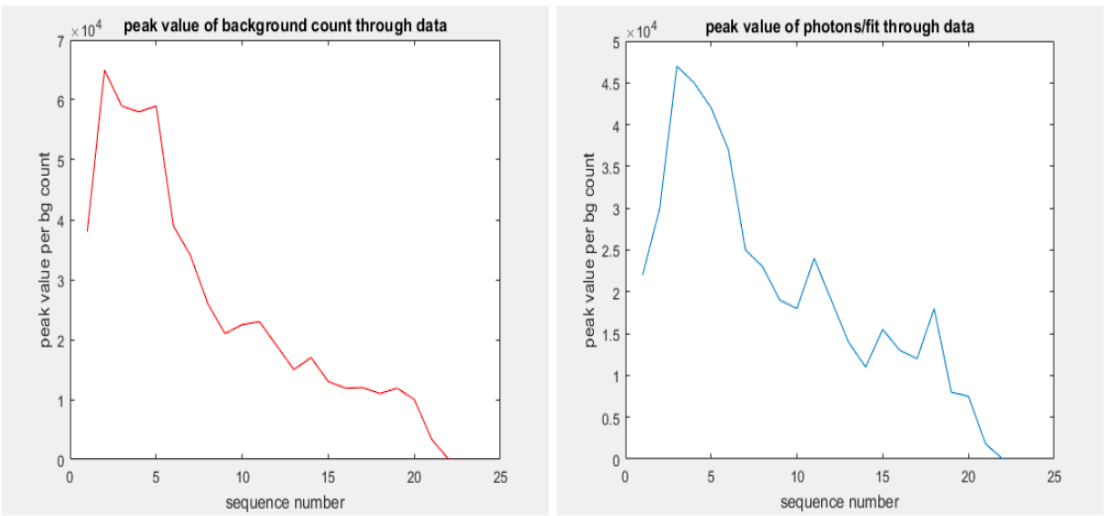

Figure 5.9: Peak value of background (left) and peak value of photons/fit (right) through the whole data set of HeLa cells imaged for 22 sets of 40,000 frames, with exposure time of 20 msec, labeled with 6 nM LifeAct-Atto655.

As we can see, by plotting the peak value of photons/fit for each sequence (each 40,000 frames), we see a drop in value that is consistent with the drop in fits/frame as the data reaches the saturation state over time as shown in Figure 5.9. Measurements

by PH papers, at the start and at the saturation point (after 7 to 8 hours from labeling), show a drop of PH value from 7 to 5 in the sealed imaging buffer. So we have a limiting time factor when imaging with lifeact in the same imaging buffer.

Now we move to our other setup which is a single particle tracking (SPT) microscope. SPT microscope has a faster sCMOS camera which is able to image down to 2 msec exposure time and the laser power into the back of the objective, from a 638 nm diode laser can be tuned to 35 mW. After more than 50 experiments, the best protocols for imaging lifeact-Atto655 and phalloidin-AlexaFluor647 are achieved through testing different labeling concentrations, different exposure times, and different fixation protocols. Here we only present the final protocol where we employ cytoskeleton fixation buffer and image on SPT microscope. For lifeact the best results are achieved for exposure time of 5 msec and for phalloidin the best results are achieved for exposure time of 10 msec. First we investigate fits/frame for imaging with phalloidin in HeLa cells on a long data set shown in Figure 5.10

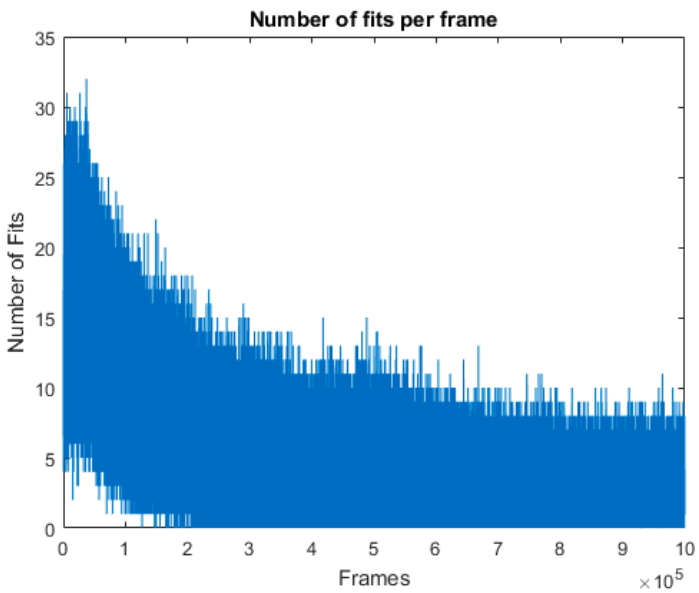

Figure 5.10: Fit per frame plot vs. time for HeLa cell, for 1 million frames of exposure time 10 msec, by Phalloidin labeling, fixed in cytoskeleton buffer.

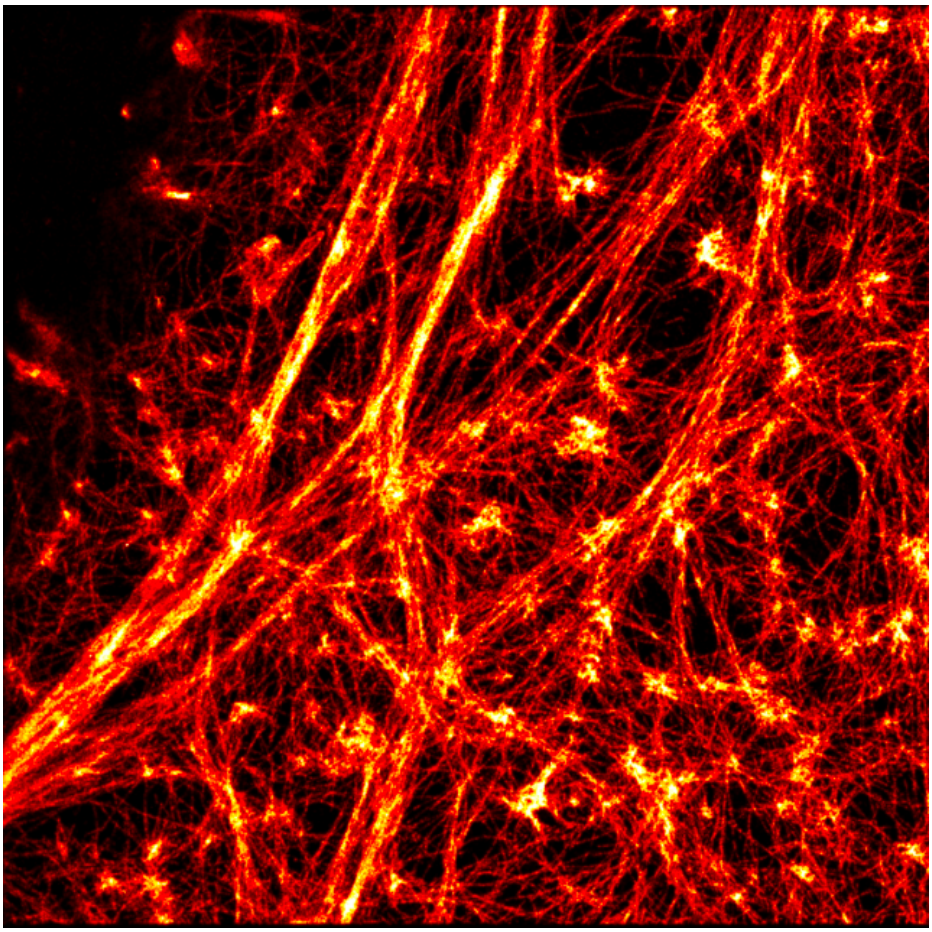

Figure 5.11: Imaging Actin in a HeLa cell for 1 million frames of exposure time 10 msec, by Phalloidin labeling, fixed in cytoskeleton buffer.

For labeling with phalloidin we do 4 hours of labeling with 2 ug/mL concentration and image in dSTORM buffer (1350 uL of TNG buffer, 150 uL of OSB, and 100 uL of MEA) at PH=8.5. As can be seen from the results, number of fits decrease rather fast through the dataset. If we reconstruct the super-resolution image from the first 200,000 frames and last 200,000 frames and compare them, the difference will be very clear, as can be predicted from the plot for fits/frame vs. time. The super-resolution reconstruction for 1 million frames still looks good as shown in Figure 5.11 since the result for the first 200,000 frames is superior. This is a big limitation for imaging

with phalloidin and means that if we take 200,000 frames with 10 msec exposure time, which is the optimum imaging time for phalloidin, the difference between the reconstructed result from the first cell and the second cell will be big. So we will be limited to image only a single cell with the best result and since washing off the dye is not easy, we will have to change the coverslip after imaging a single cell.

At this stage, a good comparison can be achieved by imaging Actin bundles and filaments in the same HeLa cell, sequentially by lifeact as the first label and phalloidin as the second label. This comparison can be seen in Figure 5.12

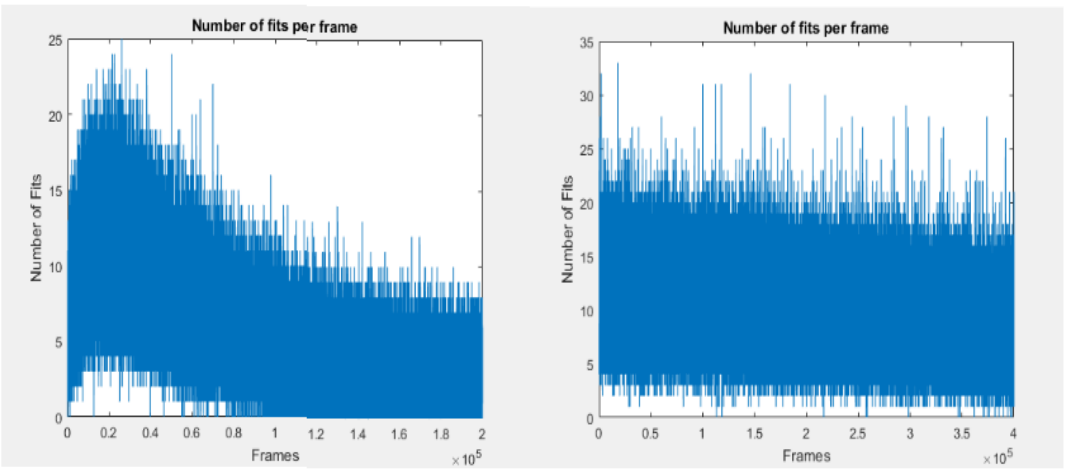

Figure 5.12: Fits per frame for phalloidin labeling(left) and lifeact labeling(right) on the same HeLa cell, for the same experiment time. Phalloidin is imaged for 200,000 frames with 10 msec exposure time while lifeAct is imaged for 400,000 frames of 5 msec exposure time.

To do this experiment, we image lifeact first (since it is easier to wash off) at 12 nM concentration in HEPES buffer (1350 uL of HEPES buffer, and 150 uL of OSB) of PH=8 at room temperature, then we take the imaging buffer out and wash the cell 3 times with 1X-PBS, then we label for 4 hours with 75 mM phalloidin in 1X-PBS, then wash it once with 1X-PBS, and image in dSTORM buffer (1350 uL of TNH, 150 uL of OSB, and 100 uL of MEA) of PH=8.5 at room temperature. In both

cases, a 30 mW laser power enters the back of the objective, and light is adjusted to be in the TIRF angle. In both cases, the sample holder is sealed by a 25 mm round coverglass to prevent oxygen from entering the buffer. Results are shown in Figures 5.13, 5.14, and 5.15.

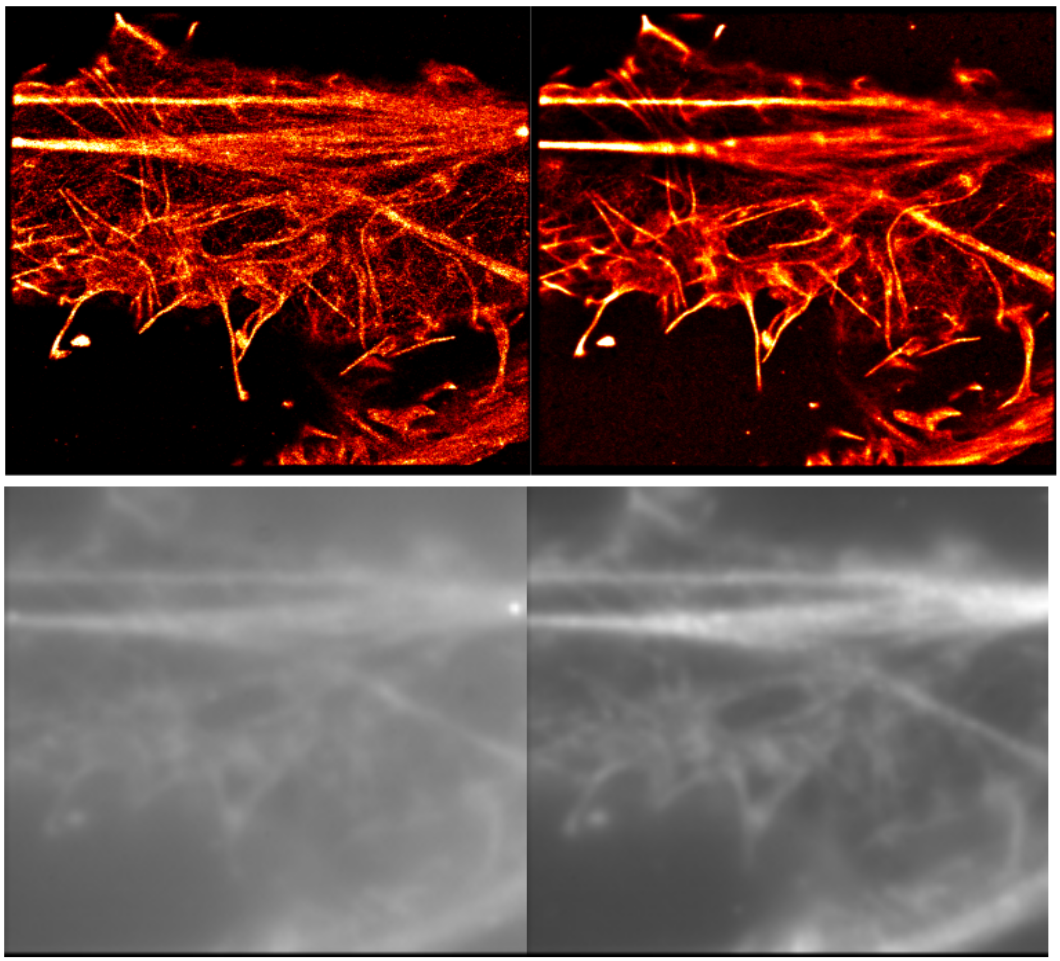

Figure 5.13: Super-resolution reconstruction of phalloidin labeling(top left) and lifeact labeling(top right). Sum image of phalloidin labeling (bottom left) and lifeact labeling (bottom right). Both labels are imaged for the same amount of time (i.e., 2000 seconds) but with different exposure times of 5 msec for lifeact and 10 msec for phalloidin. Number of total fits for phalloidin is 28.8% of the number of total fits for lifeact.

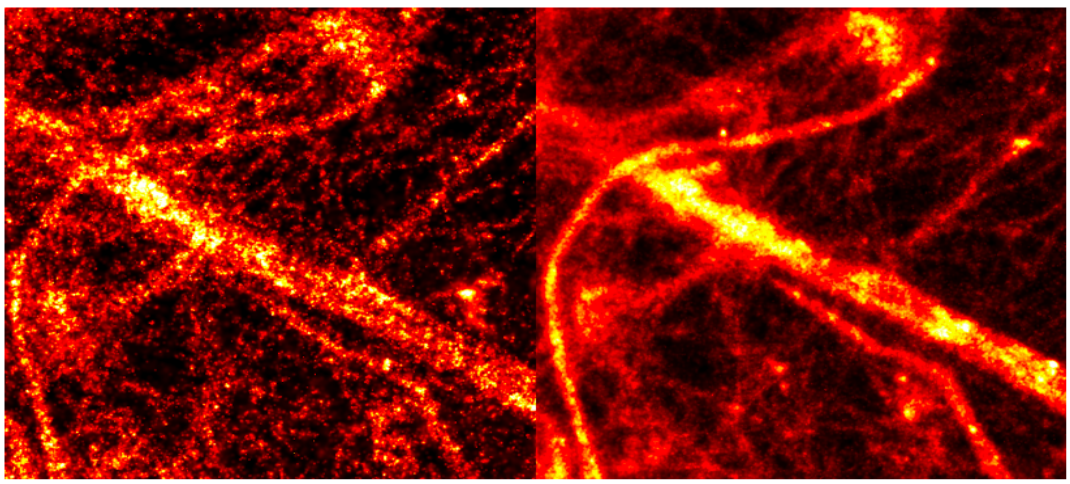

Figure 5.14: Zoomed super-resolution reconstruction of phalloidin labeling(left) and lifeact labeling(right). Both labels are imaged for the same amount of time (i.e., 2000 seconds) but with different exposure times of 5 msec for lifeact and 10 msec for phalloidin.

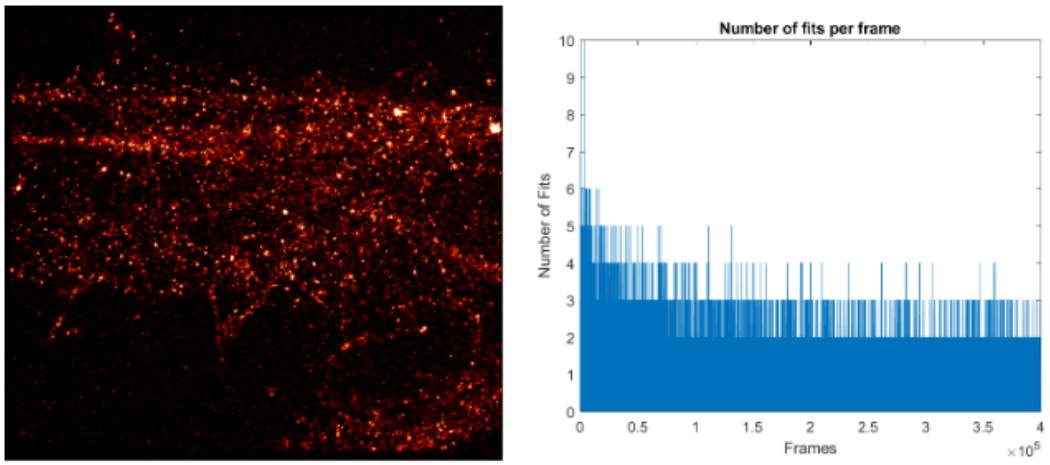

Figure 5.15: Super-resolution reconstruction of crosstalk measurement after imaging lifeact and after 3 washes with PBS, in the HEPES buffer(left). Ratio of the number of localized points for crosstalk measurement to the number of localized points for lifeact experiment, is %3.16. (right) fits/frame vs. time for crosstalk measurement.

In order to compare the statistics of the two labeling strategies used in the se-

quential scheme, here we choose 21 regions shown in Figure 5.16 on thicker bundles that are very crowded and find the ratio of accepted fits, total number of emitters, and rejected fits for lifeact vs. phalloidin.

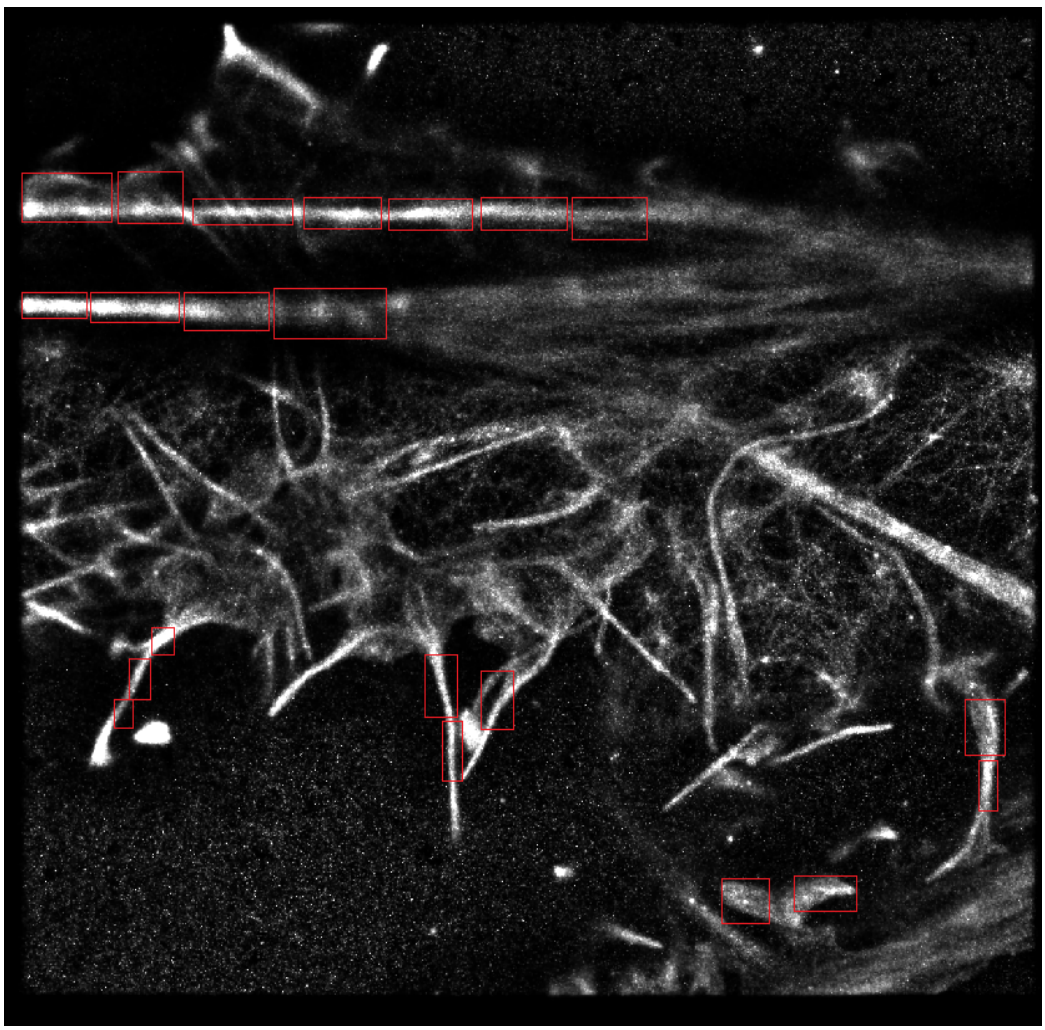

Figure 5.16: 21 regions chosen to compare statistics between lifeact and phalloidin in sequential experiment.

As can be seen from Figure 5.17, although the number of fit rejections from our single emitter fitting code is higher for lifeact, the number of total fits is more than 3 times for lifeact vs. phalloidin and also the number of accepted fits is in every case is

higher for lifeact. As a result, lifeact proves to get higher resolution for every bundle. In some of the regions it gives 4 times the number of accepted fits which mean on average, produces twice the resolution of phalloidin in the same region.

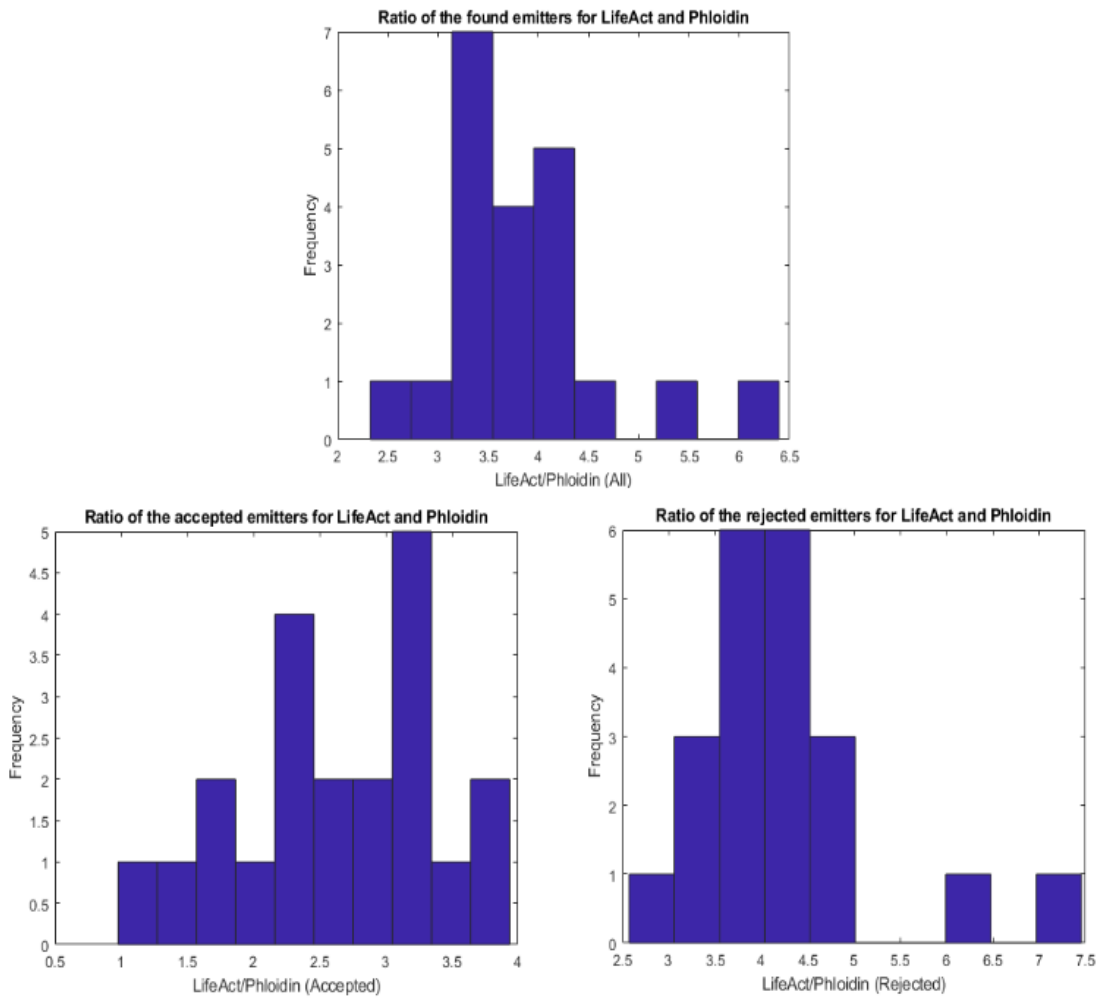

Figure 5.17: Statistics for comparing 21 regions chosen from the same HeLa cell in sequential imaging of lifeact vs phalloidin. (top) ration of number of total emitters (bottom left) ratio of number of accepted fits (bottom right) ratio of number of rejected fits

As can be seen from the results of the sequential experiment, lifeact is easy to

wash out and gives better fine details. Although we still need to perform other experiments to make sure lifeact is better for imaging actin filaments, until now the results are in favor of lifeact. Here are a list of experiments that still have to be performed.

1- lifeact imaging then 3 washes with PBS then another set of lifeact imaging on the same HeLa cell to show that the actin structure is not deteriorating and we still can get the same quality for the second experiment.
2- Phalloidin imaging as the first label then 3 washes then imaging the sample in dSTORM buffer to find out the percentage of dyes remaining on the sample. This way we can have a direct comparison between phalloidin and lifeact as the first label for a sequential imaging scheme.
3- Sequential imaging for lifeact as the first label then clathrin or tubulin as the second label.

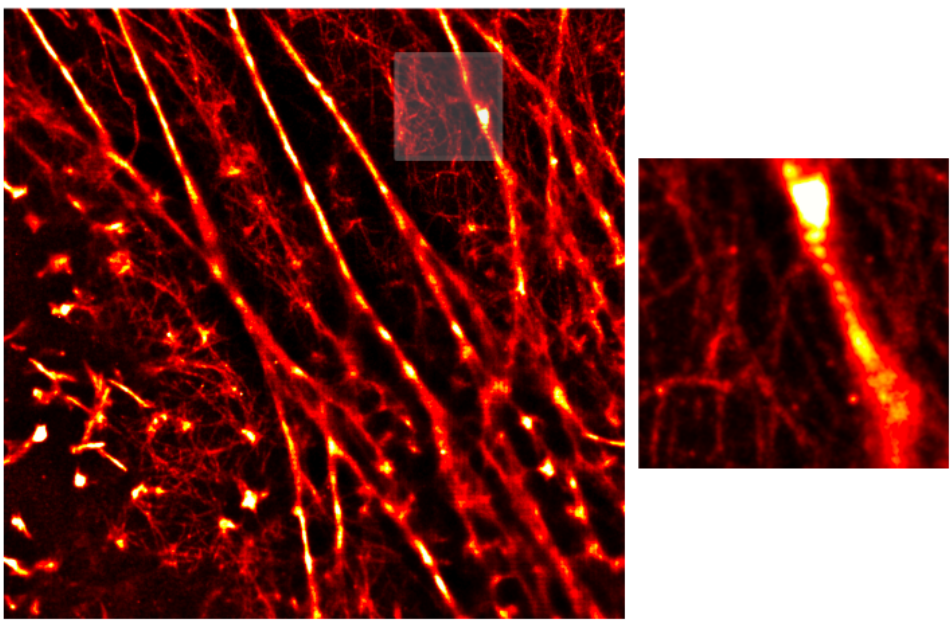

Figure 5.18: HeLa cell imaging by LifeAct labeling of 12nM, for 400,000 frames with 5 msec exposure time.

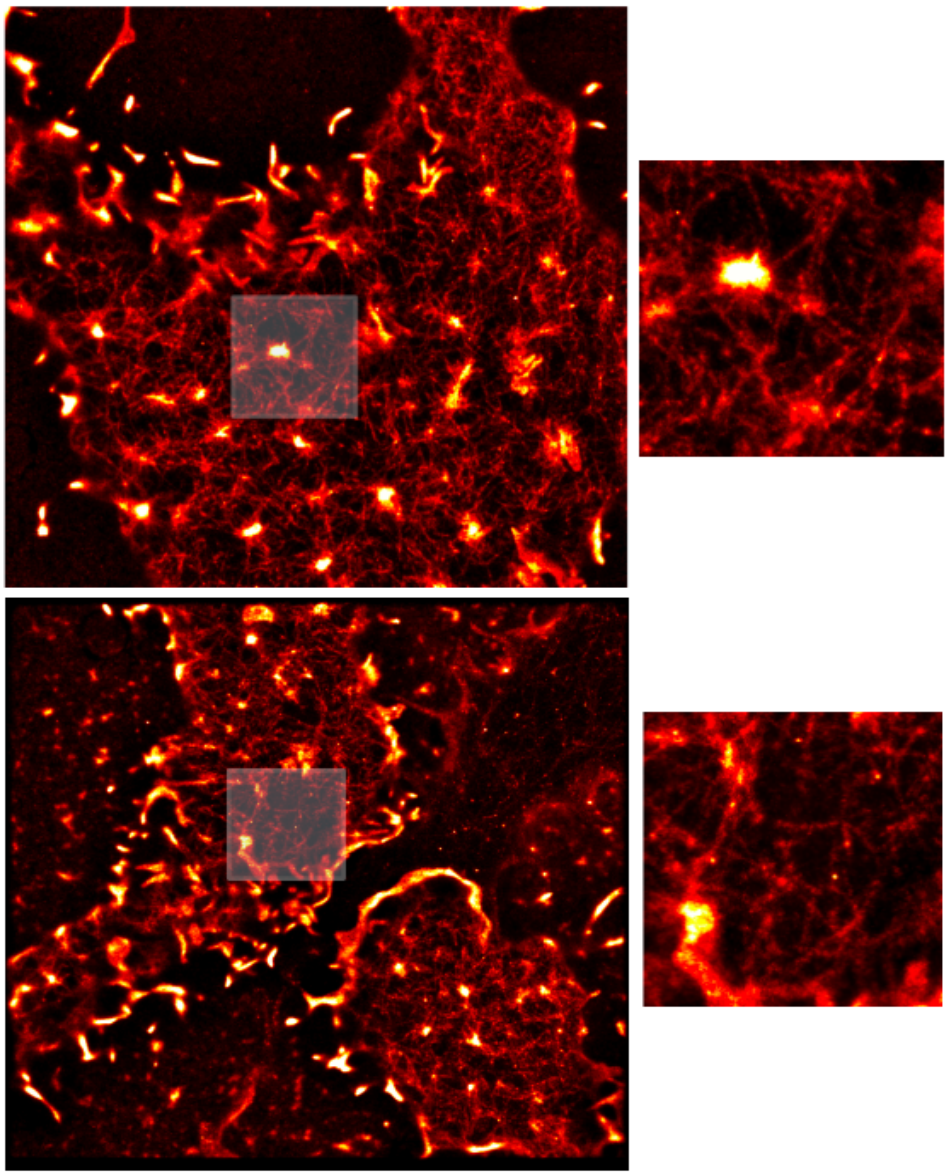

Figure 5.19: An RBL cell at the start of imaging with lifeact(top) and another RBL cell after 7 hours of imaging with lifeact(bottom), in the same HEPES buffer, with 12nM lifeact labeling and both cells imaged for 400,000 frames of 5 msec exposure time.

In Figure 5.19 we show that after 7 hours of being in the same imaging buffer, RBL cells can be still imaged with fine details. So lifeact is superior to phalloidin

for imaging multiple cells. But at this point there has been a decrease in PH of the buffer that will result eventually in a saturation effect (possibly by ruining the structures inside the cells). This problem might be solvable by simply changing the buffer after two hours of experiment, before the drop in PH reaches a unit. This will be another test that we need to perform with respect to lifeact. Fixation process for lifeact and phalloidin is as follows (courtesy to Hanieh Mazloom Farsibaf):

Cytoskeleton Buffer: (PEM) Ph 7.2
80 mM PIPES (SIGMA, P1851?25G)
5 mM EGTA (ethylene glycol-bis(β-aminoethyl ether)-N,N,N',N'-tetraacetic acid) (Sigma,E3889-25G)
2 mM MgCl2 (magnesium chloride hexahydrate, CAS 7791-18-6)

Fixation Process:
Wash 1X PBS (37 degree) on flat heater
Add warm 0.6% PFA in PEM buffer for 5 min
Add 2% PFA in PEM buffer 4 to 5 hours
Wash 2x PBS
10mM Tris for 5 to10 minutes
Wash 2×PBS
Block in PBS+5% BSA+0.05% Triton X-100 for 15 minutes
Store cells in PBS at 4C

Actin Labeling with Alexa Flour 647 Phalloidin (Thermo Fisher, Cat A22287)
75 mM (30 ul of Alexa Flour 647 Phalloidin in 400 ul PBS) for 4 hours
Wash 1x PBS

STORM buffer for Alexa Flour 647 Phalloidin: PH 8.5
150 ul OSB, 100 ul MEA (66 mM), 1350 ul TNG

Chapter 6

Conclusion and Outlook

In this dissertation, after going through a brief introduction on super-resolution microscopy, I mentioned different strategies for multi-target super-resolution imaging, and introduced the concept of a sequential imaging microscope and explained how it is beneficial for researchers in the field of biology and biomedicine who are interested in investigating the spatial organization of sub-cellular structures in a nanometer regime.

In Chapter 2, I designed a sequential microscope and optimized the design for AlexaFluor647 in order to perform multi-target automated high-throughput super-resolution imaging of fixed cells by using the dye with best photo-physical properties for super-resolution imaging. In my design I addressed three main parts: Optics, Mechanical parts related to movement control, and MATLAB classes and graphical user interfaces (GUIs) for instrument control and automation in taking the data and for live drift correction.

In Chapter 3, I characterized and optimized my design in different aspects of the optics, the mechanical parts, and the code, based on practical and experimental limitations. In this chapter, experimental tests (specifically creating a perfect overlay

of β and α tubulin strands, as the first and second target structure, in 40 cells) show the reliability of the microscope to perform multi-target imaging of structures that we do not know exactly how they should spatially organize. Design of this microscope is being put together in form of a scientific paper that I am the first author of. Another paper is being written in collaboration around the MATLAB instrumentation codes (MIC) which will contain classes written for sequential microscope.

In Chapter 4, I used sequential microscope to investigate three biological problems, two of them under the category of Autophagy, resulted in 3 publications [46, 12, 13], in collaboration with Molecular Genetics Department at UNM, and one in category of Endocytosis (ongoing research) in collaboration with Cancer Research Facility at UNM. Biology and goals behind these experiments, are explained. Experimental details and methods for analysis, are presented.

In Chapter 5, two labeling strategies are investigated. One is the DNA-strand-displacement, which I performed the experiments mainly on the TIRF microscope, but is very beneficial to implement into sequential microscope. This project lead to a paper, currently on bioRxiv. The other strategy investigates actin imaging with lifeact peptides and compares the results with the popular actin labeling strategy of using phalloidin. This project is in final stages and is going to be prestented as a scientific paper that I am the first author of.

In the end I list my suggestions on how to improve and advance imaging with sequential microscope:

1- move toward 3D imaging:
The drift correction scheme for 3D imaging already exists. We need to change the codes so we take data also in a z-stack. To do this, we need to alter our bright-field registration algorithm to take a z-stack reference when we register a cell for imaging at the start of each experiment.

2- automate the labeling process:
To do this, we need to design a new holder and to implement the microfluidics chamber into the setup, which needs alteration of the setup physically as well as writing a class in MATLAB for the chamber and to implement needed function for it in the main working class of sequential microscope.

3- use a better labeling strategy:
A better labeling strategy than the current strategy would be to implement our DNA-strand-displacement technique for sequential imaging. This way we can cut the experiment time vastly since the photobleaching step is practically reduced to the use of invader for a minute on the sample.

4- implement PSF engineering:
By using a spatial light modulator (SLM) in place of the first mirror after the first f=150 mm lens in the emission path of the microscope, which is placed at the conjugate image plane of the sample, we can create different PSF patterns and use them to the benefit of the specific biological problem we are investigating on the microscope.

5- create less drift during the experiments:
By designing a new holder from Invar, we can minimize the drift we have so even without live drift correction we can get a very small drift over course of an experiment that is smaller that the 25 nm resolution.

References

[1] Christopher C. Valley, Sheng Liu, Diane S. Lidke, and Keith A. Lidke. Sequential superresolution imaging of multiple targets using a single fluorophore. *PLoS ONE*, 10(4), 2015.

[2] LDM9T - Laser Diode Mount with Integrated Temperature Controller, 2018, Last accessed: 5/11/18.

[3] MFF101/M - Motorized Filter Flip Mount with 1" Optic Holder, M4 Tap, 2018, Last accessed: 5/11/18.

[4] ORCA-Flash4.0 V2 Digital CMOS Camera C11440-22CU/C11440-22CU01 Instruction manual version 1.7, September 2016, Last accessed: 5/11/18.

[5] MAX341/M - 3-Axis NanoMax Stage, Stepper Motors, Closed-Loop Piezos, Metric.

[6] TLD001 - T-Cube Laser Diode Controller, 2018, Last accessed: 5/11/18.

[7] LEDD1B - T-Cube LED Driver, 1200 mA Max Drive Current, 2018, Last accessed: 5/11/18.

[8] BSC203 - Three-Channel APT Benchtop Stepper Motor Controller, 2018, Last accessed: 5/11/18.

[9] TSG001 - T-Cube Strain Gauge Reader, 2018, Last accessed: 5/11/18.

[10] Geoffrey M Cooper and Robert E Hausman. *The Cell: A Molecular Approach 2nd Edition*. 2007.

[11] Jennifer Hirst and Margaret S. Robinson. Clathrin and adaptors. *Biochimica et Biophysica Acta - Molecular Cell Research*, 1404(1-2):173–193, 1998.

[12] T. Kimura, J. Jia, S. Kumar, S.W. Choi, Y. Gu, M. Mudd, N. Dupont, S. Jiang, R. Peters, F. Farzam, A. Jain, K.A. Lidke, C.M. Adams, T. Johansen, and V. Deretic. Dedicated SNAREs and specialized TRIM cargo receptors mediate secretory autophagy. *EMBO Journal*, 36(1), 2017.

[13] S. Kumar, A. Jain, F. Farzam, J. Jia, Y. Gu, S.W. Choi, M.H. Mudd, A. Claude-Taupin, M.J. Wester, K.A. Lidke, T.-E. Rusten, and V. Deretic. Mechanism of Stx17 recruitment to autophagosomes via IRGM and mammalian Atg8 proteins. *Journal of Cell Biology*, 217(3), 2018.

[14] Steven I. Hajdu. A Note from History: The first use of the microscope in medicine. *Annals of Clinical and Laboratory Science*, 32(3):309–310, 2002.

[15] Andreas Ettinger and Torsten Wittmann. Fluorescence live cell imaging. *Methods in Cell Biology*, 123:77–94, 2014.

[16] Tarik F Massoud and Sanjiv S Gambhir. Molecular imaging in living subjects: seeing fundamental biological processes in a new light. *Genes & development*, 17(5):545–580, 2003.

[17] E. Abbe. Beiträge zur Theorie des Mikroskops und der mikroskopischen Wahrnehmung. *Archiv für Mikroskopische Anatomie*, 9(1):413–418, 1873.

[18] S. Hell. Far-field optical nanoscopy. *Science*, 316(5828):1153–1158, 2007.

[19] Stefan W. Hell and Jan Wichmann. Breaking the diffraction resolution limit by stimulated emission: stimulated-emission-depletion fluorescence microscopy. *Optics Letters*, 19(11):780, 1994.

[20] Benjamin Harke, Jan Keller, Chaitanya K. Ullal, Volker Westphal, Andreas Schönle, and Stefan W. Hell. Resolution scaling in STED microscopy. *Optics Express*, 16(6):4154, 2008.

[21] Stefan W. Hell. Microscopy and its focal switch. *Nature Methods*, 6(1):24–32, 2009.

[22] Tobias Müller, Christian Schumann, and Annette Kraegeloh. STED microscopy and its applications: New insights into cellular processes on the nanoscale. *ChemPhysChem*, 13(8):1986–2000, 2012.

[23] Eric Betzig, George H Patterson, Rachid Sougrat, O Wolf Lindwasser, Scott Olenych, Juan S Bonifacino, Michael W Davidson, Jennifer Lippincott-Schwartz, and Harald F Hess. Imaging intracellular fluorescent proteins at nanometer resolution. *Science (New York, N.Y.)*, 313(5793):1642–5, 2006.

[24] Michael J Rust, Mark Bates, and Xiaowei Zhuang. Sub-diffraction-limit imaging by stochastic optical reconstruction microscopy (STORM). *Nature Methods*, 3(10):793–796, 2006.

[25] Mark Schüttpelz, Steve Wolter, Sebastian van de Linde, Mike Heilemann, and Markus Sauer. dSTORM: real-time subdiffraction-resolution fluorescence imaging with organic fluorophores. *SPIE Single Molecule Spectroscopy and Imaging III*, 7571:75710V–75710V–7, 2010.

[26] Sebastian van de Linde, Anna Löschberger, Teresa Klein, Meike Heidbreder, Steve Wolter, Mike Heilemann, and Markus Sauer. Direct stochastic optical reconstruction microscopy with standard fluorescent probes. *Nature Protocols*, 6(7):991–1009, 2011.

[27] Mark Bates, Bo Huang, and Xiaowei Zhuang. Super-resolution microscopy by nanoscale localization of photo-switchable fluorescent probes. *Current Opinion in Chemical Biology*, 12(5):505–514, 2008.

[28] H. Shroff, C. G. Galbraith, J. A. Galbraith, H. White, J. Gillette, S. Olenych, M. W. Davidson, and E. Betzig. Dual-color superresolution imaging of genetically expressed probes within individual adhesion complexes. *Proceedings of the National Academy of Sciences*, 104(51):20308–20313, 2007.

[29] Martin Andresen, Andre C. Stiel, Jonas Fölling, Dirk Wenzel, Andreas Schönle, Alexander Egner, Christian Eggeling, Stefan W. Hell, and Stefan Jakobs. Photoswitchable fluorescent proteins enable monochromatic multilabel imaging and dual color fluorescence nanoscopy. *Nature Biotechnology*, 26(9):1035–1040, 2008.

[30] Fedor V. Subach, George H. Patterson, Suliana Manley, Jennifer M. Gillette, Jennifer Lippincott-Schwartz, and Vladislav V. Verkhusha. Photoactivatable mCherry for high-resolution two-color fluorescence microscopy. *Nature Methods*, 6(2):153–159, 2009.

[31] David Baddeley, David Crossman, Sabrina Rossberger, Juliette E. Cheyne, Johanna M. Montgomery, Isuru D. Jayasinghe, Christoph Cremer, Mark B. Cannell, and Christian Soeller. 4D super-resolution microscopy with conventional fluorophores and single wavelength excitation in optically thick cells and tissues. *PLoS ONE*, 6(5), 2011.

[32] Stephan Wilmes, Markus Staufenbiel, Domenik Liße, Christian P. Richter, Oliver Beutel, Karin B. Busch, Samuel T. Hess, and Jacob Piehler. Triple-color super-resolution imaging of live cells: Resolving submicroscopic receptor organization in the plasma membrane. *Angewandte Chemie - International Edition*, 51(20):4868–4871, 2012.

[33] Ulrike Endesfelder, Sebastian Malkusch, Benjamin Flottmann, Justine Mondry, Piotr Liguzinski, Peter J. Verveer, and Mike Heilemann. Chemically induced photoswitching of fluorescent probes-A general concept for super-resolution microscopy. *Molecules*, 16(4):3106–3118, 2011.

[34] André Lampe, Volker Haucke, Stephan J. Sigrist, Mike Heilemann, and Jan Schmoranzer. Multi-colour direct STORM with red emitting carbocyanines. *Biology of the Cell*, 104(4):229–237, 2012.

[35] Ralf Jungmann, Maier S Avendaño, Johannes B Woehrstein, Mingjie Dai, William M Shih, and Peng Yin. Multiplexed 3D cellular super-resolution imaging with DNA-PAINT and Exchange-PAINT. *Nature Methods*, 11(3):313–318, 2014.

[36] Ralf Jungmann, Christian Steinhauer, Max Scheible, Anton Kuzyk, Philip Tinnefeld, and Friedrich C. Simmel. Single-molecule kinetics and super-resolution microscopy by fluorescence imaging of transient binding on DNA origami. *Nano Letters*, 10(11):4756–4761, 2010.

[37] Zhengyang Zhang, Samuel J. Kenny, Margaret Hauser, Wan Li, and Ke Xu. Ultrahigh-throughput single-molecule spectroscopy and spectrally resolved super-resolution microscopy. *Nature Methods*, 12(10):935–938, 2015.

[38] Graham T Dempsey, Joshua C Vaughan, Kok Hao Chen, Mark Bates, and Xiaowei Zhuang. Evaluation of fluorophores for optimal performance in localization- based super-resolution imaging. *Nature methods*, 8(12):1–44, 2011.

[39] Joran Deschamps, Andreas Rowald, and Jonas Ries. Efficient homogeneous illumination and optical sectioning for quantitative single-molecule localization microscopy. *Optics express*, 24(24):28080–28090, 2016.

[40] Sang Hak Lee, Murat Baday, Marco Tjioe, Paul D Simonson, Ruobing Zhang, En Cai, and Paul R Selvin. Using fixed fiduciary markers for stage drift correction. *Optics express*, 20(11):12177–83, 2012.

[41] Yina Wang, Joerg Schnitzbauer, Zhe Hu, Xueming Li, Yifan Cheng, Zhen-Li Huang, and Bo Huang. Localization events-based sample drift correction for localization microscopy with redundant cross-correlation algorithm. *Optics Express*, 22(13):15982, 2014.

[42] Michael S. Smirnov, Paul R. Evans, Tavita R. Garrett, Long Yan, and Ryohei Yasuda. Automated remote focusing, drift correction, and photostimulation to evaluate structural plasticity in dendritic spines. *PLoS ONE*, 12(1), 2017.

[43] N Marturi, S Dembele, and N Piat. Fast image drift compensation in scanning electron microscope using image registration. In *Automation Science and Engineering (CASE), 2013 IEEE International Conference on*, pages 807–812, 2013.

[44] Ryan McGorty, Daichi Kamiyama, and Bo Huang. Active Microscope Stabilization in Three Dimensions Using Image Correlation. *Optical nanoscopy*, 2(1):1, 2013.

[45] Martin Ester, Hans P Kriegel, Jorg Sander, and Xiaowei Xu. A Density-Based Algorithm for Discovering Clusters in Large Spatial Databases with Noise. *Proceedings of the 2nd International Conference on Knowledge Discovery and Data Mining*, pages 226–231, 1996.

[46] T. Kimura, J. Jia, A. Claude-Taupin, S. Kumar, S.W. Choi, Y. Gu, M. Mudd, N. Dupont, S. Jiang, R. Peters, F. Farzam, A. Jain, K.A. Lidke, C.M. Adams, T. Johansen, and V. Deretic. Cellular and molecular mechanism for secretory autophagy. *Autophagy*, 2017.

[47] Benjamin J. Nichols and Jennifer Lippincott-Schwartz. Endocytosis without clathrin coats. *Trends in Cell Biology*, 11(10):406–412, 2001.

[48] Cédric Cleyrat, Anza Darehshouri, Karen L Anderson, Christopher Page, Diane S Lidke, Niels Volkmann, Dorit Hanein, and Bridget S Wilson. The architectural relationship of components controlling mast cell endocytosis. *Journal of cell science*, 126(Pt 21):4913–25, 2013.

[49] Noboru Mizushima, Beth Levine, Ana Maria Cuervo, and Daniel J. Klionsky. Autophagy fights disease through cellular self-digestion. *Nature*, 451(7182):1069–1075, 2008.

[50] Noboru Mizushima and Masaaki Komatsu. Autophagy: Renovation of cells and tissues. *Cell*, 147(4):728–741, 2011.

[51] Asa Birgisdottir and Terje Johansen. The LIR motif crucial for selective autophagy. *Journal of cell science*, 126:3237–3247, 2013.

[52] Tomonori Kimura, Michael Mandell, and Vojo Deretic. Precision autophagy directed by receptor regulators emerging examples within the TRIM family. *Journal of Cell Science*, 129(5):881–891, 2016.

[53] Carlas S Smith, Nikolai Joseph, Bernd Rieger, and Keith A Lidke. Fast, single-molecule localization that achieves theoretically minimum uncertainty. *Nature Methods*, 7(5):373–375, 2010.

[54] J. Lin, M. J. Wester, M. S. Graus, K. A. Lidke, and A. K. Neumann. Nanoscopic cell-wall architecture of an immunogenic ligand in Candida albicans during antifungal drug treatment. *Molecular Biology of the Cell*, 27(6):1002–1014, 2016.

[55] Johnny Tam, Guillaume Alan Cordier, Joseph Steven Borbely, Ángel Sandoval Álvarez, and Melike Lakadamyali. Cross-talk-free multi-color storm imaging using a single fluorophore. *PLoS ONE*, 9(7), 2014.

[56] Jason Yi, Asit Manna, Valarie A. Barr, Jennifer Hong, Keir C. Neuman, and Lawrence E. Samelson. madSTORM: a superresolution technique for large-scale multiplexing at single-molecule accuracy. *Molecular Biology of the Cell*, 27(22):3591–3600, 2016.

[57] Mike Heilemann, Sebastian Van De Linde, Mark Schüttpelz, Robert Kasper, Britta Seefeldt, Anindita Mukherjee, Philip Tinnefeld, and Markus Sauer. Subdiffraction-resolution fluorescence imaging with conventional fluorescent probes. *Angewandte Chemie - International Edition*, 47(33):6172–6176, 2008.

[58] Benjamin Groves, Yuan Jyue Chen, Chiara Zurla, Sergii Pochekailov, Jonathan L. Kirschman, Philip J. Santangelo, and Georg Seelig. Computing in mammalian cells with nucleic acid strand exchange. *Nature Nanotechnology*, 11(3):287–294, 2016.

[59] Yuan Jyue Chen, Neil Dalchau, Niranjan Srinivas, Andrew Phillips, Luca Cardelli, David Soloveichik, and Georg Seelig. Programmable chemical controllers made from DNA. *Nature Nanotechnology*, 8(10):755–762, 2013.

[60] Lulu Qian and Erik Winfree. Scaling up digital circuit computation with DNA strand displacement cascades. *Science (New York, N.Y.)*, 332(6034):1196–1201, 2011.

[61] David Yu Zhang and Georg Seelig. Dynamic DNA nanotechnology using strand-displacement reactions. *Nature Chemistry*, 3(2):103–113, 2011.

[62] Bernard Yurke, Andrew J. Turberfield, Allen P. Mills, Friedrich C. Simmel, and Jennifer L. Neumann. A DNA-fuelled molecular machine made of DNA. *Nature*, 406(6796):605–608, 2000.

[63] Florian Schueder, Maximilian T. Strauss, David Hoerl, Joerg Schnitzbauer, Thomas Schlichthaerle, Sebastian Strauss, Peng Yin, Hartmann Harz, Heinrich Leonhardt, and Ralf Jungmann. Universal Super-Resolution Multiplexing by DNA Exchange. *Angewandte Chemie - International Edition*, 56(14):4052–4055, 2017.

[64] Brian R. Wolfe, Nicholas J. Porubsky, Joseph N. Zadeh, Robert M. Dirks, and Niles A. Pierce. Constrained Multistate Sequence Design for Nucleic Acid Reaction Pathway Engineering. *Journal of the American Chemical Society*, 139(8):3134–3144, 2017.

[65] Brian R Wolfe and Niles A Pierce. Sequence Design for a Test Tube of Interacting Nucleic Acid Strands. *ACS Synthetic Biology*, page 141020092749006, 2014.

[66] Joseph N. Zadeh, Conrad D. Steenberg, Justin S. Bois, Brian R. Wolfe, Marshall B. Pierce, Asif R. Khan, Robert M. Dirks, and Niles A. Pierce. NUPACK: Analysis and design of nucleic acid systems. *Journal of Computational Chemistry*, 32(1):170–173, 2011.

[67] Fang Huang, Samantha L. Schwartz, Jason M. Byars, and Keith A. Lidke. Simultaneous multiple-emitter fitting for single molecule super-resolution imaging. *Biomedical Optics Express*, 2(5):1377, 2011.

[68] L Luengo Hendriks. DIPimage User Manual. *Imaging*, 49(1):20–7, 2011.

[69] C M Waterman-Storer, A Desai, J C Bulinski, and E D Salmon. Fluorescent speckle microscopy, a method to visualize the dynamics of protein assemblies in living cells. *Current biology : CB*, 8(22):1227–1230, 1998.

[70] Soichiro Yamada, Sabine Pokutta, Frauke Drees, William I. Weis, and W. James Nelson. Deconstructing the cadherin-catenin-actin complex. *Cell*, 123(5):889–901, 2005.

[71] Julia Riedl, Alvaro H. Crevenna, Kai Kessenbrock, Jerry Haochen Yu, Dorothee Neukirchen, Michal Bista, Frank Bradke, Dieter Jenne, Tad A. Holak, Zena Werb, Michael Sixt, and Roland Wedlich-Soldner. Lifeact: A versatile marker to visualize F-actin. *Nature Methods*, 5(7):605–607, 2008.

[72] Kevin A. Edwards, Maddy Demsky, Ruth A. Montague, Nate Weymouth, and Daniel P. Kiehart. GFP-moesin illuminates actin cytoskeleton dynamics in living tissue and demonstrates cell shape changes during morphogenesis in Drosophila. *Developmental Biology*, 191(1):103–117, 1997.

[73] Till Bretschneider, Stefan Diez, Kurt Anderson, John Heuser, Margaret Clarke, Annette Müller-Taubenberger, Jana Köhler, and Günther Gerisch. Dynamic Actin Patterns and Arp2/3 Assembly at the Substrate-Attached Surface of Motile Cells. *Current Biology*, 14(1):1–10, 2004.

Appendix A

Optical Alignment

1. sCMOS focus: Attach a 150mm lens by an adjustable lens tube to sCMOS camera. Image a far object to make sure that your lens in at the right place from the camera and sCMOS shows a focused image of the far object. Afterwards fix the lens distance from the camera. This is the first adjustment with respect to sCMOS. Notice that detector plate is 17mm behind the camera adapter.

2. Build a collimator: Put a fiber coupler in a XY translator and attach a 75mm lens via a cage to it. Adjust the distance of the lens so the light gets collimated. Test collimation by putting light on a far wall and checking the beam size along the way.

3. Collimate light: Attach a fiber that has a laser coupled and align the z-position of the 75mm lens such that the out coming beam is collimated.

4. Attach collimator to microscope: Take objective out of its place and attach the collimator cage via a lens tube to the mirror below the objective. Attachment needs to be solid and sturdy. Attach a fiber to the fiber cap in the collimator.

5. Mirror Position and beam height: The most important thing in the microscope alignment is the correctness of the height (adjusted at 75 mm from the surface of the table) and angle of light (should be parallel to the holes on the table in the direction of emission path) with respect to the mirror placed under the objective. This mirror should be positioned the way that light reflects from it from the collimator so that the reflected light has the same height and angle all the way through the emission path. This adjustment is needed before anything else. And when this is done, all emission optics can be added and be checked. (This is correct for excitation path too. When the work with emission path is done, excitation path should be built around the collimator laser light. So you never adjust the light with respect to your emission or excitation optics but you do otherwise. Everything is adjusted based on the light you have correctly reflected from that mirror.)

6. Dichroic placement: Attach the rectangular dichroic mirror on a FFM1 Thorlabs cap that does not have any adjustment possibility (since a cap with adjustable springs will cause some drift later). Take out the dichroic mirror (that reflects the 647 nm light) out of the intersection of excitation and emission pathway. This dichroic reflects 647 nm light and passes fluorescent light emitting from the fluorophores that has a longer wavelength (but keep the dichroic mirror at the intersection of emission path and IR camera path in the place. We want to have it there when we adjust our paths. It passes the laser light.). When dichroic is in place, we can check excitation path and when it is out, we can check emission path. We first check the emission path.

7. Emission filter: Take the emission filter out of the emission path. It sits after 175 mm tube lens.

8. Emission path alignment: Align the laser light that comes out of the collimator at the direction of emission path.

First: in doing this alignment is to make all cages along the path to have the same height and be perpendicular to the light path. So applying the couple screws scheme on the table will help to have cages perpendicular to the emission path. It will look as following:
Second: use two targets along the emission path. One after the place of 175 mm tube lens and one after the place of first 150 mm lens. Light should hit the center of both targets. Align laser with 3 adjusters of the mirror below objective such that it is centered and straight in the emission path.
Strategy:
First check the emission path without any lenses in it. Then put the 175 mm tube lens and check the focus of light afterwards, then put the 150 mm lens and check the collimation afterwards, then put the second 150 mm lens and check the collimation again after that lens.
General note: Align closest target with vertical position adjuster and middle adjuster, align farthest target with horizontal and vertical adjusters. If a little error remains in the vertical adjustment, fix the mirror position and adjust the cage to make sure the beam is centered and straight through that.

9. Put dichroic mirror back in:
Put it back and now check again and adjust the emission path again if it changes because of dichroic mirror.

10. Adjust excitation path:
Check the excitation path by measuring the height of the beam that reflects from the dichroic mirror. Beam should be perpendicular to the emission path and should have the same height and angle all the way. Take out all optical elements along excitation path. Using dichroic cap adjust the angle and tight the cap in its place. Put the 175

mm tube lens in place and check it the light is still centered. If the answer is yes, put the excitation filter in and then the 100 mm lens in. After the 100 mm lens the beam should be collimated. Check if it is centered and has no angle. If it doesn?t have the same height, it is not hitting the center of one of the lenses in the path. So check the height again to hit always the center of the lenses. Next put the 50 mm lens in. Now put the iris 100 mm away from the 100 mm lens and 175 mm away from the tube lens. Iris represents an image plane from the sample plane. Next put the 50 mm lens behind 100 mm lens. Light should be centered. Now put the z-translator and xy-translator attached to the movable lens in its place. This lens is going to be face to face with tip of the metal fiber.

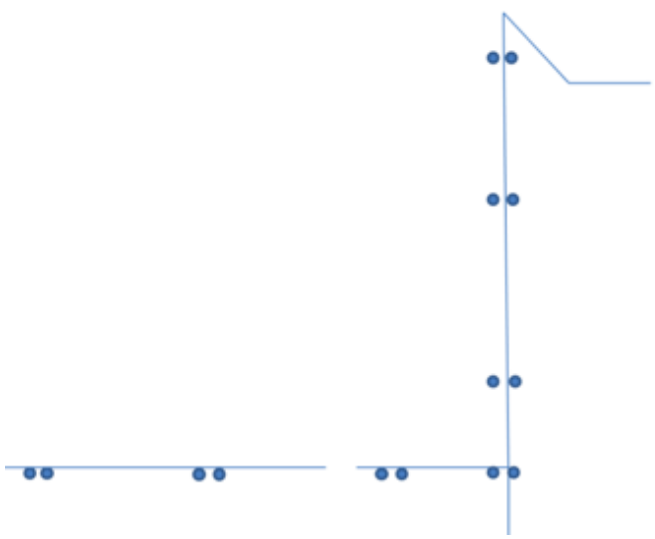

Figure A.1: Alignment using double screws on optical table

11. Take off the collimator:

Now take off the collimator cage from the objective holder.

12. Turn on 647 fiber laser and optimize fiber coupling efficiency:
Turn 647 nm Laser on and send the light through the fiber into the excitation path. Check the light coming up from the objective hole. If it?s not centered, use XY-translator to center it. Check the beam on the ceiling above the microscope and also using a DG10-1500-H1-MD (Φ 1.0 inch 1500 GRIT with center hole from Thorlabs). If beam is not centered when entering objective, PSF will not be symmetric which causes problems when taking data. Now there is a problem of power adjustment. We want high efficiency for coupling 647 light into the fiber. To this end, best way is to first not to have diffuser in the pathway, but to have all other elements. So by adjusting the lens before diffuser and the lens before the fiber at the same time, and with playing with the mirrors, we can get the highest possible efficiency.

13. Adjust the excitation circle size:
We want a specific size for our excitation circle. We want when the iris in excitation path is fully open, the circle to cover a 256×256 region. Calculations related to having our excitation circle to cover this region are done based on magnification of lenses.

14. Size and correct alignment test:
a good test would be to have a dense sample of cells and label the cells with for example anti-Clathrin-AlexaFluor647. Then turn the laser on and choose the full ROI of the sCMOS, so we have a 2048×2048 region. Now we can see the cells and the region with the power will start to blink. Now the size of blinking region should be of the full ROI when the iris on the image plane of the tip of the fiber on excitation path is fully open. Following is an example of having problem in size and in alignment.

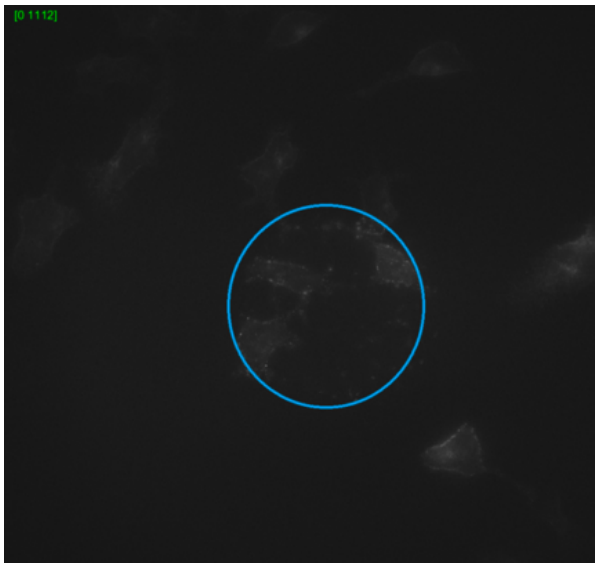

Figure A.2: Wrong power distribution

Here our alignment problem is that the circle of blinking is not at the center of the 2048×2048 region. Size problem is that the size of this circle is too big and of course is much bigger than 1/64 of the full ROI. Third problem is that although while we turn on the diffuser we see a sharper edge of the region that starts to blink comparing with neighboring regions but we still can see the neighboring cells that are not supposed to be seen.

15. Uniformity of excitation illumination beam (Top Hat illumination):
We need to have uniform illumination inside the circle of excitation light on the sample. I use 3.5uL of AlexaFluor647 dye in water with 11uM concentration between a 25mm round coverslip and a 18mm round coverslip, sealed with nail polish. I try to have only a single layer of dye on the sample to get a better focus and less scattering Images are for the case of diffuser off and on, both of a single sample at focus. I also use an iris in the excitation path at the image plane of the tip of the fiber, with 175mm distance before tube lens, to have sharper edges. Now we need to check for

the efficiency of coupling into the MM-fiber again. When we adjust Top hat profile we should not touch the optics before the fiber otherwise we would harm the efficiency badly. So it can be tuned toward better results by changing the optics after the fiber (50 mm lens and the 9 mm lens after fiber): 4.5 uL of 11uM AlexaFluor647 on a 25mm coverglass under 18mm coverglass:

16. StepperMotor home position:
You need to check three things: the home position of the stepper motor vs. position of the objective vs. position of the center of your GUI (which is button [5,6] or [6,5]). Ideally these three should be on top of each other and be the same. However based on physical positioning of your objective holder vs. NanoMax stage which are not physically connected, and space limitation on your optical table and setup, you might not be able to design everything around home position (0,0,2). So the reasonable design in this condition would be the one that positions the objective at the center of the sample holder circle as the microscope class MIC−SeqSRCollect.m starts running. Here we have two coordinate systems. First we have XY system which is based on marked vectors on the NanoMax stage by the company. Second we have XY-prime system which is based on the readout of our MIC−StepperMotor.m code written to control the 3-axis stepper motor. Red circle represents the hole in 25 mm round sample holder which we need our objective to be placed at the center of. The green square shows the movement area of the stepper motors in 2D which extends from -4 to +4 mm. Purple Square represents the region used by our GUI with 100 buttons. What we need is to have center of this square on the center of the circle. When we first setup the system, the general form is one like the figure above so it needs adjustment to get the needed result.

17. Rotation issue with MATLAB:
Based on MATLAB definitions, it counts Y as row and X as column and when ad-

dressing a pixel in the image, it addresses as (Y,X), and we should be aware of that. Also, when we take a picture with our camera, the picture appears on screen with a rotation. So there are two things we need to consider. So when we click on the taken image in the process of Auto collect, we are choosing a location that will be rotated and mirrored with respect to the live image, so we need to find the shift accordingly when we want to move the ROI from a 2048×2048 to a 256×256 for each selected cell. This issue needs to be taken care of inside the exposegrid() function inside MIC−SeqSRCollect.m. We have two mirrors between sample and sCMOS in our new setup so we have two reflections which imply two times change in coordinates from our sample to our camera.

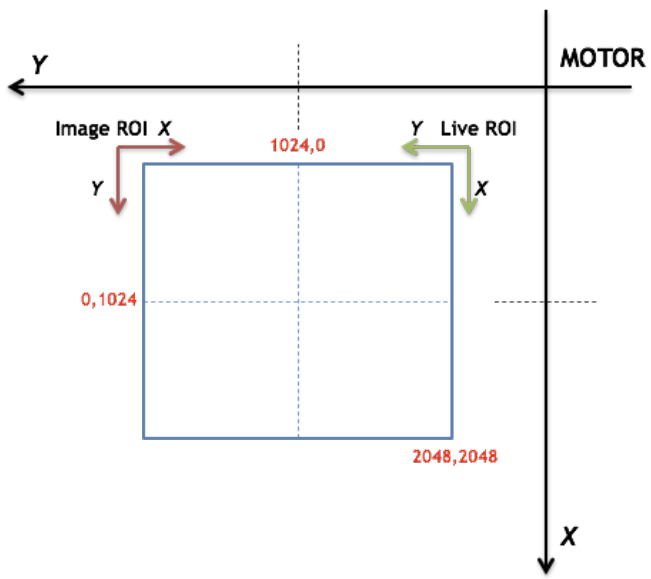

Figure A.3: sCMOS ROI directions vs. Stepper motor

18. As shown in the figure above, to fix the problem we need to change the function exposeGridPoint() under MIC−SeqSRcollect.m; In this function we click on an image and go camera should give a 256×256 ROI centered at that position. So

Stepper motors need to move from the coordinates of the center of each GUI button (each OldPos) to a new position which is the clicked position of the cell with respect to motor reference origin. By changing the code to the one presented above, this problem is solved. Here as we click, an X,Y is produced with respect to the Image ROI (not live ROI) which is calculated from top left corner of the image ROI (red coordinate system). Best way to prevent confusion about this adjustment is to bring up the live ROI, consider a cell, and move that cell to the center of the live ROI using the GUI for stepper motors. Now read the position from the GUI and close the live image, click on the related SEQ GUI button, and on the upcoming image click on the same cell and measure the deltaX and deltaY from the code (deltas show the distance from the center of image, calculated based on image ROI coordinates), so now put the deltas back into the Stepper motor GUI and bring up the live image again and check if putting the found deltas into the jog size can move your chosen cell to the center. If yes, just figure out the signs for moving in X and Y (if you have to click on $-X$ or $+X$ to go to the center- the same for Y) and put that into the code to find NewPos for X and Y based on OldPos and deltas. Since each of the four regions in the image have deltas with different sign, you need to put 4 conditions here. All this is done in the piece of code above.

19. Finding and imaging a cell after saving reference image:
This is the part we click on Autocollect button of the GUI. Main function in use here is align2imageFit() which leads to function Findzpos().

20. Cross-Correlation of the reference image and Z-stack of current position, and how it is done using Stepper motors and Piezo stage:
We take a reference image when we choose each cell and that image is saved in a RefStruct which has the intensity matrix representing the image as well the x,y,z position of the motor at the place where the cell is. When we go back to find the cell

and image it by clicking on Autocollect button of the GUI, stepper motor takes us almost to the saved position of the cell and a stack of images along z-axis is taken. Then there is a cross-correlation between the reference image and the z-stack:

$$cc = abs(ifft2(fft2(Current).*conj(fft2(Ref))))$$

cross-correlation value depends on the placement of the cell at X,Y,Z. if you can find the same Z but your X and Y is a bit different, left hand side value of the above equation will drop from 90% to 40% and lower. So it does not matter that the cells look the same but also the placement in XY should be the same to get a good cross-correlation value which is very important to image the same place for next rounds of labeling.

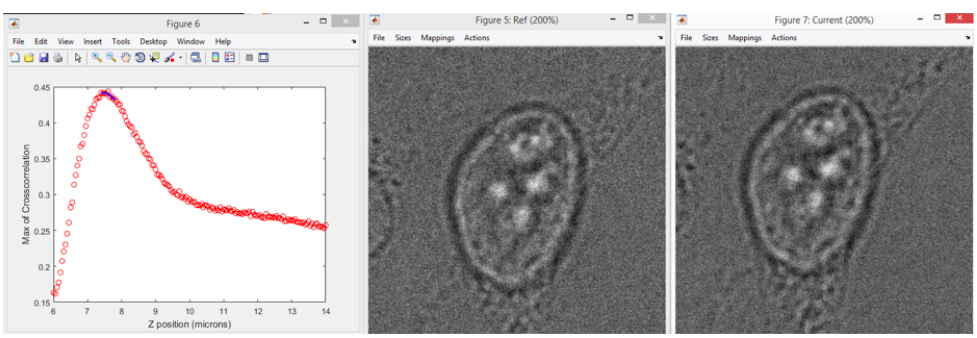

Figure A.4: Importance of noise when taking a reference image

21. Note on noise:

An important point is there should be low noise when taking reference and current image stack so you get a higher cross-correlation coefficient. Otherwise you will get bad coefficient. To get less noise you need a higher exposure time since it gathers more signal. As you see in an example in the following images, here X and Y are not the same (-10.8 and -12.6 difference in pixels) and images are noisy so we get a

low cross-correlation peak. Here the exposure time for capturing an image is 10 msec on sCMOS camera. This step is essentially done by Piezo stage, so let?s not have anything to do with Stepper motor for fine adjustments. Stepper motor has only 4 digits after the point which means it can work to the limit of 10^{-4} mm which is 100 nm. So for fine adjustments we need to use Piezo stage which can even go to 1 nm (while better to keep it at 5 nm limit). This step is essentially done by piezo stage, so lets not have anything to do with Stepper motor for fine adjustments. Stepper motor has only 4 digits after the point which means it can work to the limit of 10^{-4} mm which is 100 nm. So for fine adjustments we need to use Piezo stage which can even go to 1 nm (while better to keep it at 5 nm limit).

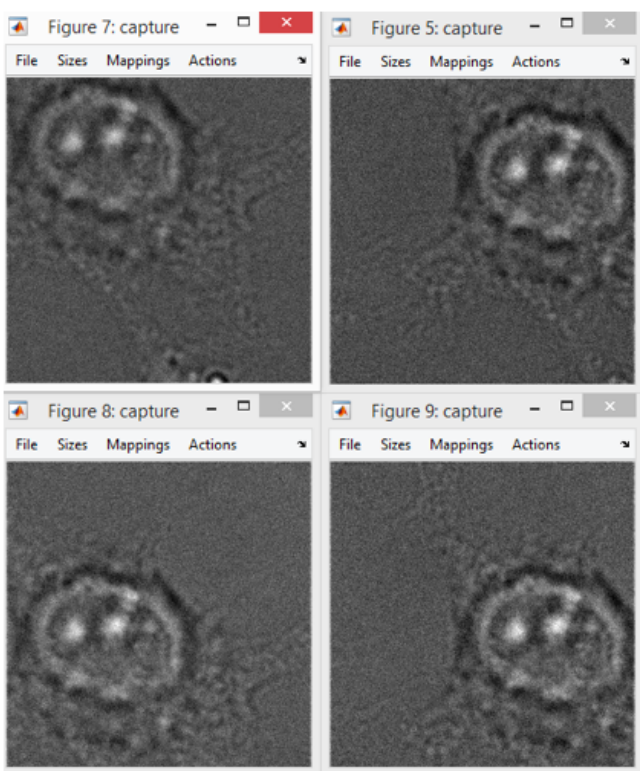

Figure A.5: Calculating the proper shift when moving the sample around by piezo stage

22. Calculating delta for each of the regions in the 256×256 ROI, we find out how we should shift a cell in XY plane in each of these four cases to have a better match and higher cross-correlation coefficient between the reference and current image (taken in the form of a Z-stack after using stepper Motor to re-find the saved position of a reference cell, and then the most likely z plane taken out of the z-stack and used to find the XYshift now). Applying XYshift is all with Piezo stage and not the motor: maximizing cross-correlation is done by piezo, since this fine tuning is out of precision of stepper motor. Here is a comparison of noise between a capture of 10 msec (left) and one of 200 msec (right).

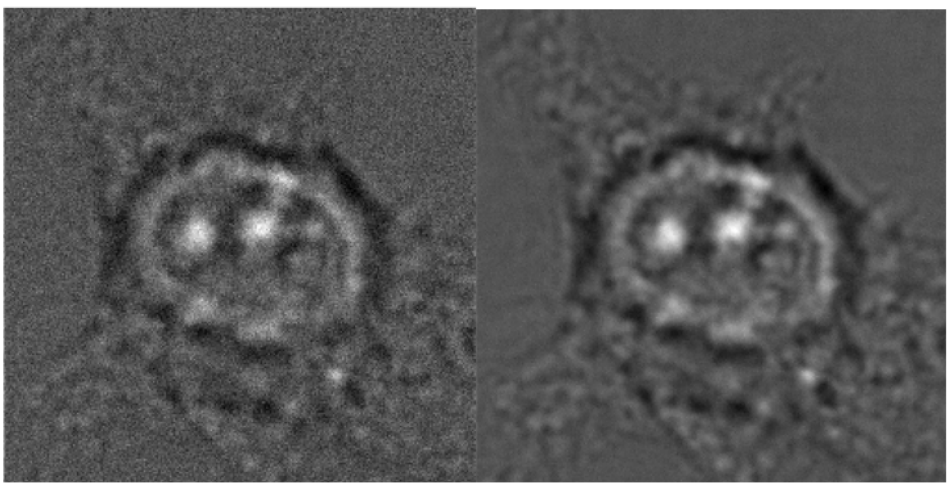

Figure A.6: Noise in IR camera

Positions of motor and piezo with respect to each other, and shiftXY signs:

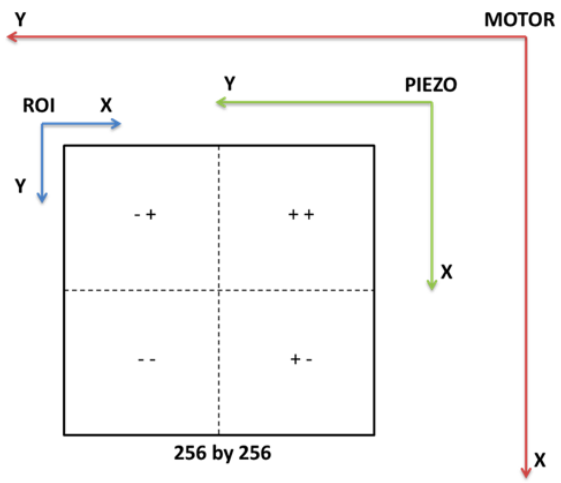

Figure A.7: Piezo stage calculation of delta

23. IR sCMOS camera takes image using startcapture() function and they are in dipImage format and puts them in work space of MATLAB with name capture, so you can use the function dip−array(capture) to find the values and plot the histogram and figure out the effect of exposuretime on contrast.

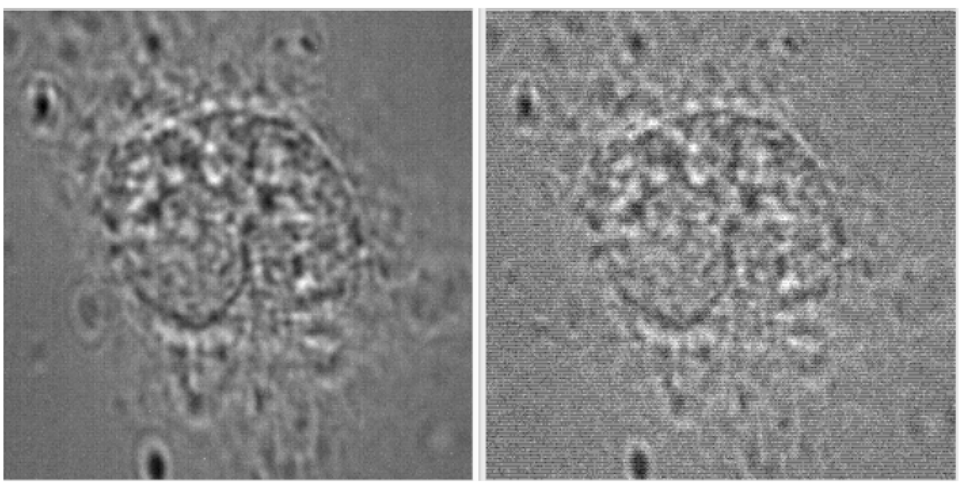

Figure A.8: Left: exptimeCap=1, right: 0.1.

Dynamic range on left is from 83 to 135 and on right from 9 to 15 in a 255 scale (8 bit). Here we still don?t have a great range in our left image.

24. A 2 step systematic test to see the problems:
You need to test two things: 1- if the registration is working 2-if stabilization is working To test 1, as microscope goes to image the same cell for new label, look to see if reference images taken are on top of each other or not. If not, your registration has problems. To test2, look at the accumulative drift in each data set for a specific label number. If the accumulative drift is not compensated and corrected, your active stabilization has problems.

25. Characteristic Drift in Y direction:
There is a specific drift in Y direction that is due to physical shape of the holder probably and can ruin the experiment if not controlled by the Active−Reg3D code. Plot is from a 20,000 frames data taken AR13 folder, cell1−label2. Here what we see is that using P-only controller, the cumulative correction is catching up with x drift (which is always non-zero with a constant offset). For z component as we see it is moving up and down zero and there isnt a specific offset like X. Z is also taken care of, but the Y drift is bigger than the jump allowed for correction so it can?t be compensated. What is needed is to adjust this corrective jump size. But generally the PI-controller will work much better. Result is the following drift image that shows a 1 nm/sec.

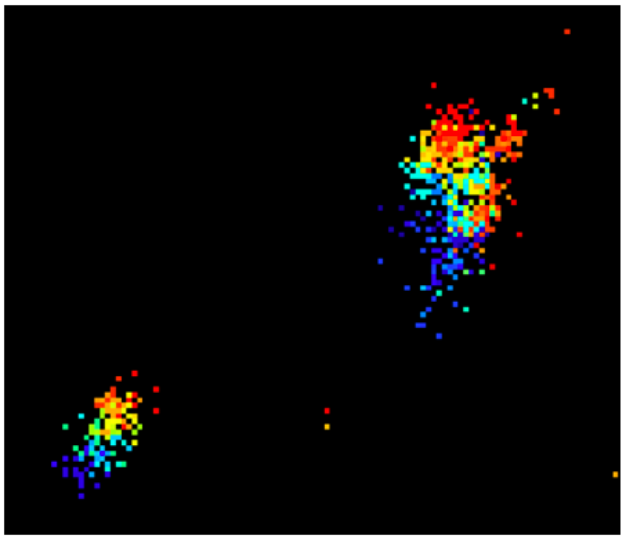

Figure A.9: Sample drift

26. Convergence and Overlay image:

There is a convergence condition when finding the cross-correlation peak. If the overlay image has red, it means there is a shift between reference and current image. Convergence is under MIC−SeqReg3DTrans() under align2imageFit() function.

27. Active Stabilization as taking the data:

Check your back projected pixel size here. You need to have a 100-150 nm bpp, so adjust your optics before the IR camera based on this fact. P-only controller cannot work perfectly for all cases. Sometimes the jumps are too big for the stage to be able to follow since there is a maximum hard-coded for the jump step size. So it is a necessity to develop a PI-controller. Here a problem that can cause the drift is change in temperature and its different effect in X,Y,and Z directions. For this problem, other than the PI-controller we need to have a good coverslip holder that has a small thermal expansion but right now we use Aluminum which has a big thermal expansion. I want to replace that with Invar alloy which is a mixture of Iron

and Nickel which has a very small thermal expansion coefficient.

28. Alignment of the IR camera:

What we want is to have the same cell at the center of both camera ROIs of 256×256 pixels when we are imaging them. To have a good alignment we need to have a fixed cap on the IR-filter cube holder that attaches to the IR filter and doesnt have any adjustable springs. Springs will make it easier to adjust but then they create their own drift which makes things complicated and needs to be checked each few days. Now having a fixed cap causes a bit problem since it is hard to adjust it exactly when camera gets connected to the cube solidly. For this purpose I disconnected them and did the adjustments.

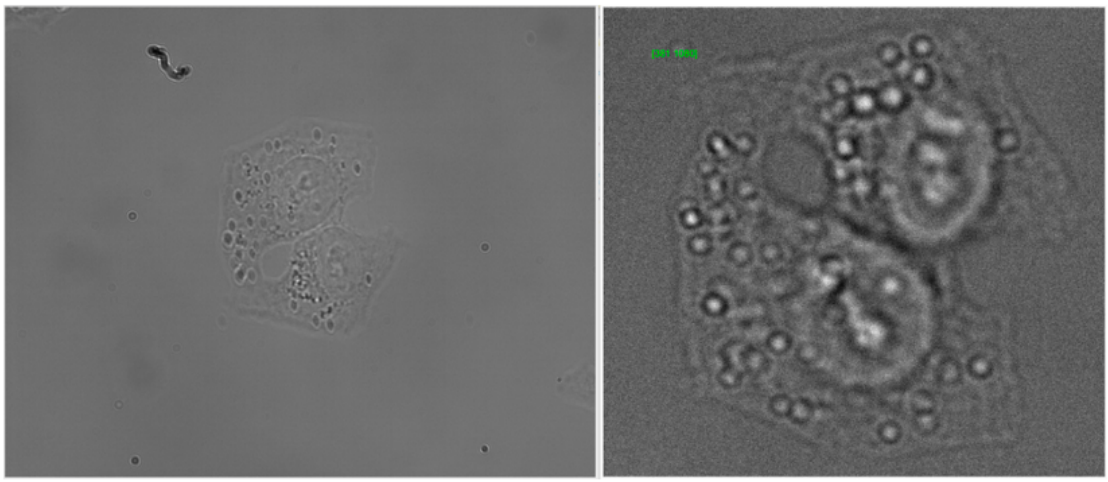

Figure A.10: Y drift

29. Impulse Response function of Piezo stage:

Here we use a bead to show how piezo stage moves. By taking data of the bead as the stage is moving, we see a pattern for a jump. We use piezo for active stabilization and cross-correlation calculations so this is important to know.

Appendix B

Efficiency of the Microscope

Efficiency of a microscope is defined as the ratio of the number of photons used to localize single molecules in a single frame, to all the photons emitted from the sample in all directions during that frame.

There are three factors effective in calculating the efficiency of the microscope. First is the objective aperture acceptance ratio which is calculated as seen in the following equation: $d\Omega=\sin\theta d\theta d\phi$ where $\Omega = \int d\Omega=(1-\cos\theta)/2$ where Ω is shown in Figure B.1 as the acceptance angle into the objective lens. Angle θ can be found from $N_a=n\times\sin\theta$. For our oil immersion objective lenses of 60X and 100X, we have respectively a numerical aperture of 1.35 and 1.49, and since the refractive index of the oil is 1.51, we get respectively θ=63.4 degree and θ=80.7 degree which produces the acceptance of %27.6 and %41.9.

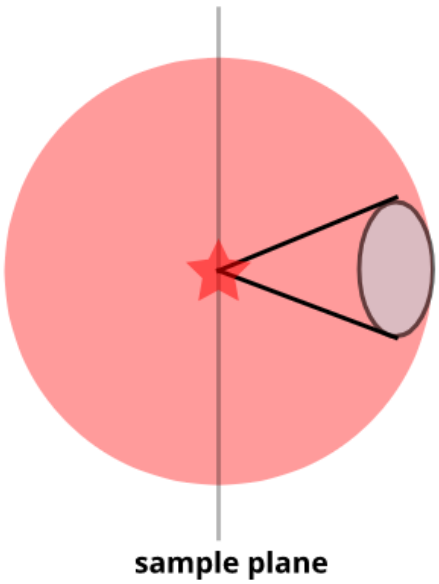

Figure B.1: Objective lens acceptance angle. An emitter on the sample plane, emits light in every direction, and the objective lens can only gather a rather small part of it.

Second factor is the loss of light that happens through optical elements between the objective lens (that is taken out for our measurement) and the camera sensor. To measure this factor, we use a collimator (as described in Appendix A) and via optical fiber, send through it the optical power of 1 mW from a 638 nm diode laser. We then use a multi-meter to measure the power after specific optical elements in emission path, as described here (note that I have taken out the first dichroic since it reflects the laser light):

1- after second beam splitter (a short-pass filter), right before the tube lens: 0.989 mW.
2- after the tube lens: 0.987 mW.
3- after the second mirror before the sensor: 0.984 mW.

4- at the sensor: 0.982 mW.

So almost %2 of light is wasted by the optical elements after the objective lens and before the sensor. For the emission light, it would be one to two percent more, based on the spectrum of the filters, so we take it as %4.

Third factor is the quantum efficiency of the sensor which is wavelength dependent and is shown in shown in Figure 2.26, and for the 670 nm emission wavelength of AlexaFluor647, we have a QE=%75. So altogether, for a 60X objective we get %27.6×%96×%75=%19.9, and for 100X objective we get %41.9×%96×%75=%30.2. This result is yet another reason that we better have the 100X design.

Appendix C

Cell Fixation and Labeling

This fixation protocol is developed by Dr. Chris C. Valley, a former postdoc at Dr. Diane Lidke lab. This is the standard protocol that I use when fixing cells to image with sequential or TIRF microscope. For the specific case of imaging actin on the SPT microscope, another better suited protocol is used that instead of PBS, uses cytoskeleton buffer. The optimization for cytoskeleton buffer is done by Hanieh Mazloom Farsibaf and the effects of this buffer on Osmolarity etc., can be found in her dissertation. Cells are ordered and plated through cancer research facility building (CRF) and I thank Shayna Lucero for preparing the samples for our lab. The fixation protocol is as follows:

1- HeLa/RBL cells plated at 20,000 cells/well (8-well chamber slide) or 225,000 cells/well (6-well plate with 20mm coverslip).
2- allowed to adhere overnight (12-16 hrs).
3- wash once with PBS at 37C.
4- two step fixation:
0.6% Paraformaldehyde, 0.1% Glutaraldehyde, 0.25% Triton X-100 for 60 seconds
4% Paraformaldehyde, 0.2% Glutaraldehyde, 1.5 to 2 hrs for standard imaging with

TIRF microscope and 2 to 2.5hrs for sequential imaging.
5- wash 2x with 1X-PBS
6- 0.1% NaBH 4 treatment for 5 to 10 minutes
7- wash 2x with 1X-PBS
8- 10mM Tris for 5 to 10 minutes
9- wash 2x with 1X-PBS
10- block in PBS + 5% BSA + 0.05% Triton X-100 for 15 minutes
11- store cells in PBS + 0.05% sodium azide at 4C

Labeling protocol for different structures are developed in our lab based on results from super-resolution experiments. The following shows the labeling strategies for most common structures that I used in this dissertation. For actin, the labeling strategy with lifeact can be found in Chapter 5. All labeling steps have to be done after fixing the cells. One important note about the labeling protocols is, each protocol needs to be optimized based on the nature of the experiment one is preparing to do.

αtubulin:
1- wash once with PBS
2- incubate with 2.5 ?g/ml anti-?-tubulin-AlexaFluor647 in 2% BSA, 0.05% Triton X-100 for 30 to 60 minutes
3- wash 3 x 5 minutes with 2% BSA, 0.05% Trition X-100
4- wash once with PBS

βtubulin:
1- wash once with PBS
2- incubate with 15 ug/ml anti-β-tubulin-AlexaFluor647 in 2% BSA, 0.05% Trition X-100 overnight at 4C

3- wash 3 x 5 minutes with 2% BSA, 0.05% Trition X-100
4- wash once with PBS

TOM 20:
1- wash once with PBS
2- incubate with 5 ug/ml anti-?-tubulin-AlexaFluor647 in 2% BSA, 0.05% Trition X-100 1 to 2 hour or overnight at 4C
3- wash 3 x 5 minutes with 2% BSA, 0.05% Trition X-100
4- wash once with PBS

Actin:
1- wash once with PBS
2- incubate with 3:40 dilution of phalloidin-AlexaFluor647 stock in PBS for 30 to 60 minutes 3- wash once with PBS

The standard imaging buffer we use is STORM buffer containing TNG, OSB, and MEA. Imaging buffer is a crucial aspect of achieving good results in an experiment. Here I provide the receipts for material in the buffer.

TN to make the OSB:
1- 50 ml of 50 mM Tris, 10 mM NaCl, PH 8.0
2- add 2.5 ml 1M Tris
3- add 0.5 ml 1M NaCl
4- add 47 ml DI water
5- add 150 ul HCl at 12 N to adjust the PH

TNG buffer:
1- 50 ml of 50 mM Tris, 10 mM NaCl, 10% (w/v) glucose, PH 8.0

2- add 2.5 ml 1M Tris

3- 0.5 ml 1M NaCl

4- 47 ml DI water

5- 5 gr glucose

6- 130 ul HCl at 12 N to adjust the PH

MEA buffer:

1 Molar stock buffer Cysteamine hydrochloride, Cat No M6500-25G, Sigma-Aldrich. Molecular weight is 136.1 gr/mole.

1- weight out 0.568 g MEA powder.

2- add the powder to a 15 ml tube.

3- add 4 ml DI water in the tube.

4- add 10 drops of NaOH at 10 N.

5- add more DI water to fill the buffer to 5 ml.

The final concentration of the MEA buffer is 1M, PH at 8.5.

Note: The MEA buffer need to be prepared every week, the old MEA buffer should be disposed in the MEA waste bottle in room 118.

OSB buffer:

Glucose oxidase from Aspergillus niger, Cat No. G2133-50KU, Sigma-Adrich. Reaction unit is 196.6 u/mg. Catalase from bovine liver, Cat No. C9322-1G. Reaction unit is 2000 - 5000 u/mg.

1- calculate the weight of powered to be measured:

Note that the reaction unit might vary from each order, always check the reaction unit when open a new bottle. The reaction unit for catalase is not a fixed value, so the above calculation uses the average value.

2- measure the calculated amount of powder on a scale, the tip is: use a 1.5 ml centrifuge tube, first weight out the glucose oxidase to around 8.6 mg, then add catalase

in the same tube, increase the weight up to 12.6 mg.

3- print label for the powder mixture and stick it to the tube.

4- put the labeled tube in the freezer.

The OSB buffer is made by adding 1 ml of 50 mM Tris, 10 mM NaCl, PH 8.0 in the tube with the powder mixture. Because the catalase usually contains small organelles, it is important to filter out those organelles so:

5- put the OSB buffer in a centrifuge, set the speed to 10 rpm and time to 5 min, then hit start.

6- extract the clear liquid on top and put it in another 1.5 ml tube.

7- Repeat steps 1 and 2.

Appendix D

Part List

Here I give the complete part list for the microscope which contains optical, mechanical, and electronic elements listed by vendor.
By Thorlabs:

1	AC080-010-A-ML	achromat doublet with f=10 mm, ϕ8 mm, M12 $\times$ 0.5
2	AC127-019-A-ML	achromat doublet with f=19 mm, ϕ1/2 inch, SM05
3	AC127-025-A-ML	achromat doublet with f=19 mm, ϕ1/2 inch, SM05
4	M105L02S-A	ϕ105 um, 0.22 NA, SMA905-SMA905 AR-Coated
5	POLARIS-K1	Low Drift ϕ1 inch mirror mount with 3 adjusters
6	BB1-E02P	ϕ1 inch back side polished broadband dielectric mirror
7	AD9T	ϕ1 inch OD, adapter for ϕ9 mm optics, internally threaded 0.38 inch
8	LMR05S/M	ϕ1/2 inch lens mount with internal and external SM05 thread, M4 Tap
9	CSV4	Hook and loop fastener cable straps with 1/4 inch (M6)
10	CS1	Screw-on cable straps
11	CMS010	cable tie bases for 7.6 mm (0.3 inch) wide ties

12	CMS011	releasable cable ties, 7.6 mm (0.3 inch) wide
13	XE25W3	quick corner cube for 25 mm rails
14	SH6M10LP	M6×1.0 low-profile channel screws
15	SM05SMA	SMA fiber adapter plate with external SM05 (0.535-40 inch)
16	CP11/M	SM05-threaded 30 mm cage plate, 0.35 inch thick, M4 tap
17	AC254-150-A	f=150 mm, ϕ1 inch achromatic doublet, ARC: 400-700 nm
18	-DMM1/M	fixed mount for ϕ1 inch D-shaped mirrors
19	BB1-E02	ϕ1 inch broadband dielectric mirror, 400-750 nm
20	MAX341/M	3-Axis NanoMax, closed loop piezo and stepper motor
21	BSC203	Three-channel APT benchtop stepper motor controller
22	TLD001	T-cube laser diode controller
23	LDM9T/M	laser diode mount with integrated temperature controller/metric
24	RBX32/M	Rack box chassis with slide out rails,M6-tapped bradboard
25	TPZ001	T-cube 150V piezo driver
26	TSG001	T-cube strain gauge reader
27	ST1XY-D/M	XY translator with differential drives
28	LEDD1B	T-Cube LED driver with 1200 mA max drive current
29	M660L3	Deep red mounted high power LED, 1200 mA
30	M850L3	IR mounted high power LED, 1000 mA
31	CXY1	30 mm cage system, XY translating lens mount for ϕ1 inch optics
32	CM1-DCH/M	30 mm cage cube with dichroic filter mount

33	KCB1	right angle kinematic mirror mount, 30 mm cage system, SM1
34	TPS002	15V/5V power supply unit for up to 2 T-cubes
35	CFH2/M	30 mm cage system stackable filter holder for ϕ1 inch optics, with plate and holder
36	PAA622	APT piezo electric feedback converter cable, Male D-type to female LEMO connectors
37	B4C/M	kinematic cage cube platform for C4W/C6W
38	CRM1/M	cage rotation mount for ϕ1 inch optics, SM1 thread, M4 tapped hole
39	HL6366DG	f=3.3 mm, NA=0.47 mounted rochester aspheric lens, 400-700 nm
40	KS1	ϕ1 inch precision mirror mount with 3 adjusters
41	A110TM-A	6.24 mm, NA=0.42, mounted rochester aspheric lens, 400-700 nm
42	A230TM-A	4.5 mm, NA=0.54, mounted rochester aspheric lens, 400-700 nm
43	BB1-E02	ϕ1 inch broadband dielectric mirror, 400-700 nm
44	C1026/M	30 mm cage clamp for ϕ25 mm posts
45	AC254-150-A	f=150 mm achromatic doublet with ϕ1 inch, 400-700 nm
46	CAB400	cable for laser diode current controller
47	AC080-020-A-ML	f=20 mm, ϕ8 mm achromatic doublet, M12$\times$0.5 threaded mount, 400-700 nm
48	SM1D12D	Ring-activated SM1 iris diaphragm
49	C4W	30 mm cage system cube, 4-way
50	CFH2-F	filter holder insert for ϕ1 inch optics for use CFH2
51	FFM1	cage compatible dichroic filter mount
52	C4W/CC	30 mm cage cube connector for C4W series

53	SM1B3	ϕ1 lens tube, 1.1 inch to 4.7 inch long
54	RS4P/M	ϕ25 pedestal pillar post, M6 taps, length=100 mm
55	PAA100	drive cable for piezo actuators, 3 m long
56	SM1V10	ϕ1 inch SM1 lens tube, 1 inch long, external thread
57	E09RMS	Extended RMS to M9×0.5 adapter
58	LA1805-B	N-BK7 plano-convex lens, ϕ1, f=30 mm, 400-700 nm
59	E06RMS	extended RMS to M9×0.5 adapter
60	SM1V05	ϕ1 inch SM1 lens tube, 1 inch long, external thread
61	RS150/M	ϕ25 mm pillar post extension, M6 taps, length=150 mm
62	ER4-P4	case assembly rod, 4 inch long, ϕ6 mm
63	RS3P/M	ϕ25 mm pedestal pillar post, M6 taps, length=75 mm
64	SM1FC	FC/PC fiber adapter plate with external SM1 (1.035 - 40 inch) thread
65	SM1P1	external SM1 thread to ϕ1 inch optic mount adapter
66	ER3-P4	cage assembly rod, 3 inch
67	SM1L30	SM1 lens tube, 3 inch thread depth, one retaining ring included
68	TPS001	15V power supply unit for a single T-cube
69	TR40/M-P5	ϕ12.7 mm×40 mm stainless steel optical post, M4 stud, M6-tapped hole
70	RS2P4M	ϕ25 mm pedestal pilar post, M4 taps, length=50 mm
71	ER2-P4	cage assembly rod, 2 inch long, ϕ6 mm
72	PH20E/M	pedestal post holder, spring-loaded hex-locking thumb-screw, L=25 mrr
73	PH30E/M	pedestal post holder, spring-loaded hex-locking thumb-screw, L=34.7 mrr
74	TR30/M-P5	ϕ12.7 mm×30 mm stainless steel optical post, M4 stud, M6-tapped hole

75	S1TM12	SM1 to M12×0.5 lens cell adapter
76	SM1RC/M	ϕ1 inch (SM1) series slim lens tube ring, M4-tapped hole
77	SM1A6T	adapter with external SM1 thread and internal SM05 thread, 040 inch thick
78	SM1T2	SM1 coupler external thread, 0.5 inch long
79	SM1A9	adapter with external C-mount thread and internal SM1 thread
80	B1C/M	blank cover plate with rubber O-ring for C4W/C6W
81	SM1A3	adapter with external SMA thread and internal RMS thread
82	CP02/M	SM1-threaded 30 mm cage plate, 0.35 inch thick, 2 retaining rings
83	SM1AB1	ϕ1 smooth bore to internal SM1 thread adapter
84	SM1AB2	ϕ1 smooth bore to external SM1 thread adapter
85	CA2912	SMA coaxial cable, SMA male to SMA male, 12 inch (304 mm)
86	SM1M10	SM1 lens tube without external threads, 1 inch length, with two retaining rings
87	SM1L05	SM1 lens tube, 0.5 inch thread depth, with one retaining ring
88	SM1L03	SM1 lens tube, 0.3 inch thread depth, with one retaining ring
89	RA180/M	post end clamp, M6 stud and fixed 90 degree clamp
90	CF125	small clamping fork, 1.25 inch counterbored slot, universal
91	RS10M	ϕ25 mm pillar post spacer, thickness=10 mm
92	RS7M	ϕ25 mm pillar post spacer, thickness=7 mm
93	SH6MS12	M6×1.0 stainless steel cap screw, 12mm long

By Optotune:

94	88-392	17 degree diffusion angle, 5 mm CA laser speckle reducer, VIS

By Edmund Optics:

95	49-656	9 mm Diameter ×12 mm EFL aspherized achromatic lens

By 80/20:

96	25-2576	50 inch of 25 mm×75 mm T-slotted profile-eight open T-slot
97	25-2576	34 inch (863.6 mm) 25 mm×75 mm T-slotted profile-eight open T-slot
98	25-2576	36 inch (914.4 mm) 25 mm×75 mm T-slotted profile-eight open T-slot
99	25-4134	25 series 4 hole-wide gusseted inside corner bracket
100	25-1961	M6 slide-in economy T-nut-centered thread
101	13-6312	M6×12 mm button head socket cap screw (BHSCS)
102	14164	10 and 25 series M4 standard drop-in-T-nut
103	XE25T4/M	self centering quick release T-nut, M4 hole
104	TB4	black hardboard, 24×24 inch, 5 mm thick
105	CA3	duster w/integrated nozzle
106	PH30E/M	ϕ12.7 mm pedestal post holder, spring, L=34.7 mm
107	TR30/M-P5	ϕ12.7 mm optical post, M4 set screw, M6, L=30 mm
108	TR40/M-P5	ϕ12.7 mm optical post, M4 set screw, M6, L=40 mm

By NewPort:

109	PAC061	Visible achromat doublet lens, 25.4 mm, f=175 mm, 400-700 nm

By Semrock:

110	Di02-R635-25×36	635 nm laser brightline laser-flat dichroic filter
111	FF01-697/75-25-D	697/75 nm brightline single-band bandpass filter
112	FF01-835/70-25	835/70 nm brightline single-band bandpass filter
113	FF750-SDi02-25×36	750 nm edge brightline single-edge short-pass dichroic beam splitter
114	FF757-Di01-25×36	757 nm edge brightline single-edge short-pass dichroic beam splitter
115	LD01-640/8-12.5	MaxDiode laser cleanup filter